

CONTENS

ADDRESS OF PUBLISHER & EDITOR'S OFFICE:

GDAŃSK UNIVERSITY
OF TECHNOLOGY

Faculty of Ocean Engineering
& Ship Technology
G. Narutowicza 11/12
80-233 Gdańsk, POLAND

tel.: +48 58 347 13 66
fax: +48 58 341 13 66

EDITORIAL STAFF:

Jacek Rudnicki
| Editor in Chief
Przemysław Wierzchowski
| Associate Editor
Rafał Szłapczyński
| Associate Editor
Aleksander Kniat
| Editor for international
relations
Kazimierz Kempa
| Technical Editor

Price:
single issue: 25 zł

Prices for abroad
single issue:
- in Europe EURO 15
- overseas USD 20

WEB:
www.bg.pg.gda.pl/pmr/pmr.php

ISSN 1233-2585

- 3 **Andrzej Chybicki, Marcin Kulawiak, Zbigniew Łubniewski**
*CHARACTERIZING SURFACE AND AIR TEMPERATURE IN THE BALTIC SEA
COASTAL AREA USING REMOTE SENSING TECHNIQUES AND GIS*
- 12 **Sławomir Gajewski**
*DESIGN OF OFDM-BASED RADIO COMMUNICATION SYSTEMS FOR COAST-
TO-SEA AND COAST-TO-AIR PROPAGATION ENVIRONMENTS*
- 20 **Artur Nowicki, Maciej Janecki, Lidia Dzierzbicka-Głowacka,
Mirosław Darecki, Piotr Piotrowski**
*THE USE OF SATELLITE DATA IN THE OPERATIONAL 3D COUPLED
ECOSYSTEM MODEL OF THE BALTIC SEA (3D CEMBS)*
- 25 **Grażyna Grelowska**
*STUDY OF SEASONAL ACOUSTIC PROPERTIES OF SEA WATER
IN SELECTED WATERS OF THE SOUTHERN BALTIC*
- 31 **Witold Gierusz**
*MODELLING THE DYNAMICS OF SHIPS WITH DIFFERENT PROPULSION
SYSTEMS FOR CONTROL PURPOSE*
- 37 **Hanbing Sun, Fengmei Jing, Yi Jiang, Jin Zou, Jiayuan Zhuang,
Weijia Ma**
*MOTION PREDICTION OF CATAMARAN WITH A SEMI-SUBMERSIBLE BOW
IN WAVE*
- 45 **Tomasz Tabaczek, Jan Kulczyk**
*HEELING MOMENT ACTING ON A RIVER CRUISER IN MANOEUVRING
MOTION*
- 52 **Paweł Dymarski, Ewelina Ciba, Tomasz Marcinkowski**
*EFFECTIVE METHOD FOR DETERMINING ENVIRONMENTAL LOADS ON
SUPPORTING STRUCTURES FOR OFFSHORE WIND TURBINES*
- 61 **A.V. Rusanow, P. Lampart, N.V. Pashchenko, R.A. Rusanov**
*MODELLING 3D STEAM TURBINE FLOW USING THERMODYNAMIC
PROPERTIES OF STEAM IAPWS-95*
- 68 **Zbigniew Korczewski**
*EXHAUST GAS TEMPERATURE MEASUREMENTS IN DIAGNOSTICS OF
TURBOCHARGED MARINE INTERNAL COMBUSTION ENGINES
PART II DYNAMIC MEASUREMENTS*
- 77 **Jerzy Kowalski**
*AN EXPERIMENTAL STUDY OF EMISSION AND COMBUSTION
CHARACTERISTICS OF MARINE DIESEL ENGINE WITH FUEL INJECTOR
MALFUNCTIONS*
- 85 **Bogdan Ligaj, Robert Sołtysiak**
*PROBLEMS OF EQUIVALENT LOAD AMPLITUDE IN FATIGUE LIFE
CALCULATIONS*
- 93 **Leszek Knopik, Klaudiusz Migawa, Andrzej Wdzięczny,**
PROFIT OPTIMALIZATION IN OPERATION SYSTEMS

Editorial

POLISH MARITIME RESEARCH is a scientific journal of worldwide circulation. The journal appears as a quarterly four times a year. The first issue of it was published in September 1994. Its main aim is to present original, innovative scientific ideas and Research & Development achievements in the field of :

Engineering, Computing & Technology, Mechanical Engineering,

which could find applications in the broad domain of maritime economy. Hence there are published papers which concern methods of the designing, manufacturing and operating processes of such technical objects and devices as : ships, port equipment, ocean engineering units, underwater vehicles and equipment as well as harbour facilities, with accounting for marine environment protection.

The Editors of POLISH MARITIME RESEARCH make also efforts to present problems dealing with education of engineers and scientific and teaching personnel. As a rule, the basic papers are supplemented by information on conferences , important scientific events as well as cooperation in carrying out international scientific research projects.

Scientific Board

Chairman : Prof. JERZY GIRTLEK - Gdańsk University of Technology, Poland

Vice-chairman : Prof. MIROSLAW L. WYSZYŃSKI - University of Birmingham, United Kingdom

Dr POUL ANDERSEN
Technical University of Denmark
Denmark

Dr MEHMET ATLAR
University of Newcastle United
Kingdom

Prof. GÖRAN BARK
Chalmers University of Technology
Sweden

Prof. SERGEY BARSUKOV
Army Institute of Odessa Ukraine

Prof. MUSTAFA BAYHAN
Süleyman Demirel University
Turkey

Prof. VINCENZO CRUPI
University of Messina, Italy

Prof. MAREK DZIDA
Gdańsk University of Technology
Poland

Prof. ODD M. FALTINSEN
Norwegian University of Science
and Technology
Norway

Prof. PATRICK V. FARRELL
University of Wisconsin Madison,
WI
USA

Prof. WOLFGANG FRICKE
Technical University Hamburg-
Harburg Germany

Prof. HASSAN GHASSEMI
Amirkabir University of Technology
Iran

Prof. STANISŁAW GUCMA
Maritime University of Szczecin
Poland

Prof. ANTONI ISKRA
Poznań University of Technology
Poland

Prof. JAN KICIŃSKI
Institute of Fluid-Flow Machinery
of PASci
Poland

Prof. ZBIGNIEW KORCZEWSKI
Gdańsk University of Technology
Poland

Prof. JANUSZ KOZAK
Gdańsk University of Technology
Poland

Prof. JAN KULCZYK
Wrocław University of Technology
Poland

Prof. NICOS LADOMMATOS
University College London United
Kingdom

Prof. JÓZEF LISOWSKI
Gdynia Maritime University Poland

Prof. JERZY MATUSIAK
Helsinki University of Technology
Finland

Prof. EUGEN NEGRUS
University of Bucharest Romania

Prof. YASUHIKO OHTA
Nagoya Institute of Technology
Japan

Dr YOSHIO SATO
National Traffic Safety and
Environment Laboratory
Japan

Prof. KLAUS SCHIER
University of Applied Sciences
Germany

Prof. FREDERICK STERN
University of Iowa, IA, USA

Prof. ILCEV DIMOV STOJCE
Durban University of Technology
South Africa

Prof. JÓZEF SZALA
Bydgoszcz University
of Technology and Agriculture
Poland

Prof. WITALIJ SZCZAGIN
State Technical University of
Kaliningrad, Russia

Prof. BORIS TIKHOMIROV
State Marine University of St.
Petersburg, Russia

Prof. DRACOS VASSALOS
University of Glasgow and
Strathclyde United Kingdom

CHARACTERIZING SURFACE AND AIR TEMPERATURE IN THE BALTIC SEA COASTAL AREA USING REMOTE SENSING TECHNIQUES AND GIS

Andrzej Chybicki, Ph. D.
Marcin Kulawiak, Ph. D.
Zbigniew Łubniewski, Assoc. Prof.
Gdańsk University of Technology, Poland

ABSTRACT

Estimation of surface temperature using multispectral imagery retrieved from satellite sensors constitutes several problems in terms of accuracy, accessibility, quality and evaluation. In order to obtain accurate results, currently utilized methods rely on removing atmospheric fluctuations in separate spectral windows, applying atmospheric corrections or utilizing additional information related to atmosphere or surface characteristics like atmospheric water vapour content, surface effective emissivity correction or transmittance correction. Obtaining accurate results of estimation is particularly critical for regions with fairly non-uniform distribution of surface effective emissivity and surface characteristics such as coastal zone areas.

The paper presents the relationship between retrieved land surface temperature, air temperature, sea surface temperature and vegetation indices (VI) calculated based on remote observations in the coastal zone area. An indirect comparison method between remotely estimated surface temperature and air temperature using LST/VI feature space characteristics in an operational Geographic Information System is also presented.

Keywords: remote sensing, coastal zone, AVHRR, GIS, surface temperature, air temperature, vegetation index

INTRODUCTION

In general, the acquisition, processing, integration, and visualization of various kinds of remotely registered data involves several important issues, including limitations in accessibility of sensors, the influence of atmosphere (presence of clouds, the need of atmospheric corrections of measured radiance etc.) [6], as well as insufficient spatial resolution or imperfection of models used for derivation of the desired parameters [17], [20], [23]. This fully applies to well-known applications of remote sensing such as land surface temperature (LST) estimation, emissivity estimation or obtaining more advanced indicators of vegetation density. Attempts to derive LST from satellite observations have been ongoing for several decades. They are mainly focused on using polar orbiting systems such as the Advanced Very

High Resolution Radiometer (AVHRR) [3] because of global coverage, relative high spatial resolution, and short revisiting time. However, accurate LST retrievals require precise determination of atmospheric corrections, as well as land surface emissivity [18], [27]. Both of these effects are addressed eg. by the split-window algorithm (split window technique, SWT), which is widely used due its simplicity [25], [26].

While the knowledge of LST estimation and retrieval is generally well established, the relationship between LST and air temperature (T_{air}) is a subject of some of the current scientific activities and achievements in the field of remote sensing. Certain works in this area explore the negative relationship between a vegetation index (VI), defined

either as normalized difference vegetation index (NDVI) or fractional vegetation cover (FVC) index, and LST calculated from satellite thermal channel data. A relationship is defined through regression analysis, and extrapolations are performed to obtain a theoretical VI value that represents a full canopy as viewed by the sensor. In this context, measurements from areas with high vegetation density are important because it was observed that for low thermal mass of the canopy, LST will likely be near the local T_{air} [22]. Many examples of satellite-based T_{air} estimation follow this concept and rely on pixel neighborhood analysis as well as LST/VI relationship.

Because air temperature (obtained e.g. from numerical weather predictions) as well as surface temperature (obtained e.g. via remote sensing) both represent phenomena which take place in a geographical context, the best means of their integration and analysis is offered by a Geographical Information System (GIS), which is a tool for creation, integration, processing and visualization of geographical data. Historically, GIS has many times been applied to integration, processing and dissemination of marine data, including satellite images [15]. In recent years, GIS has been applied to analysis of Global Navigation Satellite System (GNSS) data for the purpose of urban traffic monitoring [13], remote sensing of air and land temperatures [27], temperature monitoring of water balance in India [11] as well as estimating submarine groundwater discharge [28]. However, most of the aforementioned research has been conducted manually, and thus the proposed applications did not form operative systems [16]. At the same time, in [5] it was shown that a GIS is a very effective tool for integration of diverse types of spatial data, while in [30] it was shown that raster data such as satellite images may be successfully investigated by means of Geovisual Analytics. In this context, the application of GIS to comparison of similar data types obtained from diverse sources is a natural consequence.

The paper presents results of a detailed analysis of dependency of T_{air} on LST and VI using LST/VI space properties on a regional scale. A dedicated operational Web-GIS has been applied to direct processing and integration of LST obtained from satellite images with T_{air} obtained from an operational numerical weather prediction (NWP) model. The system processes T_{air} and LST in a geographical context and visualizes the results of their analysis with the aid of Geovisual Analytics. Because the presented method exploits the thermal characteristics of tree canopies, its application may be restricted by the forest coverage as well as length of vegetation blooming season in the analyzed area.

THEORY BACKGROUND

SWT TECHNIQUE

Algorithms of surface temperature (T_s) retrieval from multispectral imagery have been a subject of ongoing studies since the 1970s. Due to wide geographical spread and lack of dense ground in-situ measurements viability, T_s products are difficult to validate and available measurements are usually

scarce and expensive.

For the purpose of T_s estimation, the authors applied the widely described in literature method of SWT (split-window technique) algorithm. The algorithm relies on calculation of brightness temperatures from several satellite channels on the basis of the Planck Law [6], which connects the temperature T_s of a radiating surface with the radiation R_T of the wave length λ by the exponential formula:

$$R_T(\lambda, T_s) = \frac{c_1 \lambda^{-5}}{\exp\left(\frac{c_2}{\lambda T_s}\right) - 1}, \quad (1)$$

where $c_1 = 1.19104 \cdot 10^8 \text{ W } \mu\text{m}^4 \text{ m}^{-2} \text{ sr}^{-1}$ and $c_2 = 1.43877 \cdot 10^4 \text{ } \mu\text{m K}$ are the first radiation constant (for spectral radiance) and second radiation constant respectively. $R_T(\lambda, \text{LST})$ is given in $\text{W m}^{-2} \text{ sr}^{-1} \mu\text{m}^{-1}$ if the wavelength is given in μm .

In the SWT algorithm, the first-order Taylor series expansion of the Planck Law is used, which allows for linear approximation of the relation between radiance and temperature. Then, the pixel values from satellite channels representing surface temperature are combined (in the case of AVHRR, the 4th and 5th channel, which carry the 10.30 – 11.30 μm and 11.50 – 12.50 μm wavelengths, respectively), taking into account the atmospheric conditions and emissivity correction for particular channels. The simplified form of the base SWT equation for base land surface temperature T estimation may be written as follows:

$$T = T_4 + A_{SWT} + B_{SWT} (T_4 - T_5), \quad (2)$$

where T_4, T_5 - brightness temperature values in $^{\circ}\text{C}$ for 4th and 5th AVHRR channel respectively, and A_{SWT}, B_{SWT} are coefficients that depend on atmospheric transmittances.

This base LST estimation algorithm has been further improved by applying additional rules which define a more complex relation of AVHRR channel radiations to land surface emissivity and atmospheric transmittance.

EMISSIVITY ESTIMATION

According to methodology presented in [14] and [25], it was assumed that the average land emissivity for 4th and 5th AVHRR channel ϵ_{avr} and the difference of these channels emissivities $\Delta\epsilon$ are calculated on the basis of NDVI. Namely, for $0.2 < \text{NDVI} < 0.5$ the ϵ_{avr} and $\Delta\epsilon$ are calculated using the following formulae:

$$\epsilon_{avr} = 0.971 - 0.018 P, \Delta\epsilon = 0.006 (1 - P), \quad (3)$$

where

$$P = \frac{(\text{NDVI} - 0.2)^2}{0.09}, \quad (4)$$

whereas for $\text{NDVI} > 0.5$ they are fixed as:

$$\varepsilon_{avr} = 0.985, \quad \Delta\varepsilon = 0. \quad (5)$$

However, because these rules only apply to areas which exhibit dense vegetation, the pixels for which the NDVI values are less than 0.2 must be discarded from further analysis (e.g. via masking).

CLOUD SCREENING

In order to remove undesirable (cloud contaminated) pixels from the scene, the approach proposed in [23] was implemented. According to this method, during the analysis of AVHRR imagery, pixels were masked out and not included in further calculations of LST if they met any of the following criteria:

- 1) channel 1 reflectance (RED) > 0.2,
- 2) $Q = \frac{NIR}{RED} < 1.2$,
- 3) $T_4 - T_5 < -1.5^\circ\text{C}$ or $T_4 - T_5 > 4.5^\circ\text{C}$.

T_5 ESTIMATION

Finally, considering calculated water vapour and emissivity, the land surface temperature (LST) is estimated as [24]:

$$LST = T_4 + 1.4 \cdot (T_4 - T_5) + 0.32 \cdot (T_4 - T_5)^2 - 0.83 + (57 - 5W) \cdot (1 - \varepsilon_{avr}) - (161 - 30W) \cdot \Delta\varepsilon \quad (6)$$

In order to estimate sea surface temperature (SST) the McClain formula was applied:

$$SST = D_1 \cdot T_4 + D_2 \cdot (T_4 - T_5) + D_3 \cdot (T_4 - T_5)^2 + D_4 \cdot (\sec(\varphi) - 1), \quad (7)$$

where φ is satellite zenith angle. The D_1 , D_2 , D_3 and D_4 coefficient values are adjusted basing on the modelled dependencies of AVHRR channel 4 and 5 values on atmospheric transmittance, as well as comparison of the currently processed image results with reference data if available.

LST/VI SPACE

The features of LST/VI space have been under the consideration of researchers since early 1980s. The characteristic semi-triangular or trapezoidal shape of the LST/VI scatterplot is caused by low sensitivity of LST to soil moisture variations over vegetated areas, and its higher sensitivity (and thus greater spatial variation) over areas of less vegetation and bare soil.

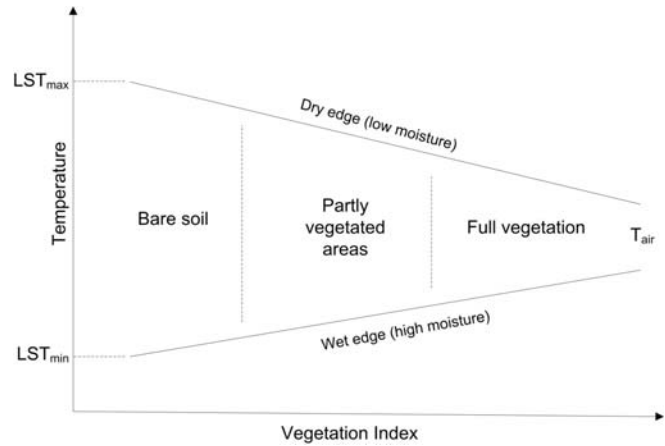


Fig. 1. Graphical representation of LST/VI feature space with key descriptors and physical interpretation

As shown in Fig. 1, the upper border of the triangle shape is the so-called “dry edge” or “warm edge” defined by the locus of points with highest LST, but which contain a differing mix of bare soil and vegetation. For the points located at or near the “dry edge”, the latent energy flux due to evapotranspiration is assumed to be equal or close to zero, and the direction of the sensible heat flux is from the soil and vegetation to the air, with decrease of its absolute value from the left to the right side of the LST/VI plot. Likewise, the bottom edge, often referred as “wet edge” or “cold edge”, corresponds to the set of pixels with lowest LST that have varying amounts of vegetation cover and are characterized by the maximum soil water content. For the points located at or near this edge, the latent energy flux due to evapotranspiration is assumed to be maximum within the area of a given VI value range, and the direction of the sensible heat flux is from the air to the soil and vegetation, with decrease of its absolute value from the left to the right side of the LST/VI plot.

The area on the left side of the triangle is assumed to reflect the combined effects of soil water content and topography variations across areas of bare soil, while the right side (and especially the triangle’s apex) equates to the status of full vegetation cover. The points filling the interior of the triangular space represent pixels with varying vegetation cover, somewhere between bare soil and dense vegetation. Note that, for data points having the same or close VI values, LST can range markedly. The explanation of this phenomena is that for an area well supplied with water, transpiration acts to cool vegetation very effectively, but as vegetation undergoes water stress the plant tends to close its stomata – with the resulting transpiration decrease leading to an increase of leaf temperature. Thus, for pixels with the same VI, those with minimum LST are assumed to have the strongest evaporative cooling, while those with maximum LST represent those with the weakest evaporation. Therefore, the “dry edge” of the shape is considered to represent the upper limit of evaporation for the different vegetation conditions found within investigated area, whereas the reverse is implied for the “cold edge”.

DATA DESCRIPTION

STUDY AREA

The presented study was conducted for the territory of the Gulf of Gdańsk, localized in the Pomorskie Voievodship of Poland, on the Southern shores of the Baltic Sea. The elevation in the area ranges from 1.8 m below sea level in the Vistula marshes to 329 meters above sea level delimited by the Wieżyca peak. Most of the voievodship (55%) is composed of coastal areas. The remaining 45% is spread between agriculture (19%), vegetation such as coniferous forest, mixed forest or natural grasslands (16%), urban areas (8%) and others (2%). The average summer daily temperatures in the area hover around 16.5 °C. The average annual precipitation ranges between 400 mm and 600 mm, which makes for some diverse hydrological and vegetation conditions.

A geographical view of the investigated area is given in Fig. 2.

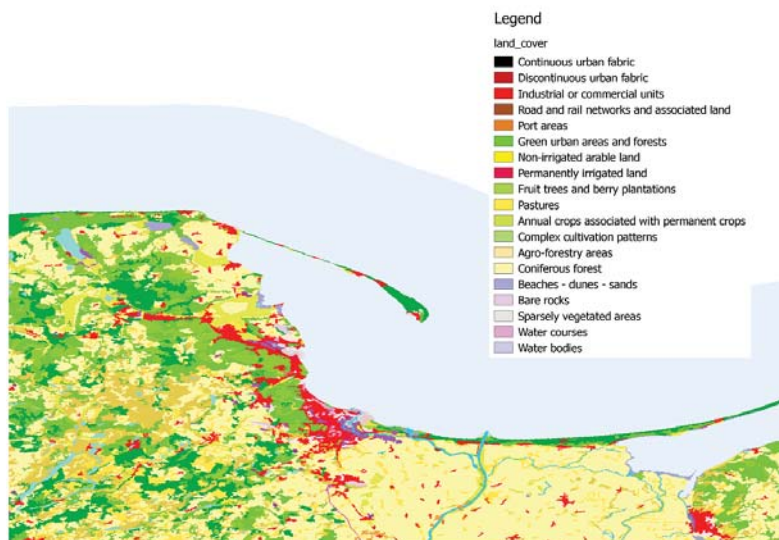


Fig. 2. Map of the analysed area. Spatial distribution of land surface types, source: Corine Land Cover data (2006)

IN-SITU OBSERVATION

Air temperature observations in the presented research were retrieved from the Land SYNOP station network which transmits observations, made on land, in the form recommended by WMO (World Meteorological Organization) standards as a SYNOP message. Currently, WMO station network consists of over 10.000 synoptic stations all over the world, and over 60 in the territory of Poland, producing hourly, 3-hour and 6-hour reports. The distribution of observation stations is far from being uniform, and does not take into account the spatial structure of environment conditions. Because of this in many situations the interpolation of meteorological air temperature observations in order to obtain data in high resolution grid may not produce satisfying results.

WRF

An alternative method for obtaining air temperatures for regional and local scale applications employs the use of numerical weather prediction models such as the Weather Research and Forecast (WRF) model. WRF is a next-generation mesoscale model, designed and developed by several organizations, such as the National Center for Atmospheric Research (NCAR), National Centers for Environmental Prediction (NCEP), National Oceanic and Atmospheric Administration (NOAA), National Aeronautics and Space Administration (NASA), Air Force Weather Agency (AFWA), and a number of collaborating institutes and universities.

Meteorological data from an NWP can be helpful during model fitting in evapotranspiration estimation, i.e. in methods for water vapour content retrieval using low resolution multispectral imagery [4], modelling solar radiation [21], radiometric correction within multispectral imaging and others.

The WRF instance used in this study was installed and configured internally at the Department of Geoinformatics in the Faculty of Electronics, Telecommunications and Informatics of Gdańsk University of Technology. The model is ran operationally by the Department since 2011. The process of configuration and adjustment of the model for local conditions was performed for several years in order to properly establish and optimize several important elements, including the parameterization scheme, microphysics scheme, surface energy flux scheme, computing grid spatial (vertical and horizontal) resolution, computing domain localisation and nesting. In the current configuration the system generates 48-hour forecasts, four times per every 24-hour operating period. The forecasts are produced in a 4 km local domain, nested in a 12 km grid regional domain. The boundaries between the local and regional domain are presented in Fig. 3. The model utilizes Grell-Devenyi ensemble parameterization scheme [10], Ferrier operational microphysics scheme [8], Noah Land Surface Model physics scheme [2] unified by NCEP/NCAR/AFWA and GFDL radiation scheme [7]. Initialization and boundary conditions data is retrieved from GFS model downloaded from NCEP online services which also provide SST in their RTG_SST_HR product i.e. for the Baltic Sea.

AVHRR

Satellite data used in the presented research was obtained from a dedicated 1.5m-wide HRPT/MetOp-A/B local satellite ground station, operated by the Department. The NOAA/MetOp AVHRR imagery is retrieved from the satellite station High Resolution Picture Transmission (HRPT) stream and converted to GeoTIFF data files in spatial resolution 1.1 km by 1.1 km per pixel. The range of recorded photographs entirely

covers the study area described in section 3.1. The applied cartographic projection is Lambert Azimuth Equal Area (LAEA) with 19°E and 52°N as central meridian and central parallel respectively (geometric centre of researched area). The HRPT stream also contains information about solar zenith [°], solar azimuth [°], nadir to pixel [°], satellite inclination [°] and raw and calibrated data for channels 1-5, which can be utilized in other applications of remote sensing techniques.



Fig. 3. The boundaries between the local domain (4 km resolution) and regional domain (12 km resolution) used in the applied instance of the WRF model

ALGORITHM IMPLEMENTATION ENVIRONMENT

In order to automate the process of data analysis, the authors have developed an operational system which integrates data from the AVHRR satellite station as well as results of numerical weather predictions in a common geographical context. The general architecture of the system is shown in Fig. 4.

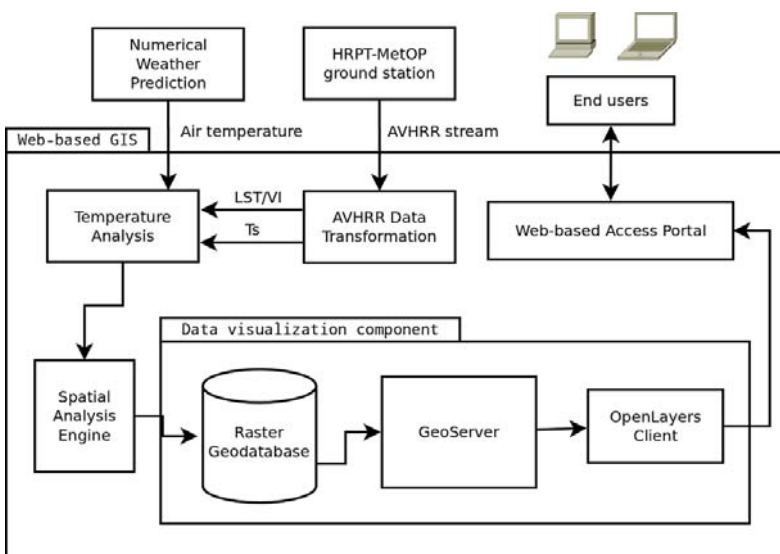


Fig. 4. Architecture of the GIS for integration and analysis of temperature data from different sources

The system consists of several modules, each responsible for specific functionality. Data from two external sources (the WRF Numerical Weather Prediction model and HRPT-MetOp satellite ground station, namely) is acquired and processed inside a Web-based Geographic Information System in order to accurately perform their analysis. First, data from HRPT-MetOp ground station is transformed from a HRPT stream to a geospatial data format. Then, the Temperature Analysis module imports the results of Numerical Weather Prediction for the same date and hour in rotated lat/lon projection and transforms it to common Lambert Azimuth Equal Area (LAEA) projection in the same spatial resolution as the obtained AVHRR data. The module then obtains LST/VI parameters of the analysed scene. The module produces georeferenced imagery of T_s and T_{air} in LAEA projection, which is passed on to the Spatial Analysis Engine. The Spatial Analysis Engine uses Geovisual Analytics to perform temperature consistency analysis between the source images. The results are stored in a spatial geodatabase from which they are retrieved by the GeoServer, which is a Web Map server with excellent support for open standards of spatial data exchange such as OGC Web Feature Service and Web Map Service. The latter is used to serve thematic layers to the Web GIS client, which uses the Open Source OpenLayers javascript library to provide the end users with a rich GIS functionality inside a standard Web browser, without the need for additional plugins. Through the client, the users may view the results of the latest temperature consistency analysis and compare them to source data or available satellite imagery at any given time.

RESULTS

The main goal of the presented research was to analyse the relationship between air temperature obtained from NWP and surface temperature retrieved from AVHRR imagery in the context of LST/VI space properties for a region with high surface type diversity. As it is known, there is significant correlation between these two quantities, however not much

attention has been paid to this subject. In general, air temperature is less spatially variable than LST. This being said, air temperature depends to a greater extent on global weather conditions than on surface characteristics and incoming radiation. Verification of air temperature estimation is relatively easy, as it can be compared with in-situ observations from SYNOP. However, verification of LST estimation causes serious difficulties due to wide geographical spread, spatial resolution of radiometer, atmospheric fluctuations etc.

Obtaining good quality AVHRR datasets for the region of Central Europe is not a trivial task due to the fact that during most of the vegetation blooming season the atmosphere contains a large amount of water vapour and clouds. High relative air humidity (60-80%) during the day causes variations in atmosphere transmittance which in turn affects values recorded by satellite thermal channels

and makes LST retrieval less accurate. This makes it hard to retrieve non-cloud-contaminated datasets for most of the considered period.

First stage of work was focused on calculating the results of LST/VI space for the analysed scene (Fig. 5).

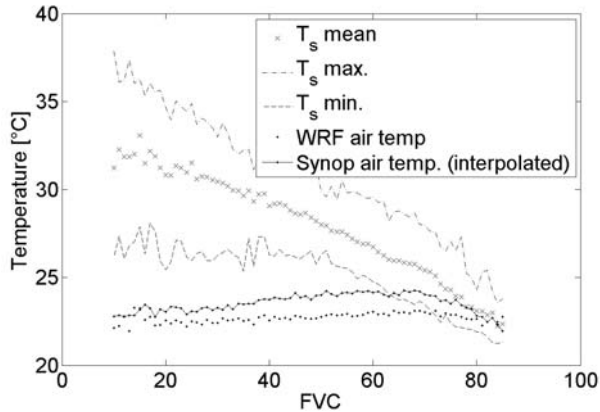


Fig. 5. LST/VI space graphic representation containing LST data, WRF NWP air temperature (T_{air}) and interpolated SYNOP observation data

In the presented case, average air temperature (from NWP and SYNOP stations) was about 23 °C. As expected, LST values were higher than T_{air} values due to high radiation (300-500 W/m²) caused by cloudless sky conditions and high sun zenith angle. According to Fig. 5, a significant rise of LST along with decreasing vegetation (expressed as fractional vegetation index) can also be observed. The presented results also appear to confirm the hypothesis that T_{air} and LST are equal for high vegetation areas. This applies to WRF T_{air} and SYNOP observation as well.

Since the respected region consists of highly diverse surface types (forests, urban areas, agriculture, sea and others), a dedicated procedure of T_s estimation was proposed. In order to estimate surface temperature for this diversified region, the satellite images acquired directly from a ground station were processed by the dedicated GIS which applied two separate masks: one mask that removes pixels that contain sea area, and a second mask that removes pixels of land surface area. Both masks also remove pixels contaminated with clouds. Once the area has been separated into land and sea, the land region is analysed using the LST estimation procedure described in [5], [6], [9], while the sea area is processed using the algorithm defined in [11] for SST estimation. After both procedures are accomplished, the hybrid result (containing data from both sources) is returned in the form of a single product. The resulting thematic layer, made available via the GIS Web Map Service, contains surface temperature (T_s) which is presented in Fig. 6.

This particular type of product is styled using a standard temperature colour bar in which areas of low temperature are represented in dark blue, and the hottest areas are coloured in dark red. This allows for easier analysis and interpretation of the produced data.

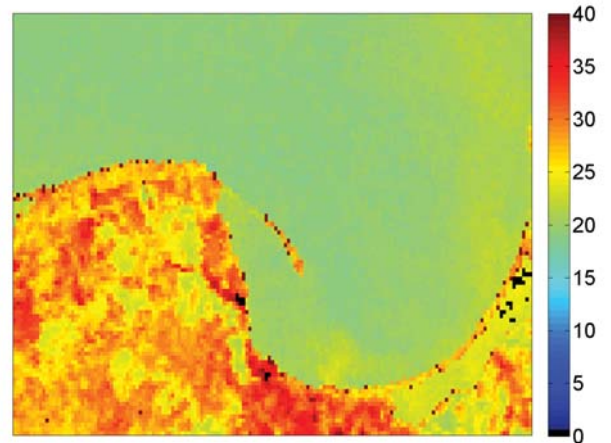


Fig. 6. Surface temperature (T_s) estimation using hybrid approach. Black pixels represent areas where due to low resolution of source data the algorithm was unable to categorize the pixel as neither land nor sea type.

The close integration of both satellite (T_s) and weather prediction model (T_{air}) data in a geographical context allows for their advanced analysis via Geovisual Analytics. Thus, for every pixel of data in the AVHRR image, the GIS retrieves the respective pixel of WRF data and performs their consistency analysis. The resulting images form a time series in the Web GIS and may be viewed by means of WMS with a TIME parameter. This allows one to not only view temperature consistency for selected dates in an organized manner, but also enables analysis of differences between times of day as well as over longer time periods. Fig. 6 shows a sample comparison of difference between T_{air} and T_s for the analysed scene within the Web-GIS client. By implementing the paradigms of Geovisual Analytics, the resulting image depicts the level of difference using user-perceptual Ordinal Pseudocolor Sequencing. Areas where the difference is less than 1 °C are marked in green, while larger differences are marked in yellow (2-3 °C), orange (3-4 °C) and red (greater than 5 °C).

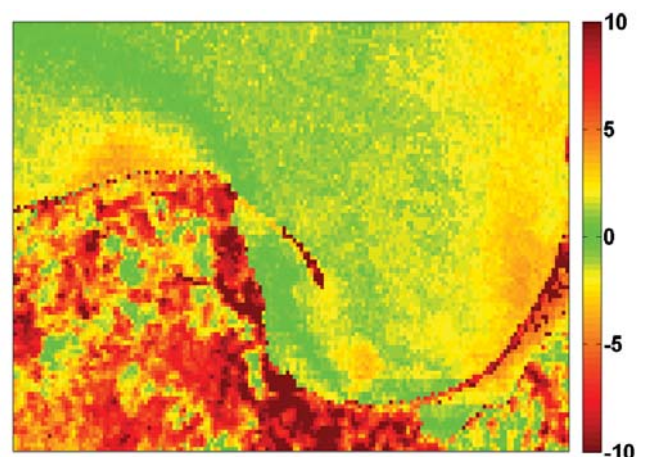


Fig. 7. Geovisual Analysis of difference between modelled T_{air} and T_s for investigated region

As it can be seen in Fig. 7, in the analysed coastal area of the Gulf of Gdańsk there are several areas which exhibit very high similarities between surface temperature (T_s) obtained from

the AVHRR sensor and air temperature (T_{air}) produced by the WRF model. In particular, although the differences between T_s and T_{air} often exceed 5 °C and reach as high as 10 degrees in some areas, there are certain places in which the gap between both values virtually disappears. The nature of this phenomenon over land can be easily discerned by comparing the geographical layout of the temperature differences with the vegetation coverage of the area, as depicted in Fig. 8.

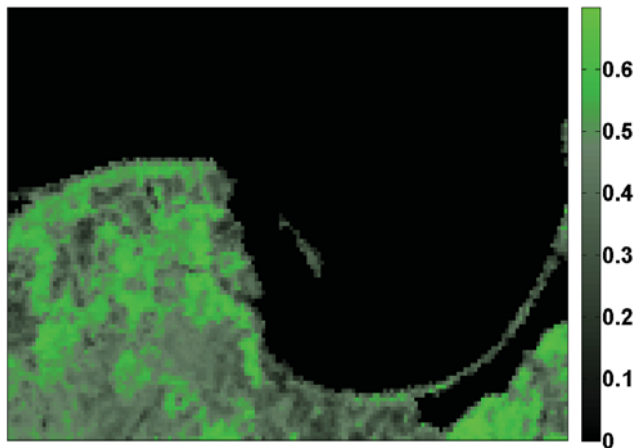


Fig. 8. NDVI spatial distribution for investigated area

As it can be observed, the biggest difference between T_{air} and T_s is noticeable for land regions with sparse vegetation (low FVC). In this case LST is higher than T_{air} by more than 5 °C. At the same time, the smallest differences may be observed for densely vegetated areas (shown in light green in Fig. 8) and areas of the Baltic Sea basin.

CONCLUSIONS

The presented work deals with the important problem of air temperature estimation using remote sensing techniques. The described research methodology uses an automated Web-GIS with direct access to AVHRR images from a satellite ground station as well as data from an operational NWP model. The images provide information on land surface properties with relatively good temporal resolution, while having moderate spectral and spatial resolution at the same time. In most meteorological applications AVHRR provides information on water temperature, cloud properties or land emissivity temperature etc. However, it does not provide information about air temperature. The presented GIS integrates results of satellite temperature analysis in a geographical context and enables their automated comparison to temperature estimation obtained from the numerical weather model. The results of the presented analysis are presented in semi-real time in the form of thematic layers, generated in accordance to the paradigms of Geovisual Analytics. The obtained results support the hypothesis that air temperature and surface temperature are equal for high vegetation areas, which has also been verified using SYNOP observations.

It should be noted that because the presented approach analyses the relationship between the values of air and surface

temperatures by exploiting the thermal characteristics of tree canopies, its application may be restricted by the forest coverage as well as length of vegetation blooming season in the analyzed area. This being said, the presented results prove that properties of LST/VI space can provide information for air temperature estimation, particularly for areas with a highly diverse distribution of surface type.

REFERENCES

1. Chen F., Dudia J.: Coupling an advanced land-surface / hydrology model with the Penn State/NCAR MM5 modeling system. *Monthly Weather Review*, 129/2001, 569-585.
2. Chen, F., K. Mitchell, J. Schaake, Y. Xue, H. Pan, V. Koren, Y. Duan, M. Ek, and A. Betts, 1996: Modeling of land-surface evaporation by four schemes and comparison with FIFE observations. *J. Geophys. Res.*, 101, 7251-7268.
3. Cracknell A. P.: *The Advanced Very High resolution Radiometer (AVHRR)*. Taylor and Francis, 1997.
4. Cristobal J., Poyatos R., Ninyerola M., Llorens P.: Combining remote sensing and GIS climate modelling to estimate daily forest evapotranspiration in a Mediterranean mountain area. *Hydrology and Earth System Sciences Discussions*, 15/2011, 1563-1575.
5. Dąbrowski J., Kulawiak M., Moszyński M., Bruniecki K., Kamiński Ł., Chybicki A., Stepnowski A.: Real-time web-based GIS for analysis, visualization and integration of marine environment data. In: *Information Fusion and Geographic Information Systems*, Springer Berlin Heidelberg, 2009, 277-288.
6. Dash P.: *Land Surface Temperature and Emissivity Retrieval from Satellite Measurements*. Institut fur Meteorologie und Klimaforschung, 2005.
7. Donner L. J., Wyman B. L., Hemler R. S., Horowitz L.W., Ming Y., Zhao M., Golaz J.-C., Ginoux P., Lin S.-J., Schwarzkopf M. D., Austin J., Alaka G., Cooke W. F., Delworth T. L., Freidenreich S. M., Gordon C. T., Griffies S. M., Held I. M., Hurlin W. J., Klein S. A., Knutson T. R., Langenhorst A. R., Lee H.-C., Lin Y., Magi B. I., Malyshev S. L., Milly P. C., Naik V., Nath M. J., Pincus R., Ploshay J. J., Ramaswamy V., Seman C. J., Shevliakova E., Sirutis J. J., Stern W. F., Stouffer R. J., Wilson R.J., Winton M., Wittenberg A. T., Zeng F.: The dynamical core, physical parameterizations, and basic simulation characteristics of the atmospheric component AM3 of the GFDL Global Coupled Model CM3. *Journal of Climate*, 24(13)/2011, 3484-3519.
8. Ferrier B. S., An efficient mixed-phase cloud and precipitation scheme for use in operational NWP models, *Eos, Trans. Amer. Geophys. Union*, 86(18)/2005.

9. Gillies R. R., Carlson T. N., Cui J., Kustas W. P., Humes K. S.: Verification of the 'triangle' method for obtaining surface soil water content and energy fluxes from remote measurements of the Normalized Difference Vegetation Index NDVI and surface radiant temperature. *International Journal of Remote Sensing* 18/1997, 3145-3166.
10. Grell, G. A., D. Devenyi: A generalized approach to parameterizing convection combining ensemble and data assimilation techniques. *Geophys. Res. Lett.*, 29/2002, 1693-1696.
11. Jain S. K., Hariprasad V., Choudhry A.: Water Balance Study for a Basin Integrating Remote Sensing Data and GIS. *Journal of the Indian Society of Remote Sensing* 39/2011, 259-270.
12. Janjic Z. I., Gerrity J. P., Nickovic S.: An Alternative Approach to Nonhydrostatic Modeling. *Monthly Weather Review*, 129/2001, 1164-1178.
13. Janowski A., Nowak A., Przyborski M., Szulwic J.: Mobile indicators in GIS and GPS positioning accuracy in cities. In: *Rough Sets and Intelligent Systems Paradigms*, Springer International Publishing, 2014, 309-318.
14. Julien Y., Sobrino J. A., Mattar C., Ruescas A. B., Jimenez-Munoz J. C., Soria G., Hidalgo V., Atitar M., Franch B., Cuenca J.: Temporal analysis of normalized difference vegetation index (NDVI) and land surface temperature (LST) parameters to detect changes in the Iberian land cover between 1981 and 2001. *International Journal of Remote Sensing*, 32/2011, 2057-2068.
15. Kulawiak M., Chybicki A., Moszyński M.: Web-based GIS as a tool for supporting marine research. *Marine Geodesy*, 33/2010, 135-153.
16. Kulawiak M., Łubniewski Z.: SafeCity - A GIS-based tool profiled for supporting decision making in urban development and infrastructure protection. *Technological Forecasting and Social Change*, 89/2014, 174-187.
17. Lillesand T. M., Kiefer R. W.: *Remote Sensing and Image Interpretation*. John Wiley, New York, 1987.
18. McClain E. P., Pichel W. G., Walton C. C.: Comparative performance of AVHRR-based multichannel sea surface temperatures. *Journal of Geophysical Research*, 90/1985, 11587-11601.
19. Michalakes J., Dudhia J., Gill D., Henderson T., Klemp J., Skamrock W., Wang W.: *The Weather Research and Forecast Model: Software Architecture and Performance*. Proceedings of the 11th ECMWF Workshop on the Use of High Performance Computing in Meteorology, 25-29 October 2004, Reading, U.K., Ed. George Mozdzynski.
20. Moszyński M., Kulawiak M., Chybicki A., Bruniecki K., Bieliński T., Łubniewski Z., Stepnowski A.: Innovative Web-Based Geographic Information System for Municipal Areas and Coastal Zone Security and Threat Monitoring Using EO Satellite Data, *Marine Geodesy*, Volume 38(3)/2015, 203-224.
21. Pons X., Ninyerola M.: Mapping a topographic global solar radiation model implemented in a GIS and refined with ground data. *International Journal of Climatology* 28/2008, 1821-1834.
22. Prihodko L., Goward S. N.: Estimation of air temperature from remotely sensed surface observations. *Remote Sensing of Environment*, 60/1997, 335-346.
23. Qin Z., Dall'Olmo G., Karnieli A., Berliner P.: Derivation of split window algorithm and its sensitivity analysis for retrieving land surface temperature from NOAA Advanced Very High Resolution Radiometer data. *Journal of Geophysical Research: Atmospheres* (1984-2012), 106/2001, 22655-22670.
24. Riddering J. P., Queen L. P.: Estimating near-surface air temperature with NOAA AVHRR. *Canadian Journal of Remote Sensing*, 32/2006, 33-43.
25. Sobrino J. A., Raissouni N.: Toward remote sensing methods for land cover dynamic monitoring: application to Morocco. *International Journal of Remote Sensing* 21/2000, 353-366.
26. Ulivieri C., Castronuovo M. M., Francioni R., Cardillo A.: A split window algorithm for estimating land surface temperature from satellites. *Advances in Space Research*, 14/1996, 279-292.
27. Vidal A.: Atmospheric and emissivity correction of land surface temperature measured from satellite using ground measurements or satellite data, *International Journal of Remote Sensing*, 12/1991, 2449-2460.
28. Wilson J., Rocha C.: Regional scale assessment of Submarine Groundwater Discharge in Ireland combining medium resolution satellite imagery and geochemical tracing techniques. *Remote Sensing of Environment*, 119/2012, 21-34.
29. Zheng X., Zhu J., Yan Q.: Monthly Air Temperatures over Northern China Estimated by Integrating MODIS Data with GIS Techniques. *Journal of Applied Meteorology and Climatology*, 52/2013, 1987-2000.
30. Zurita-Milla R., Blok C., Retsios V.: Geovisual analytics of Satellite Image Time Series. *International Environmental Modelling and Software Society (iEMSs) 2012 International Congress on Environmental Modelling*

and Software. Managing Resources of a Limited Planet:
Pathways and Visions under Uncertainty, Sixth Biennial
Meeting, Leipzig, Germany, 2012.

CONTACT WITH THE AUTHOR

Andrzej Chybicki

Gdańsk University of Technology
Narutowicza street 11/12
80-233 Gdańsk, Poland,
telephone: +48 58 347 13 26
e-mail: andrzej.chybicki@pg.gda.pl
POLAND

DESIGN OF OFDM-BASED RADIO COMMUNICATION SYSTEMS FOR COAST-TO-SEA AND COAST-TO-AIR PROPAGATION ENVIRONMENTS

Sławomir Gajewski, Ph. D.

Gdańsk University of Technology, Poland

ABSTRACT

In the paper the study of radio communication system design process for systems based on OFDM transmission is considered. The signal propagation model for 1.4 GHz frequency band is discussed, and the study of signal propagation characteristics, important from the point of view of OFDM system design, is presented. The methodology of OFDM interface design is proposed and some characteristics of the OFDM-based radio communication system are analysed.

Keywords: marine radio communication; wave propagation at sea; ground-to-sea communication; ground-to-air communication; OFDM system design; safety at sea.

INTRODUCTION

Nowadays the problem of radio communication systems design for maritime applications is very important. It is necessary for the implemented modern wideband systems to enable high-rate data transmission in internet communication and multimedia services. It is commonly agreed that the most interesting signal transmission technique for high-rate data transmission is the OFDM technique, used in the most modern cellular system, called LTE.

This study presents the principle of the use of OFDM technique for design of a wideband radio communication system for maritime applications, especially for A1 sea area, and discusses benefits from its use.

From the point of view of this study some assumptions have been made. First, the frequency band of signals transmitted over the radio communication channel is set equal to 10 MHz, which corresponds to one of the most frequently used bands in the LTE public cellular system. This assumption makes it possible to compare the presently obtained results to those achieved for the LTE system.

The centre frequency of the proposed system is set to 1.4 GHz. The use of wideband channel means that the signal transmission is done in a frequency-selective multipath channel, which affects the transmission conditions and signal performance. A characteristic transmission feature is that the connection is realized between 2 antennas. The first antenna is localised on the coast, approximately 15 m above the ground, while the second antenna is localised on a ship in the case of the coast-to-sea channel, or on a plane or helicopter (the coast-to-air channel, above the sea). In both cases the same 2-ray propagation model is used [1]. A possible high speed of the plane determines great values of Doppler spread and this is the main difference between these two propagation environments.

The proposed design methodology can be used for adapting modern high-speed data communication systems to maritime applications.

RADIO WAVE PROPAGATION

The 2-ray propagation model is one of the most often used models for radio-wave propagation in both the coast-to-sea and coast-to-air propagation environment. Also propagation measurements in these environments give, in general, similar results.

Using this model we take into account 2 components of the multipath signal propagation. The 1-st is the LOS (line-of-sight) component and the 2-nd is the component reflected from the surface of the sea [1-7].

The model is considered in 2 versions depending on the designed radio station range. The first version is applied when the curvature of the Earth is to be taken into account, and the second - when the surface is assumed flat.

The impulse response of this channel model is given by

$$h(t, \tau) = \alpha_0(t)\delta(\tau - \tau_0) + \alpha_s(t)e^{-j2\pi\frac{\Delta R_k}{\lambda}}\Gamma(t)\delta(\tau - \tau_0) \quad (1)$$

when:

$\alpha_0(t)$ – complex component representing the amplitude of the LOS component,

$\alpha_s(t)$ – complex component representing the reflected component amplitude,

$\Gamma(t) = \frac{\sin\theta - X}{\sin\theta + X}$ – reflection coefficient from the sea surface,

$e^{-j2\pi\frac{\Delta R_k}{\lambda}}$ – variable representing the phase shift between the LOS component and the reflected component, depending on the shift $\Delta R_k = X + X' - l$ relative to the wavelength λ .

The 2-ray model is presented in Fig. 1, where we can find interpretations of formulas for $I(t)$ and ΔR_k (see the model for flat Earth).

In the case of coastal transmission it is possible to receive some additional components reflected from coast obstacles. But the results presented in [1-7] show that they are not important from the point of view of OFDM system design presented in this paper.

PATHLOSS MODELS FOR 1 GHZ (L-BAND) AND 5 GHZ (C-BAND)

It is very difficult to find publications discussing the issue of loss modelling in systems similar to that analysed in the paper. We can find suitable models in [4-6]. The most recent research which best corresponds to the analysed model of the system was done by NASA [8-9].

The present research concerns the communication between the coast radio station and unmanned aerial vehicles. This research area is very popular nowadays. The research was done on the basis of 2-ray curved-Earth channel model (CE2R). In this model we take into account radio wave reflections from the waving surface of the sea (salty water).

The radio wave reflection from the irregular sea surface may be a reason why waves reach the receiver with large phase-shifts. Thus, it is assumed that the radio wave reaches the receiver as a direct component (LOS) and components reflected from the surface of the water.

The studies take into account the measurements of the radio wave attenuation with deviation dependent on many factors, in particular: water undulation, non-ideal characteristics of the antennas, occasional recording of additional multipath signal components in the receiver (in addition to those corresponding to LOS and the reflected wave), and slow signal strength fluctuations caused by imperfections of the measuring instruments.

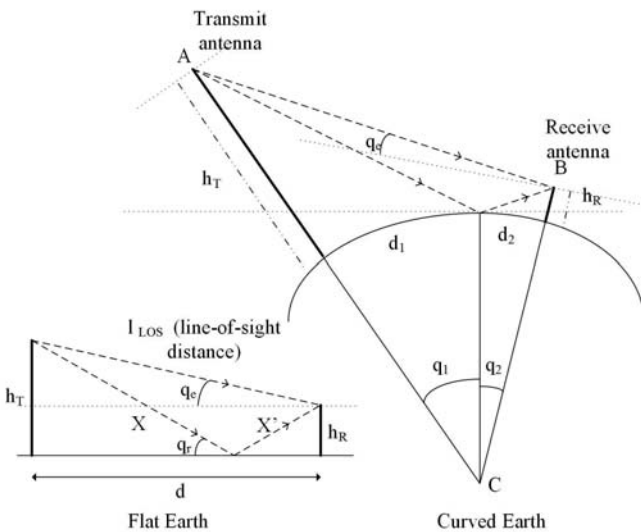


Fig. 1. 2-ray propagation model for flat and curved Earth

As a result, the here proposed propagation models (under the sea surface) are given by formulas (2-4), with parameters shown in Table 1 and Table 2 [8].

For 1 GHz band we have:

$$L(d, \theta) = \begin{cases} A_{0,L,s} + 10n_{L,s} \log(d) + X_{L,s} + \zeta L_{L,s} & \theta \geq \theta_t (d \geq d_t) \\ L_{CE2R} + L_0 + X_{L,l} + \zeta L_{L,l} & \theta < \theta_t (d < d_t) \end{cases} \quad (2)$$

where

$$L_{CE2R} = 20 \log\left(\frac{4\pi d}{\lambda}\right) - 20 \log\left(1 + D\Gamma_p e^{-j\frac{2\pi\Delta R}{\lambda}}\right) \quad (3)$$

And for 5 GHz band we have:

$$L(d, \theta) = \begin{cases} A_{0,C,s} + 10n_{C,s} \log(d) + X_{C,s} + \zeta L_{C,s} & \theta \geq \theta_t (d \geq d_t) \\ A_{0,C,l} + 10n_{C,l} \log(d) + X_{C,l} + \zeta L_{C,l} & \theta < \theta_t (d < d_t) \end{cases} \quad (4)$$

The used parameters are as follows:

- $A_{0,L,s}$ – propagation constant for 1 GHz band,
- $n_{L,s}$ – power of signal loss for 1 GHz band,
- $L_{L,s}$ – correction factor for 1 GHz frequency band,
- d – distance between antennas,
- $X_{L,s}, X_{L,l}$ – Gaussian variables of zero mean value and standard deviations $\sigma_{X_{L,s}}$ [dB] and $\sigma_{X_{L,l}}$ [dB], respectively,
- ζ – constant depending on the direction of vehicle motion: from the coast station to the vehicle $\zeta = 1$ or to the coast station $\zeta = -1$,
- L_{CE2R} – signal loss for the CE2R model and the instantaneous current location of antennas.
- L_0 – correction factor for the CE2R model,
- $L_{L,l}$ – correction factor for 1 GHz,
- λ – wave length,
- D – divergence factor due to spherical Earth shape,
- Γ_p – surface reflection coefficient, with the subscript p denoting the impinging wave polarization,
- ΔR – relative path length difference between LOS and surface reflection,
- $\sigma_{X_{L,s}}$ – standard deviation of the $X_{L,s}$ random variable representing signal fluctuations,
- $\sigma_{X_{L,l}}$ – standard deviation of the $X_{L,l}$ random variable representing slow signal fluctuations,
- $A_{0,C,s}$ – propagation constant for 5 GHz band,
- $n_{C,s}$ – power of signal loss for 5 GHz,
- $X_{C,s}, X_{C,l}$ – Gaussian variables of zero mean value and standard deviations $\sigma_{X_{C,s}}$ [dB] and $\sigma_{X_{C,l}}$ [dB], respectively,
- $L_{C,s}$ – correction factor for 5 GHz,
- $\sigma_{X_{C,s}}$ – standard deviation of $X_{C,s}$ random variable representing slow signal fluctuations,
- $\sigma_{X_{C,l}}$ – standard deviation of $X_{C,l}$ random variable representing slow signal fluctuations,
- $A_{0,l}$ – propagation constant for 5 GHz,
- $n_{C,l}$ – power of signal loss for 5 GHz,
- $L_{C,l}$ – correction factor for 5 GHz,
- d_t – distance $2.2 \leq d \leq 24$ km for the sea water,

The proposed values for the used parameters are collated in Table 1 and Table 2, for 1 GHz and 5 GHz frequency, respectively.

Selection of the model depends on the adopted threshold of elevation angle θ_t - which represents the angle between the tangent to the Earth surface at the point where the coast radio station antenna is situated, and the line from that point to the antenna on the vehicle (the plane or the ship).

It also depends on the distance d_t between the positions of the coast station antenna and the vehicle antenna (the latter being defined as the point on the ground designated by the perpendicular to the tangent to the ground at that point and the proposed vehicle antenna height).

In general, values achieved for a small elevation angle can be understood as referring to:

- the ship, for the coast-to-sea model
- the climb phase of the aircraft, for the coast-to-air model,
- or the flight at a relatively low altitude, for the coast-to-air model.

Tab. 1. Path loss parameters for 1 GHz [8]

| Parameter | Value |
|-----------------------|-------|
| $A_{0,L,s}$ [dB] | 50.6 |
| $n_{L,s}$ | 1.5 |
| $\sigma_{X,L,s}$ [dB] | 2.8 |
| $L_{L,s}$ [dB] | 1.2 |
| L_0 [dB] | 1.0 |
| $\sigma_{X,L,l}$ [dB] | 4.8 |
| $L_{L,l}$ [dB] | 1.1 |
| d_t [km] | 9.1 |

Tab. 2. Path loss parameters for 1 GHz [8]

| Parameter | Value |
|-----------------------|-------|
| $A_{0,C,s}$ [dB] | 60 |
| $n_{C,s}$ | 1.6 |
| $\sigma_{X,C,s}$ [dB] | 2.3 |
| $L_{C,s}$ [dB] | 1.7 |
| $A_{0,l}$ [dB] | 63.9 |
| $n_{C,l}$ | 1.5 |
| $\sigma_{X,C,l}$ [dB] | 2.5 |
| $L_{C,l}$ [dB] | 0.5 |
| d_t [km] | 9.1 |

It is noteworthy that under the tested conditions, the correlation time and the delay spread were very small. In a typical situation the delay spread was less than 50 ns, and only occasionally increased to 250 ns. But we should keep in mind that the developed model has also to take into account situations when the delay spread is larger due to larger channel selectivity.

Based on the conclusion resulting from observations of the models, authors propose to modify slightly the basic CE2R model (by adding two more components) for signal loss estimation at low altitude and frequencies close to 1 GHz what we can see in the formula (2). At the same time for higher altitudes ($\theta > \theta_t$) the modified model is taken into

account (see (2)). This model is only loosely associated with the CE2R model. Consequently, the CE2R model is valid for ships and low-altitude flights and climbing.

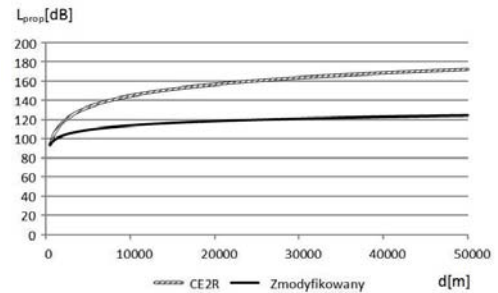


Fig. 2. Charts of propagation loss using the models given by (2) and (3) (excluding the random variable X ; $\zeta = 1$)

Signal losses L_{prop} obtained using these two models are compared in Fig. 2, presenting this quantity as a function of the distance between antennas. As we can see, the CE2R model is more restrictive than the modified one. Taking into account the empirical nature of the research, the modified model seems to be more appropriate. Consequently, the authors decided to forsake the CE2R model for the 5 GHz band for both low and high altitudes (see the formula (4)).

It is noteworthy that for maritime conditions of signal propagation the path loss is usually larger than in the case of coast-to-air transmission.

PROPAGATION LOSS MODEL PROPOSAL FOR 1.4 GHz

For 1.4 GHz transmission, the model for 1 GHz seems to be more adequate, and this model was used in the analysis. The frequency increase to 1.4 GHz results in larger signal loss, as we can see in Table 3. But the assumed parameters need verification in relevant measurements, which is planned in the future.

In the first approach we can assume that the signal loss along the Earth surface is given by

$$L[dB] = \begin{cases} A_{0,l} + 10n_l \log(d) + X_l + \zeta L_l & \theta \geq \theta_t, \text{ for planes} \\ A_{0,s} + 10n_s \log(d) + X_s + \zeta L_s & \theta < \theta_t, \text{ for planes} \\ A_{0,s2} + 10n_{s2} \log(d) + X_{s2} + \zeta L_{s2} & \theta < \theta_t, \text{ for ships} \end{cases} \quad (5)$$

with parameter values given in Tab. 3.

Tab. 3. Proposed path loss parameters for 1.4 GHz [8]

| Parameter | Value |
|------------------------|-------|
| $A_{0,l}$ [dB] | 52.6 |
| n_l | 1.5 |
| σ_{X_l} [dB] | 2.7 |
| L_l [dB] | 1.3 |
| $A_{0,s}$ [dB] | 55.3 |
| n_s | 1.5 |
| σ_{X_s} [dB] | 4.8 |
| L_s [dB] | 1.1 |
| d_t [km] | 9.1 |
| $A_{0,s2}$ [dB] | 60.3 |
| n_{s2} | 2.6 |
| $\sigma_{X_{s2}}$ [dB] | 4.8 |
| L_{s2} [dB] | 1.1 |

The parameters used in (5) are then as follows:

- $A_{0,1}$ – propagation constant for high flight altitude phase (coast-to-air model),
- $n_{0,1}$ – signal loss power for high flight altitude,
- $\sigma_{X_{1}}$ – standard deviation of random variable X_1 representing slow signal fluctuations,
- L_1 – correction factor for high flight altitude,
- $A_{0,s}$ – propagation constant for low flight altitude phase (coast-to-air model),
- $n_{0,s}$ – signal loss power for low flight altitude,
- σ_{X_s} – standard deviation of random variable X_s representing slow signal fluctuations,
- L_s – correction factor for low flight altitude,
- $A_{0,s2}$ – propagation constant for ships (coast-to-sea model),
- $n_{0,s2}$ – signal loss power for ships,
- $\sigma_{X_{s2}}$ – standard deviation of random variable X_{s2} representing slow signal fluctuations,
- L_{s2} – correction factor for ships,
- d – distance between antennas,
- X_1, X_s, X_{s2} – Gaussian variables of zero mean value and standard deviations σ_{X_1} [dB], σ_{X_s} [dB], $\sigma_{X_{s2}}$ [dB], respectively
- ζ – constant depending on motion direction from the coast station $\zeta = 1$ (moving out) or to the coast station $\zeta = -1$ (moving to the coast).

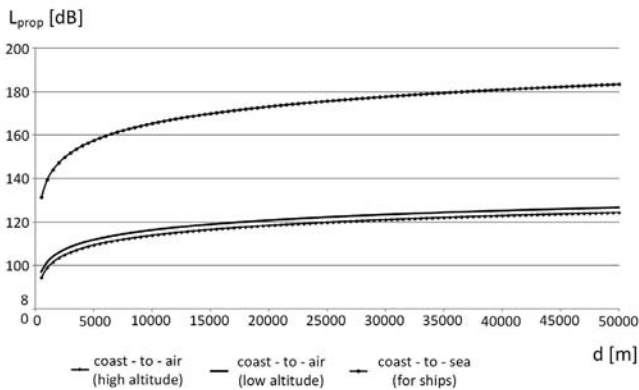


Fig. 3. Signal loss as a function of the distance, using (4) (excluding the random variable X ; $\zeta = 1$)

Charts of signal loss for the proposed model are presented in Fig. 3. We can see that the model for coast-to-sea transmission is more restrictive than the models for coast-to-air transmission.

GENERAL MODEL OF WIDEBAND CHANNEL

The model of wideband channel can be presented as the FIR filter, consisting of the delay line and not more than 4 branches, see Fig. 4. The received signal $y(t)$ is the vector sum of signals received in different propagation paths with various delays and phases. The first component is the LOS signal, of instantaneous complex amplitude $\alpha_0(t)$ and phase shift ϕ_0 . The amplitude probability of this component is given

by the Rician distribution. The 2-nd component, of the $\alpha_s(t)$ amplitude and ϕ_s phase shift, is the result of reflection from the sea surface.

The remaining components $z_1(t)$ and $z_2(t)$ additionally depend on stochastic processes which determine their existence.

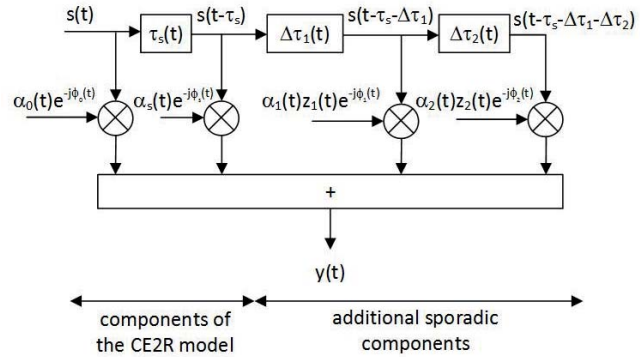


Fig. 4. Model of wideband channel

The probability distribution of the occurrence of these components is largely undefined. Nevertheless, the probability of the amplitude component of the second and other components is believed to results from the Rayleigh distribution.

MAIN PARAMETERS OF THE CHANNEL

CORRELATION TIME AND DELAY SPREAD

The research presented in [8-12] suggests that the correlation time and the delay spread for the here analysed propagation environments are very short. The delay spread was measured for a short distance between the vehicle and the coast station, and for a larger distance. In general, the delay spread is very short for the larger distance, and slightly longer for the short distance. But in both cases it does not, generally, exceed 50 ns, and only in most critical situations increases to 250 ns. This is very important information from the point of view of the OFDM system design, because small delay spread means that small time guard T_g between OFDM symbols is required. From the literature [11, 13] we know that the time guard should be a few times larger than the maximum delay spread, in order to take into account the most critical situations occurring in the propagation environment.

It appears from the presented considerations that we can set the minimum time guard approximately equal to 1 μ s. As a comparison, it is approximately 5 times shorter than the so-called short time guard used in LTE. That means that the OFDM technique is more suitable for the use in sea propagation environment than LTE, as compared to urban, suburban or rural environments.

As a result of the above reasoning, the value of minimum acceptable time guard was set to

$$T_{g,\min} = 1 \mu\text{s} \quad (6)$$

COHERENCE BANDWIDTH AND ADAPTIVE CORRECTION OF SIGNALS IN THE RECEIVER

The coherence bandwidth B_c of the multipath channel in which the correlation time equals several dozen ns can be, approximately, slightly larger than a dozen MHz, and for a few hundred ns – approximately equal to a few MHz. That means that within the band of the received signal ($B = 10$ MHz), no more than one minimum (strongly suppressed component-subcarrier of the spectrum) should be observed. And in the general case, no strongly suppressed component may be observed. However, a longer correlation time, reaching a few μ s, can cause a strong frequency selectivity.

It means that in relatively long periods of time the channel cannot be frequency selective, despite a large channel bandwidth. In this case we do not need to use correction of channel pulse response in the receiver, nor other simple solutions.

GENERAL METHODOLOGY OF OFDM INTERFACE DESIGN

As the first step, we assume the FFT size which depends on the planned number of subcarriers in the OFDM signal. Most frequently the FFT size is assumed as the power of 2. The 1024 size is preferred for a few hundred of active subcarriers, which is the case of the present project. If the designed number of subcarriers is smaller than the FFT size, then we only use active subcarriers and set other subcarriers equal to zero.

Subcarrier spacing should be much larger than the Doppler spread, which in the designed system depends on the speed of motion of vehicles. Therefore in order to take into account high speed of motion of terminals, higher Δf should be assumed. In a typical situation, the Δf value of over dozen kHz is sufficient even for very large (more than 1000 kmph) vehicle speed.

The subcarrier spacing must meet the condition

$$\Delta f \gg \Delta f_{\text{doppler}} \quad (7)$$

The sampling frequency depends on the assumed Δf and the number of subcarriers (FFT_{size}). This relation is

$$f_s = FFT_{\text{SIZE}} \cdot \Delta f \quad (8)$$

The OFDM symbol duration depends on the assumed value of Δf

$$T_{\text{OFDM}} = \frac{1}{\Delta f}$$

In the next step, the total symbol transmission period T_{TR} is to be estimated. It depends on the number of designed OFDM symbols per time unit and the duration of a single time slot. In the proposed system the time slot duration is equal to $T_{\text{slot}} = 0.5$ ms, and a single slot can transmit (N_{symp}) 6, 7 or 8 OFDM symbols. Then the total transmission period is

$$T_{\text{TR}} = \frac{T_{\text{slot}}}{N_{\text{symp}}} \quad (9)$$

Hence we have

$$T_{\text{TR}} = T_{\text{OFDM}} + T_g$$

If we know the T_{OFDM} symbol duration then we can estimate the possible time guard T_g between the transmitted OFDM symbols.

The most critical assumption for OFDM-based systems is that the T_g should be shorter than the maximum delay spread in the designed system. It means that

$$T_g < \Delta T_{\text{delay}} \quad (11)$$

and preferably $T_g \ll \Delta T_{\text{delay}}$.

Here we assumed that T_g should be a few times shorter than ΔT_{delay} , as a minimum, in a large percent of time.

CHARACTERISTICS OF PROPOSED OFDM SYSTEM

The transmission of signals in the proposed system is realized in TDD mode in a single frequency channel of 10 MHz frequency band. The working frequency is 1.4 GHz.

Tab. 4. Basic parameters for proposed radio interface

| Parameter | Value |
|--|--|
| Multiple access | OFDMA |
| Duplex method | TDD |
| Channel centre frequency | 1.4 GHz |
| Channel band | 10 MHz |
| Modulation | QPSK and 16 QAM |
| Channel coding | Convolutional coding (3,1,9) |
| FFT size | 1024 |
| Number of OFDM symbols in a single slot (per 0.5 ms) | 6, 7 or 8 |
| Physical resource size | 12 subcarriers x 8 (7 or 6) OFDM symbols |

In the radio interface we use the OFDM technique, in which the transmission over the entire frequency band is done using a number of orthogonal subcarriers transmitted simultaneously. This transmission method increases the immunity of the transmitted signal to frequency selective signal fading, which is the most problematic issue in wideband radio communication systems. The basic set of parameters is given in Table 4.

THE STRUCTURE OF PHYSICAL RESOURCE BLOCK

The basic unit of resources is the resource block. The resource block size in the system is defined in the time-frequency domain. In the time domain, the resources are divided depending on the number of OFDM symbols used in a single time slot, while in the frequency domain they are divided into a number of subcarriers. The size of the designed block is 12 subcarriers and 6, 7 or 8 OFDM symbols in a single slot, see Fig. 5.

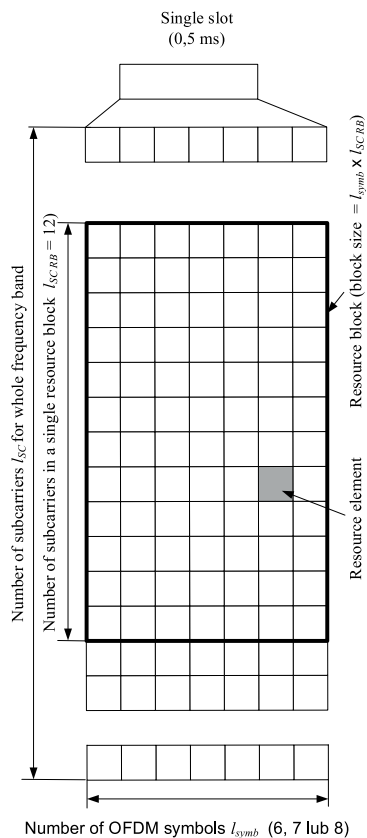


Fig. 5. The structure of physical resource block

The number of resource blocks depends on the set subcarrier spacing, which is the main issue of the analysis. A single resource block consists of data sent on 12 subcarriers in a single slot of 0.5 ms duration. The block size depends on the number of OFDM symbols per slot. A single resource element carries 2 or 4 bits, depending on the modulation type: QPSK or 16 QAM, respectively. So, the resource element it is the smallest unit of information sent on a single subcarrier in time duration of a single OFDM symbol.

ANALYSIS RESULTS

Table 5 collates results of calculation of OFDM system parameters for different values of OFDM symbols and subcarrier spacing. It determines the guard time T_g for different configurations, some of which can be accepted for the system or not.

For comparison purposes, the table includes parameters calculated for the LTE system. The R_p/R_{min} value is the indicator for the use of resources, calculated as the available throughput normalized by the minimum throughput available for the analysed conditions (in the present case it corresponds to the value for LTE with 6 OFDM symbols per slot). As we can see, the best proposal is for 8 OFDM symbols per slot when the calculated guard time is $T_g = 1.26 \mu s$, assuming that T_g should be greater than $1 \mu s$. Additionally, Fig. 6 shows the results of T_g calculation as a function of Δf , for different number of OFDM symbols, to illustrate the effect of subcarrier spacing on the guard time acceptable in the system.

The first conclusion after analysing these results is that larger number of OFDM symbols not always results in greater throughput. But large number of OFDM symbols is preferred, as it is achieved when Δf is larger. And larger values of Δf are preferable for high speeds of vehicles (which is not important for ships but very important for planes).

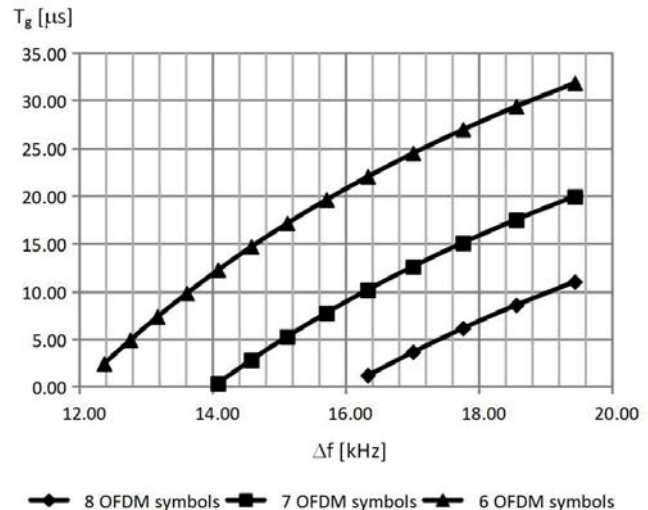


Fig. 6. Time guard as function of subcarrier spacing for different numbers of OFDM symbols in single slot

The second conclusion is that the coast-to-sea and coast-to-air environments are very good from the viewpoint of the use of OFDM transmission for data transmission, because we can use small T_g periods at relative large Δf values. It is possible to use large number of OFDM symbols for a single slot, which guarantees high spectral efficiency.

Another interesting problem is the normalized throughput available in different configurations of Δf and T_g . Relevant results are presented in Fig. 7.

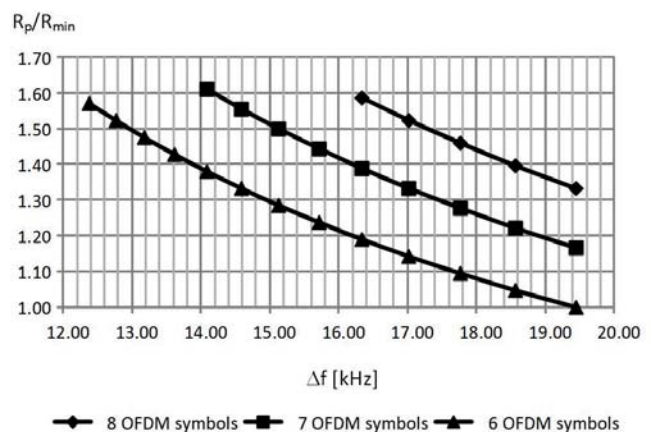


Fig. 7. Normalized throughput as function of subcarrier spacing for different numbers of OFDM symbols in single slot.

If we take into account a smaller number of OFDM symbols in the slot then we can achieve the same throughput using a smaller Δf value, as compared to the case of greater number of OFDM symbols. But if a larger Δf is preferred, it is more appropriate to use a greater number of OFDM symbols.

Tab. 5. Results of estimation of OFDM parameters for different operating conditions

| | RB | Δf | T _{OFDM} [μs] | 6 symbols | | | 7 symbols | | | 8 symbols | | | |
|--------------------------|----|------------|------------------------|--|---|----------------------------------|--|---------------------|----------------------------------|--|---------------------|----------------------------------|--|
| | | | | T _{OFDM} +T _g [μs] | T _g [μs] | R _p /R _{min} | T _{OFDM} +T _g [μs] | T _g [μs] | R _p /R _{min} | T _{OFDM} +T _g [μs] | T _g [μs] | R _p /R _{min} | |
| Proposed system analysis | 44 | 18,56 | 53,88 | 83,33 | 29,45 | 1,05 | 71,43 | 17,55 | 1,22 | 62,50 | 8,62 | 1,40 | |
| | 46 | 17,76 | 56,31 | | 27,03 | 1,10 | | 15,12 | 1,28 | | 6,19 | 1,46 | |
| | 48 | 17,01 | 58,79 | | 24,54 | 1,14 | | 12,64 | 1,33 | | 3,71 | 1,52 | |
| | 50 | 16,33 | 61,24 | | 22,10 | 1,19 | | 10,19 | 1,39 | | 1,26 | 1,59 | |
| | 52 | 15,71 | 63,65 | | 19,68 | 1,24 | | 7,77 | 1,44 | non - realizable | | | |
| | 54 | 15,12 | 66,14 | | 17,20 | 1,29 | | 5,29 | 1,50 | | | | |
| | 56 | 14,58 | 68,59 | | 14,75 | 1,33 | | 2,84 | 1,56 | | | | |
| | 58 | 14,08 | 71,02 | | 12,31 | 1,38 | | 0,41 | 1,61 | | | | |
| | 60 | 13,61 | 73,48 | | 9,86 | 1,43 | | non - realizable | | | | | |
| | 62 | 13,17 | 75,93 | | 7,40 | 1,48 | | | | | | | |
| | 64 | 12,76 | 78,37 | | 4,96 | 1,52 | | | | | | | |
| | 66 | 12,37 | 80,84 | | 2,49 | 1,57 | | | | | | | |
| | | | | | long cyclic prefix (16,67 μs) 6 symbols | | | | | | | | short cyclic prefix (5,2 μs and 4,69 μs) 7 symbols |
| LTE | 50 | 15,00 | 66,67 | 83,33 | 16,67 | 1,19 | 71,43 | ~ 4,76 | 1,39 | non - realizable | | | |

Figure 8 illustrates a very interesting case when the normalized throughput is analysed as a function of the guard time. In Fig. 8a the full range of guard time is presented, while Fig. 8b shows only, for better visualisation, the magnified range of short guard time.

We can see that the greatest throughput is achieved for the largest number of OFDM symbols in a single slot. For 7 symbols the throughput highest than 1.56 is not realizable due to excessively short guard time in this case (non acceptable T_g - less than 1 μs). That is why this throughput is considered worse than that achieved for 6 OFDM symbols.

What is very important is that the optimum number of OFDM symbols is dependent on the designed guard time and its restrictions. Note that the system is realizable only for parameters marked as points in this figure because it is dependent on the predefined resource block size (positions of these points depend on the resource block size).

For instance, from Fig. 8 we can see that:

- for T_g = 2.5 μs the best throughput is with 6 OFDM symbols only,
- for T_g = 2.85 μs the use of 7 symbols is more favourable
- but for T_g = 3,71 μs the best situation is when 8 symbols per slot are implemented.

In Fig. 8a the throughput available in LTE is compared to that of the proposed system, for 2 possible configurations of T_g in LTE (so-called short cyclic prefix and long cyclic prefix). We can see that the band of 9 MHz, against 10 MHz available in LTE, at the assumed values of T_g and Δf result in much poorer efficiency of LTE, as compared to the proposed system.

CONCLUSION

The paper proposes a design of OFDMA-based system for maritime applications. The performed analyses have revealed that for coast-to-sea and coast-to air (above the sea surface) propagation environments, very short guard periods between the transmitted OFDM symbols can be used, which provides very good conditions for OFDMA interfaces performance and enables to achieve high efficiency of the use of radio resources. These conditions are much better than those characteristic for urban and rural environments. It means that the OFDM technique is strongly recommended for use in maritime radio communication systems.

The proposed method can be adopted in multi-carrier

systems (MC-CDMA [14]). Moreover, the proposed solution can be implemented in systems using advanced frequency reuse methods, described in [15-16].

The presented analysis also reveals that the configuration of OFDM parameters for LTE is much more unfavorable, from the viewpoint of resource use, than the configurations of the proposed system.

The proposed path loss model can be taken into account when estimating the coverage of the proposed system working on the 1.4 GHz band.

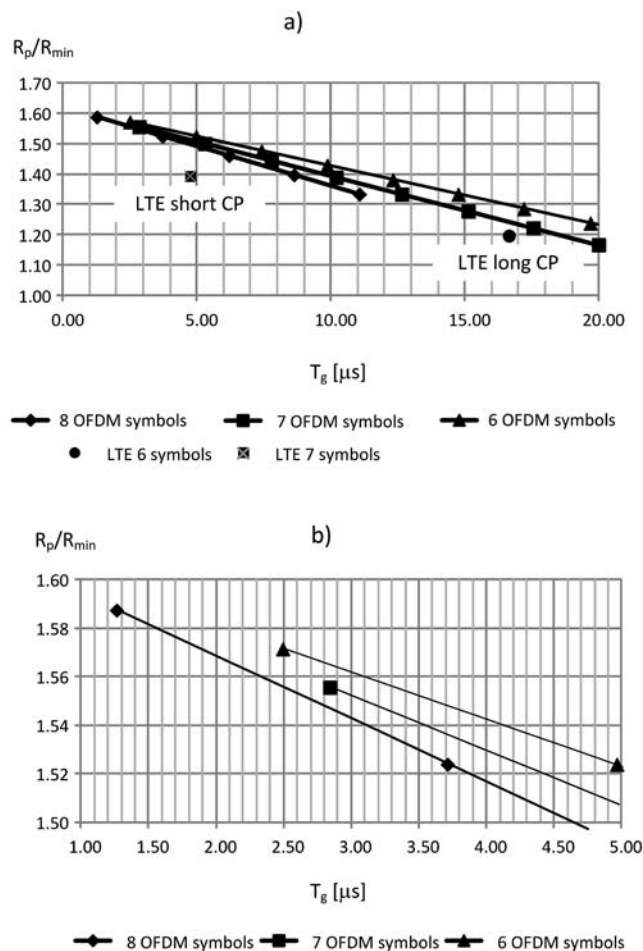


Fig. 8. Normalized throughput as function of time guard for different numbers of OFDM symbols in single slot:
a) full range of available subcarrier spacing and results for LTE;
b) narrowed range for better presentation of the best results.

ACKNOWLEDGMENTS

This work was financially supported by Polish National Centre for Research and Development under grant no. DOB-BIO6/09/5/2014.

BIBLIOGRAPHY

1. Parsons J.D., The mobile radio propagation channel, 2nd ed. Wiley 2000.
2. Zajic A., Mobile-to-Mobile Wireless Channels, Artech House, 2013.
3. Matolak D., AG Channel Sounding for UAS in the NAS, NASA, Project presentation, University of South California, 2014.
4. Matolak D., Sun R., Antenna and Frequency Diversity in the Unmanned Aircraft Systems Bands for the Over-Sea Setting, Project presentation, University of South California, 2014.
5. Matolak D., Sun R., Air-Ground Channel Characterization for Unmanned Aircraft Systems: The Over-Freshwater Setting, 978-1-4799-4891-8/14/\$31.00 2014 IEEE.
6. Matolak D., Air-Ground Channels&Models: Comprehensive Review and Considerations for Unmanned Aircraft Systems, 978-1-4577-0557-1/12/\$26.00 2012 IEEE.
7. Venkatasubramanian S. N., Propagation channel model between unmanned aerial vehicles for emergency communications, Thesis submitted for MSc, Alto University 2013.
8. Matolak D., Shalkhauser K., Kerczewski R, L-Band and C-Band Air-Ground Channel Measurement & Modeling Update, Aeronautical Communications Panel, 31st Meeting of Working Group F, Seattle, Washington, USA, 2014.
9. Matolak D., Shalkhauser K., Kerczewski R, L-Band and C-Band Air-Ground Channel Measurement & Modeling for Over-Sea Conditions, Aeronautical Communications Panel, 30th Meeting of Working Group F, Seattle, Washington, USA, 2014.
10. Newhall W.G., Mostafa R., Dietrich C., Anderson C. R., Dietze K., Joshi G., Reed J.H., Wideband Air-to-Ground Radio Channel Measurements Using Antenna Array at 2 GHz for Low-Altitude Operations, 0-7803-8140-8/03/\$17.00 2003 IEEE.
11. Haque J., An OFDM Based Aeronautical Communication System, PhD dissertation, University of South Florida, 2011.
12. Lee Y.H., Dong F., Meng Y.S., Near Sea-Surface Mobile Radiowave Propagation at 5 GHz: Measurements and Modeling. Radioengineering, vol. 23, no. 3, September 2014.
13. Yang S.,C., OFDMA System Analysis And Design, Artech House 2010.
14. Marczak A., Performance analysis of data transmission in MC-CDMA radio interface with turbo code. Telecommunication Systems, DOI 10.1007/s11235-014-9910-7, December 2014.
15. Gajewski S., Throughput - Coverage Characteristics for Soft and Partial Frequency Reuse in the LTE Downlink. In proc. of 36th International conf. on telecommunications and signal processing , TSP 2013, pp. 199-203, Rome , Italy 2013.
16. Hindias M. N., Khanam S., Reza A. W., Ghaleb A. M., Latef A. L., Frequency Reuse for 4G Technologies: A Survey. In proc. of The 2nd International Conference on Mathematical Sciences & Computer Engineering (ICMSCE 2015), At Langkawi, Malaysia, 2015.

CONTACT WITH THE AUTHOR

Sławomir Gajewski

The Faculty of Electronics, Telecommunications
and Informatics
Gdansk University of Technology
11/12 Narutowicza St.
80-233 Gdańsk
Poland

THE USE OF SATELLITE DATA IN THE OPERATIONAL 3D COUPLED ECOSYSTEM MODEL OF THE BALTIC SEA (3D CEMBS)

Artur Nowicki, M. Sc.

Maciej Janecki, M. Sc.

Mirosław Darecki, Assoc. Prof.

Piotr Piotrowski, Ph. D. *

Lidia Dzierzbicka-Głowacka, Assoc. Prof.

Institute of Oceanology, Polish Academy of Sciences, Poland

* Maritime Institute in Gdańsk, Poland

ABSTRACT

The objective of this paper is to present an automatic monitoring system for the 3D CEMBS model in the operational version. This predictive, eco hydrodynamic model is used as a tool to control the conditions and bio productivity of the Baltic sea environment and to forecast physical and ecological changes in the studied basin. Satellite-measured data assimilation is used to constrain the model and achieve higher accuracy of its results.

3D CEMBS is a version of the Community Earth System Model, adapted for the Baltic Sea. It consists of coupled ocean and ice models, working in active mode together with the ecosystem module. Atmospheric forecast from the UM model (Interdisciplinary Centre for Mathematical and Computational Modelling of the Warsaw University) are used as a forcing fields feed through atmospheric data model. In addition, river inflow of freshwater and nutrient deposition from 71 main rivers is processed by land model. At present, satellite data from AQUA MODIS, processed by the SatBałtyk project Operational System are used for the assimilation of sea surface temperature and chlorophyll a concentration. In the operational mode, 48-hour forecasts are produced at six-hour intervals, providing a wide range of hydrodynamic and biochemical parameters.

Keywords: Baltic, ecosystem, model, satellite, assimilation

INTRODUCTION

The Baltic Sea is a semi-enclosed, shelf sea. It is exposed to the influence of a number of changing environmental conditions such as atmospheric conditions, inflows of saline ocean waters from the North Sea, freshwater inflows from rivers rich in biogenic substances. Vertical stratification of the Baltic Sea is very strong and changes substantially over the year. All this makes modelling of this region a complicated problem. Even taking into account all these factors, using open boundary conditions, accurate vertical parameterization and forcing fields from state of the art weather forecasting models does not guarantee that the eco hydrodynamic model will be able to reflect the actual state of the environment. This is one of the most important reasons why the assimilation of satellite-measured data must be used in order to constrain the model and produce high accuracy results. 3D CEMBS is a coupled ecosystem model, which main task is to produce short term, 3-dimensional forecasts of main hydrodynamic and biochemical parameters of the Baltic Sea. It uses Cressman assimilation scheme [2], which is computationally very efficient, but at the same time its accuracy remains satisfactory. Satellite data used for the assimilation is measured by MODIS

device installed on the AQUA satellite. Results from this model are used in the SatBałtyk project [10], [11] as well as are presented at model's website – www.cembs.pl. These results of the model cover historical data archived since 2010 till present, as well as 48-hours forecasts updated four times a day.

3D CEMBS MODEL

The 3D CEMBS model is based on a CESM1.0 (Community Earth System Model) and was adapted to the Baltic Sea region. Its main components are coupled ocean and ice models working in an active mode, calculating hydrodynamic results, together with an ecosystem model responsible for calculating biological and chemical parameters.

Ocean model is based on a POP (Parallel Ocean Program) code [9]. It is a z-level coordinates, general circulation ocean model that solves the 3-dimensional primitive equations for stratified fluid using the hydrostatic and Boussinesq approximations. Sea ice model is based on a CICE (Community Ice Code). It uses an elastic-viscous-plastic ice rheology [3].

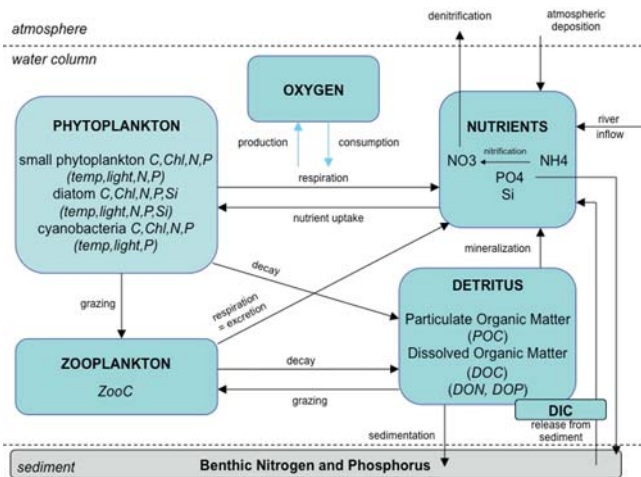


Fig. 1. Ecosystem model block diagram

Ecosystem model, presented on Fig. 1 is based on an intermediate complexity marine ecosystem model for the global domain [7] and consists of 11 main components: zooplankton, small phytoplankton, large phytoplankton, summer species, one detrital class, oxygen and the nutrients: nitrate, phosphate, ammonium and silicate.

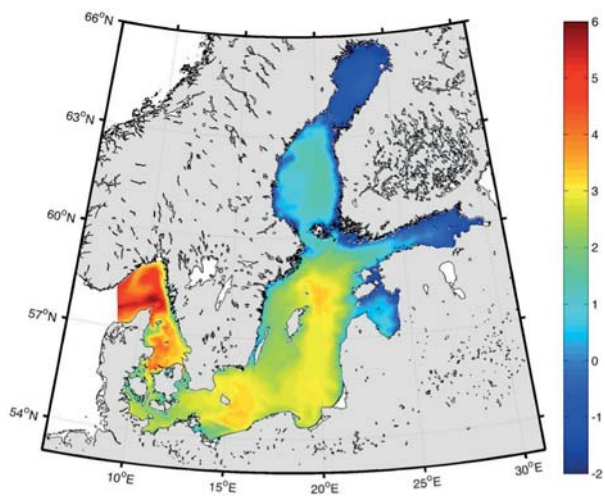


Fig. 2. Model domain with surface layer temperature

In the operational mode, 3D CEMBS is configured at horizontal resolution of 1/480, which is ca. 2km. Vertically model grid has 21 layers. The thickness of the first four layers is 5m and it grows with depth. Model domain is shown in Fig. 2. Atmospheric data from forecasts and mean values of nutrient deposition and freshwater inflow from rivers are feed through data modules. The atmospheric data, which are used as forcing fields, are calculated by the weather forecast model, which is being developed in the Interdisciplinary Centre for Mathematical and Computational Modelling of the Warsaw University. River discharge data are historical, daily averaged values

from the Balt-HYPE model of SMHI and the nutrient deposition data are monthly averaged. Discharge from 71 main rivers of the Baltic Sea basin was included. Satellite data used for assimilation are sea surface temperature and chlorophyll a concentration measured by MODIS [1]. They are at spatial resolution of 1km. Fig. 3 present the scheme of the 3D CEMBS model configuration. The model provides hydrodynamic parameters: water temperature, salinity, sea surface height, current velocity and direction, parameters of sea ice: temperature, concentration and thickness and biochemical parameters such as: dissolved oxygen, concentration of chlorophyll a, phytoplankton, zooplankton and nutrients. Detailed description of hydrodynamic and ecosystem modules as well as the operational mode is presented in Dzierzbicka-Głowacka et al. [4], [5], [6].

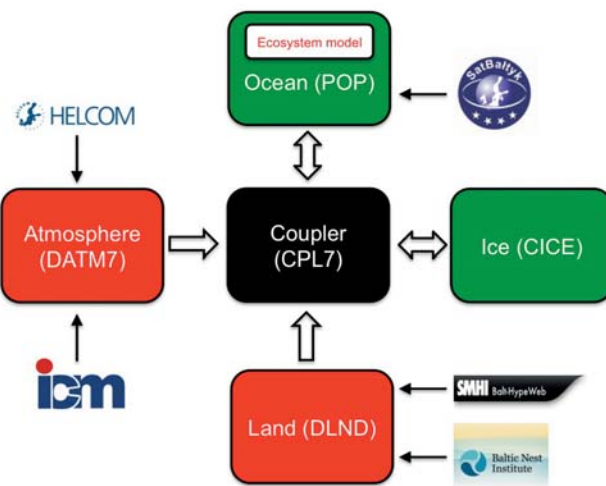


Fig. 3. 3D CEMBS block diagram

OPERATIONAL SYSTEM

Currently the 3D CEMBS model is running in an operational mode that is fully automated and controlled by specially designed system. In current configuration it provides a 48-hour forecasts every six hours. Forecasts are available with 1-hour step and archival data are stored with 6-hour step. The system consists of modules that are responsible for the subsequent steps as shown on Fig. 4. First input data such as weather forecast results, satellite data and river discharge data are gathered. All data are then interpolated to model grid and additional parameters are calculated. Then, if present, satellite data are assimilated and the forecast is calculated. Afterwards system prepares output data to be presented on a model's webpage, www.cembs.pl, and prepares archives forecast's results. Surface parameters are then properly processed and transferred to SatBałtyk database server, where they can be accessed through SatBałtyk project webpage.

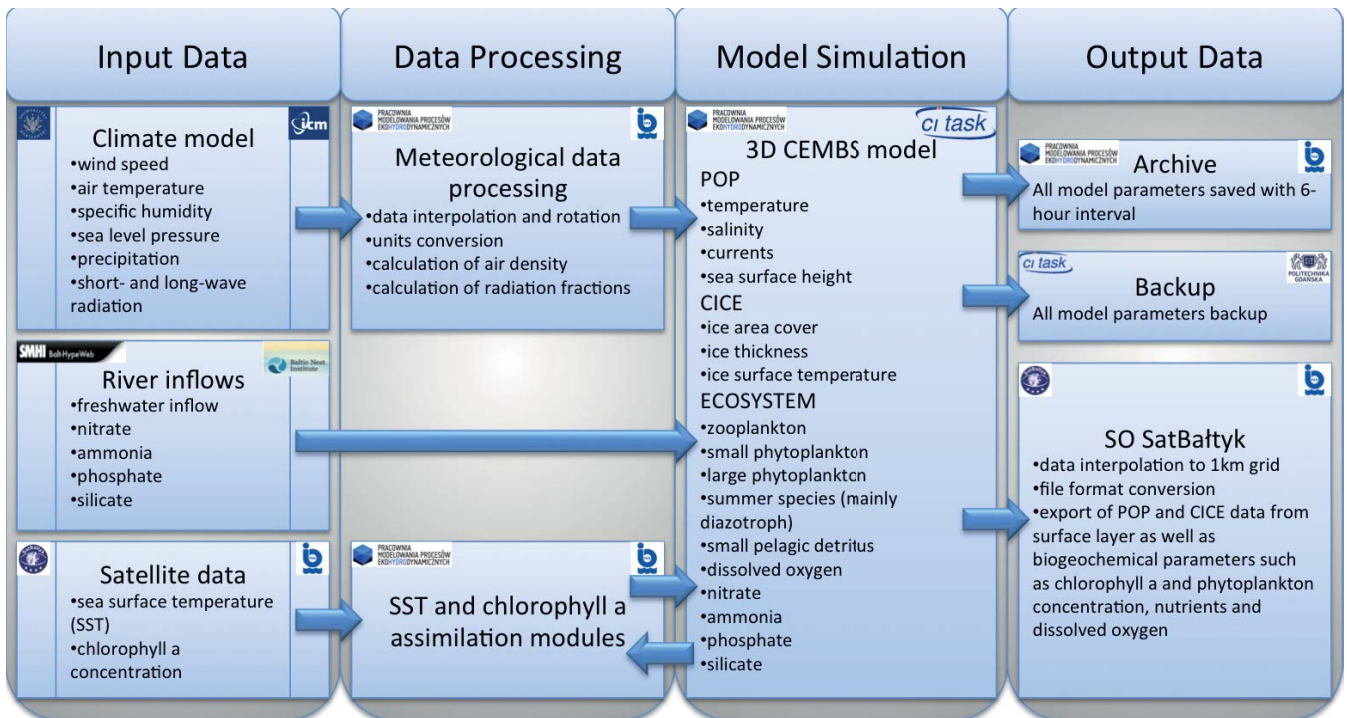


Fig. 4. Operational system block diagram

4. ASSIMILATION SCHEME

Data assimilation combines time- and space-distributed observations with a dynamic model. Satellite retrieved sea surface temperature (SST) from MODIS AQUA have been used in the temperature assimilation scheme. The level 0 raw satellite data from NASA Ocean Color Web have been processed within the standard msl12 SeaDAS code where satellite infrared MODIS bands 31 and 32 are corrected for atmospheric absorption using combinations of several MODIS mid- and far-infrared bands. ECMWF assimilation model of marine atmosphere with atmospheric properties and variability is supporting this correction. Cloud screening is based on two approaches: use of the cloud screening product (3660) and a cloud indicator derived during the SST retrieval. Data spatial resolution is around 1km. Accuracy of the retrieved SST can be considered to +/- 0.4 degrees Celsius.

3D CEMBS is designed to work in an operational mode, therefore assimilation algorithm used in the system must be accurate, yet time efficient. Data assimilation scheme proposed by Cressman is relatively simple and computationally fast, whilst remaining accurate. Thus, it seems to be an appropriate choice. Scheme implemented in presented system is sequential, meaning that only data measured in the past until the time of analysis are used. It is also intermitted, which means that the assimilated information is processed in a single small batch, which is technically easier to implement as in opposite to continuous methods. Main disadvantage of this method is possibility of obtaining unrealistic results near the edge of the spatial domain. However, such extrema were not observed in the obtained results. The Cressman assimilation scheme can be described in the following steps. Results of the previous

model's forecast are used as a background state x_b . Satellite data are then checked for errors and stored in the observations matrix y . Then for every grid-point j the analysis result x_a is calculated based on the following equation:

$$x_a(j) = x_b(j) + \frac{\sum_{i=1}^n w(i,j)\{y(i) - x_b(i)\}}{\sum_{i=1}^n w(i,j) + E^2} \quad (1)$$

E is an estimate of the ratio of the observation error to the model error, i and j are satellite and model grid-points respectively. Weight function w depends on influence radius R and distance d between model and satellite results. It is defined as follows:

$$w(i,j) = \max\left(0, \frac{R^2 - d_{ij}^2}{R^2 + d_{ij}^2}\right) \quad (2)$$

The result of the analysis is then used as an initial state for the next forecast.

Similar scheme was used in case of satellite measured sea surface chlorophyll a concentration. However, chlorophyll a concentration obtained from the model is calculated based on its values in three groups of phytoplankton: large phytoplankton (mainly diatoms) small phytoplankton, and summer species (mainly cyanobacteria). Therefore, sum of these components is used for further calculations. Since chlorophyll a concentration has a log-normal distribution, logarithms of model and satellite determined values are used in the scheme. Therefore, the equation (1) is transformed to the following form:

$$\log x_a(j) = \log x_b(j) + \frac{\sum_{i=1}^n w(i,j) \log \frac{y(i)}{x_b(i)}}{\sum_{i=1}^n w(i,j) + \epsilon_{ij}^2} \quad (3)$$

In the above equation:

$$\epsilon_{i,j} \sim \frac{x_s(i)}{x_m(j)}, \quad (4)$$

$$x = 10^{\sigma_{\log}}, \quad (5)$$

$$\sigma_{\log} = SD \left(\log \frac{X_s(i)}{X_m(i)} \right) \quad (6)$$

SD stands for standard deviation, subscripts s and m stand for satellite and model respectively, X are values of chlorophyll a concentration. Determined this way differences are then distributed between the three groups of phytoplankton, on the basis of their percentage of the total chlorophyll a concentration.

RESULTS AND DISCUSSION

The model with satellite-measured SST assimilation was calibrated and tested on data from years 2011-2012. In order to assess the impact of assimilation, the results of model with and without assimilation were then compared with in-situ measurements. [8]. After receiving satisfactory results the model was launched in the operational mode. To confirm the effectiveness of the assimilation algorithm another statistical comparison between both models and in-situ data was carried out based on data from year 2013. Parameters such as absolute mean error (systematic) $\langle \epsilon \rangle$ and root mean square error RMSE were calculated. Correlation coefficient R before and after removal of mean seasonal signal was also calculated. Table I contains the results of this comparison. As one can see the results calculated by the assimilating model are better.

Tab. 1. Statistical comparison of not assimilated and assimilated surface temperature

| Model type | R with/without mean signal | $\langle \epsilon \rangle$ [°C] | RMSE [°C] |
|-----------------|----------------------------|---------------------------------|-----------|
| not assimilated | 0.966 / 0.60 | -1.2 | 1.9 |
| assimilated | 0.977 / 0.79 | -0.10 | 1.4 |

Systematic error decreased from -1.2 °C to only -0.1 °C. Root mean square error with data assimilation is almost 25% smaller than that calculated for the model without data assimilation. The correlation coefficient of data before removal of mean signal is only slightly better. However, after removal of mean signal the difference increases significantly. This means that the changes, driven by the annual cycles are well represented by the model itself, but the assimilation allows better representation of local and short term anomalies. Fig. 5 shows the correlation of not assimilated (black) and assimilated (red) model results (x axis) with the in-situ measurements (y axis). In-situ data used for this comparison were obtained from fixed and non-fixed HELCOM stations and cover measurements of surface layer (0-5 m) temperature carried out in 2013. This plot shows that assimilated data are better correlated with in-situ measurements. The results are

very comparable to those obtained from previous comparison calculated for years 2011-2012. This is a very good example of how applying even such a simple method of satellite data assimilation can significantly improve accuracy and quality of modelling results.

In October 2014 operational version of the model was suspended due to implementation of chlorophyll a concentration assimilation algorithms. Currently system is in the testing phase, however, first trial runs show promising results. Table II presents statistical comparison that shows, how assimilation of satellite-measured chlorophyll a concentration improved model's accuracy. However, these are still early results and some issues are still to be solved. Therefore more tests and longer trial runs must be performed before applying developed technique to the operational system.

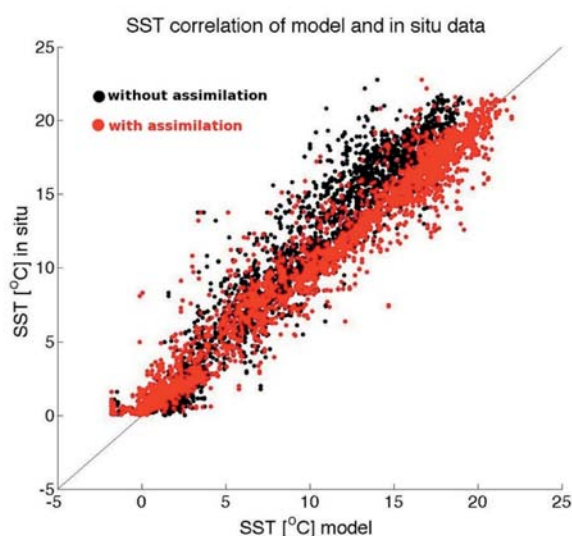


Fig. 5. Correlation of not assimilated and assimilated temperature results from year 2013

Tab. 2. Statistical comparison of not assimilated and assimilated chlorophyll a concentration

| Model type | Mean systematic error | Error factor | Upper limit of the statistical error | Lower limit of the statistical error |
|-----------------|----------------------------------|--------------|--------------------------------------|--------------------------------------|
| | $\langle \epsilon \rangle_e$ [%] | x | σ_- [%] | σ_+ [%] |
| not assimilated | -72.56% | 3.00 | 199.62% | -66.62% |
| assimilated | -66.82% | 2.76 | 176.14% | -63.79% |

ACKNOWLEDGEMENT

The partial support for this study was provided by the project Satellite Monitoring of the Baltic Sea Environment – SatBałtyk founded by European Union through European Regional Development Fund contract no. POIG 01.01.02-22-011/09

The computing presented in this paper was carried out on the Galera super computer at the Academic Computer Centre in Gdansk (CI TASK).

In-situ data used for validation were obtained from ICES Dataset on Ocean Hydrography. The International Council for the Exploration of the Sea Copenhagen. 2011,
<http://ocean.ices.dk/helcom/Helcom.aspx>

REFERENCE

1. Brown O.B., Minnett P.J.: MODIS Infrared Sea Surface Temperature Algorithm Theoretical Basis Document, Ver 2.0, 1999, http://modis.gsfc.nasa.gov/data/atbd/atbd_mod25.pdf
2. Cressman G. P.: An operational objective analysis system, *Monthly Weather Review* 87 (1959) 367-374
3. Hunke E. C., Dukowicz J. K.: An elastic-viscous-plastic model for sea ice dynamics, *J. Phys. Oceanogr.* 27 (1997) 1849-1867
4. Dzierzbicka-Głowacka L., Jakacki J., Janecki M., Nowicki A.: Activation of the operational ecohydrodynamic model (3D CEMBS) – the hydrodynamic part, *Oceanologia* 55(3) (2013a) 519-541
5. Dzierzbicka-Głowacka L., Janecki M., Nowicki A., Jakacki J.: Activation of the operational ecohydrodynamic model (3D CEMBS) – the ecosystem module, *Oceanologia* 55(3) (2013a) 543-572
6. Dzierzbicka-Głowacka L., Nowicki A., Janecki M.: The automatic monitoring system for 3D CEMBSv2 in operational Version, *Journal of Environmental Science and Engineering Technology* 1 (2014) 1-9
7. Moore J. K., Doney S. C., Kleypas J. A., Glover D. M., Fung I. Y.: An intermediate complexity marine ecosystem model for the global domain, *Deep-Sea Res.* II,49 (2002) 403-462.
8. Nowicki A., Dzierzbicka-Głowacka L., Janecki M., Kałas M.: Assimilation of the satellite SST data in the 3D CEMBS model, *Oceanologia* 57(1) (2015) 17-24
9. Smith R., Gent P.: Reference manual for the Parallel Ocean Program (POP), New Mexico, Los Alamos National Lab, 2004, pp. 75
10. Woźniak B., Bradtke K., Darecki M., Dera J., Dudzińska-Nowak J., Dzierzbicka-Głowacka L., Ficek D., Furmańczyk K., Kowalewski M., Krężel A., Majchrowski R., Ostrowska M., Paszkuta M., Stoń-Egiert J., Stramska M., Zapadka T.: SatBałtyk - A Baltic environmental satellite remote sensing system - an ongoing project in Poland. Part 1: Assumptions, scope and operating range, *Oceanologia* 53(4) (2011a) 897-924
11. Woźniak B., Bradtke K., Darecki M., Dera J., Dudzińska-Nowak J., Dzierzbicka-Głowacka L., Ficek D., Furmańczyk K., Kowalewski M., Krężel A., Majchrowski R., Ostrowska M., Paszkuta M., Stoń-Egiert J., Stramska M., Zapadka T.: SatBałtyk - A Baltic environmental satellite remote sensing system - an ongoing project in Poland. Part 2: Practical applicability and preliminary results, *Oceanologia* 53(4) (2011a) 925-958

CONTACT WITH AUTHOR

Lidia Dzierzbicka-Głowacka

Institute of Oceanology
Polish Academy of Sciences
55 Powstańców Warszawy St.
81-712 Sopot
Poland

e-mail: dzierzb@iopan.gda.pl

STUDY OF SEASONAL ACOUSTIC PROPERTIES OF SEA WATER IN SELECTED WATERS OF THE SOUTHERN BALTIC

Grażyna Grelowska, Prof.
Gdańsk University of Technology, Poland

ABSTRACT

Climate Research of the globe is a current task, in particular to confirm the general hypothesis of global warming associated with an increase in average temperature. The sea acoustic climate is derived from the concept of climate and refers to the conditions of propagation of acoustic waves in a particular basin. In this paper, the results of systematic measurements of temperature, salinity and velocity distributions of sound in the area of the southern Baltic will be presented. The focus will be on the results of extensive measurements carried out „in situ” in particular.

Keywords: sound propagation in sea water, acoustic climate of the Baltic Sea

INTRODUCTION

The increasing use of acoustic devices used for underwater research [4, 6, 13, 17], and the assessment of the seabed [14,15] causes, that the general interest of acoustic climate of underwater observation is a challenge for hydro-acousticians. Detection of the underwater sound channel in the Atlantic Ocean during the period of the Second World War made the observations and the use of variable acoustic properties of seawater become the subject of constant observation. Of course, the study of acoustic properties of the Baltic Sea took place much later. The periodic occurrence of the acoustic channel in this basin was discovered by Hela [8]. It should be mentioned, that in the early seventies of the last century, research on the study of the acoustic properties of Baltic sea was carried out in Poland [9, 25, 28]. The presence of seasonal changes in the conditions of propagation of acoustic waves is one of the elements of the research - measurement work conducted in the area of the Southern Baltic. The results presented in this article have been developed mainly on the basis of measurement data collected during research cruises made by r / v “Baltica”.

The main premise of the publication is to present the results, which on one hand are retrospective, and on the other represent a period of time, which is part of the history of the acoustic climate of the South Baltic and can be used to determine the average acoustic parameters of the tested reservoir.

The authors interest is focused on three water regions of the South Baltic sea with a relatively large depth, namely: Bornholm Deep, Gdansk Deep and Slupsk Furrow. The study period is for selected months taken as representative for the respective season of 2005.

THE OCEAN ATMOSPHERE INFLUENCE AS A HYDROLOGICAL CONDITIONS SHAPE FACTOR OF THE BALTIC SEA

The hydrological conditions of seas and oceans form the phenomena related to the interaction of the spheres of the Earth. Climate and weather on Earth are shaped by three basic climate-forming processes: heat circulation, water circulation and air circulation, as well as geographical factors: layout of land and oceans, the height above the sea level and distance from the sea (ocean).

In general, the climate of the southern Baltic is influenced much by the Atlantic Ocean and the continent of Eastern Europe [16, 18, 19, 21]. Terms of land around the Baltic Sea foster free reach of air masses from almost all directions over the sea, but when they go through the North Sea they again take on moisture. The humid air masses from the North Sea, which reach into the Baltic Sea from the west, cause the occurrence of precipitation. Continental air masses come unhindered from the east and south to the Baltic Sea. Only air masses coming from the north to the region of the Baltic Sea face an orographic natural barrier in the form of the Scandinavian Mountains. Therefore, the location of the Baltic sea favors frequent exchange of physically differing air masses. Consequently, this results in high variability of weather in a short period of time (overnight), as well as on an annual basis. This is exemplary confirmed by a sample forecast of the pressure system for tomorrow (30.11.2015) which promises fluctuations in weather as shown in Figure 1.

According to Koppen climate classification [12] the Baltic Sea is situated in the area of two types of climate: Cf - warm temperate with uniform soil moisture and Df - cold climate with uniform soil moisture (continental). The warm temperate

strip covers the south waters of the Baltic Sea. On said area, the influence of the Atlantic climate due to the prevailing winds from the western direction carrying a mass of moist air temperate is shown. Characteristic of this climate is rain throughout the year, with the largest number of them is observed in summer and lowest in winter.

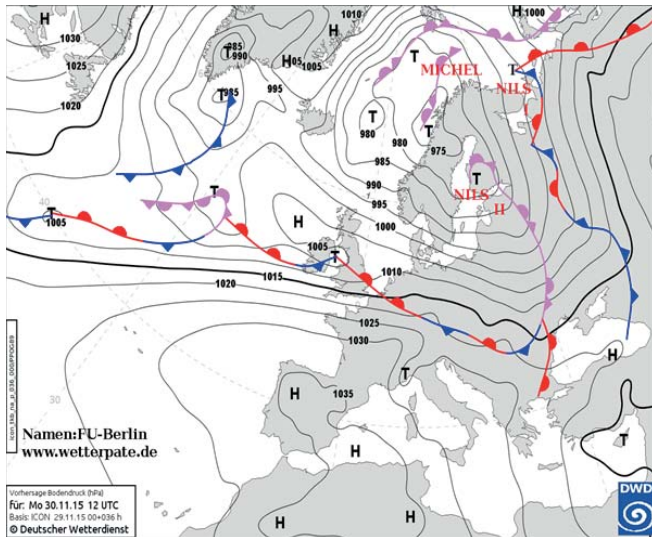


Fig. 1. Expected pressure system for Europe on 30 November 2015
[\[http://dobrapogoda.blog.pl/uklad-baryczny-nad-europa/\]](http://dobrapogoda.blog.pl/uklad-baryczny-nad-europa/)

For the Central Baltic region, the transition from marine to land climate is characteristic. A manifestation of this is the increase in daily temperature differences in the air as you move from the coast inland. In the area, winds from the eastern direction from NW to SW are prevailing, and the humidity is the highest in winter and lowest in May.

The continental climate area type Df extends over part of the Baltic Sea located to the north and east of the Öland-Kaliningrad line. Rainfall is present here in all seasons, most in August - September, and the least in March. In this area, the impact of marine climate is reduced and in the eastern part of the land climate impact increases.

The climate of the Baltic is determined by its position in two climate zones and the proximity of the Atlantic Ocean. Over the area of the Baltic Sea, in the summer come partly tropical air mass and in winter often come arctic and polar air mass. The influence of Atlantic air mass causes an increase in humidity, as well as warming in winter and cooling in summer.

SEA WATER CHARACTERISTICS CHANGES IN THE SELECTED WATERS OF THE SOUTHERN BALTIC SEA

The acoustic environment of the Baltic Sea is very complicated, which results from a wide variety of factors that shape it: the geological structure of the bottom, bottom sediments and changes in temporal and spatial hydrological conditions. The possibility to use hydro acoustic devices

to study the underwater Baltic Sea, as well as underwater communication directly depend on all these factors, with the most important changes are the thermo-halifax ones. The natural conditions of the Baltic Sea are described in detail in literature. Recently, 3 extensive monographs devoted to the Baltic sea have been published [1, 26, 27]. While reports characterizing the acoustic climate of the Baltic Sea in detail are rare [10, 5].

In literature, several reports of relationship between the conditions of propagation of acoustic waves, particularly sound velocity distributions, and spatial distributions of the temperature and salinity can be found. Usually, however, these publications are of a general nature [11, 22] or on experimental studies, which are fragmentary information on hydrological conditions and the acoustic measurements. For example, a summary of research on the measurement and simulation of transmission loss (propagation loss) in the Landsort Deep, the Gotland Deep and Bornholm Deep areas conducted in 2002-2007 are given in [3]. The existence of a sound channel creates favorable conditions for underwater communication, but its variability time-space significantly complicates these conditions [eg. 24]. Changes in distribution speed of sound in the basin, which for a short observing time, order of days, can be regarded as quasi-stationary, can be modified by the phenomenon of internal waves [23], mixing the wind [7] or the inflow of refueling water [20].

The nature of changes in the properties of seawater is significantly associated with the seasons, mainly because the effect of temperature mainly affects the characteristics of the physical-chemical properties of sea water. Of course, the content of variable salinity also impinge on the water characteristics and have slightly different character volatility [20]. The analysis covered the months of February and July, September and November. February represents the winter season, July and September represent summer and autumn in November. The results have been developed on the basis of the measurement data collected during research cruises made by r / v "Baltica". Measurements of temperature and salinity were made with the use of Neil Brown CTD probe, and the acoustic wave velocity values were determined based on an empirical relationship linking the speed of sound hydrological parameters [2].

The evaluation of changes in acoustic conditions can be made by analyzing the velocity sound distributions on a hydrological profile at particular times of the year and comparing the imaged data with the values that characterize the different regions on the basis of long-term data. The following figures (Fig. 2 - Fig. 5) show the temperature, salinity, and consequently the speed of sound distribution changes in the course of the year in the cross section through the depths of the Southern Baltic for example, data from the year 2005, not distinguishing itself with any specific anomalies.

The use of perennial statistical data is helpful in the assessment of current acoustic situation. Tables 1-6 summarize the information about the temperature, salinity and sound velocity at the surface and at the bottom of the depth of the main southern Baltic sea. The tables show the values in 2005

in individual months, and the arithmetic mean of the same parameters designated for a period of 50 years from 1960 to 2010.

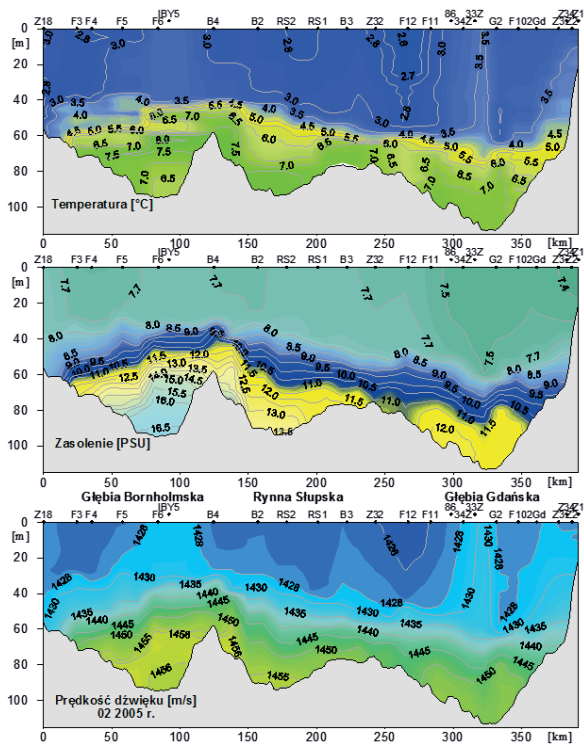


Fig. 2. Vertical distribution of temperature, salinity and sound velocity profile on the hydrological profile through the depths of the southern Baltic sea (February 2005)

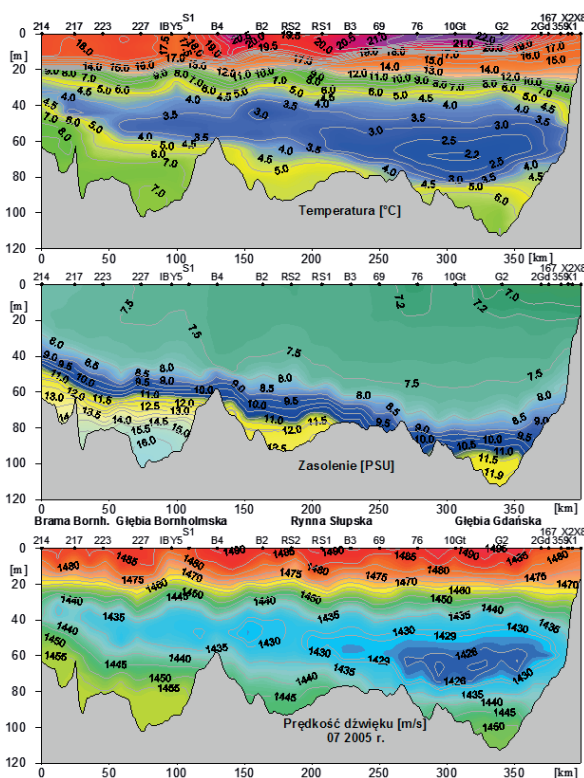


Fig. 3. Vertical distribution of temperature, salinity and sound velocity profile on the hydrological profile through the depths of the southern Baltic sea (July 2005)

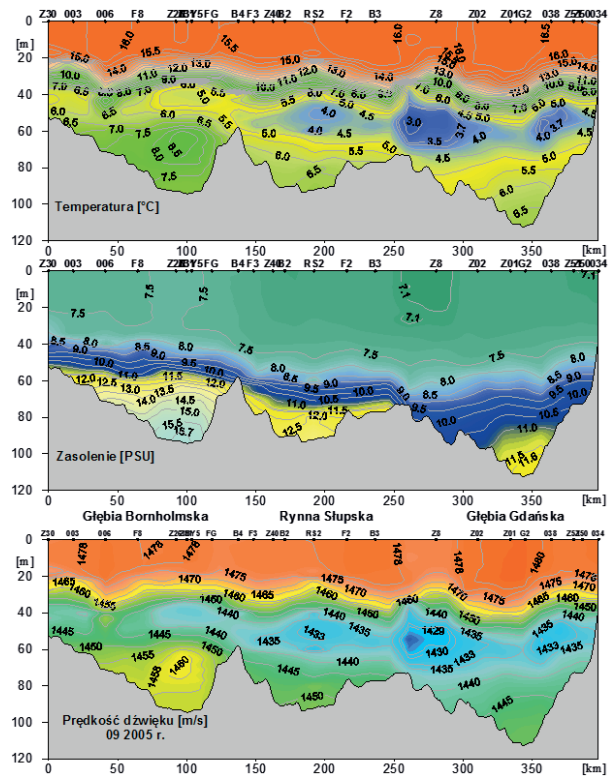


Fig. 4. Vertical distribution of temperature, salinity and sound velocity profile on the hydrological profile through the depths of the southern Baltic sea (September 2005)

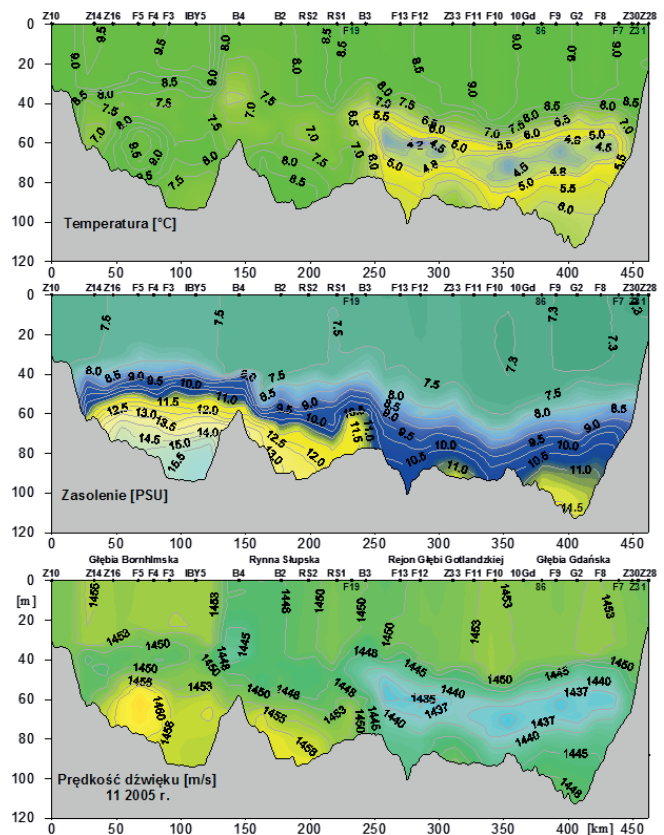


Fig. 5. Vertical distribution of temperature, salinity and sound velocity profile on the hydrological profile through the depths of the southern Baltic sea (November 2005)

Tab. 1. The values of temperature, salinity and sound velocity at the surface of water in the region of Bornholm Deep at IBY5 station in 2005

| Parametr | II | mean | VII | mean | IX | mean | XI | mean |
|---------------------|--------|--------|--------|--------|--------|--------|--------|--------|
| temperature [°C] | 3,31 | 2,40 | 17,28 | 16,33 | 16,40 | 15,57 | 9,49 | 8,52 |
| salinity [PSU] | 7,76 | 7,70 | 7,48 | 7,50 | 7,54 | 7,58 | 7,56 | 7,58 |
| Sound velocity[m/s] | 1428,6 | 1424,3 | 1482,4 | 1479,3 | 1479,6 | 1476,9 | 1454,6 | 1450,7 |

Tab. 2. The values of temperature, salinity and sound velocity at the surface of water in the region of Slupsk Furrow at RS2 station in 2005

| Parametr | II | mean | VII | mean | IX | mean | XI | mean |
|---------------------|--------|--------|--------|--------|--------|--------|--------|--------|
| temperature [°C] | 2,73 | 2,38 | 21,00 | 16,12 | 16,22 | 15,91 | 8,19 | 8,39 |
| salinity [PSU] | 7,76 | 7,66 | 7,41 | 7,54 | 7,24 | 7,43 | 7,48 | 7,51 |
| Sound velocity[m/s] | 1425,9 | 1424,1 | 1493,7 | 1478,4 | 1478,6 | 1477,7 | 1449,3 | 1450,1 |

Tab. 3. The values of temperature, salinity and sound velocity at the surface of water in the region of Gdansk Deep at G2 station in 2005

| Parametr | II | mean | VII | mean | IX | mean | XI | mean |
|---------------------|--------|--------|--------|--------|--------|--------|--------|--------|
| temperature [°C] | 3,67 | 2,38 | 22,02 | 16,55 | 16,22 | 15,53 | 9,04 | 8,95 |
| salinity [PSU] | 7,47 | 7,60 | 7,41 | 7,41 | 7,24 | 7,43 | 7,29 | 7,49 |
| Sound velocity[m/s] | 1429,8 | 1424,0 | 1496,7 | 1479,9 | 1478,6 | 1476,5 | 1452,5 | 1452,3 |

Tab. 4. The values of temperature, salinity and sound velocity at the bottom in the region of Bornholm Deep at IBY5 station in 2005

| Parametr | II | mean | VII | mean | IX | mean | XI | mean |
|---------------------|--------|--------|--------|--------|--------|--------|--------|--------|
| temperature [°C] | 6,51 | 7,03 | 6,98 | 5,58 | 7,06 | 6,34 | 7,09 | 7,62 |
| salinity [PSU] | 16,54 | 16,50 | 16,13 | 16,80 | 16,01 | 15,87 | 15,95 | 16,44 |
| Sound velocity[m/s] | 1455,1 | 1457,5 | 1456,5 | 1452,7 | 1456,7 | 1453,9 | 1456,7 | 1459,2 |

Tab. 5. The values of temperature, salinity and sound velocity at the bottom in the region of Slupsk Furrow at RS2 station in 2005

| Parametr | II | mean | VII | mean | IX | mean | XI | mean |
|---------------------|--------|--------|--------|--------|--------|--------|--------|--------|
| temperature [°C] | 7,65 | 7,06 | 5,78 | 4,81 | 6,64 | 5,50 | 8,75 | 7,33 |
| salinity [PSU] | 13,51 | 12,75 | 12,57 | 13,19 | 13,26 | 12,71 | 12,84 | 13,02 |
| Sound velocity[m/s] | 1455,9 | 1452,4 | 1447,1 | 1443,5 | 1451,7 | 1445,9 | 1459,6 | 1453,8 |

Tab. 6. The values of temperature, salinity and sound velocity at the bottom in the region of Gdansk Deep at G2 station in 2005

| Parametr | II | mean | VII | mean | IX | mean | XI | mean |
|---------------------|--------|--------|--------|--------|--------|--------|--------|--------|
| temperature [°C] | 7,13 | 6,43 | 7,01 | 5,42 | 6,71 | 5,29 | 6,41 | 5,66 |
| salinity [PSU] | 12,16 | 11,90 | 12,01 | 12,21 | 11,73 | 11,57 | 11,52 | 11,68 |
| Sound velocity[m/s] | 1452,4 | 1449,1 | 1451,8 | 1445,3 | 1450,2 | 1443,9 | 1448,8 | 1445,5 |

In the first place, the characteristic of the area of the southern Baltic Sea in the winter months (Fig. 2) will be covered. During this period, the water mixing takes place mainly by the interaction between atmosphere - hydrosphere, which is associated with the occurrence of storms as well as the convection of water movement causing mixing of the water as a function of water depth.

This comes down to determine the temperature in the range 2,6°C to about 3,5°C layer from the surface of the sea to a depth of 40-50 meters in the region of Bornholm Deep and to a depth of 60-70 meters in the area of Gdansk Deep. The water temperature at the surface in February at the study area was higher than the long-term average in the area of the Gdansk Deep at 1,03°C. Salinity was not significantly different from the averaged one. As a result of slightly higher temperature, the speed of sound at the surface was greater than the average, the biggest difference in the area of the Gdansk Deep was 5.9 m/s.

The distribution of the baseline and the salinity in the deep layer in February shows that there was a situation to deal with after the "warm" infusion of water from the North Sea in the preceding season. Still, a clear deficit of salt deep water is visible. In the following months, the salinity at the bottom in the Bornholm Deep and the Gdansk Deep gradually decreased. In Slupsk Furrow, changes in temperature and salinity during the year showed that there was another water supply more saline from Bornholm Deep Slupsk Furrow, which is a typical occurrence at area [20].

In the distribution of the velocity of sound in July, typical of early summer in the Baltic, a water layer is visible at the surface which is characterized by a high speed of sound, reaching more than 1495 m/s. This is the effect of temperature increase of surface water from about 18 °C in the region of Bornholm Deep to about 22 °C in the area of Gdansk Deep. Throughout the 2005, the surface water temperature was higher than the mean values for each of the months. In July, the surface water reached a depth of about 30 meters (Fig. 3) with a definite main thermocline, which had a base temperature of about 10.0 °C. Below the thermocline, between 30 and 60 m in the region of Bornholm Deep and 35 and 80 meters in the area of the Gdansk Deep, there was a vast layer of water from the winter with the minimum temperature of 2.1 to 3.5 °C.

In the example, a significant impact on the acoustic conditions had a deeply positioned and poorly developed halocline, which was the result of too little inflow of salt water from the North Sea. The layer of the mixed water with a salinity of approximately constant (7.2-7.5) was very extensive. In July and other months in the area of the Gdansk Deep it reached to a depth of 60 to 70 m.

In the temperature distribution in July (Fig. 3), under the seasonal thermocline, there was a layer of water which is a remnant of the winter with a thickness of 30 meters in the region of Bornholm Deep to about 40 - 50 m in the area of Gdansk Deep. This water with a temperature of 2.1 to 2.5 °C in the area of Gdansk Deep to about 3.5 °C in the region of Bornholm Deep created favorable conditions for the creation of an acoustic channel. Due to the small amount of salt water

in the deep layer, the layer of cold water was above halocline, at great depth. Minimum in the distribution of the speed of sound defining the sound channel axis was therefore at a depth of about 40 meters in the region of Bornholm Deep to about 70 meters in the area of Gdansk Deep.

In September, the surface water had a temperature of about 15.5 - 16.0 °C and the mixed temperature layer formed from the surface to about 20 m, followed by primary thermocline to a temperature of about 7.0 °C at a depth of 25 - 30 m (Fig. 4). In the eastern part of the southern Baltic sea, a layer of cold water with a temperature of 3 - 4 °C was still present, which in the region of Slupsk Furrow and Gdansk Deep create the conditions for the creation of an acoustic channel axis at a depth of about 60 meters.

In November, the temperature differences throughout the water column in the western part of the area in question were negligible, but in the area of Gdansk Deep and Gotland Deep still visible was the residual winter water as a layer at a temperature lower than the temperature of the surrounding water masses.

SUMMARY

The example of changes in hydrological conditions in the wake of the acoustic conditions presented in the article confirms the high complexity of the phenomenon of propagation of acoustic waves in a specific basin, which is the Baltic Sea. The distributions of the speed of sound, the seasonal variation resulting from the cyclical nature of the phenomenon of heat exchange on the border of the sea-atmosphere is evident. However, the course of the phenomenon of the layer of the sea physical properties change is modified by the second factor shaping the acoustic climate of the Baltic Sea, namely the inflow of saline water from the North Sea. In the discussed example, there was a situation described showing a deficit of floodwater in the deep layer. The consequence of this is deeply situated halocline - very poorly developed. Another effect of the lack of denser water in the deep layer is a greater than typically fall of low-temperature water remaining from winter. This water dropped to a depth to which a sufficient heat amount does not reach to heat it. As a result, the acoustic environment differs from the typical. The acoustic channel, which was created in this case is located lower than usually. The lower limit of this channel separates less diverse layers of water, which affects the losses of transmission and efficiency of information transmission.

ACKNOWLEDGMENTS

The paper is elaborated on the basis of hydrological measurements performed by the Sea Fisheries Institute in Gdynia.

The investigation was partially supported by the National Center for Research and Development, Grant No. DOBR/0020/R/ID3/2013/03 and Ministry for Sciences and Higher Education under the scheme of Funds for Statutory Activity of Gdansk University of Technology and Polish Naval Academy.

BIBLIOGRAFIA

1. Feistel R., Nausch G., Wasmund N.: State and Evolution of the Baltic Sea, 1952-2005. A Detailed 50-Year Survey of Metrology and Climate, Physics, Chemistry, Biology and Marine Environment, Wiley & Sons, New Jersey, 2008.
2. Fofonoff N.P., Millard R.C. Jr.: Algorithm for computation of fundamental properties of seawater, UNESCO Technical papers in Marine Science No. 44, 1983.
3. Gerdes, F. · Hofmann, H-G. · Jans, W. · Künzel, S. · Nissen, I. · Dol, H.S., Proceedings 3rd International Conference and Exhibition on Underwater Acoustic Measurements - Technologies & Results - UAM 2009, 21-26 June 2009, Nafplion, Greece.
4. Gloza I.: Identification methods of underwater noise sources generated by small ships, Acta Physica Polonica A, 119, 961-965, 2011.
5. Grelowska G.: The prevailing patterns of the sound speed distribution in the environment of the Southern Baltic, Archives of Acoustics, 25, p. 359-368, 2000.
6. Grelowska G., Kozaczka E., Kozaczka S., Szymczak W.: Underwater noise generated by a small ship in the shallow sea, Archives on Acoustics, 38, 3, 351-356, 2013.
7. G. Grelowska, E. Kozaczka, Nonlinear properties of the Gotland Deep – Baltic Sea, Archives of Acoustics, 40, 4, 2015.
8. Hela I.: The Sound Channel of the Baltic Sea, Geophysics, 5, p.153-161, 1958
9. Holec M., Ratowski J.: Pinowe rozkłady I gradient prędkości dźwięku w południowym Bałtyku I ich bieg roczny, Proc. Of the 25th Open Seminar on Acoustics, 143-151, Poznań 1978.
10. Klusek Z.: The conditions for sound propagation in the southern Baltic, Ed. Institute of Oceanology, 1, 269 pp., Sopot 1991 (in Polish).
11. Klusek Z.: The state of the Baltic Sea acoustic investigations, Proceedings of the International Conference "Underwater Acoustic Measurements: Technologies & Results" Heraklion, Crete, Greece, 28th June – 1st July 2005.
12. Koppen W.: Grundriss der Klimakunde, Berlin 1931.
13. Kozaczka E., Grelowska G.: Shipping low frequency noise and its propagation in shallow water, Acta Physica Polonica A, 119, 6, 1009-1012, 2011.
14. Kozaczka E., Grelowska G., Szymczak W., Kozaczka S.: Processing data on sea bottom structure obtained by means of the parametric sounding, Polish Maritime Research, 19, 4, 3-10, 2012.

15. Kozaczka E., Grelowska G., Kozaczka S., Szymczak W.,
Detection of objects buried in the sea bottom with the use
of parametric echosounder, *Archives on Acoustics*, 38, 1,
99-104, 2013.
16. Łomniewski K., Mańkowski W., Zaleski J.: *Morze
Bałtyckie*, Warszawa 1975.
17. Marszał J., Salamon R.: Detection range of intercept sonar
for CWFM signals, *Archives of Acoustics*, 39, 2, 215-230,
2014.
18. Mietus M., The climate of the Baltic Sea Basin, World
Meteorological Organisation, *Marine Meteorology and
Related Oceanographic Activities*, Rep. No 41, WMO/
TD-No. 999, Geneva 1998.
19. Niros A. Vihma T., Launiainen J.: Marine meteorological
conditions and air-sea Exchange processes over the
northern Baltic Sea In 1990s, *Geophysica*, Vol. 38, 1/2, 59-
87, 2002.
20. Piechura J., Beszczyńska –Moeller A.: Inflow waters in the
deep regions of the southern Baltic Sea: Transport and
transformation (corrected version). *Oceanologia*, 46(1),
113-141, 2004.
21. Piechura J.: Longterm changes in hydrological conditions
of the southern Baltic, *Bull. Sea Fish. Inst.*, 128, 1, 45-57,
1993.
22. Pihl J.: Underwater acoustics in the Baltic - a challenging
research task, *Proceedings of the International Conference
“Underwater Acoustic Measurements: Technologies &
Results”*, Heraklion, Crete, Greece, 28th June – 1st July
2005.
23. Rybak S.A., Serebryany A.N.: Nonlinear internal waves
over the inclined bottom: observations with the use of an
acoustic profiler, *Acoustical Physics*, 57, 1, 77-82, 2011.
24. Smedsrud M., Jenserud T., Characterization of long-range
time-varying underwater acoustic Communications
channels, *Acoustics 08, Proceedings of European
Conference on Underwater Acoustics*, pp. 6097-6102,
Paris 2008.
25. Śliwiński A.: *Akustyka morza*, *Enc. Fizyki Współcz.*, 880-
885, PWN, Warszawa 1983.
26. The BACC Author Team: *Assessment of climate change
for the Baltic Sea basin*, Springer, Berlin-Heidelberg, 2008.
27. The BACC Author Team, *Second assessment of climate
change for the Baltic Sea basin*, Springer, 2015.
28. Tymański P.: *Struktura akustyczna wód południowego
Bałtyku*, *Stud. Mater. Oceanol.*, 7, 183-189, 1973.

CONTACT WITH THE AUTHOR

Grażyna Grelowska
gragrelo@pg.gda.pl

Faculty of Ocean Engineering and Ship Technology
Gdańsk University of Technology
11/12 Narutowicza St.
80-233 Gdańsk
Poland

MODELLING THE DYNAMICS OF SHIPS WITH DIFFERENT PROPULSION SYSTEMS FOR CONTROL PURPOSE

Witold Gierusz, Assoc. Prof.
Gdynia Maritime University, Poland

ABSTRACT

Two different propulsion systems are analyzed from point of view of future control applications. The traditional one consists of a pushing single screw propeller and a blade rudder. The other system is based on pod (pods): pulling or pushing ones. The equations describing forces and moments generated in both systems, are presented. Exemplary results of a simulation in comparison to the real-time experiments for two ships are also shown.

Keywords: ship dynamics, simulation model, pod propulsion, conventional propulsion, tests results

INTRODUCTION

The simulation models of ship's dynamics play an important role in synthesis process of control systems. For many years most ships were equipped with conventional propulsion system with a single screw and a blade rudder. The modelling of such system was properly performed and has rich bibliography. Nowadays a different propulsion system has become more and more popular. It is based either on azimuthing thrusters (e.g. ducted ones) or pods. Unfortunately, the way the systems work is somewhat different and each of them should be modelled separately.

This article is an attempt to present distinct manners of computing the forces and moment produced by main propulsion systems, conventional one and modern, in simulation models of the ships' dynamics.

The ship floating on the water surface should be treated as a rigid body with 6 degrees of freedom (6 DOF) with 3 linear velocities and 3 angular ones. The movement of the ship can be analyzed in relation to the commonly used, two Cartesian dextrorotatory coordinate systems: the moving one fixed to the ship and the inertial one fixed to the Earth. The origin of the ship-fixed frame commonly coincides with the ship's centre of gravity, see Fig.1.

Ship dynamics can be described by means of strongly nonlinear dimensional equations based on Newton's second law.

$$\begin{aligned} m(\dot{u} + qw - rv) &= X_{tot} & (1) \\ m(\dot{v} + ru - pw) &= Y_{tot} & (2) \\ m(\dot{w} + pv - qu) &= Z_{tot} & (3) \\ I_x \dot{p} + (I_z - I_y)qr &= K_{tot} & (4) \\ I_y \dot{q} + (I_x - I_z)rp &= M_{tot} & (5) \\ I_z \dot{r} + (I_y - I_x)pq &= N_{tot} & (6) \end{aligned}$$

where:

m - mass of the ship,

I_x, I_y, I_z - moments of inertia around X-Y-Z axes, respectively,

$X_{tot}, Y_{tot}, Z_{tot}$ - total forces acting along appropriate axes,

$K_{tot}, M_{tot}, N_{tot}$ - total moments acting on the hull.

For many control applications like the heading, speed and/or trajectory stabilization it is a common practice to neglect pitch, roll and heave motion with assuming that $p = q = w = 0$. Consequently, the 6 DOF model of the ship is converted to the 3 DOF model:

$$m(\dot{u} - rv) = X_{tot} \text{ [N]} \quad (7)$$

$$m(\dot{v} + ru) = Y_{tot} \text{ [N]} \quad (8)$$

$$I_z \dot{r} = N_{tot} \text{ [Nm]} \quad (9)$$

The right hand sides of the above given equations represent forces and moments from different sources and have the form:

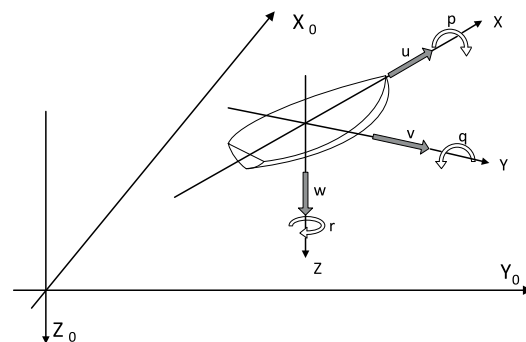


Fig.1. The Earth-fixed reference frame X₀-Y₀-Z₀ and the ship-fixed reference frame X-Y-Z.

The quantities u, v, w denote linear velocities and p, q, r angular ones.

$$X_{tot} = X_h + X_{asd} + X_{psd} + X_{dis} \quad (10)$$

$$Y_{tot} = Y_h + Y_{asd} + Y_{psd} + Y_{dis} \quad (11)$$

$$N_{tot} = N_h + N_{asd} + N_{psd} + N_{dis} \quad (12)$$

where the applied indices denote, respectively:

h - hydrodynamic phenomena related to the hull movement through the water,

asd - active steering devices like main propulsion or tunnel thrusters,

psd - passive steering devices like blade rudder,

dis - external disturbances like wind, waves etc.

Based on the above presented equations the simulation model of the ship's dynamics can be presented in a block form, Fig.2.

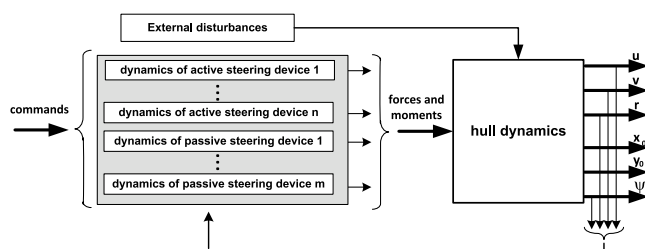


Fig.2. The block diagram of the ship dynamics model

THE FORCES AND MOMENTS ACTING ON THE HULL

HYDRODYNAMIC FORCES AND MOMENTS

To estimate the properties of the floating vessel it is essential to determine the hydrodynamic forces and moments acting on the hull. Unfortunately, it is also the most difficult problem to solve due to the fact that the functions of ship motion parameters are complicated. There are several methods to calculate the above mentioned quantities.

The most reliable seems to be a result of experimental scale-model tests in towing tanks. But such way is expensive and time consuming. In recent years two other methods became commonly used. The first one, based on semi-empirical results, uses geometrical hull dimensions and load conditions. This method was proposed by Japanese research group named MMG, organized by the Manoeuvrability Sub-Committee of JTTC. The formulas useful for hydrodynamic forces calculation were published in [7], [8], [10].

The second solution is application of a numerical method based on advanced computer techniques named CFD (Computational Fluid Dynamics) [17]. Forces resulting from the water flowing around the hull during manoeuvres and the interaction phenomena between hull, propulsion devices and blade rudder can be estimated with increasing accuracy.

The first method seems to be easier for practical implementations. When one considers the manoeuvring characteristics of the ships with different propulsion systems it should be noted that there are two ways to obtain formulas for hydrodynamic forces and moments (see the mentioned

publications of MMG group for conventional hull shape and formulas for ships equipped with pods, presented in PhD thesis of Michael Woodward [16]).

FORCES AND MOMENTS FROM MAIN PROPULSION SYSTEMS

One can consider two main cases; the traditional propulsion system consisted of a pushing single screw propeller powered by main engine, and a blade rudder, and another system based on pod (pods) propulsion, pulling or pushing one. The equations describing dynamics of both systems are shown below (The presented formulas for forces generated by main propulsion system are in general valid for ship moving with the almost constant speed (cruising speed) and the small angles between longitudinal ship axis and direction of the vessel motion, amounting no more than about $\pm 30^\circ$. In the other case, e.g. during manoeuvres, the above mentioned equations are much more complicated.)

THE SYSTEM OF SINGLE SCREW PROPELLER AND BLADE RUDDER

The main task of the ship engine is to generate the proper longitudinal force X_{prop} for ahead or astern ship motion, given by formula:

$$X_{prop} = (1-t)T_{prop} \quad (13a)$$

where:

T_{prop} - propeller thrust

t - thrust deduction factor.

When the ship has a single propeller, one can introduce a small transverse force Y_{prop} and rotating moment N_{prop} to take into account the lateral reaction of the screw propeller:

$$Y_{prop} = k_{prop} X_{prop} \quad (13b)$$

$$N_{prop} = Y_{prop} L_{prop} \quad (13c)$$

where:

k_{prop} - constant coefficient dependent on the particular propulsion system,

L_{prop} - distance between the origin of body frame and the screw propeller.

The commonly used equation for calculating the thrust is as follows [7]:

$$T_{prop} = \rho_w n_g^2 D_{prop}^4 K_T(J) \quad (14)$$

where:

ρ_w - density of water,

n_g - number of propeller revolutions,

D_{prop} - screw propeller diameter,

K_T - non-dimensional thrust coefficient,

J - advance coefficient.

The thrust coefficient K_T strongly depends on screw construction, its rotational speed and velocity of water flow around the screw propeller. This relationship is often presented graphically as follows:

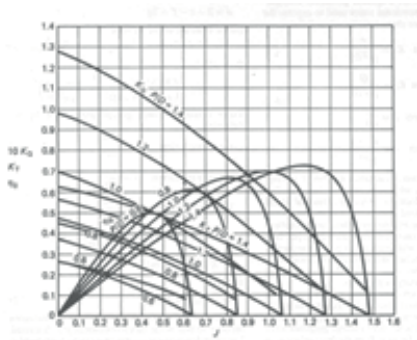


Fig.3. Open water diagram for Wageningen B5-75 screw propeller. Exemplary relationship between the thrust coefficient K_T , torque coefficient K_Q , propeller efficiency η_0 - versus the advance coefficient J [4]

According to the notation given beneath the equations (10) - (12) one can write:

$$X_{asd1} = X_{prop}, Y_{asd1} = Y_{prop}, N_{asd1} = N_{prop}$$

Forces and moment from the blade rudder are complicated product of interaction between hull, screw propeller and rudder plate. Based on the results presented in [12] and [13] one can write the following equations:

$$X_{rud} = F_{rud} \sin(\delta_{ef}) \quad (15)$$

$$Y_{rud} = (1 + a_H) F_{rud} \cos(\delta_{ef}) \quad (16)$$

$$N_{rud} = l_{rud} Y_{rud} \quad (17)$$

where:

F_{rud} - rudder normal force,

a_H - rudder induction coefficient,

δ_{ef} - effective angle of rudder deflection,

l_{rud} - distance from rudder axis to the origin of body frame.

The rudder normal force can be calculated from the following formula [15]:

$$F_{rud} = \frac{1}{2} \rho_w A_{rud} u_{rud}^2 \frac{6.13 \frac{h_{rud}}{c_{rud}}}{\frac{h_{rud}}{c_{rud}} + 2.25} \quad (18)$$

where:

A_{rud} - rudder area,

u_{rud} - average rudder inflow velocity,

h_{rud} - rudder vertical height,

c_{rud} - rudder span.

The most difficult problem related to the above given formula is proper calculation of the u_{rud} . The quantity depends (in a nonlinear manner) on ship speed and water flow direction [15].

The analysis of the rudder normal force F_{rud} for different values and signs of speed, thrust and rudder angle was presented in [15]. One can assume, for simplification, that $F_{rud} \neq 0$ only for $T_{prop} > 0$, see Fig.4.

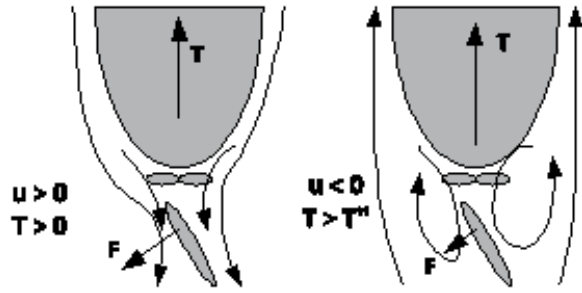


Fig.4. Two cases when the normal rudder force F_{rud} is significantly different from zero

More details can be found in [10], [12] and [15].

According to the notation given beneath the equations (10) - (12) one can also write for this case:

$$X_{psd1} = X_{rud}, Y_{psd1} = Y_{rud}, N_{psd1} = N_{rud}$$

POD (PODS) PROPULSION SYSTEM

The most important difference between the classic propulsion system and pod drive is the possibility of adjusting the pod angle in any position within the range $(-180 \div +180)$ [deg] in relation to the longitudinal axis of the ship. Moreover, the water can flow toward the pod from any angle, especially during turning manoeuvres. There are a few publications devoted to modelling motion of the ships with pod propulsion, e.g. [2], [9], [11], [14].

Fortunately, the sailing of the ship with cruising speed involves deflection of the pod (pods) within the range similar to that of the blade rudder deflection, i.e. $(-30 \div +30)$ [deg]. Therefore such mode of work is analyzed below. The main equation describing longitudinal and lateral forces resulting from pod propulsion in relation to water flow are as follows [1]:

$$F_{xpod} = \rho_w n_{pod}^2 D_{prop}^4 K_{Tx}(\delta_{rel}, J) \quad (19)$$

$$F_{ypod} = \rho_w n_{pod}^2 D_{prop}^4 K_{Ty}(\delta_{rel}, J) \quad (20)$$

where:

n_{pod} - number of pod propeller revolutions,

D_{prop} - diameter of the pod propeller,

$K_{Tx}(\delta_{rel}, J), K_{Ty}(\delta_{rel}, J)$ - non-dimensional thrust coefficients,

δ_{rel} - pod angle of attack in relation to water flow direction.

It should be emphasized that δ_{rel} is in general different in relation to the pod deflection angle δ , see Fig.5 for the case of the pulling screw propeller.

The angle σ denotes the angle of the direction of the free water stream (big blue arrow) in relation to the ship longitudinal axis.

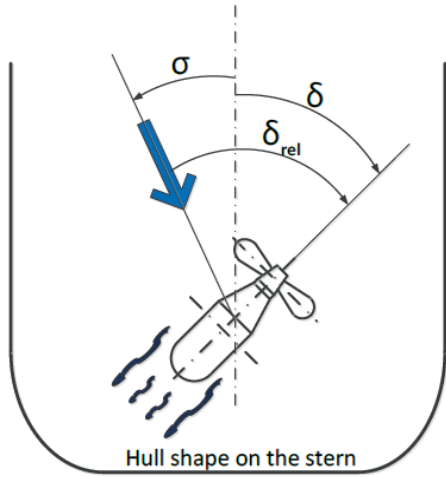


Fig.5. Definition of the relative pod angle of attack, δ_{rel}

The relationships between $K_{Tx}(\delta_{rel}, J)$ or $K_{Ty}(\delta_{rel}, J)$, and δ_{rel} are crucial in the modelling process [14]. The most reliable way to obtain them is to use open-water pod propulsion tests. Exemplary results for different advance coefficients are presented in Fig.6, [6]. Notice that $K_{Ty}(\delta_{rel}, J)$, for $\delta_{rel} = 0$ is not equal to zero!

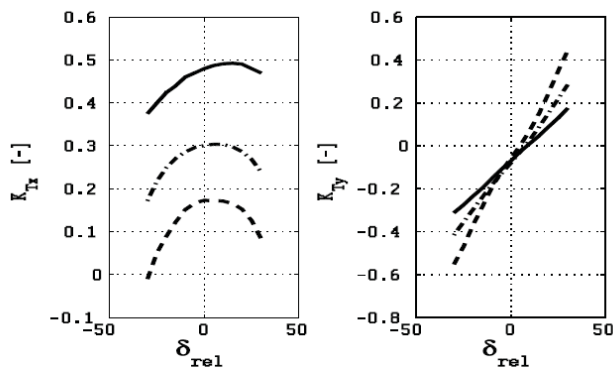


Fig.6. The non-dimensional thrust coefficients K_{Tx} and K_{Ty} in relation to the relative pod angle of attack, δ_{rel} . The solid line was drawn for $J = 0$, dash-dotted line for $J = 0.44$ and dashed line for $J = 0.71$

The forces from the equations (19) and (20) are obtained in relation to the water stream direction (blue arrow in Fig. 5). More useful for modelling of the pod dynamics are forces calculated in relation to the ship axes: longitudinal and lateral one, respectively.

Such forces and turning moment can be obtained from the following formulas:

$$X_{pod} = F_{xpod} \cos(\sigma) + F_{ypod} \cos(\sigma + \pi/2) \quad (21)$$

$$Y_{pod} = F_{xpod} \sin(\sigma) + F_{ypod} \sin(\sigma + \pi/2) \quad (22)$$

$$N_{pod} = Y_{pod} x_{pod} + X_{pod} y_{pod} \quad (23)$$

where x_{pod} and y_{pod} denote coordinates of the rotation axis of the pod in relation to the origin of the ship body frame.

According to the notation given beneath the equations (10) - (12) one can write:

$$X_{asd2} = X_{pod}, Y_{asd2} = Y_{pod}, N_{asd2} = N_{pod}$$

Another important problem related to the pod propulsion system is estimation of the resistance forces generated by the pod construction, i.e. its strut, fin and nacelle - see Fig.7.

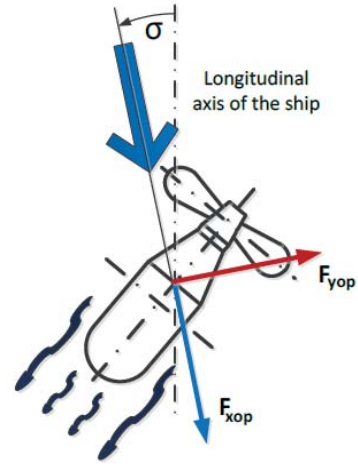


Fig.7. Definition of the longitudinal and lateral resistance forces generated by the pod construction. Big blue arrow denotes the direction of the free water stream

The formulas for the above mentioned forces in relation to the resultant water flow direction σ are as follows [16]:

$$F_{xop} = \frac{1}{2} \rho_w S_{bp} V_{rel}^2 C_{Tx}(\sigma) \quad (24)$$

$$F_{yop} = \frac{1}{2} \rho_w S_{bp} V_{rel}^2 C_{Ty}(\sigma) \quad (25)$$

where:

S_{bp} - transverse area of the strut and nacelle,

V_{rel} - velocity of resultant water flow acting on the pod body,

C_{Tx}, C_{Ty} - non-dimensional drag coefficients.

The water stream with the speed V_{rel} hitting onto the strut and nacelle is a sum of two components: the first one is the free stream resulting from the whole ship motion and the second one being an effect of the pod screw rotation. More details one can find in the already mentioned Woodward's PhD thesis.

The reliable way for obtaining values of the non-dimensional drag coefficients C_{Tx}, C_{Ty} is to perform the open-water tests of the pod without screw propeller [6]. Exemplary diagrams with results of such open-water tests are presented in Fig.8.

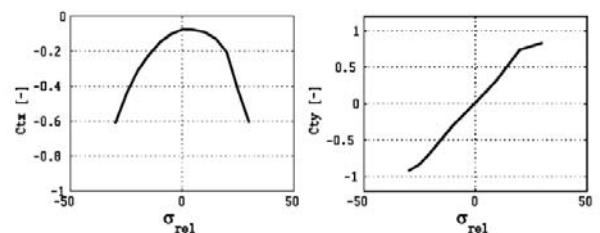


Fig.8. The non-dimensional drag coefficients C_{Tx} and C_{Ty} versus the relative resultant angle of water flow, σ

Both the forces $F_{x_{op}}$ and $F_{y_{op}}$ should be recalculated to forces X_{op} , Y_{op} and moment N_{op} in relation to the ship reference frame in the similar way as to propulsion forces.

According to the notation given beneath the equations (10) - (12) one can also write for this case:

$$X_{psd2} = X_{op}, Y_{psd2} = Y_{op}, N_{psd2} = N_{op}$$

Equations describing forces generated by other thrusters are commonly known and one can find them in e.g. [3].

THE CASE STUDY

The equations presented in the previous section were applied to create simulation models of two ships. Both ships are used in the centre for training navigators run by the Foundation for Safety of Navigation and Environment Protection at the Silm lake near Ilawa, Poland.

The ship named "Blue Lady" is an isomorphous model of the VLCC tanker in 1:24 scale. Its dynamic model was described in detail in [5] and its side view is shown in Fig.9.

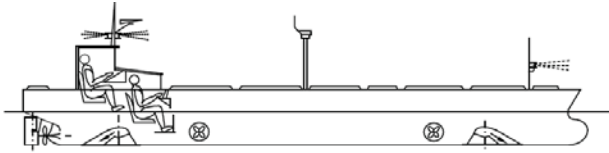


Fig.9. The side view of the model of the ship "Blue Lady"

The second ship named "Dorchester Lady" is a model of the LNG tanker in 1:24 scale. Its side view is shown in Fig.10

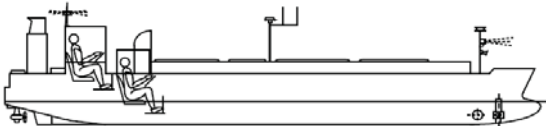


Fig.10. The side view of the model of the ship "Dorchester Lady"

Exemplary results of the experiments with simulation models of the ships and real-time trials are presented in the next four figures (The experiments on the lake Silm began with different ship heading (e.g. Fig.14) therefore the simulation runs had to repeat the same conditions.) The reference speed was adjusted to "Full-ahead" and deflections of the steering devices were set at two values: average one $\pm 10^\circ$ or $\pm 15^\circ$ and the large one $\pm 35^\circ$.

"Blue Lady"

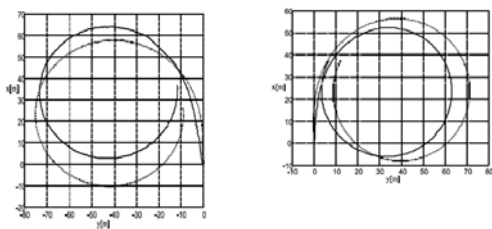


Fig.11. Trajectories of the real ship (solid line) and its model (dotted line) during turning manoeuvre with full ahead speed. Deflections of the blade rudder: $\delta = +10^\circ$ on the left hand side and $\delta = -10^\circ$ on the right hand side, respectively.

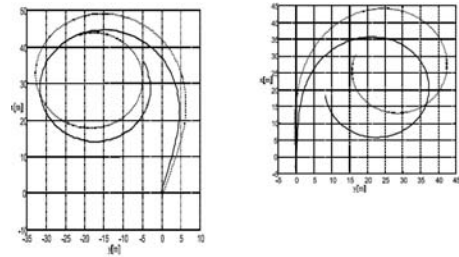


Fig.12. Trajectories of the real ship (solid line) and its model (dotted line) during turning manoeuvre with full ahead speed. Deflections of the blade rudder: $\delta = +35^\circ$ on the left hand side and $\delta = -35^\circ$ on the right hand side, respectively.

"Dorchester Lady"

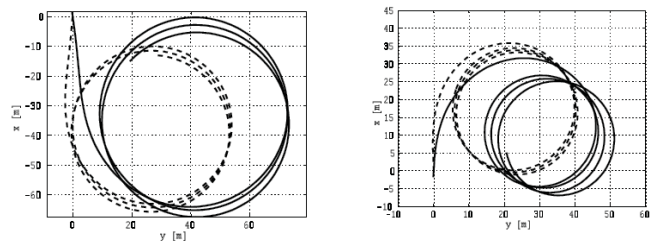


Fig.13. Trajectories of the real ship (solid line) and its model (dotted line) during turning manoeuvre with full ahead speed. Deflections of the blade rudder: $\delta = +15^\circ$ on the left hand side and $\delta = -15^\circ$ on the right hand side, respectively.

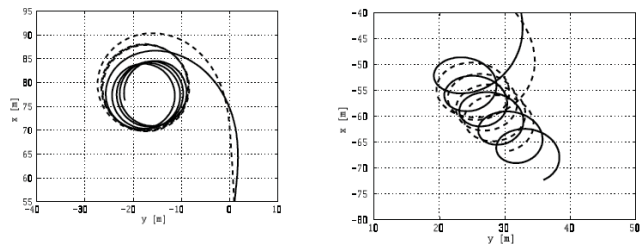


Fig.14. Trajectories of the real ship (solid line) and its model (dotted line) during turning manoeuvre with full ahead speed. Deflections of the blade rudder: $\delta = +35^\circ$ on the left hand side and $\delta = -35^\circ$ on the right hand side, respectively. Notice the strong influence of the wind in the left hand side figure.

As one can see the fitting of the "Dorchester Lady" simulation model is slightly worse than in the case of the "Blue Lady". One of the reasons for this situation can be much bigger influence of the wind blowing during experiments on the lake. The LNG tanker is more sensitive to the external disturbance due to its larger topside projected area (see also Fig.10).

CONCLUSIONS

In the article the pod propulsion system was analysed in comparison to the conventional one in similar simple working conditions. The ship movement with cruising speed during turning manoeuvre with rather small deflections of the steering devices, was presented.

It should be emphasized that the ship equipped with pods has totally different manoeuvring characteristics and poor course-keeping stability. Therefore control systems designed

for such ships have to be constructed in a different way than for the systems for conventional ships.

The described models of driving devices can be used for speed, heading and/or trajectory stabilization but DSP systems or precise steering at small speeds should comply with equations describing hull-pod and pod-pod interactions.

The proposed process for reviewing the ship's control system is an indirect method of verification which is placed between the low-cost methods of conducting research using computer simulations and tests with the use of expensive full-size ships. The potential results obtained by using the large-scale model may be considerably closer to the phenomena occurring in reality than the results that may be obtained through computer simulations. But simulation runs performed with proper and accurate computational models of the ship dynamics are an important step which enables to avoid many mistakes in control systems before they are tested in real-time experiments.

The article presents only the main equations described forces and moments acting on the ship's hull. More details can be found in the literature referred to, below.

BIBLIOGRAPHY

1. Ankudinov V., Kobylinski L. K., Review of Ability to Simulate Azimuthing Device Interactions, AZIPILOT 2., Deliverable 2.3., Public.pdf, www.transport-research.info, 2012.
2. Brandner P. Renilson M. Interaction Between Two Closely Spaced Azimuthing Thrusters, Journal of Ship Research, v.42, 1998.
3. Brix J. (Ed.), Manoeuvring Technical Manual, Seehafen Verlag GmbH, Hamburg, 1993.
4. Carlton J. Marine Propellers and Propulsion, Butterworth and Heinemann, Burlington, 2007.
5. Gierusz W., Simulation model of the ship-handling training boat „Blue Lady”, Int. IFAC Conference Control Applications in Marine Systems CAMS'01, Glasgow, Scotland, 2001.
6. Grygorowicz M., Hydrodynamics Characteristics of the Isolated Pod Model for Two-pods Propulsion System (in Polish), Report WOiO 3/03/BZ, Gdansk University of Technology, 2003.
7. Inoue S. , Hirano M. , Kijima K., Hydrodynamic Derivatives on Ship Manoeuvring, International Shipbuilding Progress, 1981.
8. Inoue S., Hirano M., Kijima K. , Takashina J., Practical Calculation Method of Ship Manoeuvring Motion, International Shipbuilding Progress, 1981.
9. Kanar J., The Semi-empirical Method for Prediction of the Driving Characteristics of the Ships with Multi-podded Propulsion (in Polish), PhD Thesis, Gdansk University of Technology, Poland, 2009.
10. Kose K., On a New Mathematical model of Manoeuvring Motions of a Ship and Its Applications, International Shipbuilding Progress, 1982.
11. Mello Petey de F., Advanced Podded Drive Simulation for Marine Training and Research, International Marine Safety Forum Meeting, Warnemuende, Germany, 2008.
12. Molland A.F. , Turnock S.R., Prediction of Ship- Rudder- Propeller Interaction at Low speeds and in Four Quadrants of Operation, Int. IFAC Conference on Manoeuvring and Control of Marine Craft MCMC'94, Southampton, UK, 1994.
13. Ogawa A. , Kasai H, On the Mathematical Model of Manoeuvring Motion of Ships, International Shipbuilding Progress, 1978.
14. Reichel M., The Prediction of the Manoeuvring Characteristics of the Ships with Azimuthing Propulsion (in Polish), PhD Thesis, Gdansk University of Technology, Poland, 2011.
15. Shouji K., Ishiguro T. , Mizoguchi S., Hydrodynamic Forces by Propeller and Rudder Interaction at Low Speed, Int. IFAC Conference MARSIM and ICSM, Tokyo, Japan, 1990.
16. Woodward M., Control and Response of Pod Driven Ships, PhD Thesis, University of Newcastle-upon-Tyne, 2005.
17. The Manoeuvring Committee. Final Report and Recommendations to the 23rd ITTC, Proc. of the 23rd International Towing Tank Conference, Venice, Italy, 2002.

CONTACT WITH THE AUTHOR

Witold Gierusz

Gdynia Maritime University
83 Morska St.
81-225 Gdynia
Poland

e-mail: wgierusz@am.gdynia.pl

MOTION PREDICTION OF CATAMARAN WITH A SEMI-SUBMERSIBLE BOW IN WAVE

Hanbing Sun, Ph.D.

Fengmei Jing, Ph.D.

Yi Jiang, M.Sc.

Jin Zou, Prof.

Jiayuan Zhuang, Ph.D.

Weijia Ma, Ph.D.

Harbin Engineering University, China

ABSTRACT

Compared with standard vessels, a slender catamaran with a semi-submerged bow (SSB) demonstrates superior seakeeping performance. To predict the motion of an SSB catamaran, computational fluid dynamics methods are adopted in this study and results are validated through small-scale model tests. The pitch, heave, and vertical acceleration are calculated at various wavelengths and speeds. Based on the overset grid and motion region methods, this study obtains the motion responses of an SSB catamaran in regular head waves. The results of the numerical studies are validated with the experimental data and show that the overset grid method is more accurate in predicting the motion of an SSB catamaran; the errors can be controlled within 20%. The movement data in regular waves shows that at a constant speed, the motion response initially increases and then decreases with increasing wavelength. This motion response peak is due to the encountering frequency being close to the natural frequency. Under identical sea conditions, the motion response increases with the increasing Froude number. The motion prediction results, that derive from a short-term irregular sea state, show that there is an optimal speed range that can effectively reduce the amplitude of motion.

Keywords: SSB catamaran; model test; overset grid; motion region; motion response

INTRODUCTION

Improving a ship's seakeeping performance and enhancing its navigational performance under stormy wave conditions are prominent research topics in the marine industry. This has given rise to a variety of high-performance vehicle and roll stabilisation technologies. The SSB catamaran, which combines the characteristics of a slender catamaran and an SSB, provides advantages such as excellent seakeeping performance, good stability, comfort, shallow draft, and a spacious deck. Because the composite hull has broad development prospects, it is necessary to predict its seakeeping performance.

The motion response of a vessel in waves can be predicted by using either the potential flow or viscous flow method. Potential flow theory is currently widely used to calculate ship motions and wave loads [1]. However, because the viscous damping force of an SSB is much greater than that of a conventional vessel in the same motion state, the effect of SSB viscous drag on pitching stabilisation cannot be reflected using this method. Therefore, the seakeeping performance of these complex vessels must be experimentally calculated. Hang has studied methods suited for predicting the seakeeping performance of vessels that use an SSB by

using STF slice theory [2]. Zhao's study of a wave-piercing SSB catamaran showed an improved seakeeping comprehensive index and significantly reduced pitching [3]. Cai conducted a model test and sea trial of a full-scale 450-ton ship. The results indicated that the composite monomer ship displayed excellent seakeeping performance; this assembly was able to significantly inhibit the longitudinal movement of the ship [4-5]. A number of studies have used theoretical calculations and model tests on a newly developed deep-V ship with a composite monomer hull. The results showed that this assembly significantly improved seakeeping performance [6-8]. Gao installed a semi-submersible hull on a wave-piercing catamaran in order to decrease pitching; the results showed, that the seakeeping performance of the ship was significantly enhanced [9]. Silva and Soares described a time-domain non-linear strip theory model of ship motions in six degrees-of-freedom and predicted the parametric rolling of an SSB containership [10].

This study analysed the seakeeping performance of a slender SSB catamaran under regular wave conditions by means of small-scale model testing and numerical simulation. Computational fluid dynamics (CFD) software

STAR-CCM+ was used for the simulation based on a six degrees-of-freedom rigid body equation and overset grid technology. By comparing the numerical and experimental results, a numerical method with a short cycle and low cost can be obtained to effectively improve the efficiency of ship optimization.

NUMERICAL SIMULATION METHOD

GOVERNING EQUATIONS

Incompressible Newtonian fluid motion conforms to both the continuity and the momentum conservation equations:

$$\frac{\partial p}{\partial t} + \frac{\partial(\rho u_i)}{\partial x_i} = 0 \quad (1)$$

$$\begin{aligned} \frac{\partial(\rho u_i)}{\partial t} + \frac{\partial}{\partial x_i}(\rho u_i u_j) = \\ -\frac{\partial p}{\partial x_i} + \frac{\partial}{\partial x_j} \left(\mu \frac{\partial u_i}{\partial x_j} - \rho \overline{u'_i u'_j} \right) + S_i \end{aligned} \quad (2)$$

where u_i and u_j are the time mean values of velocity, $i, j = 1, 2, 3$; whereas p is the time mean value of pressure, ρ is the fluid density, μ is the dynamic viscosity coefficient, $\rho \overline{u'_i u'_j}$ is the Reynolds stress, and S_i is the generalized source terms of momentum equation.

TURBULENCE MODEL

The selection of a turbulence model has a dramatic influence on the hydrodynamic calculation. There are four turbulence models widely applied in engineering calculations: standard $k-\varepsilon$, RNG $k-\varepsilon$, standard $k-\omega$, and SST $k-\omega$. The introduction of these turbulence models can be found in numerous references. After a comprehensive considering of the computational comparisons of these four common turbulence models in references [11] and [12], this paper uses the SST $k-\omega$ turbulence model because it can simulate the complex flow problems with flow separation and strong adverse pressure gradients. The equation is written as follows:

$$\begin{aligned} \frac{\partial(\rho k)}{\partial t} + \frac{\partial}{\partial x_i}(\rho k u_i) = \\ \frac{\partial}{\partial x_i} \left(\Gamma_k \frac{\partial k}{\partial x_i} \right) + G_k - Y_k \end{aligned} \quad (3)$$

$$\begin{aligned} \frac{\partial(\rho \omega)}{\partial t} + \frac{\partial}{\partial x_i}(\rho \omega u_i) = \\ \frac{\partial}{\partial x_i} \left(\Gamma_\omega \frac{\partial \omega}{\partial x_i} \right) + G_\omega - Y_\omega + D\omega \end{aligned} \quad (4)$$

where G_k and G_ω are the turbulent kinetic energies

caused by the mean velocity gradient, and Y_k and Y_ω are the turbulence dissipation rates for k and ω , respectively.

TREATMENT OF FREE SURFACE

The VOF method is adopted to capture the free surface. For a given computational domain V , Fluid 1 is in domain V_1 , and Fluid 2 is in domain V_2 . The function is defined as follows:

$$\alpha(\mathbf{x}, t) = \begin{cases} 1, & \mathbf{x} \in V_1 \\ 0, & \mathbf{x} \in V_2 \end{cases} \quad (5)$$

For a flow field composed of two incompatible fluids, $\alpha(\mathbf{x}, t)$ is in accordance with:

$$\frac{\partial \alpha}{\partial t} + \mathbf{U} \cdot \nabla \alpha = 0 \quad (6)$$

where $\mathbf{U} = (u, v, w)$ is the fluid velocity field, and the VOF function C_{ijk} is defined as the integral in the grid unit of $\alpha(\mathbf{x}, t)$ divided by unit volume, i.e.,

$$C_{ijk} = \frac{1}{\Delta V_{ijk}} \int_{I_{ijk}} \alpha(\mathbf{x}, t) dV \quad (7)$$

C_{ijk} is in accord with $(\partial C / \partial t) + \mathbf{U} \cdot \nabla C = 0$. When $C=1$, the grid is filled with Fluid 1. When $C=0$, the grid excludes Fluid 1. When $0 < C < 1$, the grid contains free surface.

GENERATING WAVE METHOD

The wave module of CFD software STAR-CCM+ is used to generate regular sinusoidal propagating waves in an infinite water depth. According to linear theory, the x - and z -components of the velocity are given by the following equations:

$$v_x = \omega \zeta_a e^{kz} \sin(\omega t - kx) \quad (8)$$

$$v_z = \omega \zeta_a e^{kz} \cos(\omega t - kx) \quad (9)$$

$$\zeta = \zeta_a \sin(\omega t - kx) \quad (10)$$

where ζ_a is the wave amplitude, $\omega = 2\pi/T$ is the wave frequency, $k = 2\pi/\lambda$ is the wave number, T is the wave period, λ is the wavelength, and x is the direction of wave propagation. z is positive when upward, with $z = 0$ the mean water level.

THE COMPUTATIONAL DOMAIN AND BOUNDARY CONDITIONS

A computational domain is established to simulate the fluid around the SSB catamaran. Dimensions are presented in Fig. 1 which consider both boundary interference and computational cost. In order to reduce interference from the sides of the computational domain, the inlet of the computational domain is defined as one ship length from the bow, the outlet is defined as three ship lengths from the stern, and the side is defined as one ship length from the

hull. To improve computational efficiency, only half of the hull is modelled and the longitudinal section is selected as the symmetry plane.

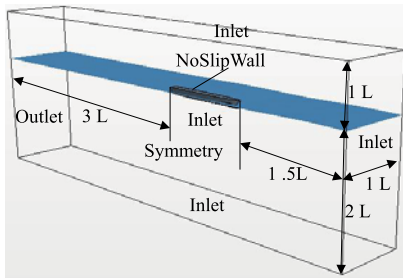


Fig. 1. Computational domain of the SSB catamaran

The head and side surfaces of the computational domain are set as the velocity inlet, the rear surface is set as the pressure outlet, and the hull surface is seen as a rigid wall.

THE MESH GENERATION AND MOTION SIMULATION

The resolution of the mesh has a significant influence on computational accuracy; thus, trimmed mesh is used to discretize the entire computational domain. In order to ensure accurate results, a boundary layer mesh of 3 near the hull and a surface mesh size of 0.003 L are selected; the free surface is also encrypted.

Overset grid and motion region techniques are applied to simulate the motion response of an SSB catamaran in waves.

In the overset grid method, the grid covering the computational domain is designated as the main grid, and the local grid containing the moving objects is designated as the slave grid. The outermost grid nodes of the subordinate parts can communicate with the main grid through interpolation. To ensure a fitted mesh division of complex shapes, the flow area is divided into sub-regions with simple geometric borders. Several researchers [13-15] have described overset grid technology in detail. Previous studies on mono-hull, catamaran, and trimaran vessels have shown, that the flow around ships with free surfaces can be effectively simulated with the overset grid method [15].

In the motion region method, the entire computational region is handled as a single entity. Momentum equations are discretised with a finite volume method in the time domain, and the non-steady solution is solved using a separation type

solver. The RANS equation and the six-degree of freedom motion equation are calculated simultaneously to simulate the motion response of an SSB catamaran. Fig. 2 shows the views of the overset mesh and the motion region mesh.

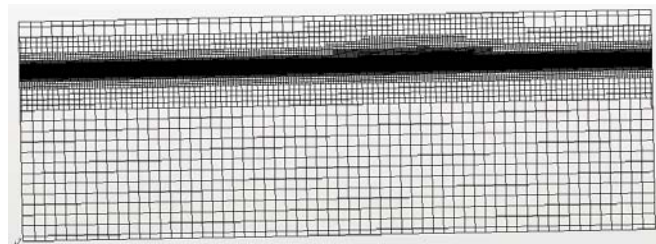
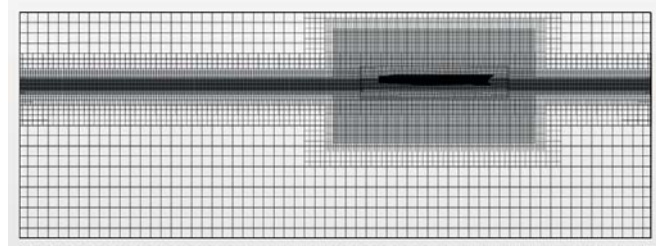


Fig. 2. Schemes of the SSB catamaran (a) Overset grid scheme (b) Motion region scheme

EXPERIMENTAL RESULTS

DESCRIPTION OF THE MODEL

A numerical simulation and model test of an SSB catamaran were carried out and the results were compared. The main dimensions are shown in Table 1 and the moulded lines are shown in Fig. 3.

Table 1. Main particulars of model

| Principal particular | value |
|--|-------|
| Length (L_m), in [mm]: | 4480 |
| Beam (B), in [mm]: | 956 |
| Demihull spacing (K), in [mm]: | 715 |
| Displacement (Δ), in [kg]: | 250 |
| Draft (T_{DWL}), in [mm]: | 152 |
| Water line length (L_{WL}), in [mm]: | 4224 |
| Longitudinal center of gravity (x_g), in [mm]: | 1980 |
| Height center of gravity (z_g), in [mm]: | 149 |
| Longitudinal rotation inertia, in [$kg \cdot m^2$] | 230 |

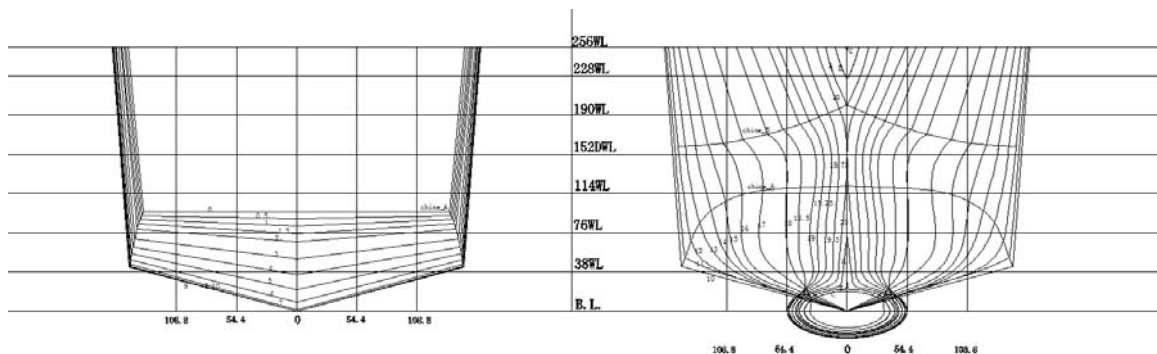


Fig. 3. Model ship lines

EXPERIMENTAL SETUP

Model tests were carried out at Harbin Engineering University, in a 108×7 m basin with a water depth of up to 3.5 m. The model was comprised of fiberglass composite materials. The model tests used the free lambent method to measure resistance, pitch, heave, and the amidships aft bow acceleration parameters. The DHDAS_5920 dynamic signal acquisition and analysis system was used for data acquisition. Fig. 4 shows the experimental setup, and Fig. 5 shows the model in the tank.

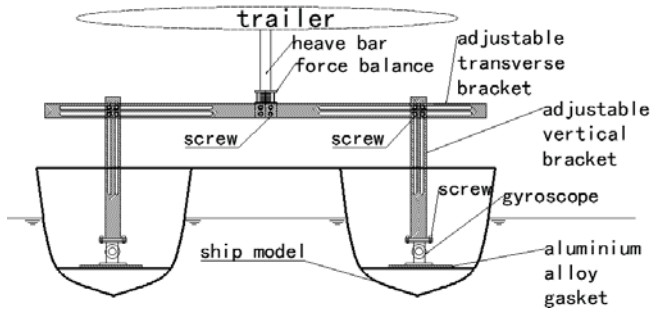


Fig. 4. Sketch of model test scheme



Fig. 5. Model in the tower tank

COMPARISON OF NUMERICAL SIMULATIONS AND EXPERIMENTAL RESULTS

Simulations of the SSB catamaran in regular waves for a head sea are computed by two numerical schemes: the overset grid and motion region methods. The inputs are a wave height/ H_a of 0.04 m, wavelengths/ λ of 2.24, 3.14, 3.59, 4.03, 4.48, 4.93, 5.38, 5.83, 6.72, 7.84 m, and Froude numbers/ F_r of 0.33 and 0.44, $F_r = v/\sqrt{gL_m}$, a time step of 0.001 s.

The calculated results are compared with the experimental values in terms of the amplitude-frequency response functions of heave, pitch, and acceleration, as shown in Figs. 6 – 11. The abscissa in each graph is the encountered frequency/ ω_e , in rad/s, whereas the ordinate in each case is the amplitude-frequency response function. To assess heave, the ordinate is the amplitude of the heave/ z_a to the wave amplitude/ ζ_a ratio, z_a/ζ_a . For pitch, it is the amplitude of the pitch/ θ_a divided by the wave amplitude/ ζ_a multiplied by the wave number/ k ,

$\theta_a/k\zeta_a$. For acceleration, it is the amplitude of the acceleration at the centre of gravity/am multiplied by the model length/ L_m , which is divided by the gravitational acceleration constant/ g multiplied by the wave amplitude/ ζ_a ratio, $amL_m/g\zeta_a$.

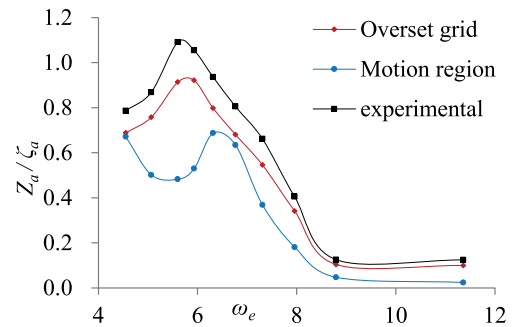


Fig. 6. Heave response curve, $F_r = 0.33$

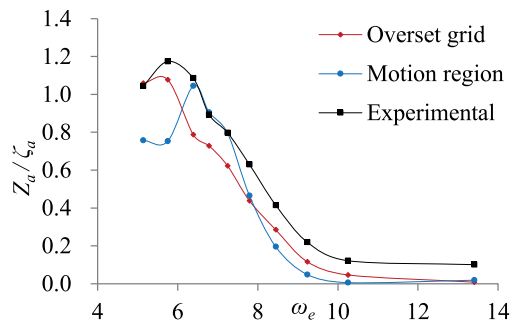


Fig. 7. Heave response curve, $F_r = 0.44$

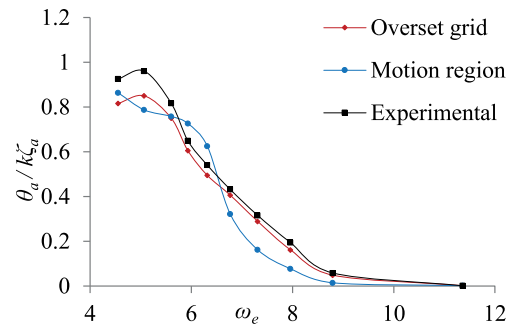


Fig. 8. Pitch response curve, $F_r = 0.33$

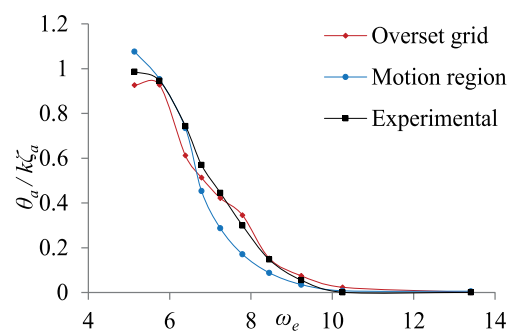


Fig. 9. Pitch response curve, $F_r = 0.44$

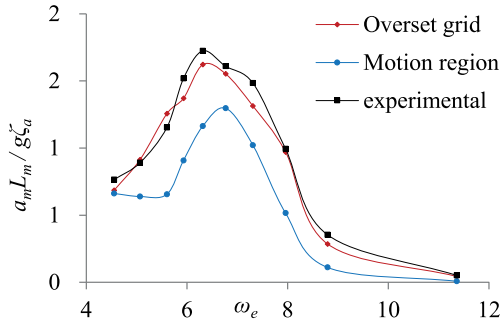


Fig. 10. Vertical acceleration response curve, $F_r = 0.33$

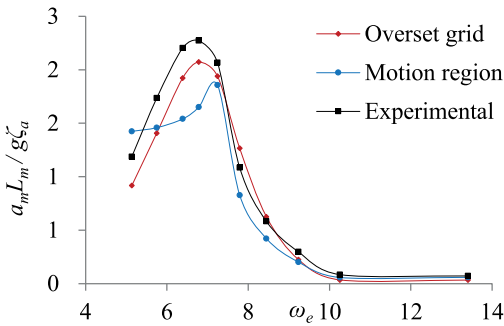


Fig. 11. Vertical acceleration response curve, $F_r = 0.44$

Figs. 6–11 indicate that the results of the two numerical calculations are consistent with the trends in experimental values. Thus, these numerical methods are capable of analysing and predicting the motion response of the SSB catamaran under regular wave conditions in a head sea. However, the results based on overset grid technology are more accurate than those based on motion region technology.

A detailed analysis of the calculation results for a wavelength of 6.72 m and Froude number of 0.33 is carried out. This wavelength is approximately 1.5 times L_m , which is generally believed to be the movement response peak.

Fig. 12 shows the test image of the model ship and the free surface waveform obtained by numerical calculation.



Fig. 12. Free surface waveform (a) Model test presentation

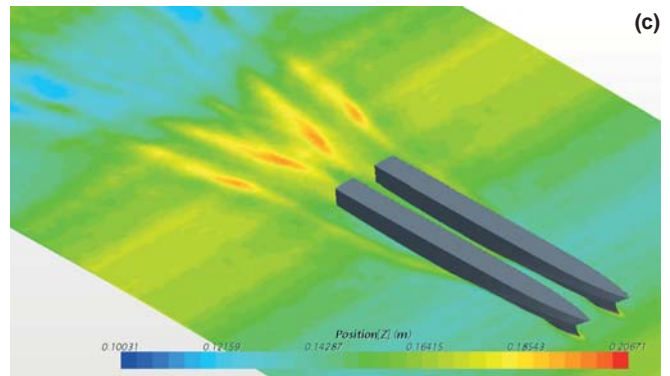
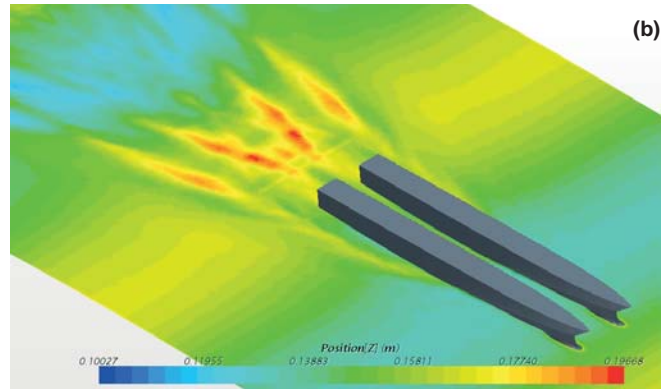


Fig. 12. Free surface waveform: (b) Overset grid method, (c) Motion region method

The time histories of the resistance and the average value are shown in Fig. 13. The time histories of the sinkage, trim angle, and vertical acceleration are shown in Fig. 14–16. The element number, computational time and error of resistance are summarized in Table 2.

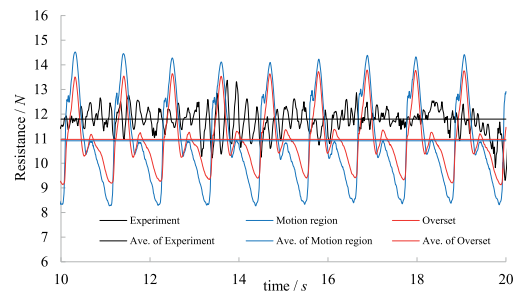


Fig. 13. Time histories and the average value of resistance

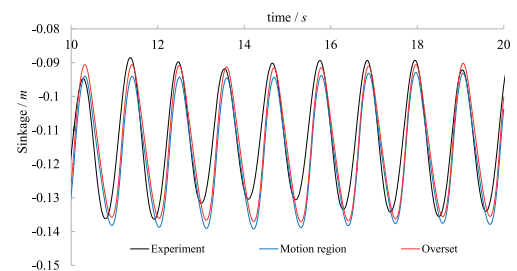


Fig. 14. Time histories of sinkage

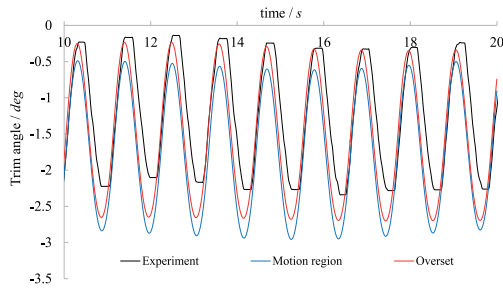


Fig. 15. Time histories of trim angle

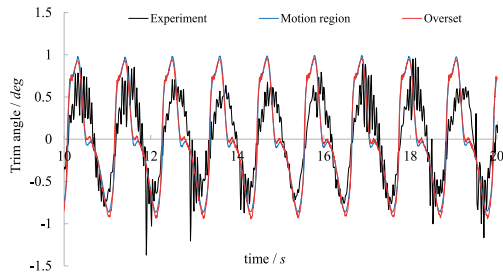


Fig. 16. Time histories of vertical acceleration

Tab. 2. Comparison of the schemes

| Schemes | Overset grid method | Motion region method |
|---------------------------|---------------------|----------------------|
| Element number | 1.37×10^6 | 1.22×10^6 |
| Computational time (hour) | 35 | 23 |
| Error of resistance (%) | 6.5 | 7.4 |

Considering both computational accuracy and computational time, overset grid method is adopted to predict the motion response of an SSB catamaran in a wave.

PREDICTION OF SEAKEEPING PERFORMANCE

It is evident from the test data, that the overset grid method is more accurate in the numerical simulation of complex hulls. The method is able to effectively forecast the seakeeping performance of an SSB catamaran, with errors of approximately 10% that do not exceed 20%. This study uses the overset grid method to calculate the motion response of an SSB catamaran at speeds of 0.727, 1.45, 1.75, and 2.62 m/s, with an amplitude of 0.02 m and wavelengths of 2.24, 3.14, 3.59, 4.03, 4.48, 4.93, 5.38, 5.83, 6.72, and 7.84 m. The results are shown in Figs. 17-18 and illustrate, that the amplitude-frequency response functions of pitch and heave increase as the encountered frequency decreases at the same speed. This is due to the motion response of the ship decreasing as the wavelength decreases. The amplitude-frequency response

functions of pitch and heave peak at a Froude number of 0.4, which is due to the wavelength of 5.83 m being approximately 1.3 times the model length. The natural pitching and heaving periods were similar to the encountered period, resulting in the emergence of a resonance phenomenon. Furthermore, the motion response of the ship increases as the speed increases at the same wavelength.

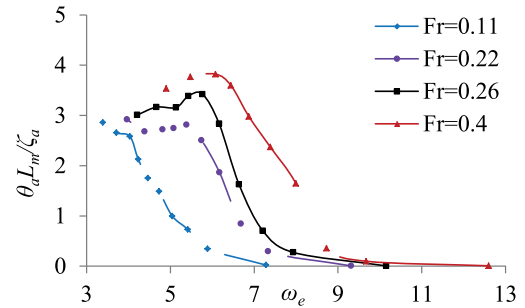


Fig. 17. Pitch response curve

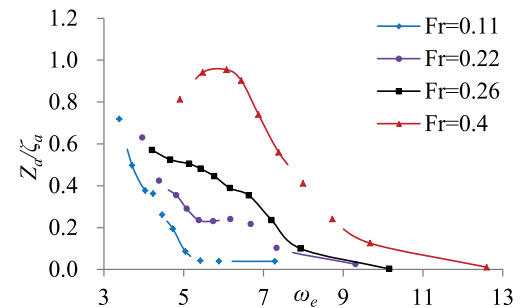


Fig. 18. Heave response curve

In calculating the numerical results, this study uses typical sea states according to the ITTC two-parameter spectrum, proposed by the International Ship Model Basin Conference [16]. The seakeeping performance of a full-scale 56 m ship in a level 2-6 sea state is shown in Figs. 19-20, where the reduced scale ratio is 12.5. The abscissa in both cases is the sea state, whereas the ordinate is significant value of pitch angle ($\theta_{1/3}$, measured in deg) and sinkage ($z_{1/3}$, measured in m).

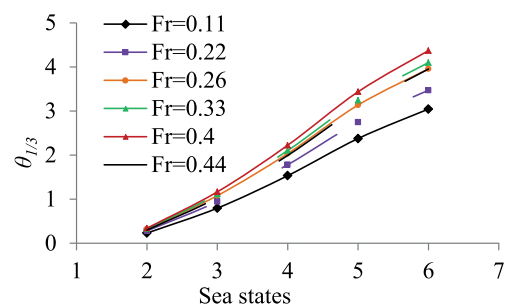


Fig. 19. Significant pitch

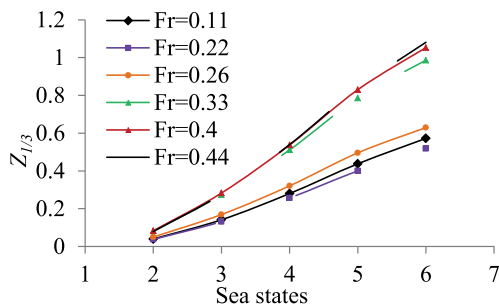


Fig. 20. Significant heave

Figs. 19-20 show that the significant values of pitching and heaving increase as the sea state increases at a constant speed. The significant values of heaving increase as the speeds increase at a constant sea state, whereas the added amplitudes decrease. The significant values of pitching have a downward trend at $Fr = 0.44$ because the encountered period deviates from the natural pitching period as the speeds increase, and the resonance region is thus avoided.

CONCLUSIONS

The results of this study show, that the motion response of an SSB catamaran under regular wave conditions can be accurately predicted by the use of an overset grid based on viscous flow numerical calculation theory. Based on the calculation of the amplitude of movement under various sea conditions, the following conclusions can be obtained.

A comparison of the results of the overset grid, the motion region methods, and the experimental data of the ship model shows, that the results obtained by the two numerical methods have similar trends. However, the overset grid is more accurate in the prediction of the motion response of an SSB catamaran under regular wave conditions when heading into the wave. Thus, the seakeeping performance of an SSB catamaran can be effectively forecast.

The motion response of an SSB catamaran under regular wave conditions in a heading wave has been simulated, the frequency response function has been solved, and the trends of heave and pitch motion at various speeds have been analysed. The results show, that the motion response of an SSB catamaran decreases with an increase in encounter frequency. However, a resonance phenomenon can occur when the encounter period approaches the natural period of heave and pitch of the ship.

The pitching and heaving motion of a 56 m SSB catamaran was calculated by using the ITTC two-parameter spectrum method, and pitch and heave amplitudes at various sea levels were obtained. The results show, that the extent of heave amplitude increase is reduced as the speed increases; the pitching amplitude shows a downtrend as Fr approaches 0.44. When an SSB catamaran is sailing in a head sea, there is an optimal speed range at which resonance can be avoided and the amplitude of movement can be reduced.

ACKNOWLEDGMENTS

This work was supported by the National Natural Science Foundation of China (Grant Nos. 51409069, 51409054 and 51509055), the China Postdoctoral Science Foundation (2015 M571397) and the Fundamental Research Funds for the Central Universities (Grant No. HEUCF150118).

BIBLIOGRAPHY

1. ODD M. Faltinsen. Hydrodynamics of high-speed marine vehicles[M]. Cambridge: Cambridge University Press, 2005.
2. Dingliang Huang, Zhidan Ai, Dianlu Xing. Research on Seakeeping Performance of Semi-Submerged Bow Ship, Shipbuilding of China, 1992, 3(1):40-46.
3. Lian'en Zhao, Yi He, Jide Li, et al. A Study on Motion Performance of Multi-hull Wave Piercer, Shipbuilding of China, 1997(4): 20-28.
4. Xingong Cai, Jide Li, Jianfang Wang. Experimental Study on Built-up Stabilizing Appendage, Shipbuilding of China, 2003, 44(3): 51- 57.
5. Xingong Cai, Jide Li. Comparative Sea Trial of a High-speed Ship with Built-up Stabilizing Appendage, Shipbuilding of China, 2003, 44(4): 13- 18.
6. Jide Li, Heng Zhang, Xiaodong Zhao. Experimental study on 4 000t deep- V hybrid monohull, Journal of Ship Mechanics, 2008, 12(5): 709-715.
7. Shuzheng Sun, Jide Li, Xiaodong Zhao, et al. Research on Longitudinal Motion Performance of Deep-V Hybrid Mono-hull, Ship Ocean Engineerin, 2009, 38(5): 54-57.
8. Xujie Wang, Shuzheng Sun, Xiaodong Zhao, et al. Research on model test of thousands-tons class high seakeeping performance hybrid monohull, Journal of Ship Mechanics, 2011, 15(4): 343-349.
9. Ni Gao, Shuzheng Sun, Zaibai Qin, et al. Model test research on WPC with semi-submerged appendage, J. Huazhong Univ. of Sci. Tech. (Natural Science Edition), 2013, 41(3): 97-100.
10. SRE Silva, CG Soares. Prediction of parametric rolling in waves with a time domain non-linear strip theory model, Ocean Engineering, 72 (2013): 453-469.
11. Rui Deng. Numerical Research on Influence of the Interceptor on Catamaran Hydrodynamic Performances [D], Harbin Engineering University, 2010.

12. Li Wang. The Applicability Analysis of the Usually Applied Turbulence Models and the Numerical Simulation of the Flow Around a Foil using VOF Method [D], Huazhong University of Science and Technology, 2007.
13. Shulian Tian. Investigation of Overset Unstructured Grids Algorithm [D], Nanjing University of Aeronautics and Astronautics, 2008.
14. Jingxin Liu, HU Akay, Akin Ecer, et al. Flows Around Moving Bodies Using a Dynamic Unstructured Overset-grid Method, International Journal of Computational Fluid Dynamics, 2010, 24(6): 187-200.
15. Faming Zhao, Chengjun Gao, Qiong Xia. Overlap grid research on the application of ship CFD, Journal of Ship Mechanics, 2011, 15(4): 332-341.
16. Jide Li. Seakeeping Performance of Ship [M], Harbin Engineering University Press, 2007.

CONTACT WITH THE AUTHORS

Fengmei Jing
Corresponding author

College of Shipbuilding Engineering
Harbin Engineering University
Nan tong street Harbin
HLJ
P. R. CHINA

e-mail: jingfengmei@hrbeu.edu.cn

HEELING MOMENT ACTING ON A RIVER CRUISER IN MANOEUVRING MOTION

Tomasz Tabaczek, Ph. D.

Jan Kulczyk, Prof.

Wrocław University of Technology, Poland

ABSTRACT

By using fully theoretical method the heeling moment due to centrifugal forces has been determined for a small river cruiser in turning manoeuvre. The authors applied CFD software for determination of hull hydrodynamic forces, and open water characteristics of ducted propeller for estimation of thrust of rudder-propellers. Numerical integration of equations of 3DOF motion was used for prediction of ship trajectory and time histories of velocities, forces and heeling moment.

Keywords: river cruiser, turning manoeuvre, heeling moment, numerical simulation

INTRODUCTION

Regulations that apply to new ships require that properties referring to stability and manoeuvrability must be proved prior to ship construction. In the case of conventional ships standard calculations of stability are carried out and external loads are estimated by using the appropriate formulae, usually given in rules of ship classification. In the cases of non-conventional ships or non-conventional ship equipment more sophisticated methods are required to evaluate loads for stability calculations.

The Directive of the European Parliament on technical requirements for inland waterway vessels [1], in the article on stability says that for passenger vessels driven by rudder-propellers the heeling moment due to centrifugal force (M_{dr}), caused by the turning of the vessel „shall be derived from full-scale or model tests or else from corresponding calculations”.

In the case of inland waterway vessels the model tests are usually not commissioned due to the relatively high cost. Full scale trials are possible only when the ship is launched and equipped. Thanks to development of theoretical methods and computational technology the „corresponding calculations” became an actual alternative.

The present authors used the equations of ship planar motion to simulate the turning manoeuvre and to determine the heeling moment acting on a small river cruiser. Data of the considered vessel were provided by Navishipproject, the ship design company of Wrocław. Ship is propelled and controlled by two rudder-propellers and a transverse bow thruster. In order to determine the heeling moment due to centrifugal force the turning manoeuvres have been simulated in deep water, at approach speed of 11 knots (5.66 m/s; $F_n = 0.295$), after sudden turning of both propulsors 35, 60 and 90 deg

to starboard. In the extreme case of 90 deg even the action of the bow thruster was considered.

RIVER CRUISER

General view and body plan of the considered vessel are shown in Fig. 1 and 2. Its main dimensions are given in Tab. 1. For enhanced manoeuvrability the ship was equipped with two rudder-propellers in nozzles and a tunnel bow thruster.



Fig.1. Views of the river cruiser

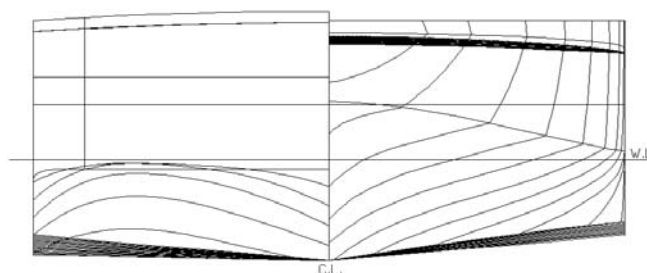


Fig.2. Body plan of the river cruiser

Tab. 1: Main dimensions of the cruiser

| | |
|---|-------|
| Length overall, L _{OA} [m] | 39.00 |
| Length between perpendiculars, L _{PP} [m] | 37.63 |
| Breadth, B [m] | 6.48 |
| Draught, d [m] | 1.10 |
| Rudder-propellers | |
| No. of blades, z | 4 |
| Diameter, D [m] | 0.85 |
| Pitch-to-diameter ratio, P/D | 0.98 |
| Expanded area ratio, A _E /A ₀ | 0.70 |

EQUATIONS OF MANOEUVRING MOTION

Ship trajectory and heading were described in the Earth-fixed coordinate system $O_{x_0y_0}$. Equations of motion were written in the coordinate system Gxy fixed to moving ship, with its origin at longitudinal position of ship's centre of gravity G (Fig.3). The assumptions were made that heel angle during manoeuvres is small, dynamic trim and sinkage in deep water can be neglected, and, consequently, only 3 degrees of freedom corresponding to surge, sway and yaw motions were considered.

The assumption of negligible small heel angle (i.e. such small that it does not affect the manoeuvring motion) was made because basic data for solving the equation of roll motion, i.e. the moment of inertia of ship around the longitudinal axis was not available (the seakeeping analysis is usually not performed for inland waterway vessels). The assumption was justified by the relatively big value of metacentric height of 2.7 m for the considered river cruiser. The validity of the assumption was proved by calculations of static and dynamic stability after the simulations are completed and heeling moments are known. Predicted values of heel angle during the turning circle manoeuvre are presented in the section 'Results of simulations'.

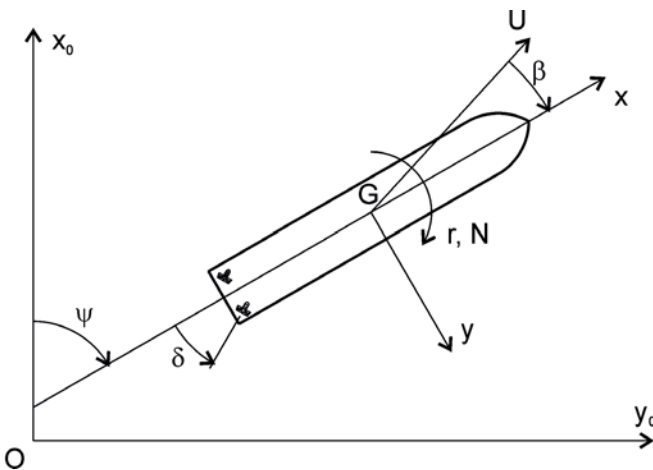


Fig.3. Coordinate systems used in mathematical description of ship motion

$$\begin{aligned} m \left(\frac{du}{dt} - vr \right) &= X \\ m \left(\frac{dv}{dt} + ur \right) &= Y \\ I_{zz} \frac{dr}{dt} &= N \end{aligned} \quad (1)$$

where u and v denote the longitudinal and transverse components of the ship velocity U ,

r - yaw rate,

X, Y - components of external force,

N - external moment,

m - ship's mass,

I_{zz} - ship's moment of inertia.

The MMG modular model [2] was adapted for external forces and moment:

$$\begin{aligned} X &= -m_x \frac{du}{dt} + m_y vr + X_H + X_P + X_{BT} \\ Y &= -m_y \frac{dv}{dt} - m_x ur + Y_H + Y_P + Y_{BT} \\ N &= -J_{zz} \frac{dr}{dt} + N_H + N_P + N_{BT} \end{aligned} \quad (2)$$

Subscripts „H”, „P” and „BT” refer to hull, propeller and bow thruster, respectively. Inertia forces due to added mass, although of hydrodynamic nature, are written as separate terms. After substitution and rearrangement the equations of motion take the following form, ready for integration:

$$\begin{aligned} (m + m_x) \frac{du}{dt} - (m + m_y) vr &= X_H + X_P + X_{BT} \\ (m + m_y) \frac{dv}{dt} + (m + m_x) ur &= Y_H + Y_P + Y_{BT} \\ (I_{zz} + J_{zz}) \frac{dr}{dt} &= N_H + N_P + N_{BT} \end{aligned} \quad (3)$$

HULL FORCES X_H, Y_H AND MOMENT N_H

The hull forces X_H, Y_H and moment N_H are approximated with the following mathematical models with hydrodynamic coefficients given in Tab. 2:

$$X_H = 0.5 \rho L d U^2 X'_H = 0.5 L d U^2 (X'_0 + X'_\beta \beta + X'_r r' + X'_{\beta\beta} \beta^2 + X'_{\beta r} \beta r' + X'_{rr} r'^2)$$

$$Y_H = 0.5 \rho L d U^2 Y'_H = 0.5 L d U^2 (Y'_\beta \beta + Y'_r r' + Y'_{\beta\beta} \beta^2 + Y'_{\beta r} \beta r' + Y'_{rr} r'^2 + Y'_{\beta\beta\beta} \beta^3 + Y'_{\beta\beta r} \beta^2 r' + Y'_{\beta r r} \beta r'^2 + Y'_{r r r} r'^3) \quad (4)$$

$$N_H = 0.5 \rho L^2 d U^2 N'_H = 0.5 \rho L^2 d U^2 (N'_\beta \beta + N'_r r' + N'_{\beta\beta} \beta^2 + N'_{\beta r} \beta r' + N'_{rr} r'^2 + N'_{\beta\beta\beta} \beta^3 + N'_{\beta\beta r} \beta^2 r' + N'_{\beta r r} \beta r'^2 + N'_{r r r} r'^3)$$

where r' denotes the non-dimensional yaw rate: $r' = rL/U$.

Tab. 2.: Hydrodynamic coefficients for mathematical model of hull forces and moment

| | | | | | |
|-------------------|----------|------------------------|----------|------------------------|----------|
| X'_0 | -0.02575 | | | | |
| X'_β | -0.02012 | Y'_β | 0.23166 | N'_β | 0.02182 |
| X'_r | -0.01389 | Y'_r | 0.06128 | N'_r | -0.02233 |
| $X'_{\beta\beta}$ | -0.00364 | $Y'_{\beta\beta}$ | 0.42991 | $N'_{\beta\beta}$ | 0.05866 |
| $X'_{\beta r}$ | 0.01889 | $Y'_{\beta r}$ | 0.16341 | $N'_{\beta r}$ | -0.06085 |
| X'_{rr} | 0.00128 | Y'_{rr} | 0.00655 | N'_{rr} | -0.02639 |
| | | $Y'_{\beta\beta\beta}$ | -0.17774 | $N'_{\beta\beta\beta}$ | -0.04237 |
| | | $Y'_{\beta\beta r}$ | -0.18127 | $N'_{\beta\beta r}$ | -0.04646 |
| | | $Y'_{\beta r r}$ | 0.11507 | $N'_{\beta r r}$ | 0.01736 |
| | | $Y'_{r r r}$ | 0.00209 | $N'_{r r r}$ | 0.00087 |

In order to determine the hydrodynamic coefficients a series of computations was carried out by using RANSE-CFD software. Ship flow in steady motion was computed in full scale of vessel, including yaw with drift combinations.

Only positive value of drift angle and yaw rate were considered because negative values were not expected during the starboard turning manoeuvre.

It was expected that the greatest heeling moment appears when the rudder-propellers are set to $\delta = 90$ deg, the ship turns and moves almost sideway. Then the model of hydrodynamic forces should be extended to high drift angles ($\beta \leq 90$ deg). However, during preliminary simulations of ship motion in turning manoeuvre it was revealed that yaw rate grows quickly (see Fig.6). Problems were encountered during CFD computations of steady ship flow at yaw rates $r' > 1.6$ due to the effect of memory (ship encounters her own wake before steady flow is attained). These authors decided to confine the model of hydrodynamic forces to $r' \leq 1.6$ and $\beta \leq 50$ deg (Fig.4). Consequently, the simulations of ship motion were stopped when the non-dimensional yaw rate exceeded the value of $r' = 1.6$. As seen in Fig.6, the computation of hydrodynamic coefficients at drift angles higher than 50 deg was not necessary.

Mathematical models (4) were adopted for good approximation of forces and moment in possibly widest range of drift angle and yaw rate. Coefficients were determined by fitting the models to computed forces. In the case of Y_H and N_H the fitting is excellent (Fig.4). The fitting of surge force X_H is good, at least for drift angles and yaw rates that occur during simulated manoeuvres, shown in Fig.6.

Added masses and added moment of inertia were approximated by using formulae developed by Yasukawa et al. [3] for barge trains of similar proportions of main dimensions ($0.012 \leq d/L \leq 0.027$; $0.048 \leq B/L \leq 0.317$; $3.89 \leq B/d \leq 11.68$):

$$m_x = 0.5\rho L^2 d (0.151 B/L - 0.244 d/L - 0.0012 B/d + 0.0018)$$

$$m_y = 0.5\rho L^2 d (2.93 d/L + 0.0226)$$

$$J_{zz} = 0.5\rho L^4 d (0.0978 d/L + 0.0025)$$

The values estimated for river user ($d/L = 0,029$, $B/L = 0,172$, $B/d = 5,89$) are presented in Tab. 3.

Tab. 3. Added masses and moment of inertia estimated for the river cruiser

| | |
|---|------------------------|
| $m_x = 10\ 600$ kg | $m_x/m = 0,056$ |
| $m_y = 84\ 300$ kg | $m_y/m = 0,45$ |
| $J_{zz} = 5\ 910\ 000$ kgm ² | $J_{zz}/I_{zz} = 0,30$ |

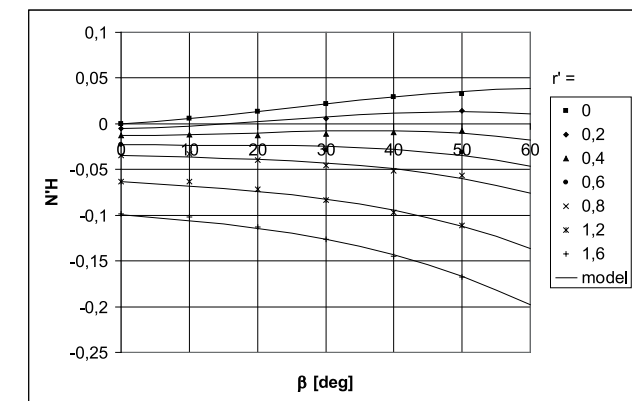
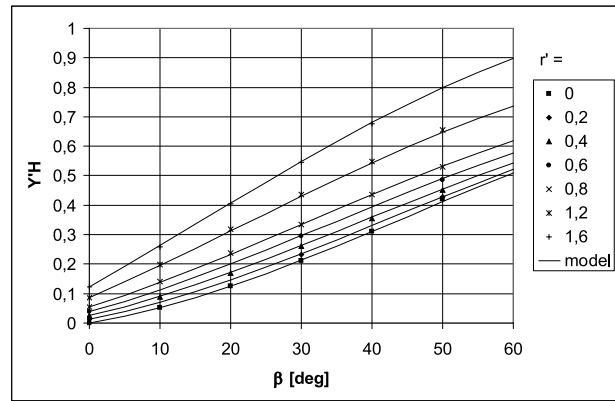
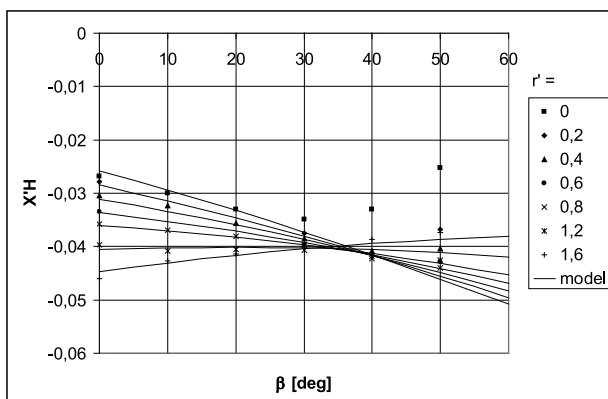


Fig.4. Fitting of the mathematical model to calculated hull forces and moment

PROPELLER FORCES X_p , Y_p AND MOMENT N_p

Azimuthing thrusters used as rudder-propellers can generate thrust in arbitrary direction determined by steering angle. In contrast to conventional propellers, the terms Y_P and N_P in mathematical model become significant. The authors applied the following formulae for estimation of propeller forces and moment. Inflow to propellers is determined by local drift angle. It was assumed, similar as in the case of conventional rudders [2], that ship's wake affects only the longitudinal inflow to propeller. Flow straightening effect of hull affecting the transverse component of inflow velocity, was neglected.

In the case of twin propeller ship each propeller force in external force model (2) is the sum of forces due to port side and starboard propeller:

$$X_p = X_p^{(p)} + X_p^{(s)} \quad (5)$$

$$Y_p = Y_p^{(p)} + Y_p^{(s)}$$

$$N_p = N_p^{(p)} + N_p^{(s)}$$

For individual propeller (Fig.5):

$$X_p^{(p,s)} = FP \cos \delta$$

$$Y_p^{(p,s)} = -FP \sin \delta \quad (6)$$

$$N_p^{(p,s)} = -X_p^{(p,s)} y_p^{(p,s)} + Y_p^{(p,s)} x_p^{(p,s)}$$

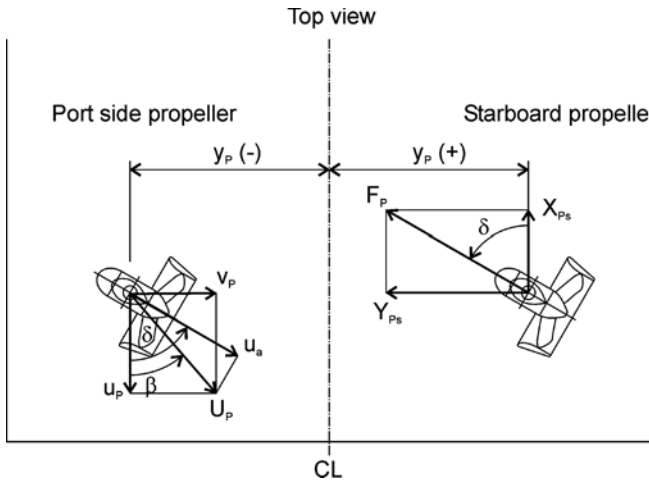


Fig.5. Forces generated by rudder-propellers

where the net force due to propeller action F_p is determined separately for each propeller (component perpendicular to propeller axis caused by oblique inflow to propeller was not considered):

$$F_p = (1-t) K_T \rho n^2 D^4 - \Delta T$$

$$\begin{aligned} J &= u_a / nD \\ u_a &= u_p \cos \delta - v_p \sin \delta \\ u_p &= u(1-w) \\ v_p &= v + x_p r \end{aligned} \quad (7)$$

- F_p -net force due to propeller action,
- δ -steering angle,
- x_p, y_p -horizontal coordinates of steering column,
- t -thrust deduction factor,
- K_T -thrust coefficient, approximated by using open water propeller characteristics $K_T(J)$,
- ρ -water density,
- n -propeller revolutions,
- D -propeller diameter.
- ΔT -loss of thrust due to presence of steering column,
- J -propeller advance coefficient,
- u_a -axial component of propeller inflow velocity
- u_p, v_p -longitudinal and transverse components of propeller inflow velocity,
- w -effective wake fraction.

For the purpose of the present simulations the open water characteristics of rudder-propeller was approximated with open water characteristics of corresponding ducted propeller from the Wageningen Ka4-70 screw series in nozzle 19A [4]:

$$K_T(J) = -0.3911 J^3 + 0.2727 J^2 - 0.5869 J + 0.5078 \quad (8)$$

Based on estimated resistance curve the propeller revolutions were adjusted to 11.4 rps to provide the approach speed of 5.66 m/s. Thrust deduction factor of 0.15 and wake fraction of 0.12 were assumed as reasonable values for ship hull with stern tunnels and azimuthing thrusters in deep water.

BOW THRUSTER FORCE Y_{BT} AND MOMENT N_{BT}

Bow thrusters are usually used when ship is manoeuvring at zero- or low speed. However, to be on the safe side, these authors considered a hypothetical case of using bow thruster at cruising speed of 11 kn.

The performance of transverse tunnel thrusters depends both on hull form of ship (on geometry of bow in the case of bow thrusters), as well as on the parameters of motion (speed and drift angle) [5]. The interaction of jet from the thruster with ship flow results in additional hydrodynamic forces acting on the hull. The lateral thruster performance rapidly decreases at non-zero ship speeds. In order to account for the variation of forces and steering moment due to bow thruster in manoeuvring motion the appropriate characteristics of thruster performance are required. Unfortunately, the authors had not the characteristics -either of the thruster to be installed on the considered river cruiser, -or of any tunnel thruster in arrangement with bow of wide-beam vessel.

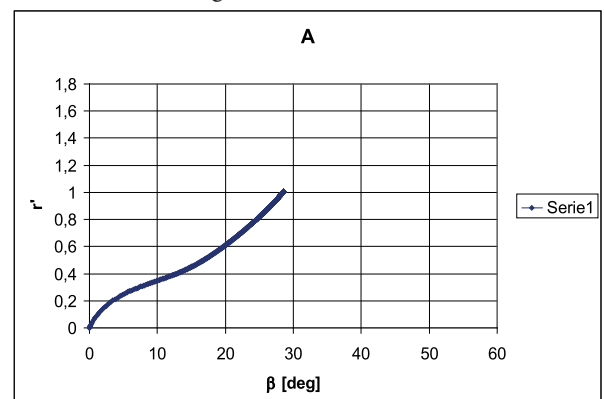
In simulation of most severe manoeuvre when the steering angle of 90 deg was applied to rudder propellers and when the highest value of heeling moment was expected, the bow thruster was set to generate the constant transverse force F_{BT} equal to its rated thrust of 540m kG - the value higher than the highest lateral force at zero ship speed.

$$\begin{aligned} X_{BT} &= 0 \\ Y_{BT} &= F_{BT} \\ N_{BT} &= F_{BT} x_{BT} \end{aligned} \quad (9)$$

where x_{BT} is the longitudinal coordinate of bow thruster.

RESULTS OF SIMULATIONS

Four manoeuvres were simulated: starboard turning with both rudder-propellers turned to 35 deg (manoeuvre A), 60 deg (B) or 90 deg (C), and starboard turning with propellers turned to 90 deg and operating bow thruster (manoeuvre D). All manoeuvres were started at approach speed of 5.66 m/s (11kn). Simulations were stopped when the limit of applicability of hydrodynamic coefficients was exceeded, i.e. drift angle exceeded 50 deg or non-dimensional yaw rate exceeded value of 1.6. It appeared that at $\delta = 35$ deg both parameters remained within limits and the vessel made a closed circle (see Fig.6 and 7).



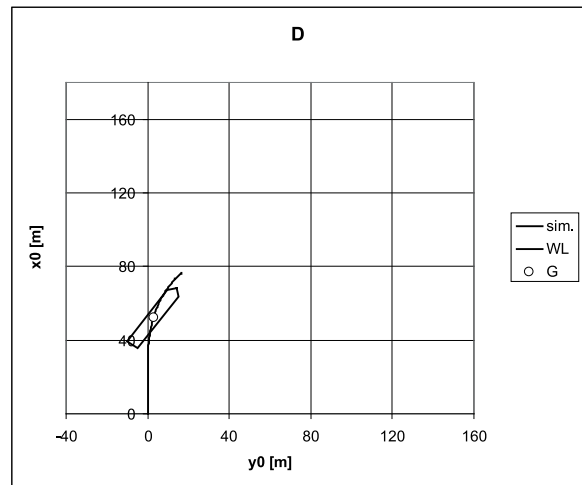
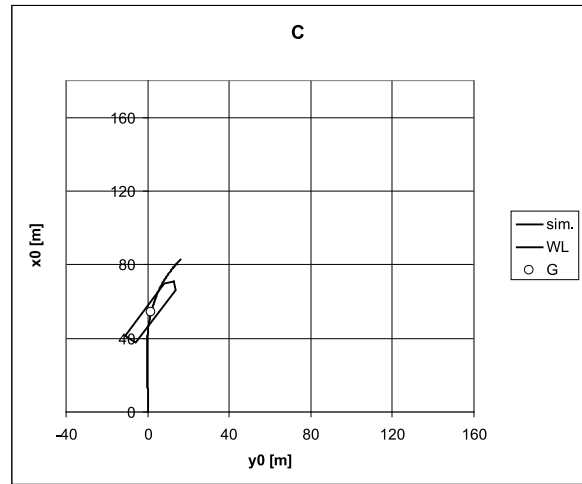
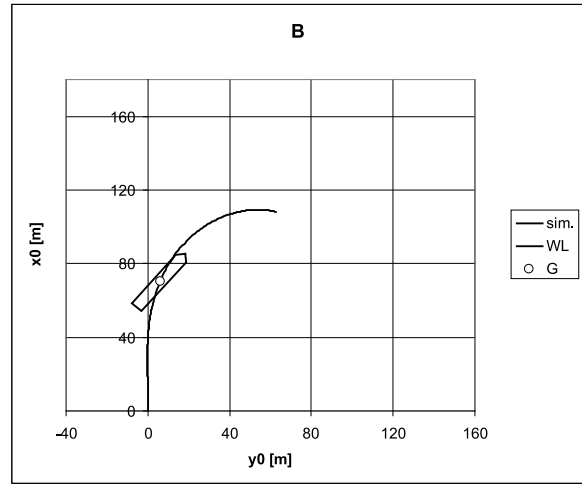
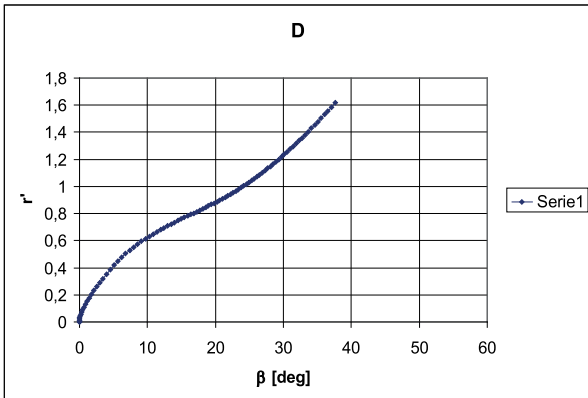
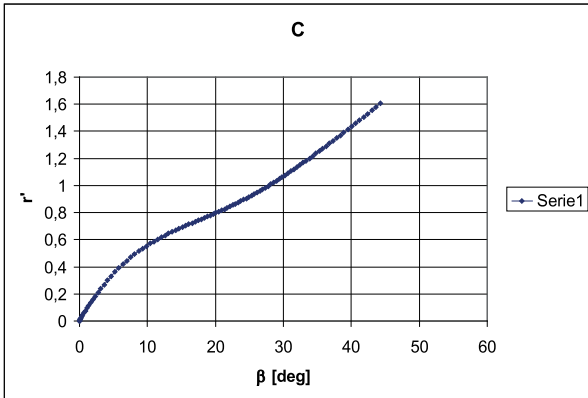
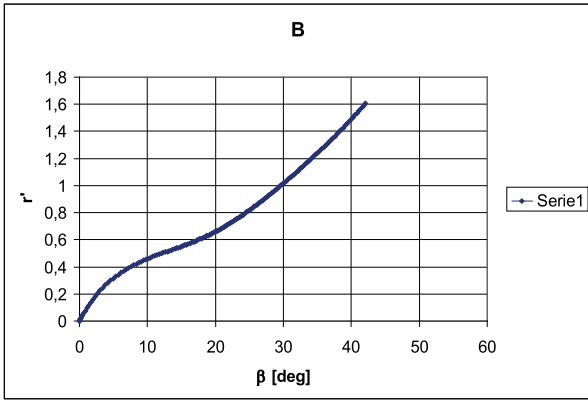


Fig.6. Drift angle β and non-dimensional yaw rate r' during simulated manoeuvres

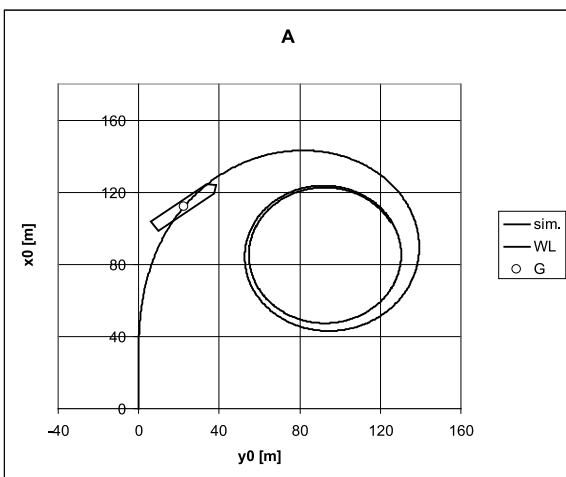


Fig.7. Trajectory of ship's centre of gravity; position of ship is marked at maximum heeling moment

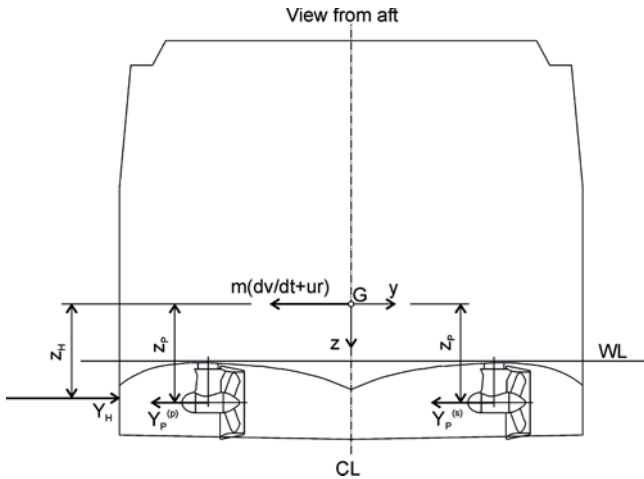


Fig.8. Forces contributing to heeling moment

Heeling moment acting on manoeuvring vessel comes from side forces included in the equation of motion (3):

$$m(dv/dt + ur) = -m_y dv/dt - m_x ur + Y_H + Y_P + Y_{BT} \quad (10)$$

where:

$m(dv/dt + ur)$ - is the inertia force on sidewise accelerating or turning ship,

$-m_y dv/dt - m_x ur + Y_H$ - hydrodynamic force, where terms $(-m_y dv/dt - m_x ur)$ come from inertia of added mass,

Y_P - side component of propeller force,

Y_{BT} - bow thruster force.

Because only heeling moment due to manoeuvring motion is considered in this paper, other sources, as e.g. wind, are omitted. According to the conventions presented in Fig.8 the resultant heeling moment is calculated about the Gx axis (at the height of ship's centre of gravity) by using the following formula:

$$M_{dr} = -(-m_y dv/dt - m_x ur + Y_H)z_H - Y_P z_P - Y_{BT} z_{BT} \quad (11)$$

where:

z_H - vertical ordinate of application point of hydrodynamic force on ship hull,

z_P - vertical ordinate of propeller axis,

z_{BT} - vertical ordinate of the centre of bow thruster outlet.

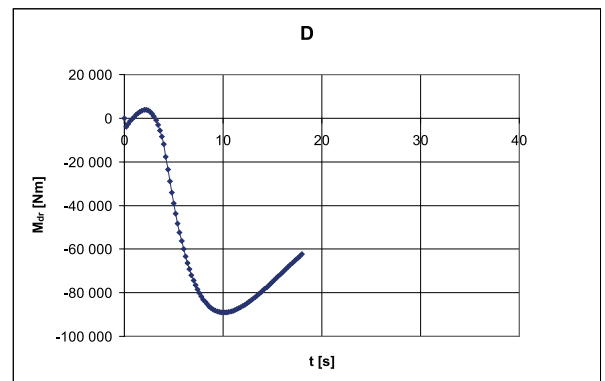
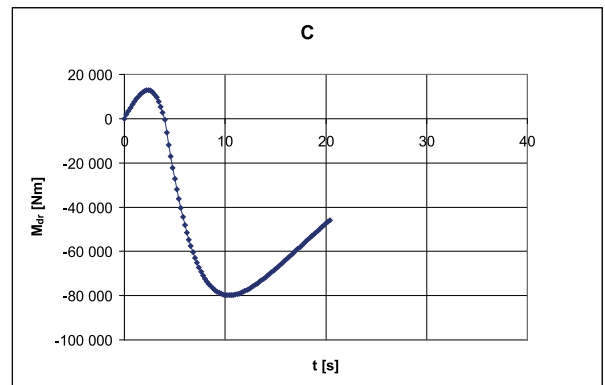
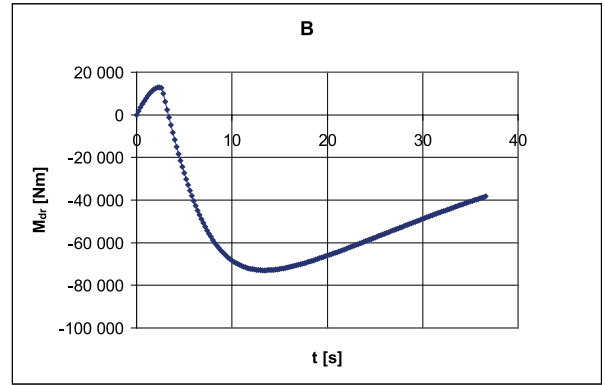
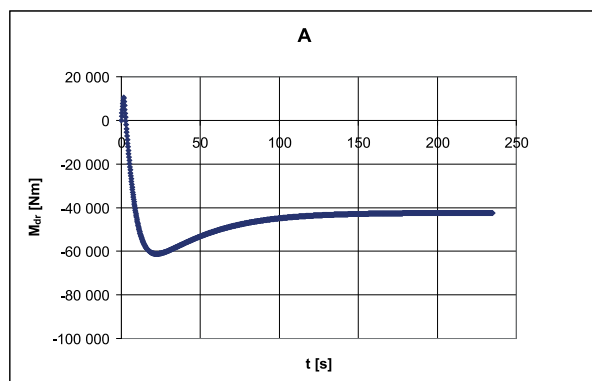


Fig.9. Time history of heeling moment

Time histories of heeling moment during simulated manoeuvres are presented in Fig.9. When the manoeuvre starts a small positive moment appears that tends to heel the ship to starboard. Next the moment due to inertia (centrifugal) forces starts to prevail. The resultant heeling moment becomes negative and tends to heel the ship outwards (to port side). The maximum heeling moment appears some 10 to 25 seconds after the start of manoeuvre, depending on steering angle of rudder-propellers.

In the manoeuvre A the steady circulation with steady velocities and heeling moment was reached after ship made about 2 circles. In the manoeuvres B, C and D the steady motion has not been reached, but one may expect, based on the manoeuvre A, that heeling moment (its absolute value) shall gradually decrease until steady circulation is attained. The extent of simulations is sufficient for the purpose of stability assessment.

In order to prove the assumption of negligible roll motion a simplified analysis of heel angle during turning circle manoeuvre was carried out by using the diagram of righting levers available from standard stability analysis carried out in the framework of design process. The highest value of heeling moment of 89.1 kNm, determined in simulations (Fig.9) was applied. It was assumed that the heeling moment is applied at the beginning of manoeuvre and remains steady. The effect of application of steady heeling moment is illustrated in Fig.10 and Fig.11. Heel angle φ during the simulated manoeuvres shall not exceed the estimated value of dynamic heel angle of 2 deg. In opinion of these authors, neglecting the roll motion in simulations did not affect the manoeuvring motion. One may suggest that the wide-beam, flat-bottomed vessels during tight turning started at full ahead speed shall not be subject to substantial heel angle or roll motion. They may be expected to move like sliding in upright position.

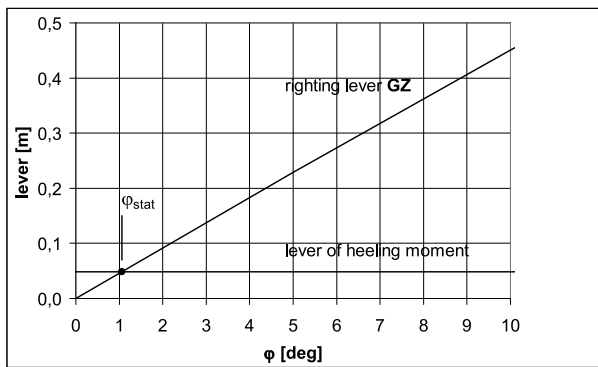


Fig.10. Static heel angle φ_{stat} of the river cruiser subject to the steady heeling moment of 89.1 kNm

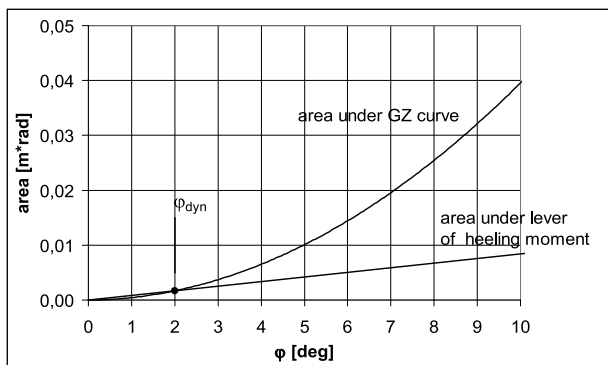


Fig.11. Dynamic heel angle φ_{dyn} of the river cruiser subject to sudden application of the heeling moment of 89.1 kNm

CONCLUSIONS

Because the proportions of main dimensions of the considered cruiser are unusual as compared with those of sea going ships, as well as because of wide extent of drift angle and yaw rate, there were no available values of hydrodynamic coefficients. Simulation of turning manoeuvre of small river cruiser propelled and controlled by rudder-propellers required the development of tailor-made model of hydrodynamic forces. Care had to be taken to adjust the scope

of applicability of mathematical models to actual parameters of motion during simulated manoeuvres.

The variation of heeling moment during turning reveals that its maximum value appears at the beginning of manoeuvre (change of heading less than 60deg) and, in order to determine data for assessment of ship stability, it is not necessary to extend the mathematical model and to continue simulation until steady turning.

Application of the numerical simulation to non-conventional ships and propulsion/steering systems requires much effort in determination of hydrodynamic and interaction coefficients.

On the other hand, the numerical simulation of ship motion has potential to predict

velocities, accelerations, forces and moments during versatile manoeuvres, and can be useful

not only for testing ship's manoeuvrability but also for assessment of stability.

ACKNOWLEDGEMENT

The authors wish to express their gratitude to the ship design company Navishipproject for providing data necessary for presented study.

REFERENCES

1. Directive of the European Parliament and of the Council of 12 December 2006 laying down technical requirements for inland waterway vessels and repealing Council Directive 82/714/EEC (2006/87/EC)
2. Y. Yoshimura: Mathematical Model for Manoeuvring Ship Motion (MMG Model), Workshop on Mathematical Models for Operations involving Ship-Ship Interaction, Tokyo, August 2005
3. H. Yasukawa, N. Hirata, K.K. Koh, K. Punayangkool, K. Kose: Hydrodynamic force characteristics on maneuvering of pusher-barge systems, Journal of Japan Society of Naval Architecture and Ocean Engineering, No. 5, 2?007 (in Japanese)
4. M. W. C. Oosterveld: Wake adapted ducted propellers, NSMB Wageningrn Piubl. No.345, June 1970
5. J. Brix (ed.), Manoeuvring technical manual, Seehafen Verlag GmbH, Hamburg, 1993

CONTACT WITH THE AUTHOR

Jan Kulczyk

Wrocław University of Technology
email: jan.kulczyk@pwr.wroc.pl
POLAND

EFFECTIVE METHOD FOR DETERMINING ENVIRONMENTAL LOADS ON SUPPORTING STRUCTURES FOR OFFSHORE WIND TURBINES

Paweł Dymarski¹, Assoc. Prof.

Ewelina Ciba¹, Ms. C.

Tomasz Marcinkowski², Ph. D.

1) Gdańsk University of Technology, Poland

2) Maritime Institute in Gdańsk, Poland

ABSTRACT

This paper presents a description of an effective method for determining loads due to waves and current acting on the supporting structures of the offshore wind turbines. This method is dedicated to the structures consisting of the cylindrical or conical elements as well as (truncated) pyramids of polygon with a large number of sides (8 or more). The presented computational method is based on the Morison equation, which was originally developed only for cylindrically shaped structures. The new algorithm shown here uses the coefficients of inertia and drag forces that were calculated for non-cylindrical shapes. The analysed structure consists of segments which are truncated pyramids on the basis of a hex decagon. The inertia coefficients, C_M , and drag coefficients, C_D , were determined using RANSE-CFD calculations. The CFD simulations were performed for a specific range of variation of the period, and for a certain range of amplitudes of the velocity. In addition, the analysis of influence of the surface roughness on the inertia and drag coefficients was performed. In the next step, the computations of sea wave, current and wind load on supporting structure for the fifty-year storm were carried out. The simulations were performed in the time domain and as a result the function of forces distribution along the construction elements was obtained. The most unfavourable distribution of forces will be used, to analyse the strength of the structure, as the design load.

Keywords: offshore wind turbine, support structure, Morison force coefficients, CFD, sea wave statistics, Baltic Sea

INTRODUCTION

The calculation method presented here has been developed within the tasks of the research project AQUILO under the full name "Development of methods for the selection of the type of support structure for offshore wind turbine in Polish sea areas".

The purpose of the task, in which this research was implemented, was to design a support structure in a given area in the Polish economic zone of the Baltic Sea. Within this project, four types of structures will be analysed: a gravity base, a tripod with piles foundation, a gravity tripod and a deep water monopile.

One of the key issues that needs to be addressed in the design of this type of construction is the determination of the hydrodynamic forces acting on the object. Such forces, along with interactions from the seabed and from the wind create a system acting on the supporting structure. This system of acting forces being due to the extreme sea and weather conditions is used to determine the dimensions of the main structural elements of the construction and is based on strength analysis.

There are three main types of methods used to determine the hydro dynamical interactions:

- approximate calculation methods, based on the coefficients for hydro mechanical forces,
- accurate computational methods - RANSE-CFD
- experimental methods (based on the method of Froude).

At an early stage of the design process, the approximate methods are most frequently used and usually are very effective. It is of a great importance that the error of such primary computations is not too large. The authors of this article decided to develop a method of calculation based on the Morison equation [1].

The Morison equation is mainly used to determine the forces acting on objects of cylindrical shape, and such have been investigated experimentally in a wide range of flow parameters. Graphs of the coefficients of forces are available [1,2,3]. Due to the fact, that the gravity base type structure has a base made up of segments which cannot be approximated as cylindrical, the authors decided to use RANSE-CFD method in order to calculate the force coefficients of these elements.

OBJECT OF THE ANALYSIS

The aim of the work was to develop an efficient computational method for determining loads from waves and currents acting on the supporting structures for offshore wind turbines and determination of the maximum load the hydro mechanical impact acting on the structure. The subject of the analysis was the gravity base and this article shows the step-by-step calculation process for this structure.

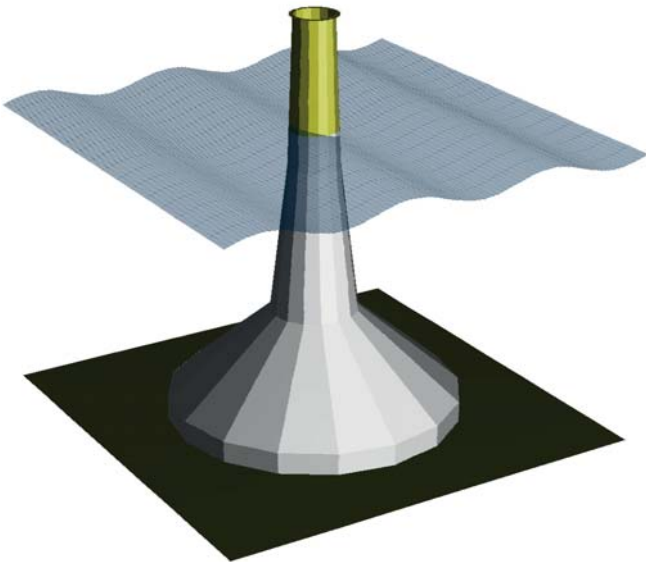


Fig. 1a. Three types of supporting structures, that were analysed in the framework of the project - Gravity base

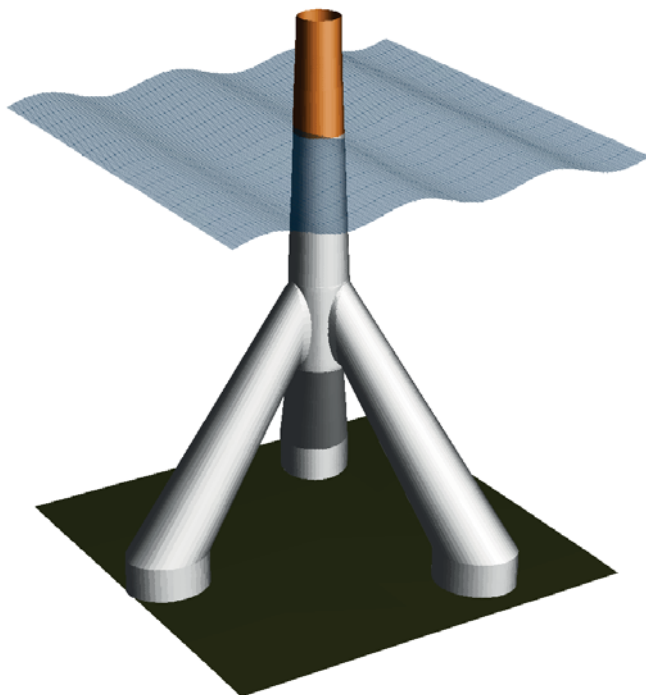


Fig. 1b. Three types of supporting structures, that were analysed in the framework of the project - Gravity tripod

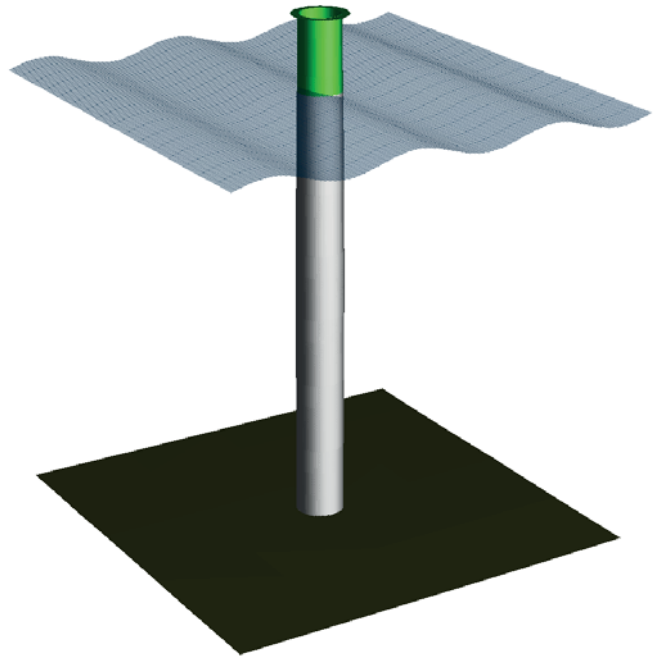


Fig. 1c. Three types of supporting structures, that were analysed in the framework of the project - Monopile

THE GRAVITY BASE STRUCTURE DESCRIPTION

The chosen support structure is a gravity base structure, the geometry of which is composed of segments of prismatic or truncated pyramid with a basis of regular hex decagon. The exact dimensions are given in Table 2, and visualization of the structure is shown in Figure 1a.

The construction material that was chosen is steel. The interior of the structure up to a height of $z = 25$ m above the seabed is to be filled in with ballast (pulp mud).

CALCULATION METHOD

THE MORISON EQUATION

The total hydro mechanical force that acts on the motionless body, which is placed in a fluid of unsteady, unidirectional flow, can be expressed by [1]:

$$F = \frac{1}{2} C_D \rho A_p |U| U + \rho V_b (1 + C'_a) \left(\frac{\partial U}{\partial t} + U \frac{\partial U}{\partial x} \right) \quad (1)$$

Where A_p is the projected area of the body on a plane normal to the direction of the flow, V_b is the volume of the body, C_D and C'_a are the drag and added mass coefficients, U is the velocity and ρ is the water density.

Coefficients C'_a and C_D depend on time, geometry of the body, Reynolds number R_e and the parameters describing the history of the flow (for example the amplitude and the period of the velocity variation). In practice, they are plotted

as functions of Keulegan-Carpenter number K_C and so called $\beta = Rn / K_C$ coefficient, which was proposed by Sarpkaya [1].

Morison equation is a simplified version of equation (1), where it is assumed, that the term in equation: dU/dt can be as approximated by $\partial U / \partial t$, hence:

$$F = \frac{1}{2} \rho C_D A_p |U|U + \rho C_M V_b \frac{\partial U}{\partial t} \quad (2)$$

where:

$C_M = 1 + C_a$, and C_a is an time averaged value of C'_a .

The above equation is used for the calculations of cylindrical shapes. When the movement of fluid particles caused by the waves is to be dealt with, this equation can be used when the cylinder diameter is not greater than about 20% of wave length λ .

Coefficients C_M and C_D can be obtained from model tests. Sarpkaya [1, 2] carried out a systematic study, based on which characteristics of coefficients C_M and C_D for a cylindrical shape as a function of K_C , β and relative roughness k_r / D were derived. Values of these coefficients for other geometries are also available in the literature [1,3].

THE METHOD FOR DETERMINING THE C_M AND C_D WITH CFD

Determination of the coefficient of the hydro mechanical reaction by CFD calculations is no different in terms of methodology to the experimental method conducted in the U-tube tank [1, 2]. The calculations are performed in the rectangular shaped tunnel, in which by means of suitably selected boundary conditions, a flow with the sinusoidal velocity is generated:

$$U(t) = U_a \sin(\omega t) \quad (3)$$

In this case, the Morison equation can be written in the following way:

$$F = \frac{1}{2} \rho C_D A_p U_a^2 |\sin(\omega t)| \sin(\omega t) + \rho C_M V_b U_a \omega \cos(\omega t) \quad (4)$$

In the above equation the first term, representing the drag force, is proportional to $\sin^2(\omega t)$. The modulus of this force reaches the maximum for $\omega t = 1/2\pi, 3/2\pi, \dots$, while the whole term equals zero for $\omega t = 0, \pi, 2\pi, \dots$. The second term of the equation is the force of inertia, which is proportional to the cosines function $\cos(\omega t)$. When the modulus of the drag force reaches its maximal value, the inertia force equals to zero, whereas when the resistance force is zero, the modulus of the inertia force reaches its maximum value. This principle allows us to determine the coefficient of forces with the use of the following formulas:

$$C_M = \frac{F}{\rho V_b U_a \omega} \quad \text{for } \omega t = 0, \pi, 2\pi, \dots \quad (5)$$

$$C_D = \frac{2F}{\rho A_p U_a^2} \quad \text{for } \omega t = 1/2\pi, 3/2\pi, \dots \quad (6)$$

Another, more advanced method is to search, through the optimization, for the coefficients C_D and C_M , so that the "theoretical" function $F(t)$ agrees with the one obtained by advanced CFD calculation.

Figure 11 shows a sample course of the function $F(t)$ with indicated value of t that is used for calculation of the C_M and C_D , where $|v| = U_a$ or $U = 0$, because then $|\partial U / \partial t| = [\partial U / \partial t]_a$.

THE USE OF MORISON EQUATION FOR CALCULATION OF THE IMPACT OF THE UNSTEADY AND NON-UNIFORM FLOW ON THE SUPPORT STRUCTURE. THE GENERAL FORM

In the previously presented equations, it was assumed, that the velocity vector is perpendicular to the axis of the cylinder and the velocity field is uniform. In the general case, for example, when dealing with the velocity field appearing in the wave motion, the velocity field is not uniform, and the direction of flow (and acceleration) is changeable. The geometry of the structure varies as well. Therefore, the force acting on the section of a structure element needs to be determined using the general formula:

$$\Delta \mathbf{F} = \left(\frac{1}{2} \rho C_D D |\mathbf{U}_n| \mathbf{U}_n + \frac{1}{4} \pi D^2 \rho C_M \frac{\partial}{\partial t} \mathbf{U}_n \right) \Delta s \quad (7)$$

Vector of velocity normal to longitudinal axis of the element of structure:

$\mathbf{U}_n = \mathbf{U} - (\mathbf{U} \cdot \mathbf{e}_s) \mathbf{e}_s$, where: \mathbf{U} velocity vector and \mathbf{e}_s is a unit vector tangent to the axis of the structure, Δs is a length of section of element in which the hydrodynamic force is calculated, D is a diameter of the section (or the longest diagonal if the section is a polygon). It is assumed, that C_M and C_D coefficients are a function of K_C , β and the geometry of the section (and adjacent sections).

The value of the force acting on the element can be therefore determined as an integral:

$$\mathbf{F} = \int_0^s \left(\frac{1}{2} \rho C_D D |\mathbf{U}_n| \mathbf{U}_n + \frac{1}{4} \pi D^2 \rho C_M \frac{d}{dt} \mathbf{U}_n \right) ds \quad (8)$$

DETERMINATION OF THE VELOCITY FIELD DUE TO WAVES AND CURRENTS

So far, we have assumed, that the velocity field is a known quantity, but just determining velocity field is not a simple task. The Maritime Institute in Gdańsk analysed the hydro-meteorological data for a particular sea area and performed long-term statistical calculations [7, 8], based on which a set of basic parameters of the waves and sea current was obtained, Figure 2, 3. The results of WAM hindcast numerical modelling [9, 10] of Baltic Sea were used to calculate wave field parameters. These parameters provided materials for long-term statistical analysis.

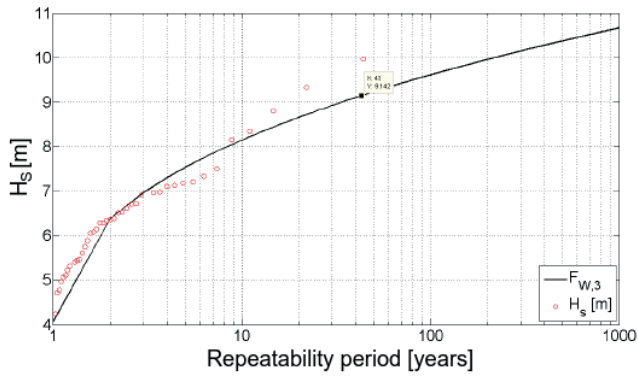


Fig. 2. Significant wave height H_s as a function of return period. Weibull distribution for location: 7,750 E, 55,50 N (Baltic Sea – Polish economic zone)

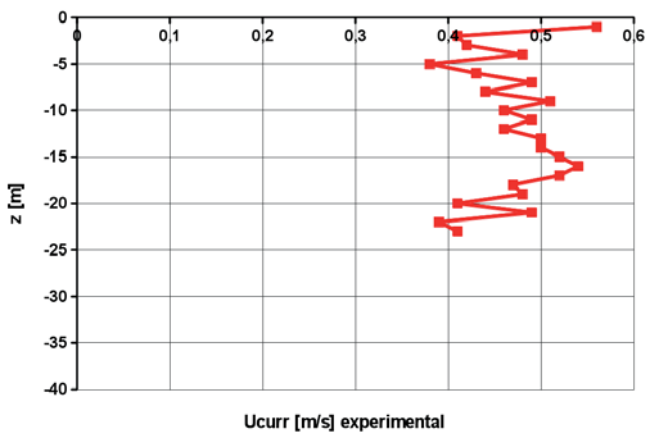


Fig. 3. Sea current velocity distribution as a function of depth. The results of measurements in the Baltic Sea during extreme storm

In this project, it was assumed, that the life time of the structure will reach 30 years with an optional extension of another 20 years, therefore, the analysis assumed parameters of the storm that happens once in 50 years. Velocities of the sea currents in the Baltic are relatively small. To calculate the desired parameters in the project, it was assumed, that the velocity of the sea current at the surface water is $U_{curr}(0) = 0.45$ m/s, which is the velocity in the relevant reservoir that appears once in 50 years.

The velocity vector as a function of depth can be approximated to the following form:

$$U_{curr}(z) = e_{curr} \left(1 + \frac{z}{d}\right)^{\frac{1}{7}} U_{curr}(0) \quad (9)$$

where:

d is the water depth, z is a vertical coordinate.

Sea current direction indicated by the unit vector e_{curr} is consistent here with the direction of the waves. Both phenomena are caused by the wind.

On the basis of statistical parameters: peak period T_p and significant wave height H_s the spectrum of sea waves in the form of the JONSWAP spectrum [4, 3] was reconstructed. The peak shape parameter γ was calculated based on the

recommendations of DNV [3]. The spectrum of waves can be thus approximated by a function:

$$S_J(\omega) = A_\gamma \frac{5}{16} H_s^2 \omega_p^4 \omega^{-5} \exp\left(-\frac{5}{4} \left(\frac{\omega}{\omega_p}\right)^4\right) \gamma \exp\left(-0.5 \left(\frac{\omega - \omega_p}{\sigma \omega_p}\right)^2\right) \quad (10)$$

Where:

$\omega_p = 2\pi/T_p$ is circular spectral peak frequency; $\sigma = 0.07$ for $\omega \leq \omega_p$ and $\sigma = 0.09$ for $\omega \geq \omega_p$ spectral width parameter $A_\gamma = 1 - 0.287 \ln(\gamma)$ is a normalizing factor,

Figure 4 presents the distribution of the spectrum of waves for specific set of data, whereas Figure 5 presents the function of the sea current velocity.

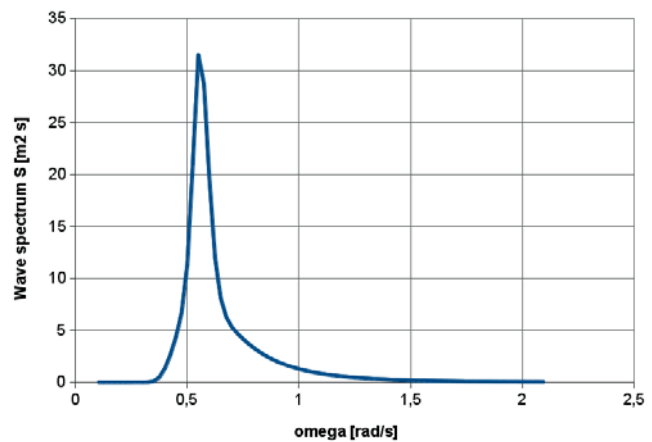


Fig. 4. Wave spectrum JONSWAP for the 50-year storm: $T_p = 11.3$ s; $H_s = 9.01$ m; $\gamma = 4.14$

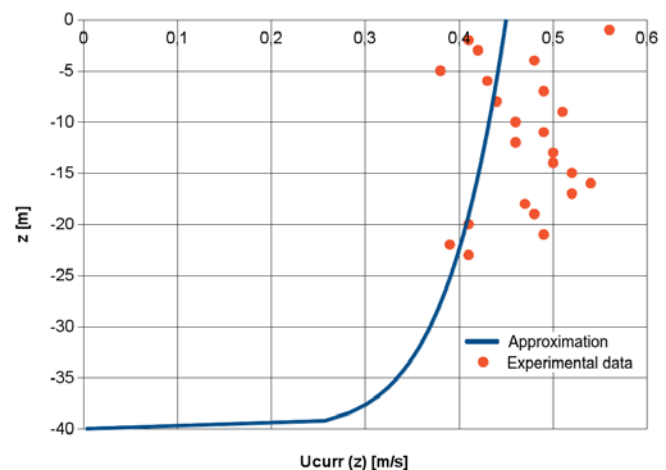


Fig. 5. Approximation of the current velocity profile for the 50-year storm

On the basis of a specific spectrum of waves, an irregular wave was generated (randomly). Due to the fact, that the depth of the reservoir is $d = 40$ m and a peak period of the wave is greater than 11 s, the chosen wave model was the second order Stokes one. Velocity field in the wave motion in the Stokes model is described as a series. This series is obtained

by replacing the graph of a continuous spectrum of waves with the discrete graph of a finite width of the “bars” $\delta\omega$.

$$U_{wave} = \sum_i u_i \quad (11)$$

where the term of series $u_i = u(\omega_i)$ is obtained from:

$$u_i = \omega_i^2 H_i \left\{ \frac{1}{2 \sinh(k_i d)} \left[\frac{\cosh[k_i(d+z)] \sin(\theta_i)}{\sinh[k_i(d+z)] \cos(\theta_i)} \right] + \frac{3}{8} \frac{k_i H_i}{\sinh^2(k_i d)} \left[\frac{\cosh[2k_i(d+z)] \sin(2\theta_i)}{\sinh[2k_i(d+z)] \cos(2\theta_i)} \right] \right\} \quad (12)$$

Where:

$H_i = \sqrt{8S(\omega_i)\delta\omega}$ is a height of i -th wave; $k_i = 2\pi / \lambda_i$ - wave number; $\theta_i = k_i x - \omega_i t + \varepsilon_i$.

Value ε_i takes a random value in the range of 0 to 2π . Subsequent values of circular frequency are defined as follows: $\omega_{i+1} = \omega_i + \delta\omega$.

The resulting velocity field is a sum of the sea current velocity and of the velocity field due to wave:

$$U = U_{curr} + U_{wave}$$

IMPLEMENTATION OF CFD CALCULATIONS TO DETERMINE THE C_M AND C_D COEFFICIENTS

The purpose of the CFD calculations was primarily to determine the coefficients for the elements of a shape other than cylindrical. The fact that the geometry is based on a hex decagon is not critical in this case. The hex decagonal prism can be treated as a cylinder. What is of importance is the fact, that the size of the polygon (its diagonal) is changing rapidly with height above the seabed z .

Flow around such geometry, and particularly around the segments of r_1 , r_2 and r_3 (Figure 12) is three dimensional, therefore there are no tables or graphs available that can be used, describing the characteristic C_M and C_D , in a function of K_C and the roughness of the surface. Wherein, when the Reynolds number takes the value of the order of 10^7 or higher, the impact of the β factor is minimal (Figure 6, 7).

Moreover, as was described previously (section 3.2), the traditional method of determination of the C_D and C_M coefficients are model tests in the U-tube tank. In the measuring area of the tank, the fluid flow is homogeneous (in space), but unsteady. The function of velocity in the time domain is a sinusoid.

The CFD model was built this way, to match the flow in the measuring area of a U-tube tank. The height of the computational domain is equal to the water depth, therefore, only a flow around the submerged part of the structure is modeled. The flow velocity at the inlet and outlet of the domain is specified as a sinusoidal function (in time), therefore the single test case can be determined by two parameters: the period T and the velocity amplitude U_A of the flow.

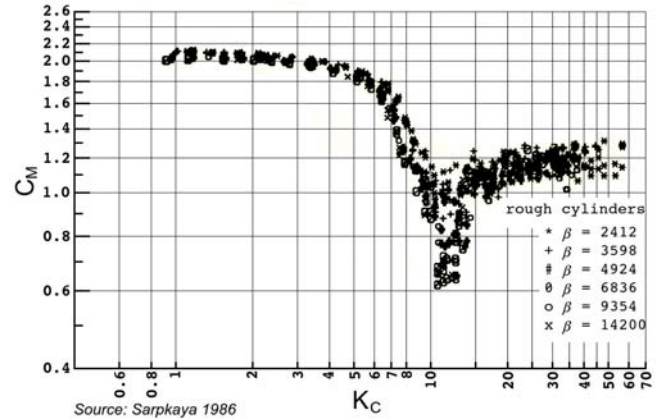


Fig. 6. Comparison of inertia coefficient C_M for six rough cylinders, $k/D=50$. Source: Sarpkaya [2]

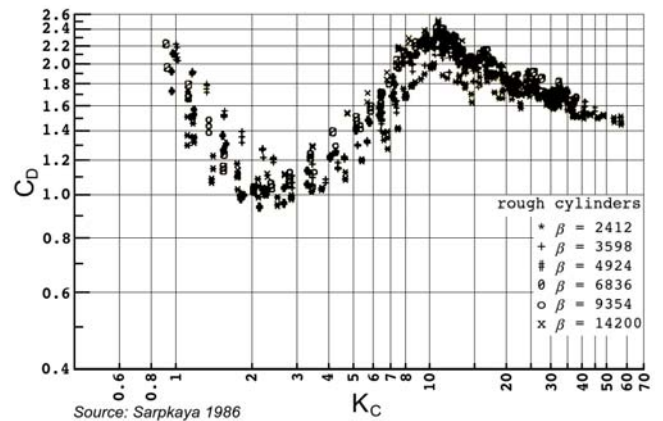


Fig. 7. Comparison of drag coefficient C_D for six rough cylinders, $k/D=50$. Source: Sarpkaya [2]

THE RANGE OF CALCULATIONS

Due to the fact, that the main objective of this work is to determine the maximum hydro dynamical loads acting on the supporting structure, the coefficients C_M and C_D will be calculated for a range of parameters resulting from the spectrum of waves and sea current for the 50-year storm on the marine area of a depth of 40 m. The calculations were performed for the following set of data:

$T = 6 \text{ s}; 8 \text{ s}; 10 \text{ s}; 12 \text{ s}; U_A = 0.5 \text{ m/s}; 1 \text{ m/s}; 2 \text{ m/s}.$

The calculations were performed for both smooth and rough walls. In total, the results were obtained for C_M and C_D at 24 calculation points. Roughness caused by the presence of marine growth was taken as $k_r = 100 \text{ mm}$, as recommended by NORSOK N-003 [3]. Relative roughness, k_r / D dependent on the length of the diagonal element varies from 0.0025 to about 0.017.

PARAMETERS USED FOR CALCULATIONS WITH CFD – THE “TECHNICAL” MODEL

Technical parameters of the computational grid are included in the Table 1. Figure 8 shows a general view of the domain of computations. The calculations were carried out in full scale.

Tab. 1. Grid parameters

| | Smooth surface | Rough surface |
|--|----------------|---------------|
| Number of control volumes | 676 570 | 6 303 391 |
| Thickness of 1st layer | 0.003 mm | 1 mm |
| Number of layers of boundary control volumes | 8 | 20 |

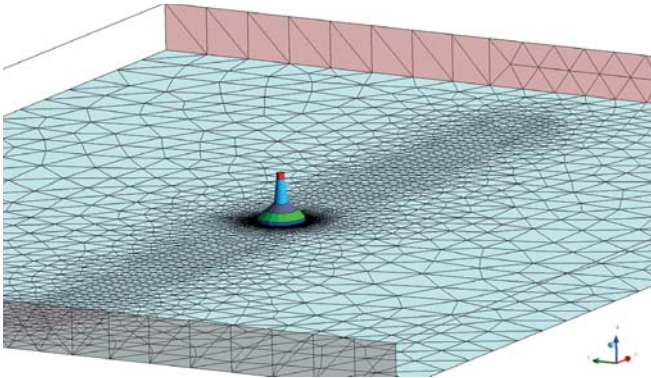


Fig. 8. The computational grid arrangement. View of the inlet/outlet and the bottom of the domain

The differences between the meshes in the case of calculation of smooth and rough structure (Table 1) are the result of turbulence models that were taken and relate mainly to the size of the elements on the surface of the structure and its boundary layer. Thickness of elements of 1st layer, in the case of a smooth structure, takes considerably lower values.

For the smooth surface $k-\omega$ SST turbulence model was employed, for which the thickness of elements of the 1st (boundary) layer (in this case 0.003 mm) should be such that the parameter Y^+ obtains values close to one.

The rough structure calculations were made on the basis of the $k-\xi$ turbulence model, with scalable wall function. In this model, the viscous sublayer is omitted, and the logarithmic velocity profile is reduced by the value of ΔB that depends on the “grain size” k_r (Figure 9).

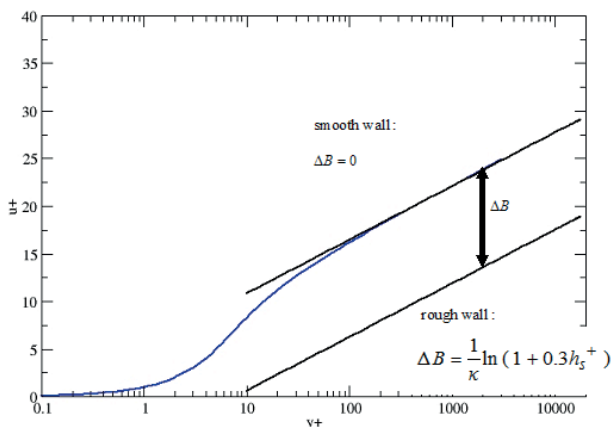


Fig. 9. Wall function for rough surface [5]

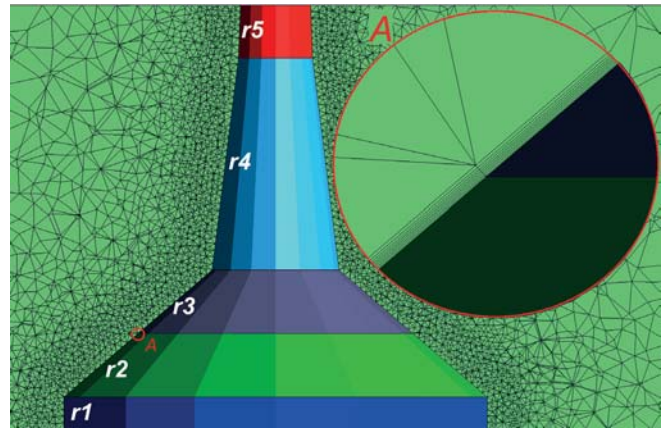


Fig. 10. Grid arrangement around surface of modelled structure. The figure also shows the numbering of segments (regions) r1, r2, r3, r4, r5

THE RESULTS OF THE CFD CALCULATIONS

As a result of the CFD calculations, graphs of hydro mechanical forces were obtained that can be induced on specific segments as a function of time (Figure 11). Based on these charts, values of the C_M and C_D coefficients were determined.

Flow visualization was also obtained in the form of streamlines, based on which, it is possible to conclude that the flow around r1, r2 and r3 was three-dimensional.

The results of the calculations are depicted in diagrams of $C_M(K_C)$ and $C_D(K_C)$, additionally showing the value of the parameter β (Figure 13, 14 - smooth surface, Figure 15, 16 - rough surface)

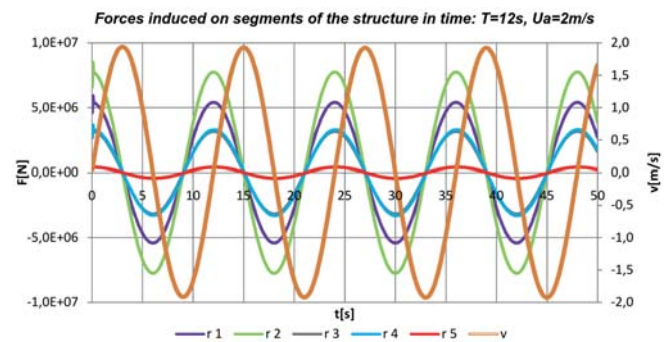


Fig. 11. Forces induced on segments of the support structure in time, for the following data: $T = 12$ s, $U_A = 2$ m/s.

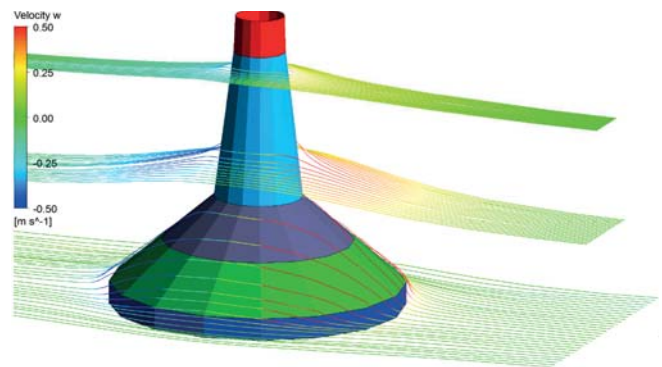


Fig. 12. Streamlines around support structure

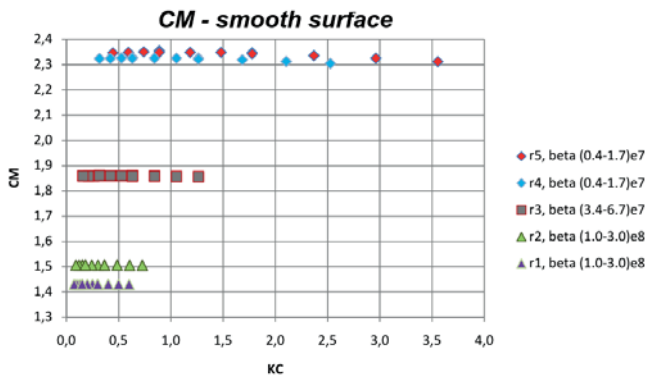


Fig. 13. A graph of the C_M as a function of K_C for the subsequent segments of the structure. Smooth surface

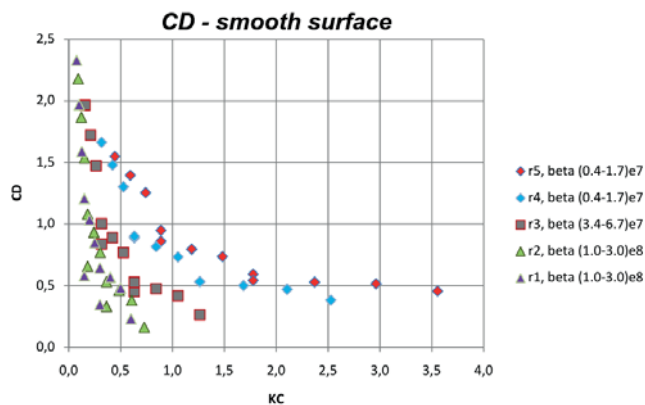


Fig. 14. A graph of the C_D as a function of K_C for the subsequent segments of the structure. Smooth surface

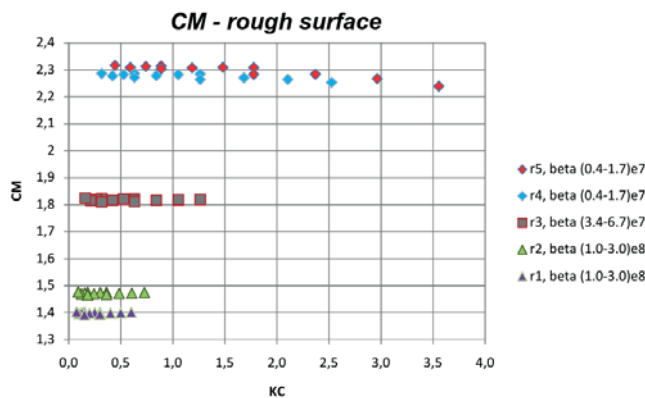


Fig. 15. A graph of the C_M as a function of K_C for the subsequent segments of the structure. Rough surface

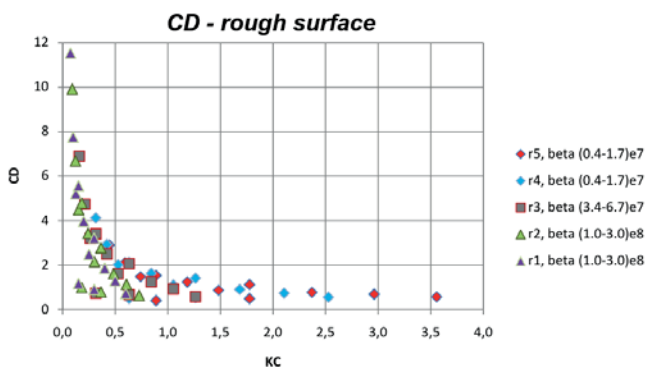


Fig. 16. A graph of the C_D as a function of K_C for the subsequent segments of the structure. Rough surface

ANALYSIS OF THE RESULTS OF CALCULATIONS OF C_M AND C_D

The resulting characteristics of C_M and C_D for a smooth surface have a waveform consistent with similar results obtained experimentally for a cylindrical shape. The shape of the curve of C_M factor for rough structure is almost identical to the plot for the smooth construction.

As expected, the force coefficients for r1, r2 and r3 segments are lower than that retrieved from the test of cylindrical shape, since the flow around such elements is three-dimensional and thus fluid particles pass by the “obstacle” on the trajectory shorter than in the case of 2D flow.

The characteristics of the drag coefficient for the rough construction seem unlikely. Perhaps the resistance is strongly overestimated for $K_C < 0.5$ (the differences are significant with respect to the results of model tests [1]). It can be seen, that the applied method of modelling of roughness is not accurate enough.

THE CALCULATION OF THE HYDRO DYNAMICAL FORCES ACTING ON THE SUPPORTING STRUCTURE SUBJECTED TO THE ACTION OF IRREGULAR WAVES AND CURRENT

SELECTION OF COEFFICIENTS OF HYDRO DYNAMICAL FORCES

Based on the results of the CFD calculations and the known experimental results [1,2], the following hydro dynamical force coefficients were identified for each item.

Factor K_C was calculated for the “representative” regular wave with the period of $T = 11.30$ s and height $H_s = 9.01$ m, which corresponds to peak period and the significant height of the 50-year storm in this sea area.

Tab. 2. Selection of the force coefficients based on the flow parameters and the geometry of the structure

| Segment | z_0 [m] | z_1 [m] | D_0 [m] | D_1 [m] | $U_a(z)$ [m/s] | K_C | β | C_M | C_D |
|---------|-----------|-----------|-----------|-----------|----------------|-------|----------|-------|-------|
| r1 | -40 | -37 | 40 | 40 | 1.29 | 0.36 | 1.19E+08 | 1.4 | 1.0 |
| r2 | -37 | -31 | 40 | 26 | 1.32 | 0.45 | 8.09E+07 | 1.5 | 1.0 |
| r3 | -31 | -25 | 26 | 12 | 1.41 | 0.84 | 2.68E+07 | 1.8 | 1.0 |
| r4 | -25 | -5 | 12 | 7 | 1.83 | 2.18 | 6.71E+06 | 2.3 | 1.0 |
| r5 | -5 | 5(15) | 7 | 6.25 | 2.82 | 4.80 | 3.26E+06 | 2.3 | 1.0 |

The value of the amplitude of the velocity was calculated for $z = 0.5$ ($z_0 + z_1$) using the linear (Airy’s) wave model:

$$U_a(z) = \frac{\pi H_w}{T} \frac{\cosh[k(z+d)]}{\sinh(kd)} \quad (14)$$

Keulegan-Carpenter number is defined as $K_C = U_a T / D$, while the β number is calculated as [1]: $\beta = D^2 / (\nu T)$. The inertia coefficient C_M was read from the Figure 15. Based on Figure 16 and the value of K_C , it was assumed, that the drag coefficient C_D for each segment is approximately 1.0.

CALCULATION OF HYDRO DYNAMICAL RESPONSE

The wave spectrum with the parameters described in subsection 3.4 corresponds to the storm duration of 3 hours. For this spectrum three wave functions were randomly chosen - all of one hour duration. For 1-hour realization of the wave not to be a periodic phenomenon, about 1200 terms of the series given by eq. (11) and (12) are required [6]. Additionally, the calculations took into account the presence of the sea current with parameters described above.

The results of calculations for the wave at which the maximum load of the construction was observed are shown below. Figure 17 shows the height of the free surface in the axis of symmetry of the structure as a function of time, whereas Figure 18 shows a resultant horizontal force acting

on the structure. The bending moment relative to the bottom of the structure ($z = -40$ m) is shown in Figure 19. It was assumed, that the maximum load is such, that the bending moment of the construction reaches its maximum. For the results presented here, the maximum stress occurs at time $t = 3450.5$ s.

For this time step, the distribution of hydro dynamical loads acting on the construction was shown on Figure 20. Loads depicted in the graph are due to the action of hydro dynamical forces that are associated with movement of fluid $F = F(U(t), \partial U(t)/\partial t)$. To these forces the hydro statistic load resulting for the seawater and the ballast located within the gravity base structure, as well as the thrust and torque of the wind turbine (transmitted through the column), weights and other forces must be added.

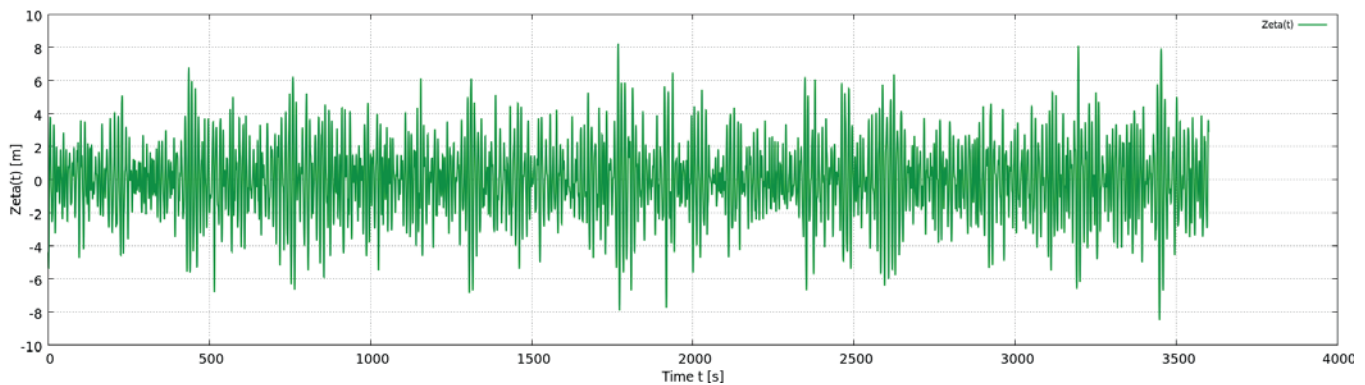


Fig. 17. The free surface level ζ in the symmetry axis of the structure in time domain

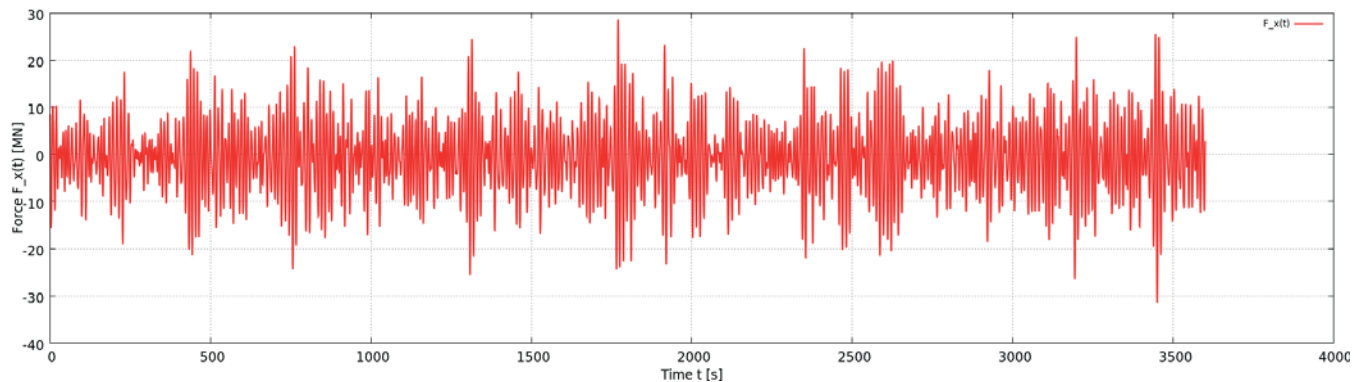


Fig. 18. The total force in the x-direction F_x induced on the structure by the wave and current

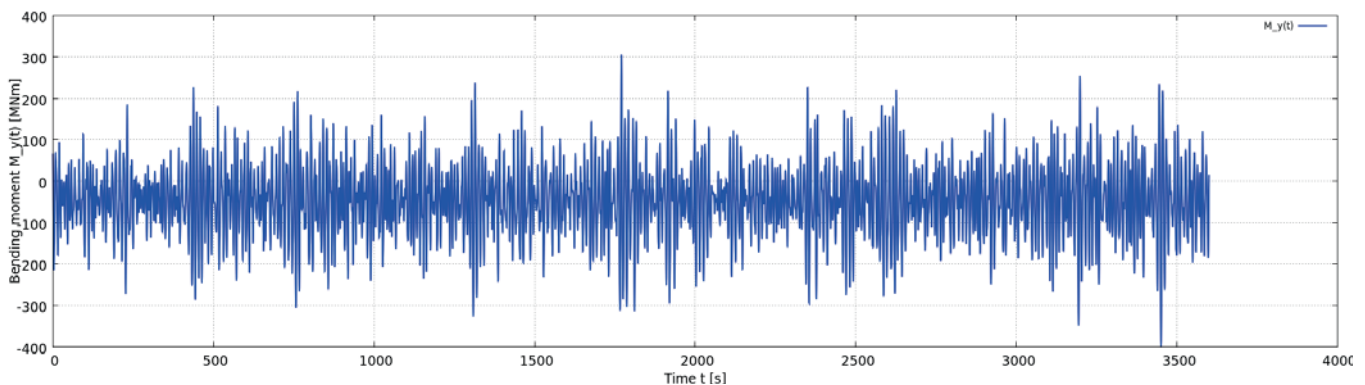


Fig. 19. The total bending moment M_y (at $z = -40$ m) induced on the structure by the wave and current

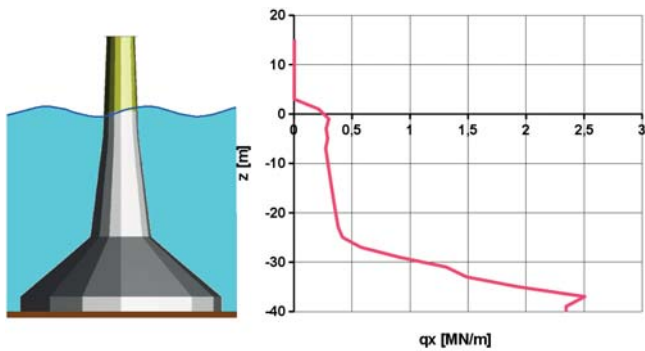


Fig. 20. Distribution of continuous load q_x due to sea wave and current as a function of z for the time step $t = 3450.5$ s (maximum value of bending moment)

SUMMARY AND CONCLUSIONS

In this article we presented a method for calculating unsteady loads acting on supporting structure for offshore wind turbines. The method is based on the expanded use of Morison equation and coefficients of the forces obtained from computations with modern CFD software - ANSYS CFX.

Based on the results of CFD analysis of segments of similar shape to a cylindrical, it was found, that the forces coefficients are close to the values obtained experimentally by Sarpkaya [1,2].

Through to the simplified approach, one can effectively define construction loads of initial design, (assuming that small changes in the geometry do not significantly affect the values of the coefficients C_M and C_D). Determination of the sequence of loads for wave lasting (in reality) three hours with the time step of 1/2 s takes about 1 to 3 hours of computing time.

These loads will be used for the design of structural elements based on FEM analysis. The methodology of FEM analysis for similar structure was presented by Żywicki et al [11].

ACKNOWLEDGMENT

CFD analysis has been performed with ANSYS-CFX solver. Calculations were carried out at the Academic Computer Center in Gdańsk (TASK).

This research was supported by The Polish National Centre for Research and Development (NCBR) under the project PBS1/A6/8/2012 "AQUILO".

REFERENCES

1. Sarpkaya T.: Wave forces on offshore structures, Cambridge University Press, 2010
2. Sarpkaya T.: In-line and transverse forces on smooth and rough cylinders in oscillatory flow at high Reynolds numbers, Monterey, California. Naval Postgraduate School, 1986

3. Recommended Practice DNV-RP-C205: Environmental conditions and environmental loads, Det Norske Veritas, October 2010
4. Levis E.V.: Principles of Naval Architecture. Vol. III – Motions in Waves and Controllability, SNAME, 1989
5. ANSYS CFX - Solver Theory Guide, ANSYS Inc., October 2012
6. Chakrabarti S.K.: Hydrodynamics of Offshore Structures, WIT Press / Computational Mechanics, 2003
7. Kamphuis J.W., Introduction to Coastal Engineering and Management, Advanced Series on Ocean Engineering: Volume 30, 2010
8. Li F., van Gelder P.H.A.J.M., Ranasinghe R., Callghan D.P., Jongejan R.B., Probabilistic modelling of extreme storms along the Dutch coast, Coastal Engineering 86, 2014
9. WAMDI Group: The WAM model – A Third Generation Ocean Wave Prediction Model. J. Phys. Oceanography, 18, 1988
10. Cieślakiewicz W., Paplińska-Swerpel B.: A 44-year hindcast of wind wave fields over the Baltic Sea, Coastal Engineering 55, 2008
11. Dymarski C., Dymarski P., Żywicki J.: Design and strength calculations of the tripod support structure for offshore power plant POLISH MARITIME RESEARCH 1(85) 2015 Vol. 22; pp. 36-46 10.1515/pomr-2015-0006

CONTACT WITH AUTHOR

Paweł Dymarski
Ewelina Ciba

Gdańsk University of Technology
Faculty of Ocean Engineering and Ship Technology
11/12 Narutowicza St.
80-233 Gdańsk
Poland

Tomasz Marcinkowski

Maritime Institute in Gdansk
Długi Targ 41/42
80-830 Gdańsk
Poland

MODELLING 3D STEAM TURBINE FLOW USING THERMODYNAMIC PROPERTIES OF STEAM IAPWS-95

A.V. Rusanow¹

P. Lampart²

N.V. Pashchenko¹

R.A. Rusanov²

¹The Podgorny Institute of Mechanical Engineering Problems

National Academy of Science of Ukraine in Kharkov, Ukraine

²The Szewalski Institute of Fluid Flow Machinery, Polish Academy of Sciences in Gdańsk, Poland

ABSTRACT

An approach to approximate equations of state for water and steam (IAPWS-95) for the calculation of three-dimensional flows of steam in turbomachinery in a range of operation of the present and future steam turbines is described. Test calculations of three-dimensional viscous flow in an LP steam turbine using various equations of state (perfect gas, Van der Waals equation, equation of state for water and steam IAPWS-95) are made. The comparison of numerical results with experimental data is also presented.

Keywords: Three-dimensional viscous flow, steam turbine, low-pressure cylinder, sets of equations of state for water and steam IAPWS-95, approximations of equations

INTRODUCTION

Throughout the last 10-15 years, the methods of viscous flow modeling based on Reynolds equations [1, 2, 3] have been widely applied in calculation, design and optimization of turbomachinery parts, including steam turbines. Adopting such approaches has made a significant improvement in gas dynamic efficiency of turbomachinery, especially with the use of 3D modeling of blade channels, including blade lean, sweep, end wall contouring, radial-axial stages. There are still a number of difficulties in numerical integration of the set of Reynolds equations related to the accuracy and stability of different schemes, formulation of boundary conditions, closing equations (turbulence modeling, equation of state etc.). Most of the application packages use rather simple state equations such as the equation of state for perfect gas, Tammann or Van der Waals equations. In many cases their use is justified and appropriate. However, in relation to the processes in which a phase transition in the working medium occurs (for example in low-pressure cylinders and condensers of conventional, nuclear and marine steam turbines), the use

of simple state equations allows modeling of flow structures and rough assessment of kinetic energy losses, but may produce significant uncertainties in the determination of quantities like temperature, mass flow rate and turbine power. In order to describe thermodynamic properties of water and steam using simpler computation methods (one-dimensional, quasisymmetric), one can implement state equations based on the Mayer and Bogomolov equation [4] whose virial coefficients are found by correlation with the experiment. At present, two international standards of state equations for water and steam are used: IAPWS-95 formula [5] for scientific calculations and its simplified version - IAPWS-IF97 formula [6] for industrial calculations. It is difficult to use these state equations in three-dimensional calculations on present-day computers since they increase the required computational time by 1 to 2 orders of magnitude. The most frequently used state equation nowadays in three-dimensional models is the equation with two terms of compressibility coefficient.

This paper presents an approach to the approximation of state equations IAPWS-95 with the use of cubic curves

for the given arrays of thermodynamic functions. The idea of a similar approximation was first presented in [7]. This method assures a sufficient accuracy of determination of thermodynamic quantities within the whole range of operation of steam turbines (the maximum error does not exceed $\pm 0,1\%$). In the paper, three-dimensional calculations of flow in LP turbines using numerous equations of state are presented and compared with the available experimental data.

METHODS FOR THE CALCULATION OF THREE DIMENSIONAL VISCOUS FLOW IN TURBINES

The calculation is carried out using the application package FlowER [3] and is based on the integration of the Reynolds equation. In order to determine turbulent effects, the Menter SST model is used [8]. The governing equations are solved with the use of implicit Godunov-type ENO scheme [9]. In order to close the Reynolds equations, equations of state for a perfect gas [10], Tammann equations [11] or Van der Walls equations [4] with constant or variable specific heats are available in the application package FlowER. A number of thermodynamic dependencies, which shape depends on the used state equation, are applied in the process of computation and post processing of results such as:

$$T=T(p,\rho) \text{ - temperature;}$$

$$\rho=\rho(p,T) \text{ - density;}$$

$$\varepsilon=\varepsilon(p,\rho) \text{ - internal energy;}$$

$$p=p(\varepsilon,\rho) \text{ - pressure;}$$

$$a=a(p,\rho) \text{ - speed of sound;}$$

$$i=i(p,\rho) \text{ - enthalpy;}$$

$$c_v=c_v(p,\rho) \text{ - specific isochoric heat;}$$

$$c_p=c_p(p,\rho) \text{ - specific isobaric heat;}$$

$$S=S(p,\rho) \text{ - entropy;}$$

$$\left(\frac{\partial \varepsilon}{\partial p}\right)_\rho = \varepsilon_p(p,\rho) \text{ - partial derivative of internal energy with respect to pressure at a constant density;}$$

$$\left(\frac{\partial \varepsilon}{\partial \rho}\right)_p = \varepsilon_\rho(p,\rho) \text{ - partial derivative of internal energy with respect to density at a constant pressure;}$$

$$\left(\frac{\partial S}{\partial p}\right)_\rho = S_p(p,\rho) \text{ - partial derivative of entropy with respect to pressure at a constant density;}$$

$$\left(\frac{\partial S}{\partial \rho}\right)_p = S_\rho(p,\rho) \text{ - partial derivative of entropy with respect to density at a constant pressure;}$$

$$\left(\frac{\partial T}{\partial p}\right)_\rho = T_p(p,\rho) \text{ - partial derivative of temperature with respect to pressure at a constant density;}$$

$$\left(\frac{\partial T}{\partial \rho}\right)_p = T_\rho(p,\rho) \text{ - partial derivative of temperature with respect to density at a constant pressure;}$$

$$i_*=i_*(p,\rho,C) \text{ - total enthalpy;}$$

$$T_*=T_*(p,\rho,C) \text{ - total temperature;}$$

$$p_*=p_*(p,\rho,C) \text{ - total pressure;}$$

$$\rho_*= \rho_*(p,\rho,C) \text{ - total density;}$$

$$\rho_{iz}=\rho_{iz}(S,p) \text{ - isentropic density;}$$

$$i_{iz}=i_{iz}(S,p) \text{ - isentropic pressure,}$$

where C – speed. Closing thermodynamic functions for perfect gas, Tammann and Van der Walls equations of state are presented in [12].

APPROXIMATION OF CLOSING THERMODYNAMIC FUNCTIONS ON THE BASIS OF THE EQUATIONS FOR THERMODYNAMIC PROPERTIES OF WATER AND STEAM IAPWS-95.

Equations of *International Association for Properties of Water and Steam* IAPWS-95 were formulated in 1995. They were determined on the basis of the fundamental Helmholtz equation $f(\rho,T)$ and can be a combination of polynomials of up to 56 elements [5]. In most cases, it is impossible to find an analytical formula for thermodynamic functions necessary for closing the Reynolds equation. This makes the direct application of IAPWS-95 for modeling three-dimensional flow ineffective in regards of computational cost. In an approach presented in [7] the closing functions are determined by interpolation of the already calculated arrays (tables) of base points of thermodynamic quantities. However, due to a significant nonlinearity of thermodynamic functions, storage of large arrays might be necessary in order to assure the acceptable accuracy in defining thermodynamic parameters in a wide range of variation of flow parameters (especially in the range of operating modes of steam turbines).

Some hints how to decrease the dimensions of the stored arrays without a loss to the precision of interpolation are described below. In the case where the independent variables for determination of the thermodynamic values are pressure and/or density, it is justified to consider the pressure and density in a logarithmic scale as independent variables. This, for example, allows us to calculate 3D flow in the HP and LP cylinders of the steam turbine where the pressure changes

from $3 \cdot 10^3$ to $2 \cdot 10^5$ Pa in the LP cylinder and from $3 \cdot 10^6$ to $2,4 \cdot 10^7$ Pa in the HP cylinder.

Another idea to reduce computational costs and still assure the acceptable accuracy of interpolation of IAPWS-95 equations is to rewrite the equations of state for a perfect gas with dimensionless compressibility coefficients depending on two independent variables, especially p and ρ . Range variations of these coefficients are much lower when compared with variations of the sought thermodynamic functions. Therefore it is justified to store the arrays of values of the dimensionless compressibility coefficients instead of values of the sought thermodynamic functions. The closing thermodynamic functions are then derived from analytical relations:

$$T = \frac{p}{\rho R z_{-t}(\rho, p)}; \quad \rho = \frac{p}{i} z_{-\rho}(i, p); \quad \varepsilon = \frac{p}{s} z_{-\varepsilon}(\rho, p);$$

$$p = \rho \cdot \varepsilon \cdot z_{-p}(\rho, \varepsilon); \quad a = \sqrt{\frac{p}{s} z_{-a}(\rho, p)}; \quad i = \frac{p}{\rho} \left(1 + \frac{z_{-\varepsilon}(\rho, p)}{z_{-t}(\rho, p)}\right);$$

$$C_v = R \cdot z_{-C_v}(\rho, p); \quad C_p = R \cdot z_{-C_p}(\rho, p); \quad S = R \cdot z_{-S}(\rho, p);$$

$$\varepsilon_p = \frac{z_{-\varepsilon}(\rho, p)}{\rho \cdot z_{-t}(\rho, p)}; \quad \varepsilon_\rho = -\frac{p}{\rho} \frac{z_{-\varepsilon}(\rho, p)}{z_{-t}(\rho, p)};$$

$$S_p = \frac{C_v}{p}; \quad S_\rho = -\frac{C_p}{\rho}; \quad T_p = \frac{1}{\rho R \cdot z_{-t}(\rho, p)}; \quad T_\rho = -\frac{p}{\rho^2 R \cdot z_{-t}(\rho, p)},$$

where g – gas constant [5], $z_{-t}(\rho, p)$, $z_{-\rho}(i, p)$, $z_{-\varepsilon}(\rho, p)$, $z_{-p}(\rho, \varepsilon)$, $z_{-C_v}(\rho, p)$, $z_{-C_p}(\rho, p)$, $z_{-S}(\rho, p)$ – interpolated dimensionless compressibility coefficients for the corresponding thermodynamic functions. While calculating the density, the independent variable T is replaced with the enthalpy, which facilitates the calculation in the two-phase flow regions. The formulas used to define the partial derivatives of internal energy, entropy, and temperatures are simplified, defined based on the assumption, that the compressibility coefficients remain constants. This simplification also increases the stability of numerical convergence of iterative processes for solving nonlinear equations. Values of dimensionless compressibility coefficients in base points are as follows:

$$z_{-t} = \frac{p}{\rho R T}; \quad z_{-\varepsilon} = \frac{\varepsilon}{R T};$$

$$z_{-\rho} = \frac{i \rho}{p}; \quad z_{-p} = \frac{p}{\rho \cdot \varepsilon};$$

$$z_{-a} = \frac{a^2}{R T}; \quad z_{-C_v} = \frac{C_v}{R};$$

$$z_{-C_p} = \frac{C_p}{R}; \quad z_{-S} = \frac{S}{R},$$

where the corresponding values p , ρ , T , ε , i , a , C_p , C_v and are calculated with the use of IAPWS-95 formulations [5]. The interpolation of the compressibility coefficient is determined

with the use of cubic polynomial curves. The entire iteration method is described in detail in [12].

EVALUATION OF APPROXIMATION ERROR FOR CLOSING THERMODYNAMIC FUNCTIONS.

For the approximation of dimensionless compressibility coefficients and closing thermodynamic functions of two independent variables, two-dimensional arrays of base points (4001×2001) are used. A solid line in Fig. 1 shows the area for the evaluation of arrays of independent variables - pressure and density:

$$500 \text{ Pa} < p < 3,5 \cdot 10^7 \text{ Pa}; \quad 4 \cdot 10^{-3} \text{ kg/m}^3 < \rho < 210 \text{ kg/m}^3.$$

In the same picture, a dashed line surrounds the working area of steam turbines. Relative approximation errors (an average error based on 1000 points randomly selected from the considered area, or a maximum error) in defining thermodynamic functions were calculated as relative deviations of the value found from the proposed approximation from the value obtained with the help of IAPWS-95 tables:

$$\xi_{mean} = \text{mean} \left| \frac{f_{approx} - f_{IAPWS}}{f_{IAPWS}} \right|,$$

$$\xi_{max} = \text{max} \left| \frac{f_{approx} - f_{IAPWS}}{f_{IAPWS}} \right|$$

The average approximation error for all the calculations does not exceed 0,05 %, the maximum error - 0,8 %. Within the working area of steam turbines, the average approximation error does not exceed 0,01 %, maximum - 0,1 %, with the largest errors appearing in the region of low pressure and wet steam.

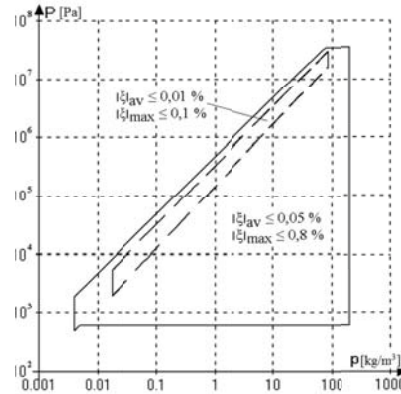


Fig. 1. Working area for approximation of steam properties

COMPUTATIONAL RESULTS

The presented method of calculation of 3D flow was tested for the case of a low pressure cylinder of a five-stage steam turbine of 360 MW (Fig. 2). The obtained results were compared with the available experimental data [13].

Radial guide vanes are placed at the inlet to the turbine. The stator and rotor blades in all but one stage are shrouded

with shrouds equipped with typical labyrinth seals. The rotor blades in the last stage are free-tip. There are two extraction points downstream of stage 3 and 4. The scheme of regenerative extractions, tip-leakage and labyrinth seal flows in meridional view is presented in Fig. 2.

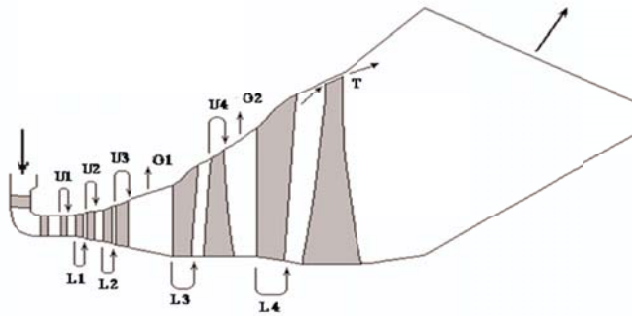


Fig. 2. Meridional cross section of the low pressure flow part of a 360 MW steam turbine. The scheme of leakage and extraction flows, O1, O2 - regenerative extractions, T - tip leakage clearance over unshrouded rotor blades, U1-U4 - labyrinth seal slots at the upper contour, L1-L4 - labyrinth seal slots at the lower contour.

In order to define boundary conditions for the inlet and outlet of the computational domain, experimental data obtained in [13] are used:

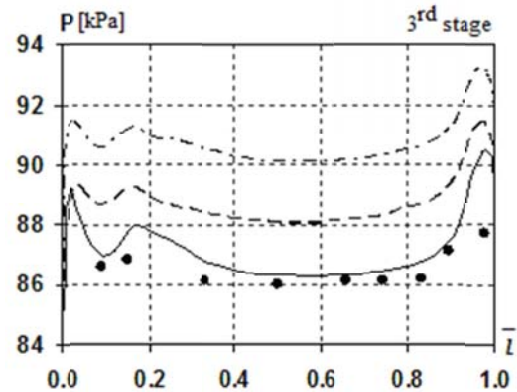
- total pressure at the inlet - 519 kPa, total temperature at the inlet - 539 K;
- static pressure at the outlet - 6,2 kPa.

The initial data for modeling regenerative extractions and labyrinth seal flows were determined earlier in [14] using a one-dimensional approach. They are included in Table 1. The flow directions in the labyrinth seals are nominal and are also indicated in Fig. 2. The calculations are made on a structural H-type grid of about 4 million cells in total refined in the boundary layers, according to the assumed turbulence model.

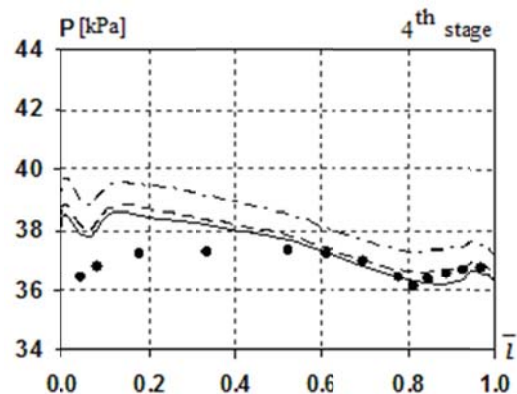
The integral characteristics of flow in the third, fourth and fifth stage of the turbine are calculated first with the use of the equation of state for a perfect gas with variable specific heats (calculation 1), second with the use of the Van der Waals equation of state (calculation 2) and third with the use of the presented method of approximation of IAPWS-95 properties (calculation 3). Figs. 3 and 4 show the comparison

of experimental and calculated total and static pressure as well as pitch and swirl angle downstream of stage 3, 4 and 5.

a)



b)



c)

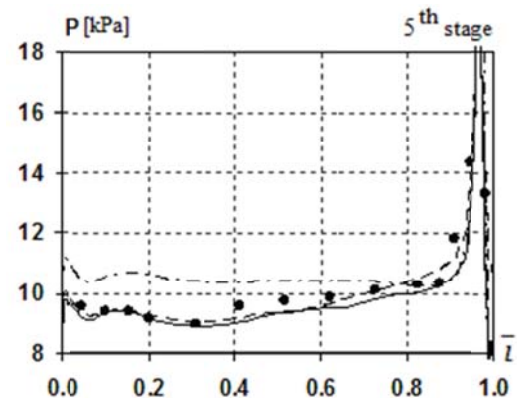


Table 1. Initial data for modeling regenerative extractions and labyrinth seal flows

| Position | Stage | Blade row | G, kg/c | T ₀ *, K |
|----------|-------|-----------|---------|---------------------|
| U1 | 1 | rotor 1 | 2,00 | 537,8 |
| L1 | 2 | stator 2 | 1,90 | 487,8 |
| U2 | 2 | rotor 2 | 1,40 | 487,8 |
| L2 | 3 | stator 3 | 1,21 | 437,8 |
| U3 | 3 | rotor 3 | 1,10 | 437,8 |
| O1 | 3-4 | - | 5,50 | - |
| L3 | 4 | stator 4 | 0,54 | 387,8 |
| U4 | 4 | rotor 4 | 1,10 | 387,8 |
| O2 | 4-5 | - | 5,00 | - |
| L4 | 5 | stator 5 | 0,36 | 337,8 |

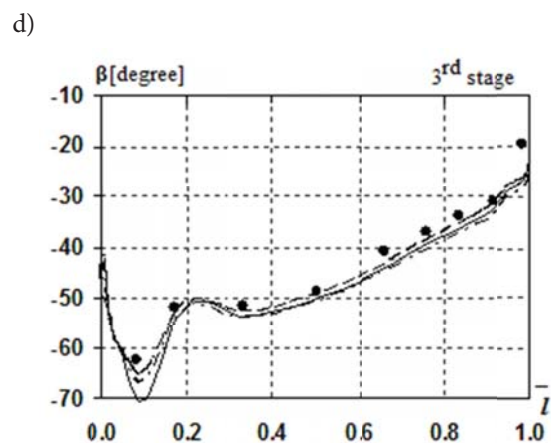
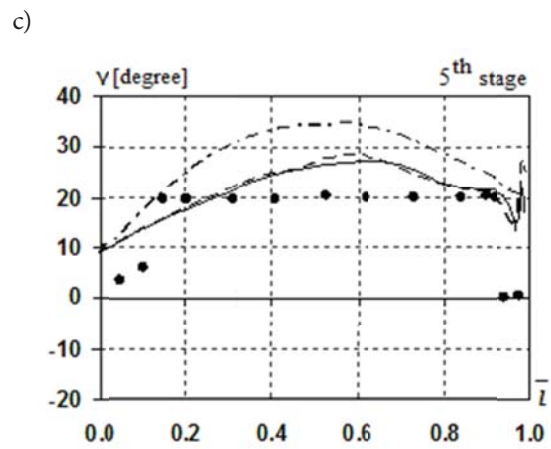
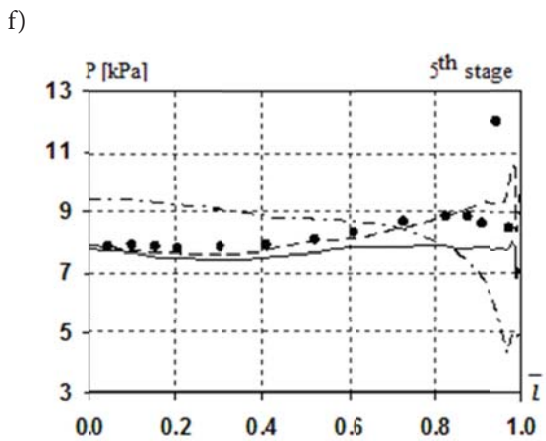
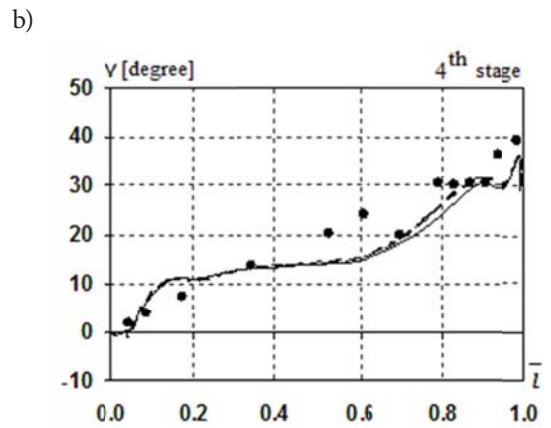
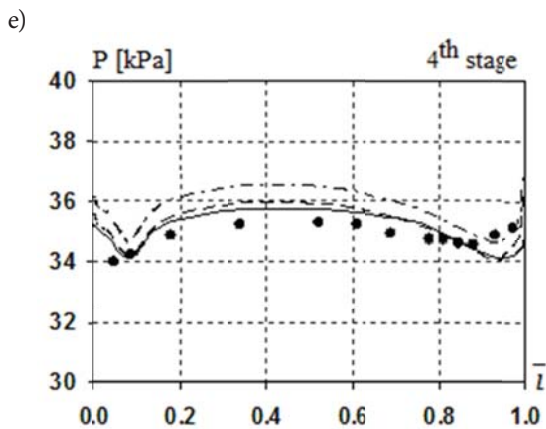
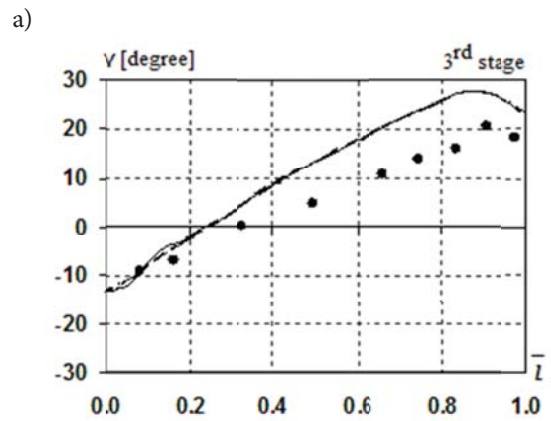
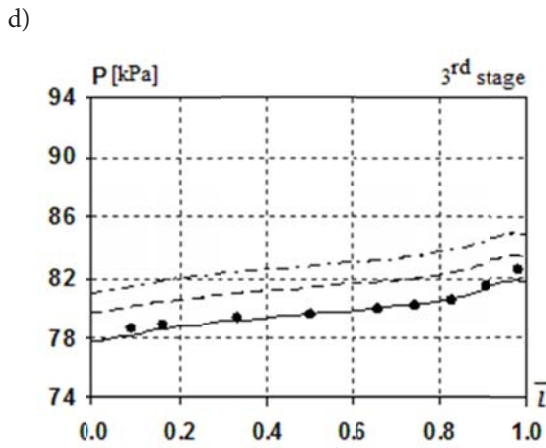
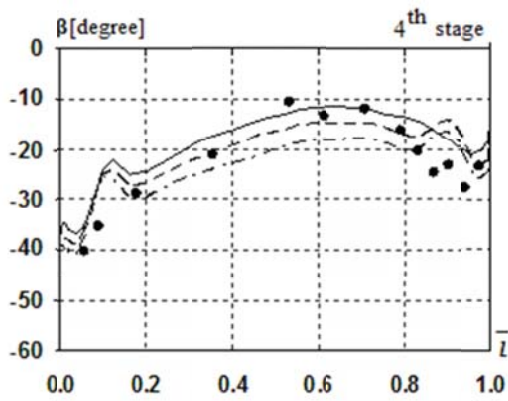


Fig. 3. Total pressure (a, b, c) and static pressure (d, e, f) distribution along the channel height in stage 3, 4 and 5;

••• experiment, - - - calculation 1, - · - · - calculation 2, - · - · - calculation 3

The presented examples prove consistency of the experimental and calculated data. It is clear that, the best fit belongs to calculation 3, that is to the method of approximation of IAPWS-95 properties. It should also be noted, that constants in the equations of state used for calculations 1 and 2 were found from experimental data, while it is not necessary to use these data for calculation 3.

e)



f)

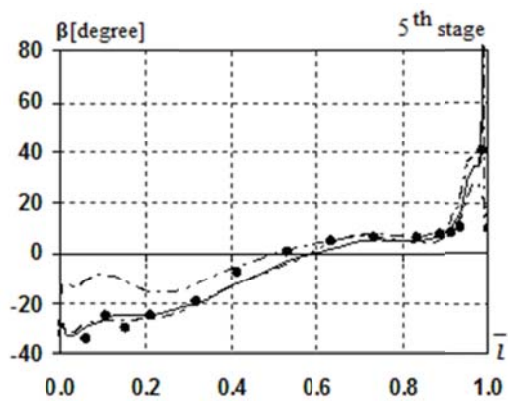


Fig. 4. Pitch angle (a, b, c) and swirl angle (d, e, f) distribution along the channel height in stage 3, 4 and 5;
 ●●● experiment, ---- calculation 1, -.-.- calculation 2,
 ----- calculation 3

CONCLUSIONS

The paper presents an approach to approximate equations of state for water and steam (IAPWS-95) for the calculation of three-dimensional flow in an LP steam turbine. The comparison of numerical results with experimental data is also presented. The average approximation error of evaluation of thermodynamic functions within the working area of turbine is lower than 0,01 %, the maximum error remains below 0,1 %. Test calculations of three-dimensional viscous flow in an LP steam turbine are also made using various equations of state (perfect gas, Van der Waals equation, equation of state for water and steam IAPWS-95). It is shown, that the presented method of approximation of IAPWS-95 properties provides the best fit of computational and experimental results.

LITERATURE

1. ANSYS Products, Terms & Conditions. ANSYS, Inc. All Rights Reserved, available on: <http://www.ansys.com>
2. Wróblewski W., Dykas S., Gepert A., 2009, Steam condensing flow modeling in turbine channels, Int. J. Multiphase Flow; Vol. 35(6), pp. 498-506.
3. Yershov S., Rusanov A., 1996, The Application Package FlowER for the Calculation of 3D Viscous Flows Through Multi-Stage Turbomachinery. Certificate of state registration of copyright No. 77, Ukrainian Agency for Copyright and Related Rights, 19.02.1996.
4. Nashchokin V., Semyonov S., 1980, Engineering Thermodynamics and Heat Transfer, Moscow, High School.

Table 2. Integral characteristics of the investigated LP turbine

| Parameter | Experiment | Calculation 1 | Calculation 2 | Calculation 3 |
|------------------------------|------------|---------------|---------------|---------------|
| In the outlet part - stage 1 | | | | |
| P, k Pa | – | 321,23 | 16,1 | 314,4 |
| T, K | – | 504,85 | 00,7 | 494,4 |
| In the outlet part - stage 2 | | | | |
| P, k Pa | – | 190,31 | 86,7 | 182,8 |
| T, K | – | 471,24 | 64,2 | 443,0 |
| In the outlet part - stage 3 | | | | |
| P, k Pa | 79,9 | 80,02 | 78,61 | 79,84 |
| T, K | 371,2 | 421,04 | 11,2 | 367,4 |
| I, kJ/kg | 2647 | 2690 | 2643 | 2646 |
| G, kg/c | 107,9 | 108,31 | 08,7 | 107,6 |
| In the outlet part - stage 4 | | | | |
| P, k Pa | 34,9 | 35,86 | 35,3 | 35,32 |
| T, K | 346,4 | 380,03 | 69,2 | 346,1 |
| I, kJ/kg | 2531 | 2568 | 2526 | 2520 |
| G, kg/c | 100,9 | 101,91 | 02,2 | 101,2 |
| In the outlet part - stage 5 | | | | |
| P, k Pa | 8,3 | 8,24 | 8,22 | 8,23 |
| T, K | 314,8 | 320,53 | 20,6 | 313,7 |
| I, kJ/kg | 2350 | 2390 | 2387 | 2370 |
| G, kg/c | 96,0 | 100,1 | 91,7 | 95,1 |

5. IAPWS-95, Revised Release on the IAPWS Formulation 1995 for the Thermodynamic Properties of Ordinary Water Substance for General and Scientific Use, available on: <http://www.iapws.org>
6. IAPWS-IF97, Revised Release on the IAPWS Formulation 1997 for the Thermodynamic Properties of Water and Steam, available on: <http://www.iapws.org>
7. Yershov S., Rusanov A., 2002, Numerical simulation of three-dimensional viscous flows in turbomachines for imperfect gas, Part 1. Problem Statement. *Probl. Engineering*, Vol. 5, No. 4, pp. 18-25.
8. Menter F., 1994, Two-equation eddy viscosity turbulence models for engineering applications. *AIAA J.*, Vol. 32, No 11., pp. 1299–1310.
9. Yershov S., 1994, Quasi ENO scheme of high accuracy for Euler and Navier+Stokes equations, *Math. Modeling*, Vol. 6, No. 11, p. 58–64.
10. Sommerfeld A., 1964, *Thermodynamics and Statistical Mechanics (Lectures on Theoretical Physics)*, Academic Press.
11. Godunov S. Zabrodin A., Ivanov M., 1976, Numerical solution of multidimensional problems of gas dynamics, Moscow, Nauka.
12. Rusanov A., Yershov S., 2008, Mathematical modeling of unsteady gas-dynamic processes in flow-through parts of turbomachinery, Institute of Mechanical Engineering Problems, Kharkiv.
13. Marcinkowski S., Gardzilewicz A., Gluch J., 1999, Results of extended flow measurements in the LP part of 18K370 steam turbine, *Rep. Diagnostyka Maszyn*, Gdańsk, No. 11/99.
14. Lampart P., Rusanov A., Yershov S., Marcinkowski S., Gardzilewicz A., 2005, Validation of 3D RANS Solver With a State Equation of Thermally Perfect and Calorically Imperfect Gas on a Multi-Stage Low-Pressure Steam Turbine Flow, *Journal of Fluids Engineering*, Vol. 127, pp. 83 – 93.

CONTACT WITH THE AUTHOR

Piotr Lampart

The Szewalski Institute of Fluid Flow Machinery
 Polish Academy of Sciences in Gdańsk
 e-mail: lampart@imp.gda.pl
POLAND

EXHAUST GAS TEMPERATURE MEASUREMENTS IN DIAGNOSTICS OF TURBOCHARGED MARINE INTERNAL COMBUSTION ENGINES PART II DYNAMIC MEASUREMENTS

Zbigniew Korczewski, Prof.
Gdańsk University of Technology, Poland

ABSTRACT

The second part of the article describes the technology of marine engine diagnostics making use of dynamic measurements of the exhaust gas temperature. Little-known achievements of Prof. S. Rutkowski of the Naval College in Gdynia (now: Polish Naval Academy) in this area are presented. A novel approach is proposed which consists in the use of the measured exhaust gas temperature dynamics for qualitative and quantitative assessment of the enthalpy flux of successive pressure pulses of the exhaust gas supplying the marine engine turbocompressor. General design assumptions are presented for the measuring and diagnostic system which makes use of a sheathed thermocouple installed in the engine exhaust gas manifold. The corrected thermal inertia of the thermocouple enables to reproduce a real time-history of exhaust gas temperature changes.

Keywords: diagnostic, internal combustion engine, exhaust gas temperature

INTRODUCTION

Analysing temperature and pressure changes of the exhaust gas leaving the cylinders of a turbocharged marine engine within one operating cycle provides opportunities for direct qualitative and quantitative assessment of the enthalpy flux of successive pressure pulses of the exhaust gas supplying the turbocompressor. Its value, expressed in J/ OWK deg within one operating cycle for a single-cylinder four-stroke engine (each cycle corresponds to two crankshaft revolutions), is calculated by integrating the exhaust gas enthalpy flux formula within the endpoints defined by crankshaft rotation angles:

$$\bar{H}_{imp(OWK)} = \int_0^{720} \dot{m}_{sp} \cdot c_{sp}(T_{sp}) \cdot T_{sp} d\alpha_{OWK} \quad (1)$$

In case of a multi-cylinder engine in which the collecting

manifold (or manifolds) supplying the turbocompressor has a number of individual exit passages from particular cylinders connected to it, the enthalpy flux is to be integrated within precisely defined endpoints (240 OWK degrees for a four-stroke engine) which result from: (1) the operating sequence of the cylinders, (2) the opening and closing angles of the exhaust valves in particular cylinders, (α_{OWK}^{OZW}) and (α_{OWK}^{ZZW}) respectively, and (3) the angles of overlapping of successive exhaust gas flow pulses (α_{OWK}^N):

$$\bar{H}_{imp(OWK)} = \int_{\alpha_{OWK}^{OZW}}^{\alpha_{OWK}^{ZZW-N}} \dot{m}_{sp} \cdot c_{sp}(T_{sp}) \cdot T_{sp} d\alpha_{OWK} \quad (2)$$

To express in J/s the enthalpy flux of the pressure pulses of the exhaust gas supplying the turbocompressor within one engine operation cycle, the result of integration of Eq. (1) or

(2) is to be multiplied by a conversion ratio which converts the crankshaft revolution angles to a corresponding time expressed in seconds:

$$\bar{\dot{H}}_{imp(sek)} = \frac{n}{60 \cdot 360} \cdot \bar{\dot{H}}_{imp(OWK)} \quad (3)$$

MEASURING HIGH-SPEED EXHAUST GAS TEMPERATURE CHANGES

In the adopted research method a key metrological issue is to calculate the average time-histories of high-speed changes of the exhaust gas temperature in a selected control cross section of the turbocharger inlet channel¹. This requirement results from the fact that successive individual time-histories are deformed, as a consequence of errors in the exhaust gas temperature and pressure measurements, and disturbances, mainly connected with: non-repeatability of the fuel combustion process in successive cylinders, fluctuations of the rotational speed of the crankshaft, wave phenomena in the flow channels (reflection, resonance and/or interference of waves), operation of the engine rotational speed controller, etc., [Korczeński, 2003].

In order to reproduce reliable time-histories, factors which cause their deformation are to be minimised by approximating the measured results in the crankshaft revolution angle domain. Many methods to approximate the measured high-speed variables are available [Polanowski and Zellma, 1997, Polanowski, 2007]. A method which is very simple and simultaneously reveals satisfying accuracy from the point of view of the diagnostic purpose of the analysis is the so-called method of synchronous averaging, described by [Korczeński, 2008, Korczeński and Zacharewicz, 2012]. This approximation method has been already used to measure high-speed air and exhaust gas pressures in flow channels of marine engines.

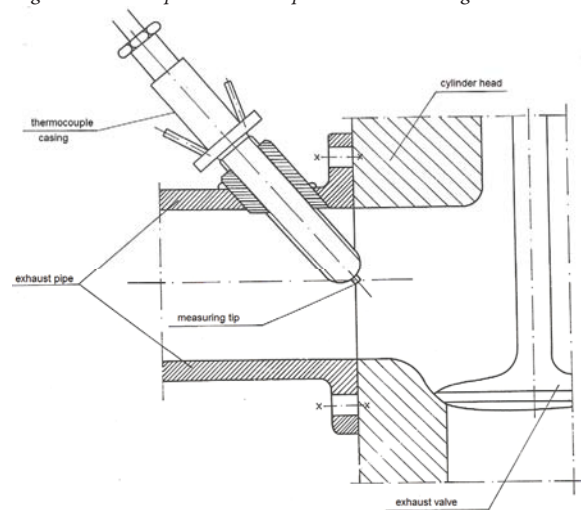
Another metrological issue of high importance is to secure the required resolution of the exhaust gas temperature measurement, at least of the order of 0,1 OWK degree (3600 measuring points per one crankshaft revolution), which in case of marine engines with the rotational speed of up to 1000 rpm requires the use of recorders with minimal sampling frequency of 60 kHz. 8,33 operating cycles are executed during one second of four-stroke engine operation, which means that one operating cycle lasts 0,12 second and the above mentioned recorder will be able to record 7200 measuring samples per one operating cycle. This sampling frequency is believed to allow the time-history of exhaust gas temperature changes to be reliably reproduced. At the same time, taking into account that signal recoding for synchronous averaging purposes should last at least 16 operating cycles, which corresponds

¹ The methodology to calculate instantaneous mass flow rates of the exhaust gas supplying the turbocharger, based on dynamic measurements of the stagnation pressure and static pressure recorded in two control cross sections of the exhaust gas exit channels, has been described in detail by [Korczeński, 2003] and is not discussed here.

to 32 crankshaft revolutions in the four-stroke engine (and 16 revolutions in the two-stroke engine), all this will result in writing 230.400 bytes to the memory of a single-channel recorder with 12-bit measuring card. At present, A/D converter cards with those parameters are easily available on electronic market.

When designing an effective diagnostic system for a marine engine working in real operating conditions at the assumption that this system bases on high-speed temperature measurements², the essential metrological problem is the selection and installation of thermocouples in the turbocharger inlet channel. First attempts in this area were made in Poland by Prof. Stanisław Rutkowski of the Naval College in Gdynia (now: Polish Naval Academy) in the 1970s [Rutkowski, 1976]. Having a measuring system at his disposal which was considered very advanced for those years, he managed to record time-histories of exhaust gas temperature changes in a laboratory single-cylinder four-stroke Diesel engine. The temperature was measured directly behind the exhaust valve (Fig. 1), on the background of the developed indicator graph – Fig. 2.

Fig. 1. Thermocouple installation place in the exhaust gas exit channel



[Rutkowski, 1976]

a)



² Performed on the engine installed in the ship engine room.

b)



Fig. 2. Time-histories of changes of: exhaust gas temperature, cylinder pressure, and GMP piston position vs. crankshaft rotation angle in single-cylinder four-stroke Diesel engine in two different technical states [Rutkowski, 1976]: a) reference state – full technical ability, b) state of partial technical ability – after introducing engine combustion chamber leakiness (compression pressure decreased from 3,53 to 3,13 MPa).

The research aimed at determining diagnostic relations between the cylinder compression pressure drop and the dynamics of changes of the recorded exhaust gas temperature. Based on the performed calculations, the following dynamic properties of the recorded signal were determined:

- maximal amplitude of instantaneous values of the exhaust gas temperature,
- rate of temperature increase and decrease,
- engine crankshaft rotation angle at which the maximal temperature is recorded.

Dynamic changes of the exhaust gas temperature were measured using a specialised³ ultra-miniature CrNiTi thermocouple having thermo electrode wires of 0,15 mm in diameter. The thermocouple was installed in the sheath of 6 mm in diameter and cooled in the water flow of precisely defined flow rate (min. 15 dm³/min) to prevent the water from boiling. During the measurements the open weld of the thermocouple protruded by about 1,5 mm from the sheath. The apparatus bearing the name of the loop recorder, made by the Austrian company Honeywell, was used to amplify and record the signal generated by the thermocouple.

The comparison analysis of the numerical data characterising the recorded high-speed time-histories of exhaust gas temperature and pressure in the engine cylinder clearly indicate obvious thermodynamic consequences of partial loss of combustion chamber tightness: the decrease of the compression pressure results in: (1) the increase of the maximal amplitude of the instantaneous temperature values of successive exhaust gas flux pulses, (2) higher intensity of temperature decreases and increases, and (3) the decrease of the OWK angle at which the temperature maximum is

³ The thermocouples were made to measure dynamically the temperature of powder gases in cannons.

recorded.

Theoretically, the recorded time-histories of the exhaust gas temperature changes could be used for formulating more in-depth diagnostic conclusions oriented on assessing energy consequences of the combustion chamber leakiness. Unfortunately, this turned out impossible due to limitations imposed by the analogue nature of operation of the measuring apparatuses used for measurements:

- loop recorder – the loop as the elements which records high-speed changes of thermoelectric voltage, reveals certain mechanical inertia which precludes its reliable on-line reproduction. At the same time, after developing the photo-sensitive paper of the loop recorder, the only possibility of quantitative comparison analysis of the recorded exhaust gas flux temperature and pressure pulses consisted in their manual planimetry.
- water cooled thermocouples – leaving aside the threat of possible sheath tightness loss and the resultant water flow into the engine workspace, the open weld of the thermoelement is exposed to the action of the high temperature exhaust gas in direct vicinity of the exhaust valve. This high temperature provokes intensive oxidation and diffusion processes, which change the chemical composition and crystalline structure of the thermocouples, with all further consequences for the recorded thermoelectric voltage, and the durability and reliability of the thermocouple.

The above arguments, supported by new possibilities introduced by dynamically developing numerical measurement systems and computer tools of numerical processing of the recorded measurement data, and by personal metrological experience gained by the author during many years of diagnostic examination of thermal and flow systems of internal combustion engines, were the reason why a decision was made to improve remarkably the technology of exhaust gas temperature measurements in Diesel engines, in order to allow it to be used for evaluating the technical state of real objects – engines installed in ship engine rooms.

EVALUATING DYNAMIC PROPERTIES OF THE THERMOCOUPLE

The starting point in designing the measuring and diagnostic system to analyse high-speed changes of the marine engine exhaust gas temperature is proper selection of the place for installing thermocouples. Obviously, the lower the top value of the interval of variations of the measured exhaust gas temperature, the longer the durability and reliability of the used thermocouple. Consequently, the most appropriate place for installing thermocouples seem to be the exhaust manifold region situated directly at turbocompressor inlet, i.e. the place where thermocouples for standard exhaust gas temperature measurements are installed (see Fig. 5 in Part I of the article). Also other arguments, such as good accessibility and serviceability of the engine element which enables easy preservation of its undisturbed functioning, speak in favour of

this selection. Indeed, exhaust gas flux pulses in this manifold region are much weaker than at cylinder exits, but the basic diagnostic goal here is limited to determining the enthalpy flux of successive pressure pulses of the exhaust gas supplying the turbocompressor in the same fixed control cross section of the manifold.

The next stage in designing the measuring system is selecting the thermocouple and method of its installation in the flow channel. These decisions make the basis for developing a mathematical model of the structure of the thermocouple. Taking into account exhaust gas flow conditions enables to evaluate basic dynamic parameters of the thermocouple, which are the time constant and the attenuation coefficient. These values are needed to determine thermal inertia of the thermocouple to be used for measuring the periodically changing exhaust gas temperature. Evaluated is the response of the thermocouple (treated as a dynamic element with concentrated parameters) to sinusoidal exhaust gas temperature excitation, including the phase shift and the amplitude of changes of the temperature T_{spp} recorded by the thermocouple with respect to the excited real changes of the exhaust gas temperature T_{sprz} – Fig. 3.

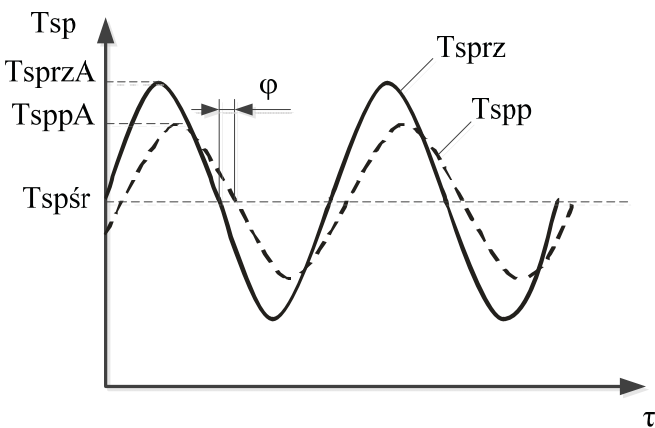


Fig. 3. Thermocouple response to sinusoidal exhaust gas temperature excitation

Selecting the structural material of thermo electrodes used in the thermocouple should ensure the highest possible measuring sensitivity. It is possible due to the use of low-resistance materials which allow high thermoelectric voltage to be generated. In the reported case, after thorough analysis of the available offers a decision was made to use a sheathed thermocouple of K (NiCr-Ni) type, with sheath diameter of 0,5 mm and thermo electrode diameter of 0,1 mm. The insulating material is most often the ceramic powder MgO, while the structural material of the sheath is the nickel-chromium alloy Inconel, which reveals high resistance to corrosion, in particular stress corrosion. This material ensures long lasting operation of the thermocouple up to the temperature of 1100 K, without catalytic reaction to the exhaust gas⁴. The thermometric (voltage) characteristic of the NiCr-Ni thermoelement is linear and sufficiently steep

⁴ The corrosion resistance of the Inconel alloy at the presence of CO₂ and SO₂ in the exhaust gas at temperatures exceeding 800 K is much weaker.

within the used measuring range [Wiśniewski, 1983].

Most producers offer three versions of sheathed thermocouples which differ by the response delay time to the set fluid temperature excitation. Structurally, these thermocouples have: (1) the weld insulated from the sheath (Fig. 4), (2) the weld welded to the sheath (Fig. 5), and (3) the open weld (Fig. 6)⁵. However, technical specification of the thermocouple does not specify flow conditions, determined by the type and velocity of the flowing medium, to which this delay time relates. In this situation, dynamic properties of the thermocouple used in high-speed engine exhaust gas temperature measurements should be determined analytically.

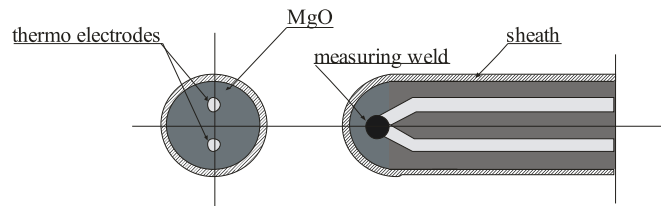


Fig. 4. Longitudinal and cross section of the final part of the sheathed thermocouple with the weld insulated from the sheath

To limit maximally the disturbances resulting from heat exchange by radiation between the thermocouple, exhaust gas, and flow channel walls, which may affect the performed dynamic measurements of unsteady exhaust gas temperature, the thermocouple should be installed in a cylindrical insulating shield (of 10 mm in diameter) which also stagnates the flowing exhaust gas. A standard thermocouple of the engine's measurement system is planned to be adopted for this purpose (Fig. 5).

On the other hand, to minimise the exhaust gas temperature measurement error resulting from the heat flow along the thermocouple sheath, the measuring length of the section l flowed around by the exhaust gas should be at least five times as long as the outer sheath diameter D_{sp} ⁶, and positioned in such a way that the inlet to the stagnating chamber of the shield is in the axis of the flow channel.

After assuming the simplest zero-dimensional model of the thermocouple and the plane temperature distribution in the sheath and thermo electrodes, and neglecting heat exchange by radiation⁷ between the thermocouple, exhaust gas, and the

⁵ The sheathed thermocouple with open weld reveals best dynamic characteristics, which are accompanied, however, by the lowest durability, especially when working in the exhaust gas flow (the time counted in minutes). That is why this type of thermocouple is not used in diagnostic practice.

⁶ The longer the measuring segment of the thermocouple flowed around by the exhaust gas of the temperature equal to the measured temperature, the larger the isothermal area around the thermocouple and the smaller the effect of the heat flow along the sheath on the measurement result.

⁷ It was assumed that the exhaust gas does not absorb and does not emit radiation, while the emissivity of the polished thermocouple sheath made

insulating shield, the unsteady energy balance equations for the final segment of the thermocouple flowed around by the engine exhaust gas can be determined in the following way:

- change of the internal energy accumulated in the sheath and in the ceramic insulation material (MgO) is equal to the flux of heat transfer from the exhaust gas to walls and insulation:

$$\frac{dU_p}{d\tau} = A_{zp} \cdot \alpha_{wp} \cdot \left(T_{sp} + r \cdot \frac{c^2}{2 \cdot c_{psp}} - T_p \right) \quad (4)$$

- change of the internal energy accumulated in the thermo electrodes is equal to the flux of heat convected through the sheath and the ceramic insulation material (MgO):

$$\frac{dT_{te}}{d\tau} = A_{te} \cdot \frac{1}{R_{\lambda p}} \cdot (T_p - T_{te}) \quad (5)$$

where: A_{zp} – outer surface of the sheath flowed round by the exhaust gas,

A_{te} – total surface of thermo electrodes in the measuring section of the thermocouple,

T_{sp} – temperature of the exhaust gas,

T_p – temperature of the sheath,

T_{te} – temperature of the thermo electrodes,

c – averaged velocity of the exhaust gas flow in the channel,

r – temperature recovery coefficient (for the stagnating chamber situated perpendicularly to the exhaust gas flow direction – values ranging between 0,90 and 0,96⁸ are assumed [Wiśniewski, 1983]),

c_{psp} – averaged specific heat of the exhaust gas at constant pressure,

α_{wp} – thermal transmittance between the exhaust gas and the sheath,

$R_{\lambda p}$ – averaged specific resistance of heat conduction by the sheath and the insulating material:

$$R_{\lambda p} = \frac{s}{\lambda_p} \quad (6)$$

λ_p – averaged heat transfer coefficient of the constructional material of the sheath and insulation,
 s – thickness of the sheath.

After expanding and relevant transformations, a system of ordinary differential equations of the first order was obtained which describes the heat transfer process in the thermocouple during the unsteady exhaust gas flow:

$$\frac{dT_p}{d\tau} = \frac{A_{zp} \cdot \alpha_{wp} \cdot \left(T_{sp} + r \cdot \frac{c^2}{2 \cdot c_{psp}} - T_p \right)}{C_{pi}} \quad (7)$$

of the alloy Inconel 600 and that of the insulating shield covered with silver are negligibly small ($\epsilon_{Inconel}=0,11-0,16$, $\epsilon_{Ag}=0,03-0,05$).

⁸ The temperature recovery coefficient for turbulent flow is also determined from the formula which makes use of the Prandtl number: $r = \sqrt[3]{Pr}$. For $r=1$ the measured exhaust gas temperature corresponds to the stagnation temperature.

$$\frac{dT_{te}}{d\tau} = \frac{A_{te} \cdot \frac{1}{R_{\lambda p}} \cdot (T_p - T_{te})}{C_{te}} \quad (8)$$

where:

C_{pi} – total thermal capacity of the constructional material of the sheath and insulation:

$$C_{pi} = m_{Inconel} \cdot c_{Inconel} + m_{MgO} \cdot c_{MgO} \quad (9)$$

C_{te} – total thermal capacity of the constructional material of the thermo electrodes:

$$C_{te} = m_{NiCr} \cdot c_{NiCr} + m_{Ni} \cdot c_{Ni} \quad (10)$$

After determining the averaged temperature of the sheath and the insulating material from Equation (8) we get:

$$T_p = \frac{C_{te} \cdot \frac{dT_{te}}{d\tau}}{A_{te} \cdot \frac{1}{R_{\lambda p}}} + T_{te} \quad (11)$$

and after two-sided differentiation:

$$\frac{dT_p}{d\tau} = \frac{C_{te}}{A_{te} \cdot \frac{1}{R_{\lambda p}}} \cdot \frac{d^2 T_{te}}{d\tau^2} + \frac{dT_{te}}{d\tau} \quad (12)$$

Placing formulas (11) and (12) into Equation (7) we arrive at the final form of the equation describing the dynamics of the analysed type of thermocouple⁹:

$$T_{sp} = -r \cdot \frac{c^2}{2 \cdot c_{psp}} + T_{te} + \left(\frac{C_{pi}}{A_{zp} \cdot \alpha_{wp}} + \frac{C_{te}}{A_{te} \cdot \frac{1}{R_{\lambda p}}} \right) \cdot \frac{dT_{te}}{d\tau} + \frac{C_{pi}}{A_{zp} \cdot \alpha_{wp}} \cdot \frac{C_{te}}{A_{te} \cdot \frac{1}{R_{\lambda p}}} \cdot \frac{d^2 T_{te}}{d\tau^2} \quad (13)$$

The form of Equation (13) reveals that the thermocouple with the weld insulated from the sheath is the second order inertial term, and its time constant is described by the equation:

⁹ Constant values in the equation, which characterise the constructional structure of the thermocouple, can be determined from characteristic dimensions of the sheath and thermo electrodes, taking also into account the density, specific heat, and heat transfer coefficient of the used materials. At the same time in engineering calculations, the thermal transmittance is assumed as a constant which only depends on the velocity and temperature of the flowing exhaust gas.

$$\tau_{cz} = \sqrt{\frac{C_{pi}}{A_{zp} \cdot \alpha_{wp}} \cdot \frac{C_{te}}{A_{te} \cdot \frac{1}{R_{\lambda p}}}} \quad (14)$$

When analysing dynamic properties of the thermocouple with the weld welded to the sheath (Fig. 5), an assumption is to be made that the weld measures the temperature T_k of the sheath end

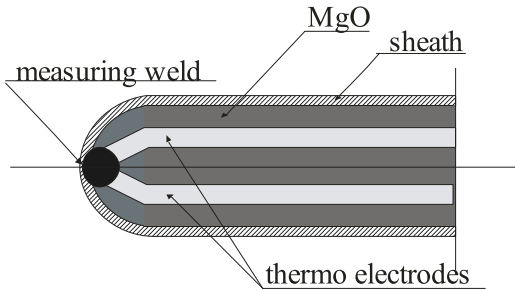


Fig. 5. Longitudinal section of the final part of the sheathed thermocouple with the weld welded to the sheath

Like in the previous case, assuming additionally that the heat transfer between the sheath and the exhaust gas takes only place by convection, and that the temperature at each point of the measuring segment of the sheath (a dynamic element with concentrated parameters) is constant and equal to the temperature of the weld, this type of thermocouple can be modelled as the dynamic element of the first order described by the following balance equation:

$$\frac{dU_k}{d\tau} = A_{zp} \cdot \alpha_{wp} \cdot \left(T_{sp} + r \cdot \frac{c^2}{2 \cdot c_{psp}} - T_k \right) \quad (15)$$

Relevant transformations lead to the following form of the thermocouple dynamics equation:

$$T_{sp} = \frac{C_p}{A_{zp} \cdot \alpha_{wp}} \cdot \frac{dT_k}{d\tau} + T_k \quad (16)$$

This time the time constant is described by the formula:

$$\tau_{cz} = \frac{C_p}{A_{zp} \cdot \alpha_{wp}} \quad (17)$$

where:

C_p – thermal capacity of the constructional material of the sheath:

$$C_p = m_{Inconel} \cdot c_{Inconel} \quad (18)$$

Comparing Equations (14) and (17) reveals that the time constant of the thermocouple with the weld welded to the sheath is smaller than that of the thermocouple with the weld insulated from the sheath, and the difference is the total thermal capacity of thermo electrodes and the insulating material

related to relevant heat transfer surfaces. We should keep in mind, however, that this approach is substantial simplification, as in practice, the thermo electrodes are to be added to the weld in calculations, which would lead to slight increase of the thermocouple's time constant. Nevertheless, the value which is much more difficult to assess analytically is the increase of the time constant due to heat transfer from the measuring weld via thermo electrodes to the insulating material, the more so that at the same time the heat is delivered to the thermo electrodes through the sheath and the insulating material.

The shortest time of thermocouple response to the set exhaust gas temperature excitation can be obtained using the sheathed structure with open weld – Fig. 6

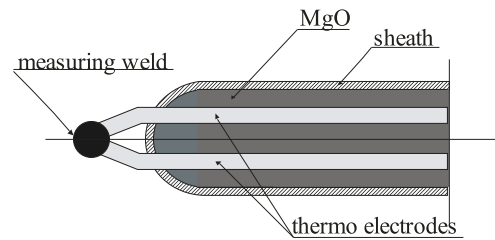


Fig. 6. Longitudinal section of the final segment of the sheathed thermocouple with open weld.

From the point of view of unsteady process modelling, the measuring weld can be considered a dynamic element with concentrated parameters. Assuming that the weld has the shape of a sphere and all its surface is involved in convection heat transfer (only) from the exhaust gas flowing around it¹⁰, its dynamic characteristic can be described by the following balance equation:

$$\frac{dU_s}{d\tau} = A_s \cdot \alpha_{ws} \cdot \left(T_{sp} + r \cdot \frac{c^2}{2 \cdot c_{psp}} - T_s \right) \quad (19)$$

which after expanding takes the following form :

$$T_{sp} = \frac{C_s}{A_s \cdot \alpha_{ws}} \cdot \frac{dT_s}{d\tau} + T_{sk} \quad (20)$$

where: A_s – surface of the measuring weld,
 T_{sp} – temperature of the exhaust gas,
 T_s – temperature of the measuring weld,
 α_{wp} – thermal transmittance between the exhaust gas and the measuring weld.

The time constant of the thermocouple is given by the formula:

$$\tau_{cz} = \frac{C_s}{A_s \cdot \alpha_{ws}} \quad (21)$$

When calculating the thermal capacity C_s of the measuring

¹⁰ In fact, like for the sheathed thermocouple with the weld welded to the sheath, thermal consequences of the presence of electrodes near the weld to the time constant are to be additionally taken into account.

weld, we should take into account that, due to technological reasons, its diameter is up to twice as large as that of the welded thermo electrodes:

$$C_s = m_s \cdot c_s \quad (22)$$

The most difficult task in the presented procedure is to determine analytically the thermal transmittance in formulas (14), (17) and (21). It is a function of many variables, including: the velocity and nature of the exhaust gas flow which define the thickness of thermal boundary layer, and thermophysical properties of the exhaust gas with a given chemical composition (viscosity, density, specific heat, and heat transfer coefficient) as temperature functions.

The thermal transmittance is determined based on the similarity of heat transfer (penetration) processes, the dimensional analysis (the π theorem formulated by Buckingham in 1924), and experiments. Empirical formulas which are most often used in engineering calculations to determine the thermal transmittance between the thermocouple sheath or the measuring weld (only) and the exhaust gas (in both directions) for the turbulent flow in the channel are given in the following form:

$$\alpha = Nu \cdot \frac{\lambda_{sp}}{d} \quad (23)$$

where: λ_{sp} – thermal conductivity of the exhaust gas at given temperature,

d – characteristic linear dimension, for instance the measuring weld diameter¹¹,

Nu – Nusselt number, characterising the relation between the heat transfer intensity and the temperature field in the boundary layer of the exhaust gas flow:

$$Nu = f(\text{Re}, \text{Pr}) \quad (24)$$

where: $\text{Re} = \frac{d \cdot c \cdot \rho_{sp}}{\eta_{sp}}$ – Reynolds number,

$\text{Pr} = \frac{\eta_{sp} \cdot c_{psp}}{\lambda_{sp}}$ – Prandtl number

c – velocity of the exhaust gas flow,

ρ_{sp} – density of the exhaust gas,

η_{sp} – dynamic viscosity of the exhaust gas,

A form of the function defining the Nusselt number is to be decided upon after experimental investigations performed for a given case of turbulent flow. For instance, the Nusselt

¹¹ Nusselt, Reynolds and Grashof numbers include a characteristic linear dimension, which is to be qualitatively the same for similar systems, i.e. understood in the same way by the author and the user of the criterion equation. In this situation, a parameter bearing the name of so-called equivalent diameter d_e , is frequently used. For the thermocouple having a cylindrical shape it can be determined as the ratio of the volume V to the surface A of the sphere having the same volume as the thermocouple flowed around by the exhaust gas: $d_e = 6V/A$. For the sheathed thermocouple with open spherical measuring weld of the diameter d : $d_e = d$.

number for the flow around a spherical measuring weld of the thermocouple can be determined from the formula worked out by Frössling [Furmański and Domański, 2004]:

$$Nu = 2 + 0,6 \cdot \text{Re}^{1/2} \cdot \text{Pr}^{1/3} \quad (25)$$

This way, the methodology to determine the thermal transmittance is reduced to determining the Reynolds and Prandtl numbers, and calculating the Nusselt number from the criterial equation (25). The obtained results make the basis for calculating α from a properly transformed function being a definition of Nu (23).

An aspect which also should be taken into account when analysing the dynamics of high-speed engine exhaust gas temperature measurements is the inertia of the entire data transmission system, including the converter, measuring card, recorder, etc. However, based on the requirement of simultaneous measurements of the exhaust gas pressure and temperature in the flow channel to calculate the enthalpy flux of the exhaust gas supplying the turbocompressor we can assume that this inertia is negligibly small.

Consequently, using the calculating formulas given in [Wiśniewski, 1983] we can calculate the phase shift of changes of the temperature recorded by the thermocouple with respect to real temperature changes in the exhaust gas:

$$\varphi = -\text{arctg} \varpi \cdot \tau_{cz} \quad (26)$$

where: ϖ – frequency of temperature change pulsations.

The real amplitude of exhaust gas temperature changes can also be determined as:

$$T_{sprzA} = T_{sppA} \cdot \sqrt{1 + \varpi^2 \cdot \tau^2} \quad (27)$$

As a result, a real time-history of changes of high-speed engine exhaust gas temperature can be reproduced based on properly recalculated temperature values recorded by the thermocouple:

$$T_{sprz} = T_{spsr} + T_{sppA} \cdot \sin(\varpi \cdot t - \text{arctg} \varpi \cdot \tau) \quad (28)$$

A sine qua non condition for using the above formulas to assess dynamic characteristics of the thermocouple is sufficient regularity of exhaust gas temperature changes within one engine operation cycle. Otherwise, two thermocouples of identical thermophysical characteristics but of different diameters are to be used for measurements, according to the methodology proposed for the first time by H. Pfriem in 1936. Unfortunately, in the next 80 years this methodology was not used in practice for diagnostic examination of workspaces of internal combustion engines.

FINAL REMARKS AND CONCLUSIONS

Dynamic exhaust gas temperature measurements in selected control sections of the manifold supplying the turbocompressor enable to calculate the enthalpy flux of successive pressure pulses of the exhaust gas leaving engine cylinders. Its value, averaged over one operating cycle, brings important diagnostic information on the technical state of cylinder workspaces, and of the injection and charge cycle systems. To make this information available, we should work out the technology of measurement and mathematical processing of the recorded high-speed exhaust gas temperature signal, which will enable to reproduce truly its real time-history as the function of engine crankshaft revolution angle. Research of this type is planned to be performed in real operating conditions on a marine four-stroke engine Sulzer type A, using an ultra-miniature thermocouple made of a material revealing very good conductivity and minimal thermal inertia. This thermocouple will be mounted in a properly modified sheath used by a standard thermocouple. The measuring procedure will be based on the method first used by Prof. Stanisław Rutkowski to examine a laboratory engine in 1976.

BIBLIOGRAPHY

1. Buczek A., Nocoń J., Słupek S.: Thermo technology (in Polish). AGH, Kraków, 2002.
2. Furmański P., Domański R.: Hest transfer (in Polish). Oficyna Wydawnicza Politechniki Warszawskiej, Warszawa, 2004.
3. Jaremkiewicz M., Taler D., Sobota T.: Measuring transient temperature of the medium in power engineering machines and installations. Elsevier. Applied Thermal Engineering. 29 (2009), 3374 – 3379.
4. Korczewski Z.: Method to diagnose turbocharged marine engines based on results of examination of gas dynamics processes in the exhaust gas system (in Polish). Diagnostyka, Vol. 28/2003 r., p. 87-95
5. Korczewski et al.: Method to diagnose warship engines with limited ability for intra-cylinder pressure measurements based on results of examination of gas dynamics processes in the turbo-charging system (in Polish). Research project No. 0T00B02129 financed by MNiSW. AMW Gdynia, 2008.
6. Korczewski Z.: An entropy function application within the selection process of diagnostic parameters of marine diesel and gas turbine engines. Polish Maritime Research, 2(65)/2010, Vol.17, p. 29-35.
7. Korczewski Z.: Exhaust gas temperature measurements in diagnostic examination of naval gas turbine engines. Part III. Diagnostic and operating tolerances. Polish Maritime Research, No. 4(71)/2011, Vol.18, p. 49-53.
8. Korczewski Z.: Analysing possible use of the diagnostic model of piston-crankshaft systems in internal combustion engines and evaluating its practical applicability for controlling rationally the operation of these engines taking into account an expert system (in Polish). Publication within the framework of the research project Nr N509 494638 financed by MNiSW. Gdansk University of Technology, 2012.
9. Korczewski Z., Zacharewicz M.: Alternative diagnostic method applied on marine diesel engines having limited monitoring susceptibility. Transactions of the Institute of Measurement and Control, Great Britain SAGE - Vol. 34, No. 8/December/2012, 2012, p. 937-946.
10. Kluj S.: Diagnostics of marine machinery (in Polish). Monographic publication. AM Gdynia 2000.
11. Pfriem, H.: Zur messung vernderlicher temperaturen von gasen und flssigkeiten (On the measurement of fluctuating temperatures of gases and fluids). Forschung auf dem Gebiete des Ingenieurwesens,7(2)/1936, pp. 85-92 (in German).
12. Piotrowski I., Witkowski K.: Operation of marine internal combustion engines (in Polish). Monographic publication. Gdynia Maritime University, Gdynia 2002.
13. Polanowski S., Zellma M.: The peak value determination of cylinder pressure rate with the basic splines or follow-up approximation. Journal of KONES'97, s. 297-303, 1997.
14. Polanowski S.: A study of methods to analyse indicator diagrams in the aspect of marine engine diagnostics (in Polish) . Zeszyty Naukowe AMW, nr 169A. Gdynia 2007.
15. Rutkowski S.: Using dynamic exhaust gas temperature measurements in diagnostics of marine internal combustion engines (in Polish). A copy of a typed abstract of the article written in 1976.
16. Rychter T., Teodorczyk A.: Theory of piston engines (in Polish). WKiŁ, Warsaw 2006.
17. Scott W.: Diagnosing Causes of High EGT in Marine Engines. Marine Machinery, Engines & Controls. Edited by Lamar Stonecypher (updated: 11/2/2011).
18. Wisłocki K.: Charging systems for high-speed internal combustion engines (in Polish). WKiŁ, Warszawa 1991.
19. Wiśniewski S.: Technical thermodynamics (in Polish). WNT, Warszawa 2005.

20. Wiśniewski S.: Temperature measurements in examination of engines and thermal facilities (in Polish). WNT, Warszawa 1983.
21. Woodyard D.: Pounders marine diesel engines and gas turbine. Great Britain ELSEVIER, 2004 (eighth edition).
22. Wojnowski W.: Marine internal combustion engine power plants. Part I (in Polish). Polish Naval Academy. Gdynia 1998.
23. www.intercars.com.pl

CONTACT WITH THE AUTHOR

Zbigniew Korczewski

Gdańsk University of Technology
11/12 Narutowicza St.
80 - 233 Gdańsk
POLAND

AN EXPERIMENTAL STUDY OF EMISSION AND COMBUSTION CHARACTERISTICS OF MARINE DIESEL ENGINE WITH FUEL INJECTOR MALFUNCTIONS

Jerzy Kowalski, Ph. D.
Gdynia Maritime University, Poland

ABSTRACT

The presented paper shows the results of the laboratory study on the relation between chosen malfunctions of a fuel injector and composition of exhaust gas from the marine engine. The object of research is a marine 3-cylinder, four-stroke, direct injection diesel engine with an intercooler system. The engine was loaded with a generator and supercharged. The generator was electrically connected to the water resistance. The engine operated with a load between 50 kW and 250 kW at a constant speed. The engine load and speed, parameters of the turbocharger, systems of cooling, fuelling, lubricating and air exchange, were measured. Fuel injection and combustion pressures in all cylinders of the engine were also recorded. Exhaust gas composition was recorded by using a electrochemical gas analyzer. Air pressure, temperature and humidity were also recorded. Emission characteristics of the engine were calculated according to ISO 8178 standard regulations. During the study the engine operated at the technical condition recognized as „working properly” and with simulated fuel injector malfunctions. Simulation of malfunctions consisted in the increasing and decreasing of fuel injector static opening pressure, decalibration of fuel injector holes and clogging 2 neighboring of 9 fuel injector holes on one of 3 engine cylinders.

Keywords: marine diesel engine, exhaust gas composition, toxic emission, laboratory investigation, fuel injector malfunctions

INTRODUCTION

By the end of the 20th century the main development directions of piston engines were fuel consumption reduction and increase of the structure reliability. Development in this direction is limited due to fuel heating value. Fuel consumption reduction of the internal combustion engines also leads to a reduction of emission of chemical compounds containing carbon and hydrogen. Fuel quality improvement and reduction of sulfur content in fossil fuels also leads to reduction of the emission of sulfur compounds into the atmosphere. Piston engines emit considerable amounts of compounds of the group of nitric oxides (NO_x), which result from oxidation of nitrogen contained in the charging air. Since the beginning of the 21st century, the development of piston engines has been determined by limiting regulations of volatile toxic compounds emission. In the case of onboard operated engines, in 1998 year, International Maritime Organization (IMO) introduced regulations on limitation of NO_x emission for engines installed on ships after 2001 year with nominal power above 130 kW [1], [2].

It should be noted that the above mentioned limitations relate to newly constructed engines, whereas over 50% of fleet consists of ships older than 15 years (over 42,5 thousand ships above 100 gross tonnage) [3]. Owners of the mentioned ships are not obliged to control NO_x emission. Sea-going

vessels usually have one or more piston engines installed for propulsion (main engine propulsion). They are usually large, low-speed, two-stroke engines or smaller, medium-speed, four-stroke engines. The ships are fitted also with engines driving power generators. In this case practically only medium-speed, four-stroke engines are applied. Steam or gas turbines are less frequently used. In the oldest ships diesel engines with mechanically controlled direct fuel injection and turbocharged, were used.

Rational onboard engines operation consists in reparation or adjustment only in the case of observing markedly deviations of diagnostic signals from their nominal values. Such approach reduces operation cost, however, causes a significant increase of toxic compounds emissions and fuel consumption. For this reason, to introduce changes in the organization of marine engine operation, is necessary. However, the mentioned changes must be preceded by a determination of emission characteristics of toxic compounds for engines operating with malfunctions of functional systems.

It should be noted that relatively few results of experimental research concerning emission characteristics of marine diesel engines with mechanically controlled fuel injection, conducted in the past decade, are available. This is due to

high cost of the experiment. It should be noted that main propulsion engines generate nominal power of about 5 to 20 MW, and electric power generator engines of about 200 to 1000kW. Such large nominal power of engines causes fuel consumption measured in tons per hour.

Sarvi et al. [4], [5], [6] present emission characteristics of a large, medium-speed diesel engine with parameters similar to those of marine engines. Desantes et al. [7], [8] show influence of fuel injection characteristics on emission characteristics and parameters of combustion in one-cylinder engine. Weiser, in his doctorate thesis [9] presents results of direct measurements on 9-cylinder medium-speed engine, and Cooper [10] presents emission characteristics from chosen ships. More detailed data about the influence of fuel injection pressure are available from [12] and [13]. Both the studies present optical measurements of fuel spray process in engine cylinder by schlieren? photography technique and particle image velocimetry. Kyriakides et al. [14] present a model of heavy fuel spray atomization for marine diesel engine, and Danov [15] presents a model describing combustion parameters in a large marine diesel engine.

Lack of new research activities concerning the impact of marine diesel engine malfunctions on emissions induced this author to undertake research on the issue. This paper presents the results of laboratory tests on the effects of selected fuel injector malfunctions on the level of emission. The fuel injector malfunctions are obtained by decreasing and increasing the opening pressure of the fuel injector and using the injector with decalibrated and clogged holes.

LABORATORY TEST STAND AND PROCEDURE

The study were carried out by using an AL25/30 Cegielski-Sulzer marine, 3-cylinder, four-stroke, direct - injection diesel engine with an intercooler system, installed in the Laboratory of Internal Combustion Engines, Gdynia Maritime University. The engine was loaded with a generator electrically connected to the water resistance and supercharged by a VTR 160 Brown-Boveri turbocharger. During the tests the engine was fuelled with diesel oil of the properties presented in Tab.1, and operated at the constant speed equal to 750 rpm. The fuelling system of the engine consisted of a Bosch mechanically - controlled fuel pumps connected to injectors with multi-hole nozzles. This type of engine is commonly used as a electric power generator or main propulsion system with controllable pitch propeller [11]. Engine load and speed, parameters of the turbocharger, systems of cooling, fuelling, lubricating, and air exchange, were measured. The composition of exhaust gas was also recorded by using electrochemical gas analyzer with infrared carbon dioxide sensor. Air pressure, temperature and humidity were also recorded by laboratory equipment. All the mentioned results were recorded with one-second sampling time. Injection and combustion pressures in all cylinders of the engine were also recorded. A schematic diagram of the laboratory test stand is presented in Fig.1. Values of the most important engine parameters are given in Tab.2.

Tab.1 Diesel fuel oil properties

| Parameter | Value | Unit |
|-----------------------------|-------|--------------------|
| Density at 15°C | 827,3 | kg/m ³ |
| Kinematic viscosity at 40°C | 2,636 | mm ² /s |
| Cetane number | 53,2 | – |
| Sulfur content | 3,8 | mg/kg |

Tab.2. Parameters of the AL25/30 engine

| Parameter | Value | Unit |
|---------------------|-------|------|
| Max. electric power | 250 | kW |
| Rotational speed | 750 | rpm |
| Cylinder number | 3 | – |
| Cylinder diameter | 250 | mm |
| Stroke | 300 | mm |
| Compression ratio | 12,7 | – |

The experimental study consists of 5 stages, of 3 observations each, at different simulated malfunctions of the fuel injector installed in 2nd cylinder of the engine. During each start of observation, the engine was loaded up to the maximum load equal to 250kW measured as an electric power of the generator, and, after stabilization of exhaust gas temperature behind the turbine, engine operating parameters were recorded for 3 to 5 minutes. During this time, injection and combustion pressures in all cylinders of the engine were recorded for 16 full turnover of engine shaft with intervals equal to 0,5°.

Then the load of the engine was decreased by 10 kW, and after stabilization of exhaust gas temperature behind the turbine, engine operating parameters were recorded again. The observation was continued with loads up to 50 kW at a constant speed. The engine did not work under the load of 190 kW due to resonance vibrations. Stages of experiment were set as follows:

- 1st stage - during operation of the engine assumed as “working properly”,
- 2nd stage - during operation of the engine with opening pressure decreased to 15MPa,
- 3rd stage - during operation of the engine with opening pressure increased to 35MPa,
- 4th stage - during operation of the engine with a nozzle with 8 holes of 0,375mm diameter,
- 5th stage - during operation of the engine with a nozzle with 2 , out of 9, neighboring holes clogged.

Values of the parameters of fuel injector in 2nd cylinder are presented for the considered stages in Tab.3.

Tab.3. Parameters of fuel injector in 2nd cylinder

| Parameter and unit | Stage | | | | |
|------------------------|-------|-------|-------|-------|-----------|
| | 1 | 2 | 3 | 4 | 5 |
| Number of holes | 9 | 9 | 9 | 8 | 9 – 2 = 7 |
| Hole diameter [mm] | 0,325 | 0,325 | 0,325 | 0,375 | 0,325 |
| Opening pressure [MPa] | 25 | 15 | 35 | 25 | 25 |

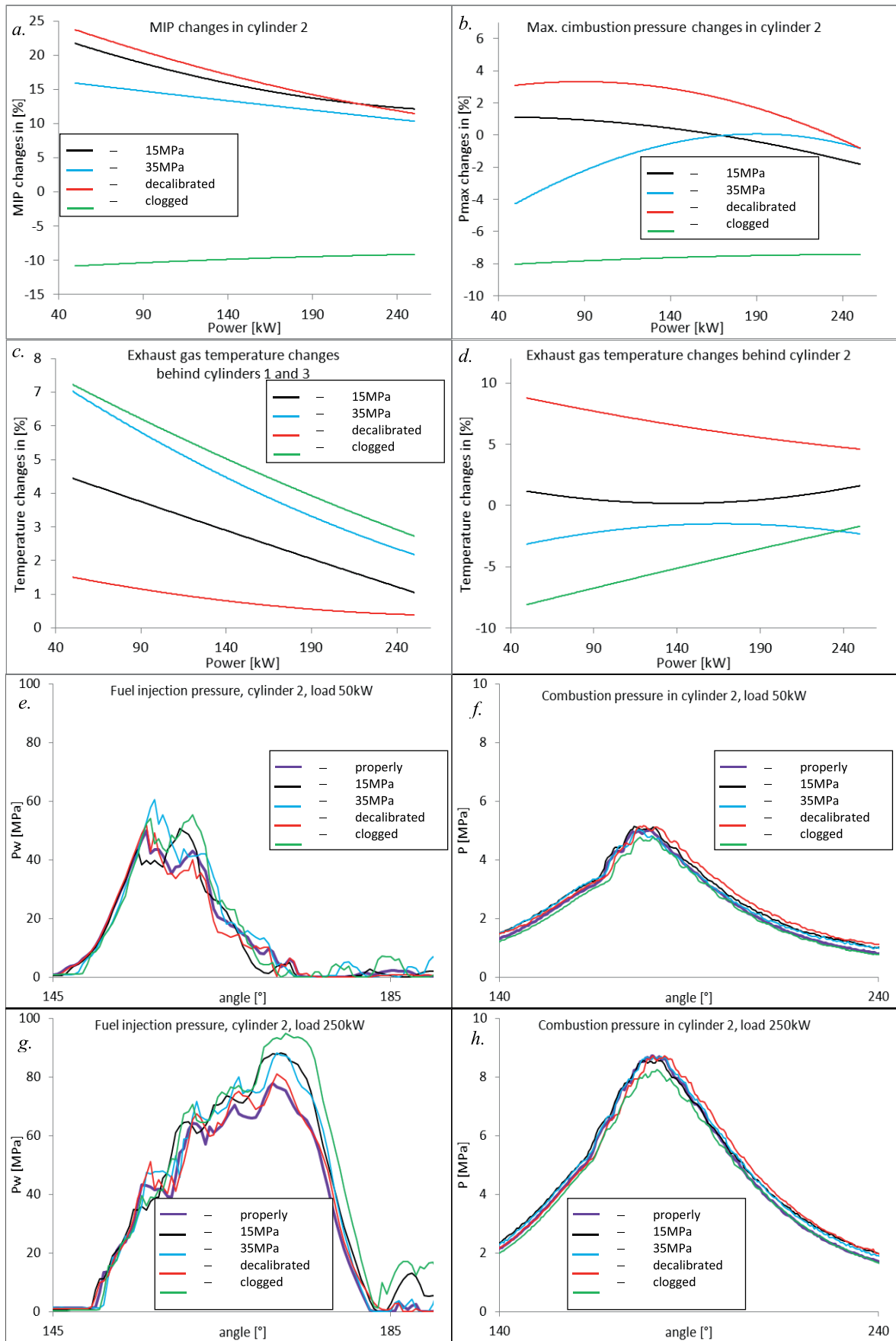


Fig.2. Changes in thermodynamic parameters of gas mixture in engine cylinders

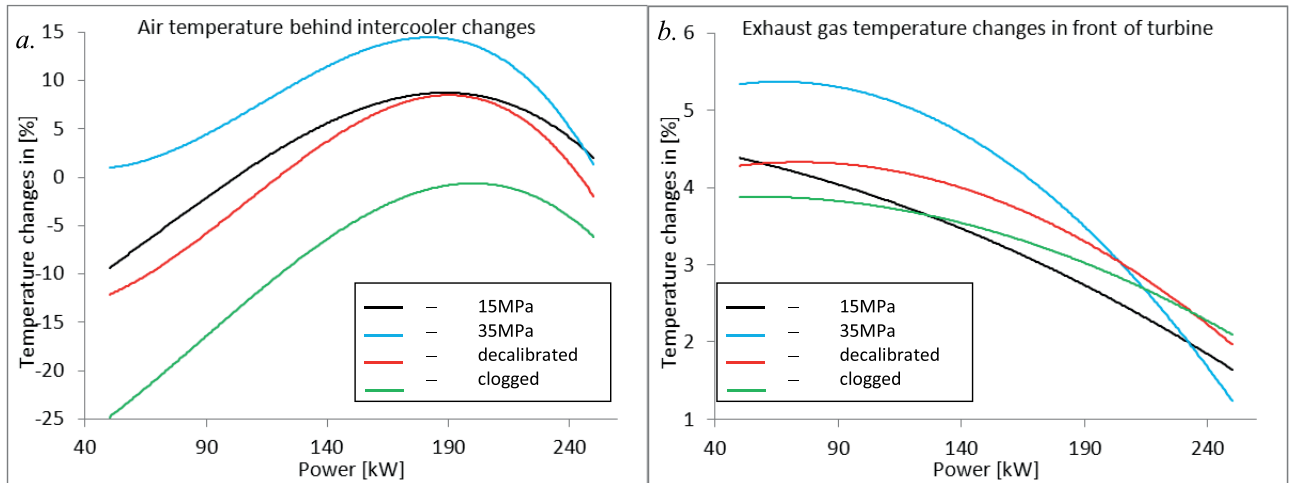


Fig.3. Changes in thermodynamic parameters of air and exhaust gas

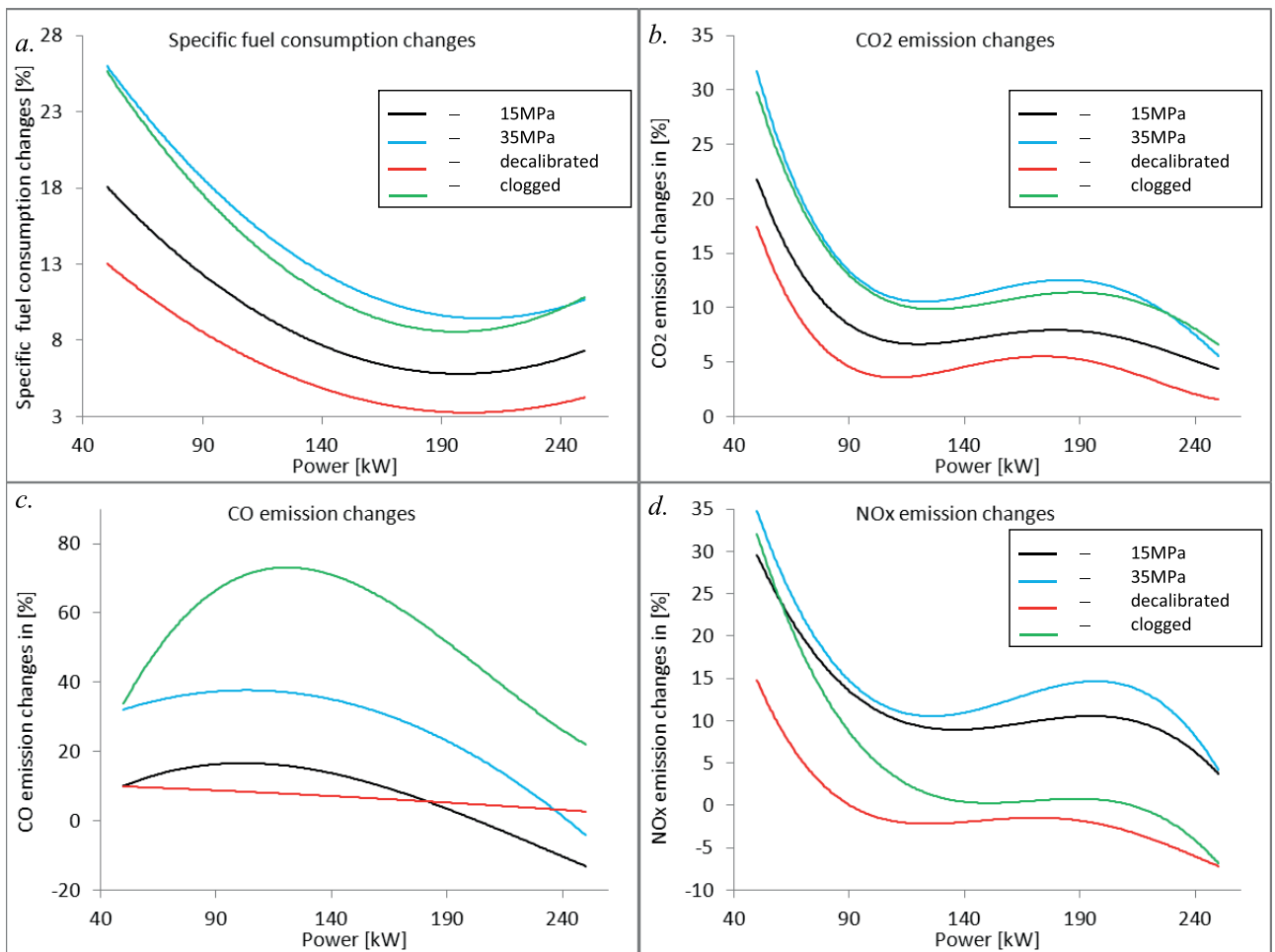


Fig.4. Changes in specific fuel consumption and emission characteristics

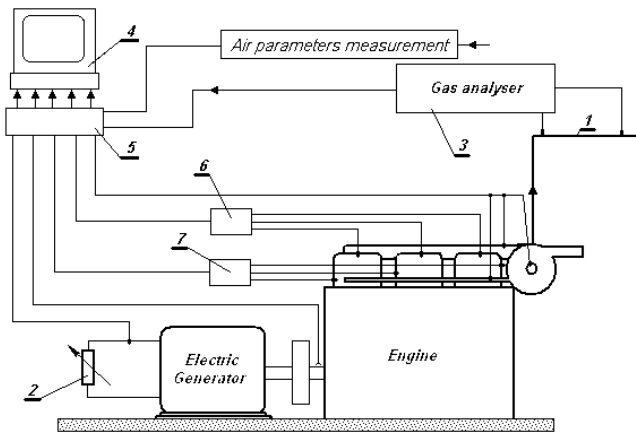


Fig.1. Schematic diagram of the laboratory test stand:
 1 - exhaust duct, 2 - water resistance, 3 - gas analyzer, 4 - computer, 5 - A/C converter, 6 - combustion pressure indicator, 7 - injection pressure indicator

RESULTS AND DISCUSSION

Fig.2, 3 and 4 present the results of the laboratory study. Fig.2 presents pressure and temperature changes of fuel and combustion mixture in engine cylinders.

Fig.3 presents changes in thermodynamic parameters of air and exhaust gas, and Fig.4 presents changes in fuel consumption and emission characteristics. All the mentioned changes in parameters were compared to those of the engine recognized as “working properly”. Emission characteristics were obtained from laboratory measurements and calculations according to ISO 8178 regulations [16]. All the presented results are mean values achieved from the performed observations.

DECREASED OPENING PRESSURE OF FUEL INJECTOR

The second stage of the experimental study is based on the reduction of the static opening pressure of fuel injector at 2nd cylinder in accordance to the values presented in Tab.2. Such malfunction can be caused by damage of the fuel injector spring.

Average values of the results obtained for this stage of the study are represented by black lines. Fig.2e and Fig.2g present average values of fuel injection pressure characteristics for 48 full rotations of engine shaft, the fuel pressure increase along with the progress of the fuel injection process. The results are obvious and consistent with results presented e.g. in [17]. It should be noted that in the case of the operation of the “working properly” engine (violet line) at low loads, fuel pressure is larger at the start of the injection process. An increase of fuel pressure leads to the increase of the fuel reach in the cylinder and the reduction of the average diameter of injected fuel droplets [18], [19]. In the case of low engine load the phenomena are not desirable due to the low concentration of fuel vapour in cylinder volume. Injection pressure drop causes slight lengthening of the combustion process in the engine at large loads. According to the results presented in Fig.2a and Fig.2b, the injection pressure decrease does not

cause significant change of maximum combustion pressure. Extension of the combustion process increases the mean indicated in-cylinder pressure (MIP) by 20% at low loads. According to the data presented in Fig.2c and Fig.2d, the decrease of the opening pressure in fuel injector does not change the temperature of the exhaust gas behind the 2nd cylinder, however, it increases temperature of the exhaust gas from other cylinders. For this reason mean temperature of exhaust gas in front of the turbine (Fig.3b) slightly increases. As a result, the amount of energy supplied to the turbine also increases. This causes supplying larger amount of air to the cylinders. A drop of the air temperature at low engine loads presented in Fig.3a, promotes delivering more air into the cylinders. These phenomena are correlated with an increase of fuel droplets reach in the cylinder and deteriorate combustion conditions. The effect of this is a significant increase of fuel consumption (Fig.4a) by up to 18%. The increase of the amount of air and fuel causes the exhaust gas amount to increase. In Fig.4b, Fig.4c and Fig.4d changes of the engine emission characteristics are presented. According to the presented results the increase of the fuel consumption at low engine loads also causes 20% increase of carbon dioxide (CO₂) emission.

There is also the increase of nitric oxides (NO_x) emission by 30% at low engine loads. This is due to the increase of combustion temperature in other cylinders and the increase of the amount of air supplied to the engine.

According to the presented results a drop of fuel injector opening pressure on one of the cylinders is clearly visible only during the engine operation at low loads.

The mentioned malfunction causes significant increase in fuel consumption and the increase in amount of CO₂ and NO_x emission.

INCREASED OPENING PRESSURE OF FUEL INJECTOR

In the 3rd stage of the laboratory research the static opening pressure of the fuel injector on the 2nd cylinder, was increased. Such malfunction may be caused by improper adjustment of the fuel injector spring. Changes of engine operating parameters for the “working properly” engine are presented in blue in the graphs. According to Fig.2e and Fig.2g the considered malfunction causes the increase of fuel injection pressure during whole injection process in all considered engine loads. Fuel injection time is slightly longer too. The obtained results are consistent with [20] and [21]. It causes a fuel consumption increase (Fig.4a) especially at low engine loads. It should be noted that the increase of fuel consumption is in this case the largest among all considered engine malfunctions.

The effect of this is 10-15% MIP increase at all considered engine loads (Fig.2a). According to the data presented in Fig.2, the increase of the opening pressure of fuel injector causes a slight drop of the maximum combustion pressure for engine at low loads and a slight decrease in temperature of the exhaust gas from the 2nd cylinder.

The temperature increase of exhaust gas from other engine cylinders, particularly apparent at low engine loads, is visible.

As for the case of fuel injector opening pressure drop, the temperature of exhaust gas in front of turbine increases (Fig.3b).

The result of the simulated malfunction is a combustion deterioration manifested by an increased carbon monoxide (CO) emission by up to 40% for the engine operating at partial loads (Fig.4c). According to the results presented in Fig.4a, the increase of the opening pressure of the fuel injector causes a 10-25 % increase of the fuel consumption and a 5-30 % increase of the CO₂ emission (Fig.4b). The result of the increase of the fuel consumption is qualitatively consistent with the results presented in [22].

The deterioration of the combustion process in a damaged cylinder and the change of the performance characteristics of the other cylinders can cause a combustion temperature increase, which is manifested by the increase of the NO_x emissions (Fig.4d).

The considered malfunction can be recognized in practice, during onboard operation, by measuring the CO, CO₂ and NO_x emissions at low engine loads. The described malfunction causes a fuel consumption increase at all considered engine loads.

DECALIBRATED FUEL INJECTOR HOLES

During this stage of the experimental study the fuel injector nozzle in the 2nd cylinder was changed. The changed injector nozzle parameters are presented in Tab.2. The change results in the increase of the summary cross section area of nozzle holes by 18.3%. The results obtained in the stage are represented by the red line. The expected result should be a reduction of the fuel injection time, resulting from the increase of the cross section area of nozzle holes and the increase of the average droplet diameter of injected fuel [22]. According to the values presented in Fig.2e and Fig.2g, the characteristic of the fuel injection pressure experiences no significant change. This is probably due to the insufficient change in diameter of the injector holes. According to the results given in Fig.2f and Fig.2h, the increase of the mean diameter of the fuel droplets causes the increase of combustion time. The result of this is MIP increase by 14-23 % (Fig.2a) for small changes of the maximum injection pressure (Fig.2b). The abnormal shape of the fuel injection increases fuel consumption, but only at the low engine loads (Fig.4a). The increase of the mean fuel droplet diameter increases the fuel evaporation time, which may cause the combustion temperature to increase. The evidence of this situation is an increase in NO_x emission (Fig.4d). The presented temperature changes and longer combustion time make the exhaust gas temperature increasing behind the 2nd cylinder too (Fig.2d). The effect of the fuel consumption increase and the increase of the exhaust gas temperature behind the 2nd cylinder is a slight increase of the exhaust gas temperature in front of the turbine, which is a similar result to those obtained in the 2nd and 3rd stage of the research (Fig.3b).

The presented malfunction causes a CO₂ emission increase at low engine loads (Fig.4b). This is a direct consequence of the fuel consumption increase. It should be noted that

a decalibration of the fuel injector holes does not cause any significant changes in the CO emission characteristics (Fig.4c).

From the assessment of the onboard engine operation it can be concluded that the presented change of the fuel injector parameters causes a significant increase of the exhaust gas temperature behind the cylinder, the increase of NO_x and CO₂ emissions and of the fuel consumption. The results are clearly visible in the low engine load conditions.

CLOGGED FUEL INJECTOR HOLES

The last considered malfunction is clogging the neighboring 2, out of 9, holes of the fuel injector nozzle on the 2nd cylinder. The "baking" of the injector nozzle holes is a common malfunction in onboard operational practice. The average results for this malfunction are represented by green lines.

The clogging of the injector nozzle causes, according to the data presented in Fig.2e and Fig.2g, the decrease of the summary cross section area of the fuel injector holes. The effect of this is the increase of the fuel injection pressure and the extension of time of the fuel injection into the cylinder. The increase of the fuel injection pressure causes a drop of mean diameter of the fuel droplets [18], [19] and the increase of the fuel richness in the cylinder [17]. It should be pointed out that by clogging 2 neighboring holes of the fuel injector some areas of the combustion chamber are left with a fuel deficiency. According to the results from Fig.2a and Fig.2b, it causes 10% MIP decrease and 8% decrease of the maximum combustion pressure at all considered loads of the engine.

The effect of the decreased combustion pressure is clearly visible in Fig.2f and Fig.2h too. Inaccurate fuel and air mixing is a cause of an incomplete combustion in cylinder. According to the results given in Fig.4c it causes even 70% increase of the CO emission. The result of an insufficient combustion is a drop of the exhaust gas temperature behind the cylinder (Fig.2d), which is visible especially at low engine loads. Power deficiency in the 2nd cylinder must be compensated by the load increase in the other cylinders. Therefore, the temperature of the exhaust gas from the other cylinders increases (Fig.2c) and the temperature in front of turbine increases too (Fig.3b). Abnormal combustion in the 2nd cylinder is also a cause of a fuel consumption increase. According to the results presented in Fig.4a, even 25% increase of fuel consumption at low engine load conditions, followed. Similarly to the previously described cases of malfunction, also in this case a fuel consumption increase results in the increase of CO₂ emissions (Fig.4b). The considered malfunction also increases NO_x emissions at the low engine loads, which is caused by the increase of the combustion process temperature behind the 2nd cylinder and the increase of the fuel consumption. According to the results given in Fig.4d, the engine operation at high loads effects in 5% decrease of the NO_x emission. The reasons for this should be sought in operation of the other engine cylinders at higher loads. Increased loads result in the reduction of the NO_x emission.

The discussed malfunction increases fuel consumption and decreases combustion pressure at all considered engine loads. The emission measurements show even 70% increase of CO emission at medium engine loads and about 30% increase of CO₂ and NO_x emissions at low engine loads.

CONCLUSIONS

As a result of the experimental study the following conclusions can be drawn:

1. The decrease of the static opening pressure of the fuel injector in one of the engine cylinders is clearly visible only at low engine loads conditions. The malfunction causes the increase of CO₂ and NO_x emission and significantly small changes of CO emission.

2. The increase of the static opening pressure of the fuel injector in one of the engine cylinders causes the increase of the emissions of the measured gaseous compounds, qualitatively similar to that in the case of the engine operation with the decrease of the static opening pressure of the fuel injector.

3. The increase of the cross-section area of the fuel injector holes in one of the engine cylinders causes the increase of the exhaust gas temperature behind the cylinder with such malfunction and slight temperature fluctuations of the exhaust gas from the other engine cylinders. Emission measurements demonstrated only small changes of the CO emission and a decrease of the NO_x emission at high engine load conditions.

4. Clogged fuel injector holes cause the decrease of the combustion pressure in all considered loads of the engine. Emission measurements demonstrated the increase of the CO emission even by up to 70% at medium engine loads and the increase of the CO₂ and NO_x emission at low engine loads, by up to 30%.

ACKNOWLEDGMENTS

The project was financially supported by the National Science Centre of Poland (a grant based on the decision No. DEC-2011/01/D/ST8/07142)

BIBLIOGRAPHY

1. Revised Marpol Annex VI. Regulations for the Prevention of Air Pollution from Ships. Resolution MEPC.176(58). International Maritime Organization, 2008
2. Technical Code on Control of Emission of Nitrogen Oxides from Marine Diesel Engines. Resolution MEPC.177(58). International Maritime Organization, 2008
3. The world merchant fleet in 2011. Statistics from Equasis, 2012

4. A. Sarvi, C. J. Fogelholm, R. Zevenhoven: Emissions from large-scale medium-speed diesel engines: 1. Influence of engine operation mode and turbocharger, Fuel processing technology 89 (2008), pp. 510 ÷ 519
5. A. Sarvi, C. J. Fogelholm, R. Zevenhoven: Emissions from large-scale medium-speed diesel engines: 2. Influence of fuel type and operating mode, Fuel processing technology 89 (2008) , pp. 520 ÷ 527
6. A. Sarvi, R. Zevenhoven, Large-scale diesel engine emission control parameters, Energy 35 (2010), pp. 1139 ÷ 1145
7. J.M. Desantes, J. Benajes, S. Molina, C.A. Gonzalez: The modification of the fuel injection rate in heavy-duty diesel engines. Part 1: Effects on engine performance and emissions, Applied Thermal Engineering 24 (2004) , pp. 2701÷2714
8. J.M. Desantes, J. Benajes, S. Molina, C.A. Gonzalez: The modification of the fuel injection rate in heavy-duty diesel engines. Part 2: Effects on combustion, Applied Thermal Engineering 24 (2004), pp. 2715÷2726
9. G.A. Weiser: Modelling of Combustion and Nitric Oxide Formation for Medium-Speed DI Diesel Engines: A Comparative Evaluation of Zero- and Three-Dimensional Approaches, Doctors Thesis, Swiss Federal Institute of Technology Zurich, 2001
10. D.A. Cooper: Exhaust emissions from ships at berth, Atmospheric Environment 37 (2003) , pp. 3817÷3830
11. J. Carlton: Marine Propellers and Propulsion , Third Ed., Elsevier Ltd., 2012
12. W. Xiangyi, X. Feng, L. Wang: Experimental Study on Characteristics of Conical Spray and Combustion for Medium Speed D.I. Diesel Engine, SAE Technical Paper 930598, 1993, doi:10.4271/930598
13. T. Sarjovaara, H. Hillamo, M. Larimi, T. Olenius: Optical In-Cylinder Measurements of a Large-Bore Medium-Speed Diesel Engine, SAE Technical Paper 2008-01-2477, 2008, doi:10.4271/2008-01-2477
14. N. Kyriakides, C. Chryssakis, L. Kaiktsis: Influence of Heavy Fuel Properties on Spray Atomization for Marine Diesel Engine Applications, SAE Technical Paper 2009-01-1858, 2009, doi:10.4271/2009-01-1858
15. S. Danov, A. Gupta: Effect of Sauter Mean Diameter on the Combustion Related Parameters in a Large-Bore Marine Diesel Engine, SAE Technical Paper 1999-01-0224, 1999, doi:10.4271/1999-01-0224
16. ISO8178regulation. International Organization of Standardization

17. J. B. Heywood: Internal Combustion Engine Fundamentals, McGraw-Hill, 1988
18. C. D. Rakopoulos, E. G. Giakoumis: Speed and load effects on the availability balances and irreversibilities production in a multi-cylinder turbocharged diesel engine, Applied Thermal Engineering 17 (1997), pp. 299÷313
19. C. D. Rakopoulos, E. G. Giakoumis: Simulation and analysis of a naturally aspirated IDI diesel engine under transient conditions comprising the effect of various dynamic and thermodynamic parameters, Energy Conversion and Management 39 (1998) pp. 465÷484
20. J.M. Desantes, J. Benajes, S. Molina, C.A. Gonzalez: The modification of the fuel injection rate in heavy-duty diesel engines. Part 1: Effects on engine performance and emissions, Applied Thermal Engineering 24 (2004) , pp. 2701÷2714
21. J.M. Desantes, J. Benajes, S. Molina, C.A. Gonzalez: The modification of the fuel injection rate in heavy-duty diesel engines Part 2: Effects on combustion, Applied Thermal Engineering 24 (2004), pp. 2715÷2726
22. I. Celikten: An experimental investigation of the effect of the injection pressure on engine performance and exhaust emission in indirect injection diesel engines, Applied Thermal Engineering 23 (2003), pp. 2051÷2060
23. K. K. Kuo: Principles of combustion. John Wiley, 2005

CONTACT WITH THE AUTHOR

Jerzy Kowalski

Gdynia Maritime University
 Department of Engineering Sciences
 Morska 81-87 Street
 81-225 Gdynia
 Poland

tel.: +48 58 6901331

fax: +48 58 6901399

e-mail: jerzy95@am.gdynia.pl

PROBLEMS OF EQUIVALENT LOAD AMPLITUDE IN FATIGUE LIFE CALCULATIONS

Bogdan Ligaj, Assoc. Prof.

Robert Sołtysiak, Ph. D.

University of Technology and Science in Bydgoszcz, Poland

ABSTRACT

This paper presents issues of fatigue life calculations in operational load conditions. The assumed runs were so processed as to get a set of sinusoidal cycles by using the following methods: full cycles counting method and rainflow counting method. On the basis of such sets of cycles of the varying parameters S_{mi} and S_{ai} were prepared block load spectra of equivalent amplitudes S_{az} , obtained with the use of an original method of these authors, in which two-parameter fatigue characteristics were applied. The work resulted in comparison of fatigue life results for load spectra determined by using the assumed cycles counting methods and the assumed two-parameter fatigue characteristics: the model IM, model II, model III and model IV, respectively.

Keywords: operational load, equivalent load amplitude, two-parameter fatigue characteristics, fatigue life

INTRODUCTION

One of choice criteria for design features of machine parts are calculations in the area of material fatigue, dealing with range of fatigue life estimation in random load conditions. According to theory of stochastic processes, operational loads can be numbered among a group of either narrow or broad spectrum. Essential differences in fatigue life between the above mentioned loads deal with participation of cycles from a given range of values of the stress ratio R and occurrence of cycles of large amplitude values (where the maximum amplitude $S_a \approx S_{max}$).

Fatigue life calculations for narrow spectrum loads are executed with the use of block load spectra (the spectra 1D) prepared on the basis of sets of cycles determined by means of one of the cycles counting methods: peak counting method, simple-range counting method, full cycles counting method, range-pair counting method and rainflow counting method. In [2] it was stated that choice of a cycles counting method for loads of the type does not significantly impair results of fatigue life calculations carried out with application of the fatigue characteristics $N(S_a)$ (the characteristics 1D).

In the case of broad spectrum loads, execution of fatigue calculations is based on load spectra which describe variability of the cycle parameters S_{mi} and S_{ai} , exemplified by correlation tables expressed in S_a-S_m or $S_{min}-S_{smax}$ reference system (the spectra 2D). To apply spectra of the type is necessary as in the load occur cycles of stress ratio from the range $-\infty < R < 1$ and they impact fatigue life [4]. Choice of a cycles counting method is an important element of preparation of the load spectra 2D. Out of the known methods [2, 3], the peak counting method is not advised for preparation of broad

spectrum loads because it leads to the most unfavourable load conditions which make calculated fatigue life underestimated in comparison to experimental results. Other, above mentioned cycles counting methods are considered advisable for preparation of loads of the type. In fatigue life calculations the two-parameter fatigue characteristics $N(S_a, S_m)$ are used, that allows to take into account influence of cycles of a given value of the stress ratio R on fatigue life.

This work is aimed at comparison of results of fatigue life calculation obtained for the load spectra prepared with the use of the selected cycles counting methods as well as the two-parameter fatigue characteristics. The calculations have been carried out by means of the equivalent load spectra of a block form, produced on the basis of the two-parameter fatigue characteristics described in the subject-matter literature as: the model IM, model II, model III and model IV.

This work contains characteristics of operational loads which make it possible to assess load spectrum breadth as well as to conduct counting the cycles by means of the following methods: the full cycles counting method (FCM) and the rainflow counting method (RFM) [2, 3]. The produced load spectra 2D have been converted into block spectra 1D on the basis of which fatigue life has been determined. Results of the calculations have been subjected to a comparative analysis allowing to formulate final conclusions.

OPERATIONAL LOAD

In Fig. 1 are presented runs of stress changes in a structural element, which were recorded in operational load conditions. Because they are intended for application to fatigue life calculations they are given in the relative form S_i/S_{max} where

S_{max} stands for maximum value of stress change occurring in a load run.

A cursory analysis of the assumed runs reveals significant differences concerning frequency of load changes as well as occurrence of cycles with large amplitude values. An analysis of static and dynamic load components has been conducted on the basis of statistical parameters, i.e. mean and variance. Their values are presented in Tab. 1. For the assumed runs the mean value is close to zero (Tab. 1, col. 2), however variance values show differences between runs. It implies a different form of loads in the range of amplitudes of cycles covered by their content.

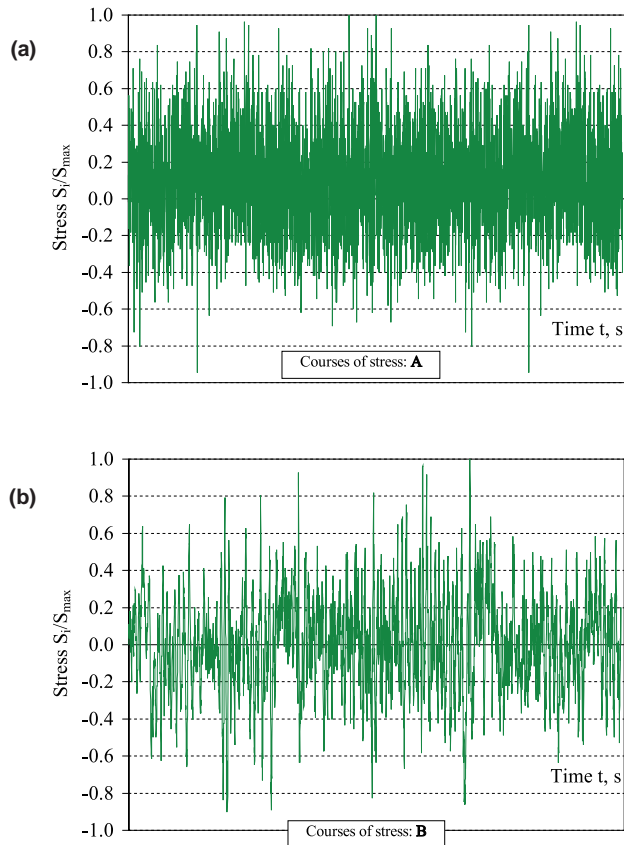


Fig. 1. Fragments of runs (courses) of stress changes in the form of the relative values S_i/S_{max}

Tab. 1. Values of the selected statistical parameters of the load S_i/S_{max}

| Load run | Statistical parameter | | | |
|----------|-----------------------|----------|----------|----------|
| | Mean | Variance | Skewness | Kurtosis |
| 1 | 2 | 3 | 4 | 5 |
| A | -0.0026 | 0.1400 | 0.0600 | -0.7406 |
| B | 0.0160 | 0.0780 | -0.0748 | 0.2775 |

Values of skewness and kurtosis are also given in Tab. 1. Skewness represents a degree of asymmetry of a distribution around its mean, and kurtosis determines a relative peak or flat form of a distribution in relation to normal distribution [1]. Therefore on the basis of the presented results (Tab.1, col. 4 and 5) as well as of an analysis of values in load runs (not given in this paper due to its restricted volume) it can be assumed that the distribution of values in the runs is close to normal.

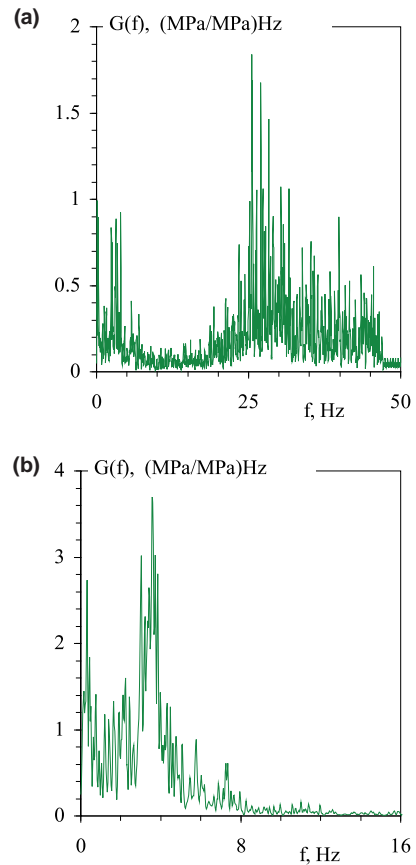


Fig. 2. Spectral power density for runs of S_i/S_{max} loads: a - the run A, b - the run B

A complex frequency structure of the analyzed load runs is illustrated by spectral power density function diagrams shown in Fig. 2. The range of significant frequencies for the run A is $0 < f < 47$ Hz, and for the run B - $0 < f < 12$ Hz. The observed differences in frequency structure and values of variance (being a measure of stress amplitudes) of load runs are connected with excitation factors which occur during operation. The analyzed load runs can be numbered among the group of broad-spectrum loads, that is implied by a characteristic form of the diagrams of spectral power density functions.

Another way of assessing the load spectrum breadth which does not require using a complex statistical analysis, is to determine value of the factor I expressed as follows:

$$I = \frac{N_i}{N_e} \quad (1)$$

In Eq. (1) N_i is number of intersections of mean value level by increasing and decreasing half-cycles, and N_e is number of local extrema occurring in a run (sum of minimum and maximum values). The method is described in [5]. The determined values of I-factor are the following: for the run A - $I_A = 0.8411$, for the run B - $I_B = 0.3828$. On this basis the assumed load runs can be numbered among the group of broad-spectrum loads. The conclusion is in line with that resulting from statistical analysis.

BLOCK SPECTRUM OF LOADS

Load runs were subjected to a procedure of determining the set of sinusoidal cycles.

The following cycles counting methods were assumed: full cycles counting method (FCM) and rainflow counting method (RFM) [2, 3].

The determined data sets contained sinusoidal cycles of the parameters S_{ai}/S_{max} and S_{mi}/S_{max} from the range of the stress ratio $-\infty < R < 1.0$, that is characteristic for broad -spectrum loads. Based on the collected data, were prepared the cycles sets having $S_m = 0$ and the equivalent amplitude S_{azi} determined on the basis of two-parameter fatigue characteristics.

METHOD FOR DETERMINING THE EQUIVALENT LOAD SPECTRA

For determining the equivalent amplitude S_{azi} the

two-parameter fatigue characteristics (TFC) is used. For purposes of this work the two-parameter fatigue characteristics called :

the model IM (Fig.3a) [6], model II (Fig.3b) [6], model III (Fig.3c) [6] and model IV (Fig.3d) [6] were used. The method for determining the equivalent amplitude S_{azi} consists in determining a line of constant fatigue life ($N = \text{const}$) for an arbitrary sinusoidal load cycle of the parameters S_{mi} and S_{ai} (the point G in Fig.3), by using the two-parameter fatigue characteristics. The point G is interpolated to the point of intersection of the constant fatigue life line and the axis of ordinates of the TFC coordinate frame (the point C) for which the mean stress value is equal to $S_m = 0$. In this way the equivalent load cycle of the stress ratio $R = -1$ was determined. It should be stressed that all load cycles located on the constant fatigue life line ($N = \text{const}$) have the same equivalent amplitude S_{azi} regardless of in which TFC zone they are located.

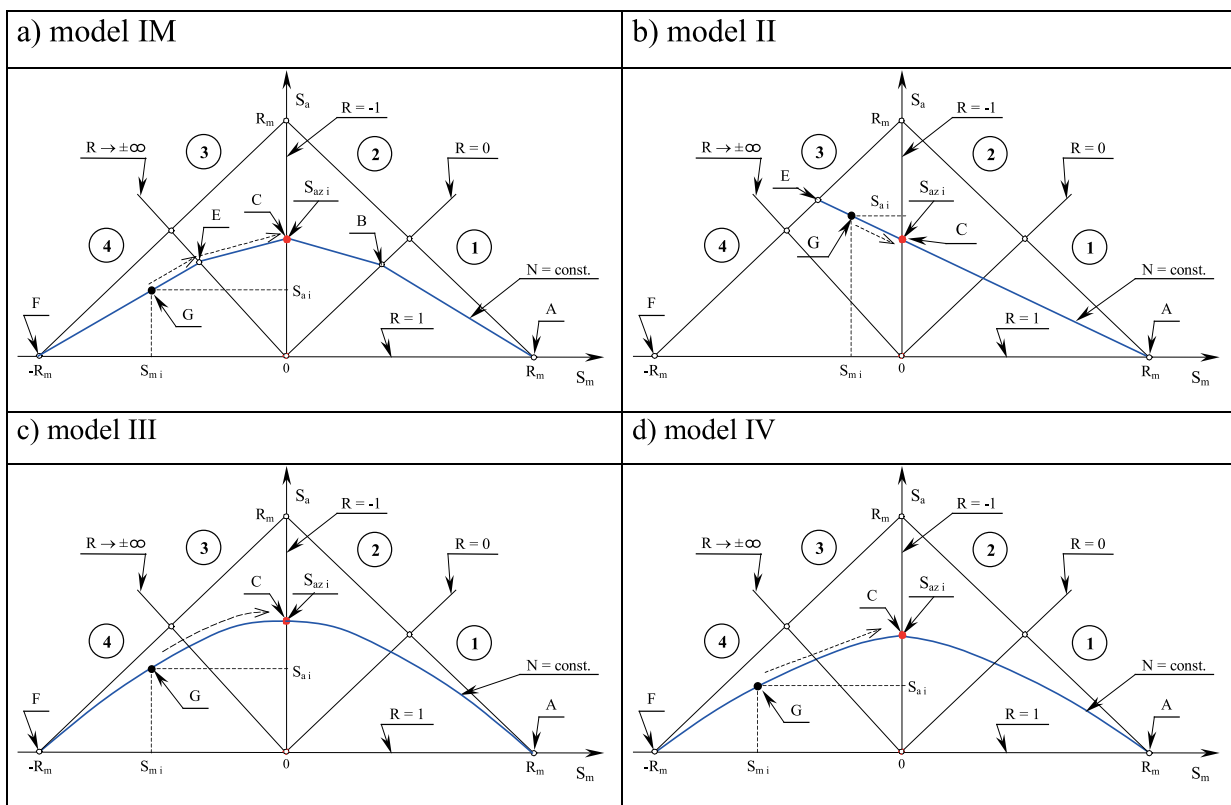


Fig. 3. Schematic presentation of the mathematical models of TFC characteristics : a - model IM [6], a - model II [4], c - model III [4], d - model IV [4]

The model IM of the two-parameter fatigue characteristics (Fig.3a) is a modified model I [6] which represents a generalization of the Serensen's limiting stress diagram over the HCF and LCF ranges. In Fig 3, figures 1 through 4 stand for the variability ranges of the cycle stress ratio R. Form of the expression describing the constant fatigue life lines ($N = \text{const}$) for particular TFC zones is as follows :

- zone 1

$$N = N_0 \left[\frac{S_{f(-1)} \cdot (R_m + S_{a(R)}^{(T)} - S_{m(R)}^{(T)})}{S_{a(R)}^{(T)} \cdot R_m \cdot (1 + \psi_N)} \right]^{m(-1)} \quad \text{for } 0 < R < 1 \quad (2)$$

- zone 2

$$N = \frac{N_0 \cdot (S_{f(-1)})^{m(-1)}}{(S_{a(R)}^{(T)} + \psi_N \cdot S_{m(R)}^{(T)})^{m(-1)}} \quad \text{for } -1 \leq R \leq 0 \quad (3)$$

- zone 3

$$N = \frac{N_0 \cdot (S_{f(-1)})^{m(-1)}}{(S_{a(R)}^{(T)} - \psi_N \cdot S_{m(R)}^{(T)})^{m(-1)}} \quad \text{for } -\infty < R < -1 \quad (4)$$

- zone 4

$$N = N_0 \left[\frac{S_{f(-1)} \cdot (R_m + S_{a(R)}^{(T)} + S_{m(R)}^{(T)})}{S_{a(R)}^{(T)} \cdot R_m \cdot (1 + \psi_N)} \right]^{m(-1)} \quad (5)$$

for $1 < R < +\infty$

The model II [4] is a generalization of the Goodman's formula over the limiting fatigue life ranges LCF and HCF. The constant fatigue life line ACE corresponds to a constant fatigue life for sinusoidal load of varying parameters S_m and S_a contained in the range $-\infty < R < 1,0$. The mathematical model of the characteristics is of the following form:

$$N = N_0 \left[\frac{S_{f(-1)} \cdot (R_m + S_{a(R)}^{(T)} + S_{m(R)}^{(T)})}{S_{a(R)}^{(T)} \cdot R_m \cdot (1 + \psi_N)} \right]^{m(-1)} \quad (6)$$

The Gerber's mathematical model was applied to forming the model III [4] of the two-parameter fatigue characteristics. The constant fatigue life line ($N = \text{const}$) is described by the following formula:

$$N = N_0 \left[\frac{S_{f(-1)}}{S_{a(R)}^{(T)}} \left(1 - \left(\frac{S_{m(R)}^{(T)}}{R_m} \right)^2 \right) \right]^{m(-1)} \quad (7)$$

The model IV [4] was formed on the basis of ellipse equation describing the limiting stress line. The mathematical model of the characteristics is of the following form:

$$N = N_0 \left[\frac{S_{f(-1)}}{S_{a(R)}^{(T)}} \sqrt{1 - \left(\frac{S_{m(R)}^{(T)}}{R_m} \right)^2} \right]^{m(-1)} \quad (8)$$

BLOCK LOAD SPECTRA

By applying the above described method for determining the equivalent amplitudes S_{az} , block load spectra were determined for the assumed operational runs. It was based on sets of sinusoidal cycles produced by means of the assumed cycles counting methods. The applied two-parameter fatigue life characteristics were made for C45 steel with the following properties [7] in loading conditions:

- static ones: $E=211029\text{MPa}$, $R_m = S_y = 682\text{MPa}$, $R_c = S_u = 458\text{MPa}$,
- cycling ones : $m_{(-1)} = 9.80$, $C_{(-1)} = 1.054 \cdot 10^{29}$,
- $S_{f(-1)} = 223.5\text{MPa}$, $k = 0.1378$, $\psi_N = N^{-k}$.

The block load spectra used in fatigue life calculations were determined separately for each of the assumed values of S_{max} contained within the variability range: $200\text{MPa} \leq S_{\text{max}} \leq 600\text{MPa}$. Because of a limiting volume of this paper only the example block load spectra for $S_{\text{max}} = 400\text{MPa}$ are presented for the stress change runs marked: A (Fig.4) and B (Fig.5). In the below attached tables are additionally given values characteristic for the block load spectra: in tab. 2 – spectrum filling factor ζ , in Tab. 3 – values of maximum equivalent amplitudes $S_{az \text{ max}}$.

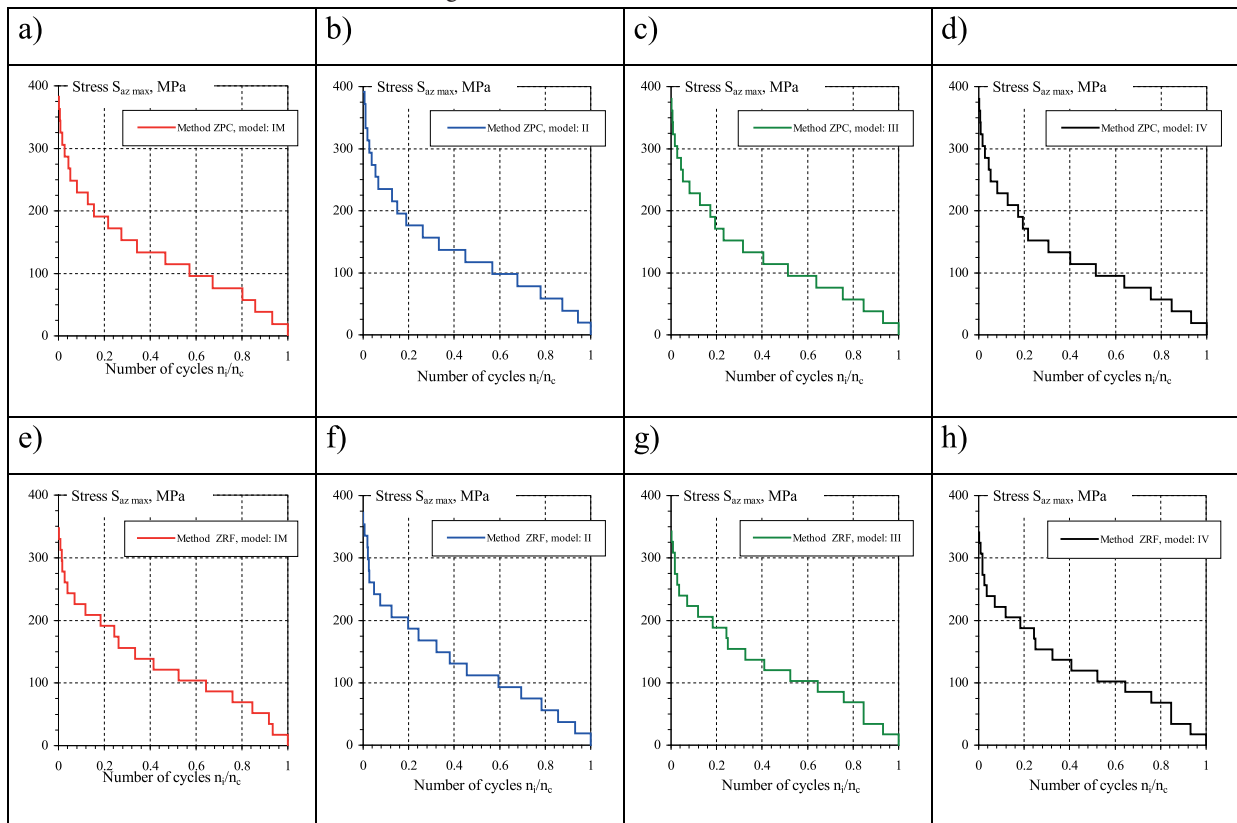


Fig. 4. Block load spectra for $S_{\text{max}} = 400\text{MPa}$, determined for the run A by using the following cycles counting methods: a-d – full cycles counting method (FCM), e-h – rainflow counting method (RFM)

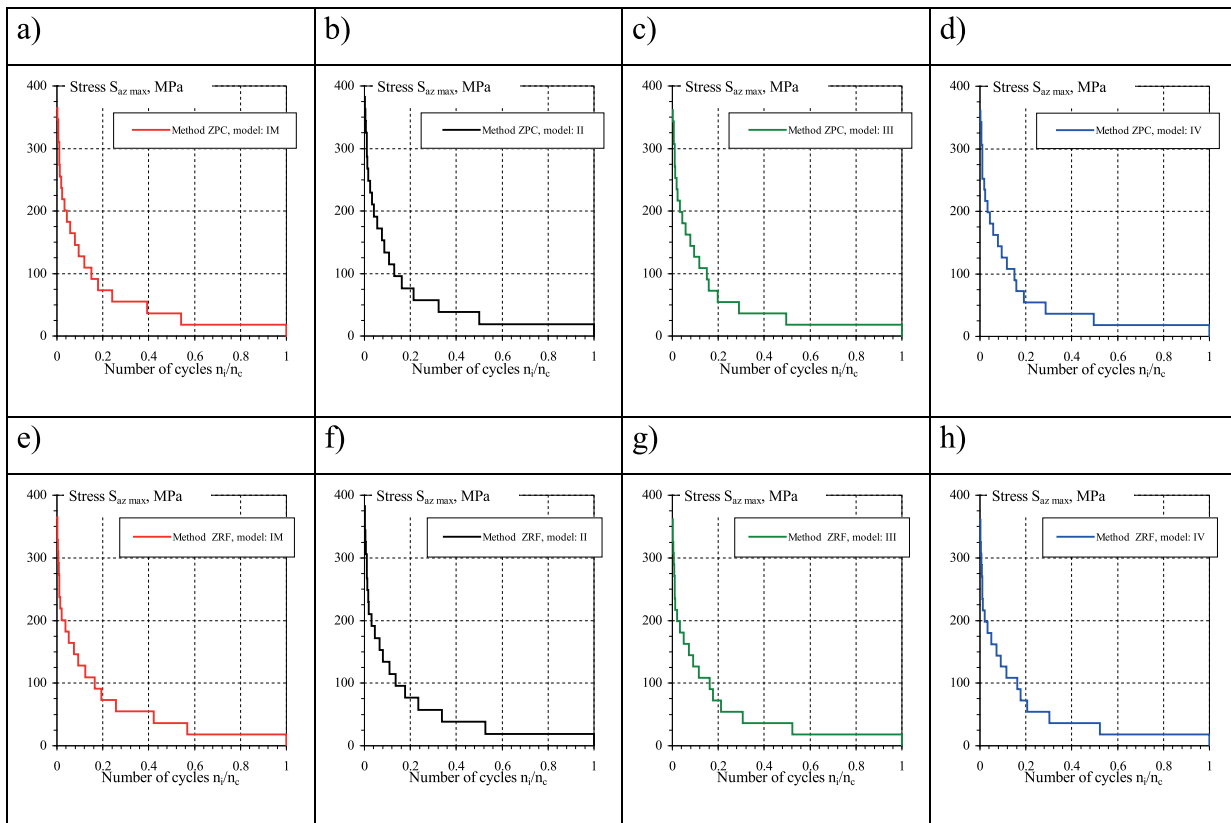


Fig. 5. Block load spectra for $S_{az\ max} = 400$ MPa, determined for the run B by using the following cycles counting methods: a-d – full cycles counting method (FCM), e-h – rainflow counting method (RFM)

Tab.2. Values of the spectrum filling factor ζ

| Cycles counting method | Load run | Two-parameter characteristics | | | |
|-----------------------------------|----------|-------------------------------|----------|-----------|----------|
| | | Model I | Model II | Model III | Model IV |
| Full cycles counting method (FCM) | Run A | 0.3327 | 0.3292 | 0.3181 | 0.3167 |
| | Run B | 0.1509 | 0.1407 | 0.1401 | 0.1396 |
| Rainflow counting method (RFM) | Run A | 0.3680 | 0.3404 | 0.3630 | 0.3625 |
| | Run B | 0.1531 | 0.1413 | 0.1411 | 0.1406 |

Tab. 3. Values of the maximum equivalent amplitude $S_{az\ max}$

| Cycles counting method | Load run | Two-parameter characteristics | | | |
|-----------------------------------|----------|-------------------------------|----------|-----------|----------|
| | | Model I | Model II | Model III | Model IV |
| Full cycles counting method (FCM) | Run A | 382.4 | 391.5 | 380.3 | 380.2 |
| | Run B | 364.9 | 382.4 | 361.3 | 360.6 |
| Rainflow counting method (RFM) | Run A | 347.3 | 372.8 | 342.7 | 341.3 |
| | Run B | 364.9 | 382.4 | 361.3 | 360.6 |

From the analysis of the parameters contained in Tab. 2 and 3 it may be concluded that as a result of cycles counting by means of the methods: full cycles counting method (FCM) and rainflow counting method (RFM), were determined the data sets differing to each other by share of cycles (especially those of large values of S_{a1}/S_{max}) in spectrum for particular loads. This is confirmed by values of spectrum filling factor ζ (Tab.2) as well as values of maximum equivalent amplitude $S_{az\ max}$ (Tab.3). In the case of the run A can be observed significant differences in load spectra (concerning both ζ and

$S_{az\ max}$ values), resulting from the assumed cycles counting method and used TFC model. In the case of the run B the differences in load spectra concern first of all the used two-parameter fatigue characteristics, whereas the cycles counting method did not have any influence on values either of ζ or $S_{az\ max}$.

RESULTS OF CALCULATIONS

The fatigue life calculations were conducted in stress mode by using Wöhler fatigue life diagram experimentally determined under load of $R = -1$. Its equation is of the following form:

$$\log S_a = -\frac{1}{9.80} \log N + 2.9611 \quad (6)$$

In the calculations the Palmgren-Miner's hypothesis on linear fatigue damage summation was used [8]; expressed as follows:

$$D = \sum_{i=1}^k \frac{n_i}{N_i} = 1.0 \quad (7)$$

and, results of fatigue life were presented in the form of a number of used load blocks, calculated from the equation:

$$\lambda = \frac{1}{D} \quad (8)$$

The calculations performed with the use of the equivalent load spectra made it possible to produce fatigue life diagrams in the coordinate frame $S_{max} = f(\lambda)$, where S_{max} is maximum stress value in load run. In Fig. 6 results of the calculations are presented in the form of fatigue life diagrams for the runs A and B.

Their preliminary assessment (Fig. 6) shows that the smallest fatigue life has been obtained for the load spectra determined by using the PCM method for the run A, that

results from the greater value of the equivalent amplitude $S_{az_{max}}$. The largest fatigue life has been reached for the run B and the RFM cycles counting method. Comparison of the results in the context of application of two-parameter fatigue characteristics to determining the equivalent load spectrum, shows that the smallest fatigue life was obtained for TFC model II, and the fatigue life values for the models: IM, III and IV are close to each other.

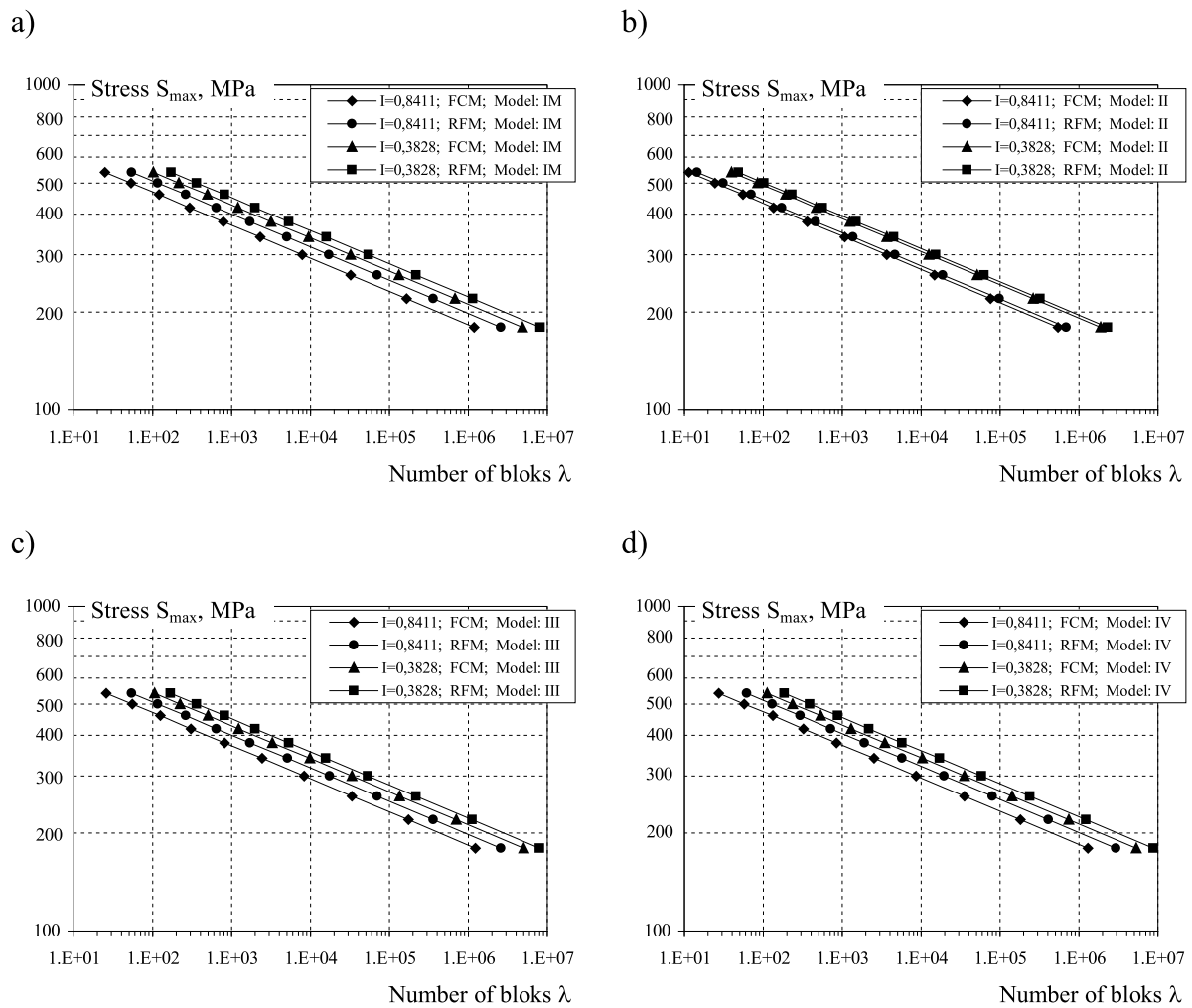


Fig. 6. Results of fatigue life calculations for load spectra determined by using two-parameter fatigue characteristics: a - model IM, b - model II, c - model III, d - model IV

ANALYSIS OF RESULTS OF THE RESEARCH

Differences between calculation results obtained for the assumed load runs as well as the applied method of cycles counting were determined on the basis of an analysis of value of the difference in relative fatigue lives $\delta_{(N)}$, calculated from the equation:

$$\delta_{(N)} = \frac{N_{(x)} - N_{(R=-1)}}{N_{(R=-1)}} \quad (10)$$

Value of the fatigue life $N(x)$ is that expressed by number of cycles determined from calculations, whereas $N_{(R=-1)}$ is that read from Wöhler diagram for value of the stress amplitude S_a ($S_a = S_{max}$). The results read from Wöhler diagram served as the reference point in the analysis. Values of relative differences between the analyzed characteristics are presented graphically in Fig. 7.

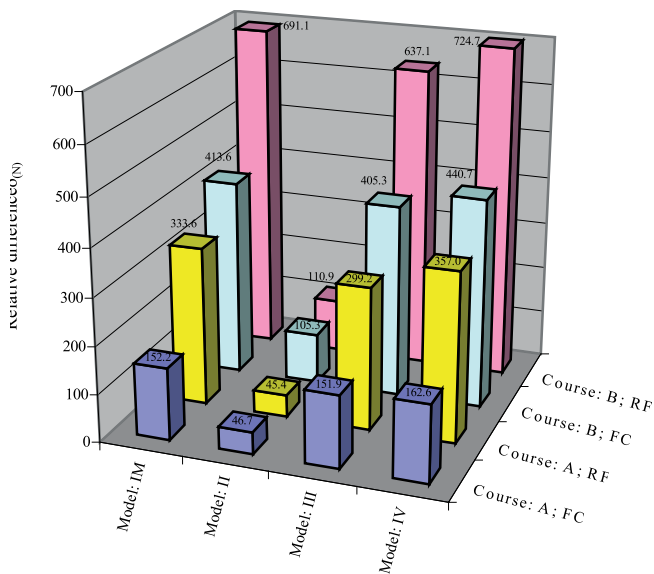


Fig.7. Values of relative differences in fatigue life for the assumed operational loads subjected to cycles counting by means of the selected methods as well as two-parameter models of fatigue characteristics

A detailed analysis indicates that the hardest load conditions were obtained for the run A subjected to processing by means of the full cycles counting method (FCM). Values of the relative differences in fatigue life are contained within the range from $\delta_{(N)II} = 46.7$ to $\delta_{(N)IV} = 162.6$. The largest fatigue life was reached for the model IV of two-parameter fatigue characteristics and all the block load spectra. In the case of the models: IM, III and IV similar results of fatigue life were obtained for particular equivalent load spectra. It results from rather small differences in values of the spectrum filling factor ζ and equivalent amplitude $S_{az,max}$. The smallest value of fatigue life was obtained for the model II of TFC characteristics as a consequence of occurrence, in the equivalent load spectrum, of cycles of significantly higher amplitude values in relation to the spectrum determined for the models: IM, III and IV.

The presented results of calculation of the relative differences $\delta_{(N)}$ make it also possible to determine relations between the assumed cycles counting methods. For the load run A the difference in fatigue life results, obtained during calculations performed according to the models: IM, III and IV, shows increase of fatigue life by about 100% for equivalent load spectra determined by using the rainflow counting method (RFM) in relation to the full cycles counting method (FCM). In the case of the load run B an increase in fatigue life also occurs but it reaches only about 40%.

SUMMARY

The way of preparing the equivalent load spectra, combined with application of the selected cycles counting methods (full cycles counting method and rainflow counting method) and two-parameter fatigue characteristics, revealed differences in results of fatigue life calculations. It may be stated that the calculation results are influenced by the assumed cycles

counting method and TFC model. In view of the close fatigue life results obtained for the models: IM, III and IV it is possible to use one of them for preparing the equivalent load spectra to be applied to calculations for a given kind of structural materials [4].

The presented set of fatigue life calculation methods makes it possible to take into account mean value of load cycles (having stress ratio values different from $R = -1$) in calculations where Wöhler fatigue life diagram determined for $R = -1$, is used. It is of a great importance in the case of estimating fatigue life of machinery elements working in conditions of broad - spectrum operational loads.

Choice of a model for determining the equivalent load spectra is associated with cyclic properties of a considered material. For example, the cyclic properties of S355J0 steel can be described by means of the model: IM, III and IV of two-parameter fatigue characteristics [4]. On this basis it is advisable to apply the above mentioned models of fatigue characteristics to calculations conducted in the preliminary stage of structural design process.

ABBREVIATIONS:

- FCM – full cycles counting method,
- PCM – peak counting method,
- RCM – simple-range counting method,
- RFM – rainflow counting method,
- RPM – range-pair counting method,
- TFC – two-parameter fatigue characteristics,
- HCF – range of high cycle fatigue,
- LCF – range of low cycle fatigue.

BIBLIOGRAPHY

1. Bendat J.S., Pierdol A.G., Methods of analysis and measurement of random signals (in Polish), PWN, Warszawa, 1976.
2. Kocańda S., Szala J., Fundamentals of fatigue calculations (in Polish), PWN, Warszawa, 1997.
3. Norma ASTM, Standard practices for cycle counting in fatigue analysis, ASTM Designation: E 1049-85 (Reapproved 1990).
4. Ligaj B., Szala G., Experimental verification of two-parametric models of fatigue characteristics by using the tests of S355J0 steel as an example, Polish Maritime Research, No.1 (2010), pp. 39-50.
5. Szala J., Loads and fatigue life of machine elements (in Polish), University of Technology and Agriculture, Bydgoszcz 1989.
6. Szala G., Ligaj B., Description of cyclic properties of steel in variability conditions of mean values and amplitudes of loading cycles, Materials Science Forum, Fatigue Failure and Fracture Mechanics, Vol. 726, 2012, pp. 69-76.

7. Szala G., Theoretical and experimental analysis of two-parametric fatigue life characteristics of structural steels (in Polish), 1st part of the monograph titled: Two-parametric fatigue life characteristics of structural steels and their experimental verification, Publishing House of Operation Technology Institute , State Research Institute, Radom, 2011.
8. Szala G., Comments on linear summation hypothesis of fatigue failures, Polish Maritime Research, No.3 (2014), pp. 77-85.

CONTACT WITH AUTHOR

Bogdan Ligaj

bogdan.ligaj@utp.edu.pl

Robert Sołtysiak

robert.soltysiak@utp.edu.pl

University of Technology and Science in Bydgoszcz
Faculty of Mechanical Engineering
Department of Mechanics and Machine Design
7 Prof. S. Kaliski Street
85-796 Bydgoszcz
Poland

phone:

(+48) 52 340 82 53

(+48) 52 340 82 78

PROFIT OPTIMALIZATION IN OPERATION SYSTEMS

Leszek Knopik, Assoc. Prof.

Klaudiusz Migawa, Assoc. Prof.

Andrzej Wdzięczny, Ph. D.

Bydgoszcz University of Science and Technology, Poland

ABSTRACT

The aim of this study is to analyse the effect of reducing the number of secondary damage to profit from the work of a technical object. Considering the criterion function that describes the average profit from the work of a technical object in the operation system. The study analyses a model of profit optimization, in which the design criterion function is based on the properties of Poisson branch process. Criterion function that describes the average gain is considered in the work at sufficiently general factors. Profit lifting model from the work of a technical facility is numerically exemplified. For the analysed electrical subsystem, intervals of time between the initial damage have exponential distribution, and between secondary damage - gamma distribution. In the presented example, the ability of profit optimization in operation systems of technical objects is demonstrated.

Keywords: Branching Poisson process, primary failure, secondary failure, gamma distribution, mean profit, hazard function

INTRODUCTION

In practice of the operational modes of transport, such as ships, issues regarding safety and reliability are very important. Issues of traffic safety of ships are considered in [6, 7]. An important issue in the operation of vessels is the reliability and readiness of the ship subsystems [8, 9]. In real operation systems, elimination of damage to a technical object is a desired action, which allows to provide the required level of reliability and increases the profits from the operation of a technical object. Reducing the number of defects can be achieved by improving the quality of diagnosis and improving the quality of repairs. Such actions require expenditures for equipment diagnostic subsystems and training of employees. It is known, that eliminating all or most of the damage is in practically impossible. This is related to high costs and expenditure on equipment diagnostic and repair subsystems. However, some measures for partial reduction of damage may be suitable. This work presents a model describing the change in profit while reducing some of the sudden or early damage. In practical reliability tests, a very important role is played by lifetime (time to failure) probability distributions of technical objects. The primary task in building operation process models is the identification of the available experimental data of lifespan time types distribution. These distributions describe the time to failure of an element, subsystem and operation system. Some damage arising in the operation process are the result of natural processes of wear and degradation of technical objects elements. However, other damage may result from inaccurate and ineffective repair of technical object parts that were damaged previously and

also be the result of improper organization of repairs and insufficiently accurate diagnosis. Such damage in operation is called secondary. Improvement of this state often requires additional expenditure on diagnostic equipment and training of personnel. Analysis of operation systems work leads to the observation that damage to the technical object can be divided into two subsets. The first is the original damage, the other secondary damage. Secondary damage arises most frequently as a result of ineffective technical object items repair of previous damage. This fact makes the studied intervals population of time damage a statistically heterogeneous collection. In this case, for the description of life time, a mixture of probability distributions may be used. Mixtures of probability distributions were used as technical objects lifetime models in [15, 16, 17]. Analysis of the mechanism of damage generation leads to the conclusion, that most often original damage generates a series of secondary damage. In [18] an attempt to solve this problem has been undertaken based on the insight, that the time intervals between subsequent secondary damage in relation to the time interval between original damage are generally lower. Criterion function studied in [18] uses the properties of mixtures of probability distributions. Time to failure probability distributions are intensively used in the theory and practice of reliability. In practice, we encountered many situations of probability distributions conformance testing of time to failure with the known distributions. However, in operation practice, there are often situations where a the technical object is damaged suddenly and the recorded damage intervals are relatively small. The probability distribution of time to damage due to the heterogeneity is convenient to be described using mixtures

of probability distributions. Time to failure in [16] is described by a distribution of exponential and Rayleigh mixture. Often in engineering practice, sudden damage are considered to be those, that occur on the same day after the repair. In this case, it is expedient to use mixtures of the known distributions such as exponential decay, gamma and Weibull distribution with a single point distribution. The problem of estimating parameters, when considering the mixture of single-point distribution with exponential distribution has been studied in [1, 12, 13, 14, 20, 21]. Parameter estimation of single-point distribution mixture with gamma distribution is presented in [22], while with the Weibull distribution in [23]. It is the motivation to use as a model the process of damage stationary branch Poisson process. The first time the Poisson branch process to describe the damage process was introduced by Bartlett [2] and Lewis [3, 19]. The study demonstrates, that this process can be an adequate model of the process of damage to the electrical subsystem for certain means of transport. The profits model uses the properties of Poisson branch process and the function describing effort to improve the diagnostics of a technical object state.

BASIC DEFINITIONS AND CONCEPTS

The study assumes, that T is a positive random variable describing the life time of a technical object till it gets damaged. The non-negative random variable T has a finite mean value ET , distribution function $F(t)$ satisfying the condition $F(0) = 0$, reliability function $R(t) = 1 - F(t)$, the probability density $f(t)$. In this case, the risk function is defined as $\lambda(t) = f(t) / R(t)$. In reliability theory and planning of preventive repair, a very large role has the distribution equivalent to the given distribution of the random variable T . The cumulative distribution of the equivalent distribution (see [4]) corresponding to the distribution with the cumulative distribution $F(t)$ is defined as:

$$F_E(t) = \int_0^t R(u)du / ET$$

where ET is the mean value of a random variable T .

The variable probability density with equivalent distribution is expressed by the formula:

$$f_E(t) = R(t) / ET$$

the equivalent distribution of risk function is equal to:

$$\lambda_E(t) = R(t) / (ET R_E(t))$$

where $R_E(t) = 1 - F_E(t)$.

Many considerations in the theory of reliability use the function of the residual lifetime. If the condition $ET < \infty$ is satisfied, then the average residual lifetime function of the variable T is with $R(t) > 0$ defined as:

$$m(t) = E(X - t | X > t) = \int_t^\infty R(u)du / R(t)$$

whereas with condition $R(t) = 0$ it is assumed, that $m(t) = 0$. The properties of $m(t)$ function were studied in [5, 10, 11]. The give equality is true:

$$ET = m(0) = \int_0^\infty R(u)du$$

THE DAMAGE PROCESS MODEL

In this chapter, a model of the damage process is presented. The damage process has been constructed as a superposition of two processes. It is assumed, that a sequence of independent random variables Z_1, Z_2, \dots is considered, where each of them determines the time to original failure. The original damage generates an additional series S of secondary damage. The intervals between secondary damage is determined by Y_1, Y_2, \dots, Y_S . An assumption has been assumed, that random variables Y_1, Y_2, \dots, Y_S are independent and have the same distribution reliability function $R_Y(t)$. The random variable S can take the values $0, 1, 2, \dots$. The combined process is the superposition of the original damage process and secondary damage process. In the superposition of the processes, both types of damage are indistinguishable. The process is called the Poisson stationary branch process. The original damage resulting from the impact of the natural processes of wear and degradation of a technical object are separated by time intervals $Z_i, i = 1, 2, \dots$. The first original damage occurs after the initial time Z_1 and may generate secondary damage because of inefficient repair after time Y_1 . However, the repair of secondary damage may also be inefficient and after time Y_2 another secondary damage may occur.

It is convenient to assume, that the random variables Z_1, Z_2, \dots are independent and have the same exponential distribution with density, then

$$f_Z(t) = \lambda \exp(-\lambda t),$$

where $\lambda > 0$ and $t \geq 0$.

A sequence of random variables $Z_i, i = 1, 2, \dots$ is generated by Poisson stationary process. Time between following damage in Poisson stationary branch process will be marked with T . In [3, 19] it was shown, that the reliability function of the random variable T is given by:

$$R_T(t) = \frac{1 + ES \times R_Y(t)}{1 + ES} \exp\{-\lambda t - \lambda \times ES \int_0^t R_Y(u)du\} \quad (1)$$

Based on this formula, one can determine most of the probabilistic properties of the process. Introducing designation

$$ET_T(t) = \int_0^t R_T(u)du$$

for $ET_T(t)$ occurs

$$ET_T(0) = 0$$

$$ET_T(\infty) = ET$$

Integrating equation (1) can be shown, that

$$ET_T(t) = (1 - \exp(-\varphi(t)) / (\lambda (1 + ES)))$$

where

$$\varphi(t) = \lambda t + ES \int_0^t R_Y(u) du \quad (2)$$

Then, a formula for the mean value ET can be written

$$ET_T(\infty) = ET = 1 / (\lambda (1 + ES))$$

In [3, 19] formulas for the variance D²T have been derived from:

$$D^2T = (1 + 2 ES \exp(-\lambda (1 + ES)) EY) / (\lambda (1 + ES))^2$$

The variation coefficient V is now expressed by the formula:

$$V = 1 + 2 ES \exp(-\lambda (1 + ES)) EY$$

The lower and upper limit for the variance and coefficient of variation based on [3, 19] can be written as:

$$1 / (\lambda^2 (1 + ES)^2) \leq D^2T \leq (1 + 2 ES) / (\lambda^2 (1 + ES)^2)$$

$$1 \leq V \leq 1 + 2 ES$$

The last equality shows, that coefficient of variation for the time between damage is always greater than or equal to 1. From the reliability theory, it is known, that the coefficient of variation V is equal to 1 for the exponential distribution. The function of the average residual time of a random variable T can be written as:

$$m(t) = (ET - ET(t)) / R_Y(t)$$

and

$$m(t) = 1 / \varphi'(t)$$

Based on the above considerations, the following properties can be formulated for a random variable:

Property 1. Function m(t) of the average residual time of a random variable T is increasing

Property 2. For function $\varphi(t)$ the inequalities $\varphi'(t) > 0$ and, $\varphi''(t) \leq 0$ are true.

Property 3. Risk function of a random variable T has the form:

$$\lambda_T(t) = \varphi'(t) - \varphi''(t) / \varphi'(t)$$

Property 4. Cumulative distribution of equivalent distribution is expressed by the formula:

$$F_E(t) = 1 - \exp(-\varphi(t)) \text{ for } t \geq 0$$

Property 5. The risk function of an equivalent distribution is expressed by the formula:

$$\lambda_E(t) = \varphi'(t)$$

Example 1. The object of the research in this example is a company holding 190 public transport buses. The company uses buses of different brands and types. In the example, it is considered that n = 1149 of time intervals between successive electrical bus subsystem damage. It is assumed, that the intervals between the secondary damage have gamma distribution with probability density in the form of:

$$f(x) = \frac{1}{\beta^\alpha \Gamma(\alpha)} x^{\alpha-1} e^{-x/\beta}$$

where $x > 0, \alpha > 0, \beta > 0,$

$\Gamma(\alpha)$ means the gamma function defined by the formula:

$$\Gamma(\alpha) = \int_0^\infty x^{\alpha-1} e^{-x} dx$$

To evaluate the parameters of the distribution function of reliability (1) the method of maximum likelihood has been used. Parameters of the gamma distribution describe the time distribution between secondary damage rated by maximum likelihood method. The parameters of this distribution have values: $\alpha = 2,592,$ $\beta = 0,3632.$ The parameter λ of exponential distribution describing the distribution of time between the original damage was assessed as: $\lambda = 0,03804.$ The average value of a series of secondary damage has been rated as $ES = 1,9997.$ On the basis of estimated values of the parameters α, β, λ and $ES,$ calculated were the average value of time between original damage $EZ = 26,88,$ the value of the average time between secondary damage $EY = 0,9415.$ The value of the average time between any damage is equal to $ET = 8,7630.$ The compliance of empirical distribution of time between damage with the distribution set by the reliability function $RT(t)$ defined by the formula (1) was tested using two tests of conformity: $\lambda -$ Kolmogorov and $\chi^2 -$ Pearson test. The calculated statistics value $\lambda = 0,647$ is correspondent to the value of the level of significance $p = 0,21,$ while for the test $\chi^2 -$ Pearson calculated $\chi^2 = 39,3,$ at $p = 0,28.$ The applied compatibility tests confirm the high compatibility of the analysed data with the distribution resulting from the applying the Poisson stationary branch process to describe the process of damage with the function of reliability given by formula (1). The estimation of the damage parameters process model and testing its compatibility with data from the actual process of operation of the bus electric subsystem is illustrated in Figure 1.

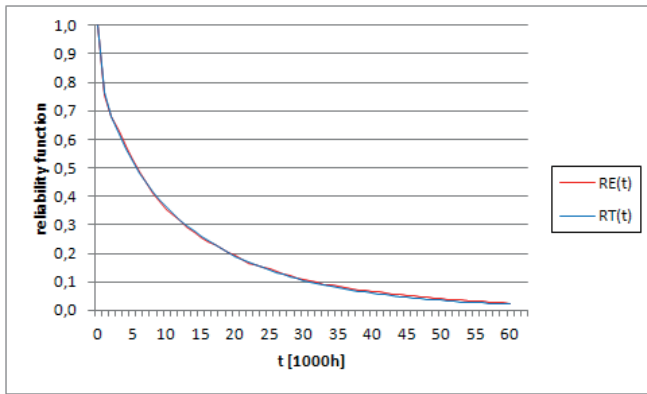


Fig. 1. Theoretical $R_t(t)$ and empirical $R_e(t)$ function reliability chart

Figure 1 shows the course of empirical reliability function $R_e(t)$ and the reliability function of the test model $R_t(t)$.

PROFIT OPTIMIZATION MODEL BASED ON POISSON BRANCH PROCESS

It was assumed, that the average profit from the work of a technical object is proportional to the mean time till damage ET. This profit was determined by $g_1(t)$ and assumes that

$$g_1(t) = e / (\lambda (1 + t))$$

where $e > 0, 0 \leq t \leq ES$.

It is obvious, that $g_1(0) = e/\lambda$ means profit from the work of a technical object, in which there are no secondary damage, while $g_1(ES) = e/(\lambda (1 + ES))$ is the profit from the work before trying to invest in reducing the number of secondary damage. The reduction of secondary damage amount is realized in the model by reducing the average value of ES, whereas other parameters of the reliability function (1) remain unchanged.

By $h_2(t) = -g_2(t)$ effort to eliminate secondary damage has been marked. It has been assumed, that the function $g_2(t)$ is twice differentiable on the interval $(0, ES)$ and meets the following assumptions:

$$g_2(t) < 0, g_2(0^+) = -\infty, g_2(ES^-) = 0, \quad (3)$$

$$g_2'(t) > 0, g_2'(0^+) = +\infty, g_2'(ES^-) = 0, \quad (4)$$

$$g_2''(t) < 0, \quad (5)$$

Criterion function expressing the average profit from the work of a technical object has the form;

$$g(t) = g_1(t) + g_2(t)$$

At this point of work, it was assumed, that the function $g_2(t)$ has the form:

$$g_2(t) = \frac{b}{t^2} + \frac{c}{t} + d$$

Criterion function for the optimization problem is now as follows:

$$g(t) = \frac{a}{1+t} + \frac{b}{t^2} + \frac{c}{t} + d$$

where $a = e/\lambda$.

From the form of function $g_2(t)$ is clear, that $g_2(t) = -\infty$ if and only if $b < 0$, and $g_2(ES^-) = 0$ if and only if

$$b + c ES + d (ES)^2 = 0 \quad (6)$$

Derivative $g_2'(t)$ is:

$$g_2'(t) = -\frac{2b}{t^3} - \frac{c}{t^2}$$

Equality $g_2'(0^+) = +\infty$ occurs because $b < 0$. Equality $g_2'(ET) = 0$ is true if and only if

$$b = -0,5c ES \quad (7)$$

One can check, that if $b = -0,5c ES$, then $g_2'(t) \geq 0$, for $t \in (0, ES)$.

The second order derivative is given by formula:

$$g_2''(t) = \frac{6b}{t^4} + \frac{2c}{t^3} \quad (8)$$

Equality $g_2''(0^+) = -\infty$ is true because $b < 0$.

From inserting (7) into equation (6) we have

$$g_2''(t) = \frac{-3cES}{t^4} + \frac{2c}{t^3}$$

From the form of the last formula, it is concluded, that if $t \in (0, ES)$, then $g_2''(x) < 0$.

From inserting (8) into (9), one gets

$$d = -e/(2 ES)$$

The function $g_2(t)$ can be written as:

$$g_2(t) = -\frac{1}{2} \frac{cES}{t^2} + \frac{c}{t} - \frac{c}{2ES}$$

From the embodiment of the above written formula, one can see, that function $g_2(t)$ depends only on parameter c , whereas the criterion function depends on a and c .

Below, the criterion function $g(t)$ is tested by formula (6).

It is known, that $g(0^+) = 0$ if and only if $b < 0$. The derivative of the criterion function has the form

$$g'(t) = \frac{-a}{(1+t)^2} - \frac{2b}{t^3} - \frac{c}{t^2}$$

It is easy to note, that $g'(0^+) = +\infty$ and that

$$g'(ES) = -\frac{a}{(1+ES)^2} < 0$$

Thus, the derivative $g'(t)$ changes the sign from + to - in the interval (0, ES).

The following shows, that the sign change occurs exactly once. The second order derivative of the criterion function is given by formula:

$$g''(t) = \frac{2a}{(1+t)^3} + \frac{6b}{t^4} + \frac{2c}{t^3}$$

Taking into account (7) one can store the following inequality:

$$g''(t) < \frac{2a}{t^3} + \frac{2c}{t^3} - \frac{3cES}{t^4}$$

Inequality $g''(t) < 0$ comes from inequality

$$2(a+c)t - 3cES < 0$$

If $2a < c$, then for $t \in (0, ES)$ occurs $g''(t) < 0$. This means, that the derivative $g'(t)$ changes sign from „+” to „-” exactly once. One, one can formulate:

Conclusion: If $2a < c$ and relations (3), (4) and (5) are true, then the criterion function $g(t)$ reaches a clear maximum in the interval (0, ES).

The following example contains the numerical illustration of this proposal.

Example 2. In the analysed example, the base is the process model of the electrical system failures considered in example 1 of this work. The intervals between the original damage have the exponential distribution with parameter $\lambda = 0,03804$, whereas intervals between secondary damage have the gamma distribution with parameters $\alpha = 2,592$, $\beta = 0,3632$. The average value of the secondary damage value length has been assessed as $ES = 1,9997$.

In the discussed example, it is assumed, that the ratio of the criterion function is $a = 0,0833$. The calculations were performed for three different values of the parameter c , $c \in \{0,8; 1; 1,2\}$. Figure 2 shows the waveform of the criterion function for three different values of the parameter c . Each analysed realization of the criterion function is achieves a maximum value at a certain point.

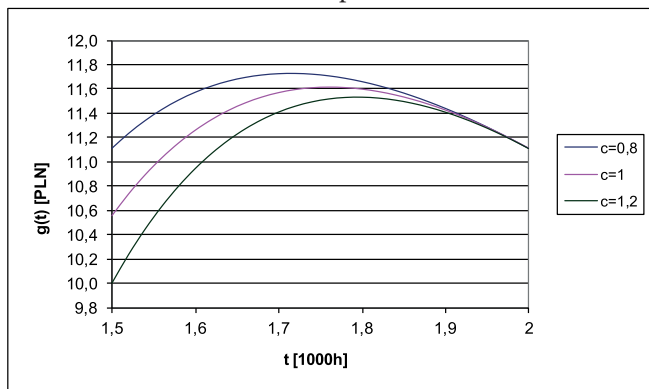


Fig. 2. The dependency of the average profit $g(t)$ from time t [1000h]

CONCLUSIONS

The study shows, that if the general conditions of the process of damage are met, it is possible to raise the profits of the operation of a technical object in the operation system. The basic assumption in this work is the presence of two types of damage that are called original and secondary damage in this work. The model of profit function has been based on the properties of the Poisson branch process. The numerical example presented in the second part of the work shows, that it is possible, under certain expenditures to eliminate secondary damage and obtain higher profits in the operation system.

BIBLIOGRAPHY

1. Aitchison, I.: On the distribution of a positive random variable having a discrete probability mass at origin, *Journal of the American Statistical Associations*, vol. 50, pp. 901–908, 1955
2. Bartlett, M. S.: The spectral analysis of point processes, *Journal Royal Statistical Society, Series B* 25, pp. 264–296, 1963
3. Cox, D.R. and Lewis, P.A.W.: *The Statistical Analysis of Series of Events*, Methuen, NewYork, John Wiley, 1966.
4. Deshapande, J. V. and Kochar, S.C.: Aspects in positive ageing, *Journal of Applied Probability*, 23, pp. 748–758, 1986
5. Ghai, G.L. and Mi, J.: Mean residual life and its association with failure rate, *IEEE Transactions on Reliability*, vol. 48, No. 3, pp. 262–266, 1999
6. Girtler, J.: Application of theory of semi-Markov processes to determining distribution of probabilistic process of marine accidents resulting from collision of ships. *Polish Maritime Research* 1(81) 2014, vol.21
7. Girtler J., Kitowski Z., Kuriata A.: *Safety of ship at sea* (in Polish), WKiŁ, Warszawa 1995
8. Girtler J. : *Availability of sea transport means*. *Archives of Transport, Polish Academy of Sciences Committee of Transport, Quarterly*, vol. 9, pp. 3-4, Warsaw 1997
9. Girtler J. : *Possibility of marine diesel engines*. *Journal of Polish CIMAC*, No. 1 vol. 4, Gdańsk 2009
10. Guess, F. and Proschan, F.: *Mean Residual Life: Theory and Applications*, *Handbook of Statistics*, Editors: Krishnaiah, P.R. and Rao, C.R., Elsevier Science Publishers, Amsterdam, vol. 7, pp. 215–224, 1988
11. Hall, W.J. and Wellner, J.A.: *Mean residual life*, *Statistics and Related Topics*, Eds. Csorgo J.N., Rao J.N.K. and Saleh A.K. Md, E., North Holland, Amsterdam, pp. 169–184, 1981

12. Jayade, V. P. and Parasad, M. S.: Estimations of parameters of mixed failure time distribution, *Communications Statistics, Theory and Method*, vol. 19, pp. 4667–4677, 1996
13. Kale, B. K. and Muralidharan, K.: Optimal estimating equations in mixture distributions accommodating instantaneous or early failures, *Journal Indian Statistical Associations*, vol. 38, pp. 317–329, 2000
14. Kleyle, R.M. and Dahiyam R.L.: Estimation of parameters of mixed failure time distribution from censored data, *Communications Statistics, Theory and Method*, vol. 4, pp. 873–882, 1975
15. Knopik, L.: Mixture of distributions as a lifetime distribution of a technical object, *Scientific Problems of Machines Operation and Maintenance*, vol. 45, 2(165), pp. 53–60, 2010
16. Knopik, L.: Model for instantaneous failures, *Scientific Problems of Machines Operation and Maintenance* vol. 46, 2(166), pp. 37–48, 2011
17. Knopik, L.: Statistical analysis of failures, *Journal of Polish CIMAC, diagnosis, reliability and safety*, vol. 7, No. 2, pp. 91–96, 2012
18. Knopik, L.: Model of profit improvement in maintenance system, *Journal of Polish CIMAC, diagnosis, reliability and safety*, vol. 7, No. 2, pp. 91–96, 2013
19. Lewis, P.A.W.: A branching Poisson process model for the analysis of computer failure patterns, *Journal Royal Statistical Society, B* 26, pp. 398–456, 1963
20. Muralidharan, K.: Test for mixing proportion in mixture of a degenerate and exponential distributions, *Journal Indian Statistical Associations*, vol. 37, pp. 105–119, 1999
21. Muralidharan, K.: The UMVUE and Bayes estimate of reliability of mixed failure time distribution, *Communications Statistics, Simulation Computer*, vol. 29, No. 2, pp. 603–158, 2000
22. Muralidharan, K. and Kale B.K.: Modified gamma distribution with singularity at zero, *Communications Statistics, Simulation Computer*, vol. 31, No. 1, pp. 143–158, 2002
23. Muralidharan, K. and Lathika, P.: Analysis of instantaneous and early failures in Weibull distribution, *Metrika* vol. 64, pp. 305–316, 2006

CONTACT WITH THE AUTHOR

Leszek Knopik

Faculty of Management
Bydgoszcz University of Science and Technology
Fordońska 430 St.
85-790 Bydgoszcz
Poland

e-mail: knopikl@utp.edu.pl

Klaudiusz Migawa

Faculty of Mechanical Engineering,
Bydgoszcz University of Science and Technology
Prof. S. Kaliskiego 7 St.
85-763 Bydgoszcz
Poland

e-mail: klaudiusz.migawa@utp.edu.pl

Andrzej Wdzięczny

Faculty of Mechanical Engineering
Bydgoszcz University of Science and Technology
Prof. S. Kaliskiego 7 St.
85-763 Bydgoszcz
Poland

e-mail: andy@utp.edu.pl